

---

**Abrasive Wear Behaviour of Steels and  
Advanced HVOF-Sprayed WC-M Coatings**

---

**Saied Mehran Nahvi, BEng**

**Thesis submitted for the degree of  
Doctor of Philosophy**

**Department of Mechanical, Materials, and Manufacturing  
Engineering  
The University of Nottingham**

**April 2011**

# Abstract

---

This thesis concerns a study of the three-body abrasive wear behaviour of two groups of materials with different abrasive particles using the Dry Sand Rubber Wheel (DSRW) test method. This investigation can be divided into three sections:

In the first section, the abrasion of a range of steels with an ash from a biomass power station was compared with that observed for abrasion with a conventional silica abrasive. It was seen that the wear rate of the steels when abraded with silica increased in proportion to the applied load and decreased with the hardness of the steel. However, the bottom-ash was more friable than the silica abrasive, and as such, significantly more abrasive crushing was observed during the tests with the bottom-ash abrasive. It is proposed that the wear is dominated by abrasion by the larger particles in the distribution, and that damage is limited by the maximum load which the particles can sustain before failing.

In the second section, the motion of particles in the DSRW test with silica abrasive against a range of steels, as a function of applied load and the hardness of the steels was studied. The results showed that particle rolling through the contact is favoured by low applied loads and low testpiece hardness whereas particle sliding through the contact is favoured by high applied loads and high testpiece hardness. A model was proposed to provide an analysis of the motion of particles in the DSRW test. The effect of hardness on particle rotation is well predicted by the model, but the effect of the applied load on particle motion observed experimentally is opposite to that which is predicted by the model. The

shortcomings of the model are discussed, and the model has been qualitatively modified to account for this discrepancy.

In the third section, five different WC-metal cermet powders were deposited as coatings by HVOF thermal spraying. These were a WC-nickel alloy, a WC-iron alloy and three types of WC-Co powders with different carbide grain sizes. Characterisation of the coatings showed decomposition of WC during spray process for all the coatings. The results show different solubilities of W and C in the binders and different precipitation characteristics. DSRW tests were performed to assess the wear resistance of the coatings with silica and alumina abrasives. It was found that the coatings had different wear rates and mechanisms when abraded with silica compared with alumina. The differences in the wear behaviour of the coatings are due to the differences in powder characteristics, the extent of reaction and decarburisation during spraying, and the subsequent development of the microstructure in the coating during splat solidification at high cooling rates.

# Publications

---

- 1- Particle motion and modes of wear in the dry sand-rubber wheel abrasion test

Author(s): Nahvi, SM; Shipway, PH; McCartney, DG

WEAR Volume: 267 Issue: 11 Pages: 2083-2091 Published: 2009

- 2- Effects of particle crushing in abrasion testing of steels with ash from biomass-fired powerplants

Author(s): Nahvi, SM; Shipway, PH; McCartney, DG

WEAR Volume: 267 Issue: 1-4 Pages: 34-42 Published: 2009

# Acknowledgement

---

I wish to express my appreciation to my supervisors, Professors Philip Shipway and Graham McCartney for their supervision, advice and encouragement throughout my PhD.

I especially want to express my gratitude to Professor Philip Shipway who has always been very supportive and patient and his efforts are sincerely appreciated.

It is a pleasure to acknowledge the assistance I have received in the laboratory works from many members of staff, technicians and colleagues in the Wolfson building. Special thanks go to Mr. Keith Dinsdale and Dr. Nigel Neate who have helped me on numerous occasions.

Last but not least, I would like to express my deepest affection and gratitude to my spouse, Safura for her continual support, love and encouragement and also Ahmad, Mahdi and Mohammad, my darling sons for making my stay in UK most enjoyable and memorable.

# Contents

---

<b>Abstract</b> .....	<i>ii</i>
<b>Publications</b> .....	<i>iv</i>
<b>Acknowledgement</b> .....	<i>v</i>
<b>Contents</b> .....	<i>vi</i>
<b>Nomenclature</b> .....	<i>x</i>
<b>Chapter 1 Introduction</b> .....	<b>1</b>
<b>Chapter 2 Literature Review</b>	
2.1 <u>Abrasive Wear</u> .....	<b>9</b>
2.1.1 Introduction.....	9
2.1.2 Types of Wear.....	10
2.1.3 Abrasive Wear Processes.....	12
2.1.3.1 Two and Three-body Abrasion Wear .....	12
2.1.3.2 Open and Closed Abrasive Wear .....	13
2.1.3.3 High and Low stress Abrasive Wear.....	14
2.1.4 Mechanism of Abrasive Wear .....	14
2.1.4.1 Plastic Deformation.....	15
2.1.4.2 Fracture.....	16
2.1.5 Variables Affecting Abrasive Wear.....	17
2.1.5.1 Properties of the Particle .....	17
2.1.5.2 Properties of the Material .....	19
2.1.5.3 Characteristics of the Test setup and Environment.....	20
2.1.6 Abrasive Wear Tests.....	22
2.1.6.1 Laboratory Abrasive Wear Tests.....	22
2.1.6.2 Standard Test of Abrasive Wear .....	23
2.1.6.3 Dry Sand Rubber Wheel Test.....	24
2.1.6.4 Rubber Wheel Variables .....	25
2.1.7 Abrasive Wear Behaviour of Steels.....	27
2.1.8 Abrasive Wear with Ash Particles.....	28
2.1.8.1 Introduction .....	28
2.1.8.2 The Ash Originating From Combustion.....	28
2.1.8.3 Coal Ash.....	29
2.1.8.4 Biomass Ash.....	30
2.1.8.5 Abrasive Testing of the Ash.....	31
2.1.9 Abrasive Wear of WC-Metal Coatings.....	31
2.1.9.1 Introduction .....	31
2.1.9.2 Abrasive Wear of Sintered WC-Metal Cermets.....	32
Wear Mechanism.....	32

Microstructural and Mechanical Properties.....	34
2.1.9.3 Abrasive Wear of Thermally Sprayed WC Coatings .....	37
2.1.9.4 Variables Affects on Abrasion Performance.....	38
Feedstock powder .....	38
Decomposition of WC .....	39
WC Grain Size and Content .....	44
Porosity .....	46
2.1.9.5 Abrasive Wear Mechanisms.....	47
2.1.9.6 Abrasive Wear Resistance.....	48
2.2 <u>HVOF- Sprayed WC Cermet Coatings</u> .....	51
2.2.1 Introduction.....	51
2.2.2 HVOF Process Variables.....	53
2.2.2.1 Feedstock Powder.....	54
2.2.2.2 Fuel Gas.....	55
2.2.2.3 Powder Carrier Gas .....	55
2.2.2.4 Gun Design.....	56
2.2.2.5 Stand Off Distance .....	56
2.2.2.6 Travers Speed.....	56
2.2.3 Sintered WC Cermet Materials.....	57
2.2.4 Thermally Sprayed WC coatings.....	57
2.2.4.1 Feedstock Powder.....	58
2.2.4.2 Phase Transformation during spraying process.....	59
2.2.4.3 Phase Content and Composition.....	62
2.2.4.4 Microstructure and Mechanical Properties.....	64

### Chapter 3 Experimental Procedures

3.1 <u>Abrasive Wear Testing</u> .....	82
3.1.1 Introduction.....	82
3.1.2 Test Method and Apparatus.....	83
3.1.3 Characterisation of Abrasive Particles.....	84
3.1.3.1 Abrasive Materials .....	84
3.1.3.2 Analysis of Size.....	85
3.1.3.3 Morphology.....	85
3.1.3.4 Hardness .....	85
3.1.3.5 Fracture Strength .....	86
3.1.4 Characterisation of Worn Surfaces.....	86
3.1.4.1 Wear Scar Investigation .....	86
3.1.4.2 Profilometry Assessment.....	86
3.1.4.3 Temperature of Sample during Wear Testing.....	87
3.1.4.4 Particles Fragmentation Following Wear Test.....	87
3.2.5 Abrasive Wear Testing of Steel Substrates .....	88
4.2.5.1 Test Materials .....	88
4.2.5.2 Hardness Testing.....	89
3.1.6 Abrasive Wear Testing of Sprayed Coatings.....	89
3.2 <u>Coating Properties and Characterizations</u> .....	90
3.2.1 Materials .....	90
3.2.1.1 Powders .....	90
3.2.1.2 Substrates.....	90

3.2.2	Spray Systems and Parameters .....	91
3.2.3	Characterisation of Powder Feedstock .....	91
3.2.3.1	Size Analysis .....	91
3.2.3.2	X-ray Diffraction (XRD).....	92
3.2.3.3	Scanning Electron Microscopy (SEM) and EDX Analysis.....	92
3.2.4	Characterisation of Coatings.....	93
3.2.4.1	XRD.....	93
3.2.4.2	SEM.....	93
3.2.4.3	Microhardness .....	93
3.2.4.4	Chemical Analysis.....	94
3.2.4.5	Phase Volume Fraction and WC Grain Size Analysis .....	94
3.2.4.6	Porosity.....	95
3.2.4.7	Fracture Toughness .....	95

## Chapter 4 Abrasive Wear of Steel Substrates: Results and Discussion

4.1	<u>Introduction</u> .....	101
4.2	<u>Results</u> .....	102
4.2.1	Characterisation of Abrasive Particles.....	102
4.2.1.1	Abrasive Materials .....	102
4.2.1.2	Morphology and Particle Size Analysis .....	102
4.2.1.3	Mechanical Properties .....	103
4.2.1.4	Particle Density .....	104
4.2.2	Characterisation of Steel Substrates .....	105
4.2.2.1	Analysis of Elements.....	105
4.2.2.2	Hardness .....	106
4.2.3	Characterisation of Wear Performance.....	106
4.2.3.1	Abrasion of Steels .....	106
4.2.3.2	Temperature of Wear Samples during the Test.....	108
4.2.3.3	Particles Fragmentation during Wear Test.....	109
4.2.3.4	Particles in Contact Zone during Abrasion .....	111
4.2.3.5	Particle Loading During Abrasion testing.....	112
4.3	<u>Discussion</u> .....	115
4.3.1	Abrasive Wear of steels with Ash .....	115
4.3.1.1	Abrasive Particle Characteristics.....	115
4.3.1.2	Wear Behaviour.....	116
4.3.2	Abrasive Wear of Steels with Silica .....	119
4.3.2.1	Wear Rate and Mechanisms .....	119
4.3.2.2	Particle Motion during Abrasion.....	120
	Effect of Sample Hardness .....	121
	Effect of Applied Load.....	125
	General Observations .....	127
4.3.2.3	Effect of Silica Particle Size and Shape on Wear .....	128

## Chapter 5 Characterisation of Coatings: Results and Discussion

5.1	<u>Introduction</u> .....	158
-----	---------------------------	-----

5.2	<u>Results</u> .....	159
5.2.1	Characterisation of Powders .....	159
5.2.1.1	Chemical Analysis.....	159
5.2.1.2	Morphology and Particle Size Analysis .....	159
5.2.1.3	Microstructure and Phase Analysis .....	160
5.2.2	Characterisation of As-Sprayed Coating .....	161
5.2.2.1	Chemical Analysis.....	161
5.2.2.2	Microstructure and Phase Analysis .....	161
5.2.2.3	Mechanical properties .....	165
5.3	<u>Discussion</u> .....	165
5.3.1	Characterisation of Powders .....	165
5.3.2	Characterisation of As-Sprayed Coating .....	166

**Chapter 6 Abrasive Wear of HVOF Sprayed Coatings:  
Results and Discussion**

6.1	<u>Introduction</u> .....	187
6.2	<u>Results</u> .....	188
6.2.1	Characterisation of Abrasive Particles.....	188
6.2.1.1	Abrasive Materials .....	188
6.2.1.2	Morphology and Particle Size Analysis .....	188
6.2.1.3	Hardness .....	189
6.2.2	Characterisation of Worn Surfaces .....	189
6.2.2.1	Abrasion of Coatings.....	189
6.2.2.2	Wear Scar Investigation .....	191
6.3	<u>Discussion</u> .....	195
6.3.1	General Observations.....	195
6.3.2	Abrasive Wear with Silica.....	197
6.3.3	Abrasive Wear with Alumina .....	202

**Chapter 7 Conclusions**

7.1	<u>Abrasion of Steel Substrates</u> .....	236
7.2	<u>HVOF-Sprayed WC Cermet Coatings</u> .....	238
7.3	<u>Abrasion of the WC Cermet Coatings</u> .....	239
7.4	<u>Industrial Aspects</u> .....	242

**Chapter 8 Future Work .....** 244

<b>References</b> .....	246
-------------------------	-----

# Nomenclature

---

Al	aluminium
Al <sub>2</sub> O <sub>3</sub>	aluminium oxide (alumina)
APS	air plasma spraying
AR <sub>p</sub>	particle aspect ratio
ASTM	the American Society for Testing and Materials
at%	atomic percent
BCC	body-centered cubic
BOD	ball-on-disc
BSE	backscattered electron
C	carbon
°C	degree Celsius
Cermet	ceramic-metal composite
C <sub>3</sub> H <sub>8</sub>	propane
CO	carbon monoxide
CO <sub>2</sub>	carbon dioxide
Co	cobalt
Co-I	powder or coating of WC-17wt% Co with carbide size of ~1 μm
Co-II	powder or coating of WC-17wt% Co with carbide size of ~0.8 μm
Co-III	powder or coating of WC-17wt% Co with carbide size of ~0.5 μm
Cr	chromium
Cu	copper
D-Gun	detonation gun
DSRW	dry sand rubber wheel
$d_p$	particle diameter
D <sub>WC</sub>	tungsten carbide grain size
EDX	energy dispersive X-ray analysis
FCC	face-centred cubic
Fe	Iron
Fe (powder/coating)	powder or coating of WC-15wt% iron alloy (FeCrAl) with carbide size of ~0.5 μm
H <sub>c</sub>	cermet hardness

## *Nomenclature*

HCP	hexagonal closed packed
gf	gram force
H <sub>2</sub>	Hydrogen
H	hardness, kgf mm <sup>-2</sup>
H <sub>a</sub>	abrasive hardness, kgf mm <sup>-2</sup>
H <sub>s</sub>	surface hardness, kgf mm <sup>-2</sup>
H <sub>v</sub>	Vickers hardness, kgf mm <sup>-2</sup>
HVAF	high velocity air fuel
HVOGF	high velocity oxygen-gaseous fuel
HVOF	high velocity oxy-fuel
HVOLF	high velocity oxygen-liquid fuel
IRHD	International Rubber Hardness Degrees
K	Kelvin
kgf	kilogram force
K <sub>IC</sub>	fracture toughness
kV	kilovolt
λ	binder mean free path
λ	wavelength
LPPS	low pressure plasma spraying
m	metre
mA	miliampere
M <sub>6</sub> C	generic formula for eta carbides Co <sub>2</sub> W <sub>4</sub> C and Co <sub>3</sub> W <sub>3</sub> C
M <sub>12</sub> C	generic formula for eta carbides Co <sub>6</sub> W <sub>6</sub> C
MPa	megapascal where 1MPa = 1000000 Pa
N	Newton
Ni	nickel
Ni (powder/coating)	powder or coating of WC-15wt% nickel alloy (NiMoCrFeCo) with carbide size of ~0.6 μm
Q	volume wear per unit sliding distance
R <sub>a</sub>	mean roughness (μm)
rpm	revolution per minute
s	second
SE	secondary electron
SEI	secondary electron image

## *Nomenclature*

SEM	scanning electron microscopy
SiC	silicon carbide
SiO <sub>2</sub>	silicon oxide (silica)
TEM	transmission electron microscopy
Top-Gun	a type of HVOF gun
$V_f^{\text{Co}}$	cobalt volume fraction
$V_f^{\text{WC}}$	tungsten carbide volume fraction
VPS	vacuum plasma spraying
Vol%	volume percent
W	total applied normal load, N
W	tungsten
WC	tungsten carbide
W <sub>2</sub> C	di-tungsten carbide
WC-Co	tungsten carbide with cobalt binder
wt%	weight percent
XRD	X-ray diffraction
XRF	X-ray fluorescence

# Chapter 1

---

## Introduction

---

Wear occurs in many different industrial situations, and results in high costs due to equipment failure, replacement of wear parts and downtime during repairs. In addition, wear may influence the quality of the products involved. Wear is defined as the progressive removal of material from a surface due to mechanical movement with or without chemical processes. Among the various wear mechanisms, abrasive wear is the most important one due to its destructive character and its high occurrence frequency (50% of total wear failures) [1]. In abrasive wear, detachment of material from surfaces in relative motion is caused by hard particles between the opposing surfaces or fixed in one of them. Its control and minimisation depends essentially on not only the appropriate selection of materials, but also understanding the mechanisms which are responsible for the abrasive wear of these materials.

Due to its importance, much work has been conducted in the area of abrasive wear and a correspondingly large number of test methods have been used to evaluate abrasion resistance of materials. Often, test apparatus are designed with a specific service application in mind [2]. Test methods can be broadly divided into those

where the abrading medium is loose as it passes over the testpiece (commonly termed three-body abrasion) and those where the abrading medium is fixed in orientation as it passes over the testpiece (commonly termed two-body abrasion) [3]. The most commonly employed test setup for three-body abrasion is that encompassed in the ASTM standard G65 [4], commonly known as the dry sand–rubber wheel (DSRW) test (Fig. 1.1). In this test, a stream of particles is fed through the loaded contact between a test specimen and a rotating rubber wheel; the abrasive particles pass through the contact region once only. Since the rubber wheel rotates and the abrasive passes through the gap, it is clear that no permanent embedment of the particles onto the sample surfaces can take place. Instead a particle can traverse through the contact either by rolling or by becoming temporarily embedded into the rubber wheel and being dragged through and forming a groove in the metal sample as it does so.

The DSRW test has been employed to examine the abrasion behaviour of a very wide range of materials. In many programmes, the test is used simply to provide a quantitative ranking of the abrasion resistance of different materials. For example, the behaviour of a series of steels with a wide range of hardness has been tested, and whilst good correlation was found between wear rates and hardness, the operative mechanisms of wear were never examined [5, 6].

In DSRW abrasion, the operative mechanisms of wear depend largely upon the material properties (e.g. hardness, ductility, toughness) along with the manner in which the particles move through the contact between the wheel and specimen. The particles may embed into the moving rubber wheel and slide across the

sample material through the contact region (generally termed two-body abrasion) or pass through the contact region by rolling between the rubber wheel and the sample (generally termed three-body abrasion). Whilst it has been recognised that the manner in which the particles move through the contact affects the mode of wear and thus ultimately the rate of material removal, the motion of particles through the contact zone has itself been shown to depend upon a number of parameters associated with the system, amongst them particle shape, applied load and the hardnesses of the test surface and counterbody [7-9].

However, despite the recognition of the critical role of the particle motion in controlling the mode and thus (potentially) the rate of abrasive wear, surprisingly little work has examined the basic mechanics of the particle motion in the DSRW test. In a few papers, models to describe the motion of individual particles have been formulated and presented, which examine the moments upon such particles during a test [8, 10]. The model of Fang et al. [10] considers the motion of a particle in terms of the turning moment acting upon the particle; the simplicity of this model makes it useful for studying the effects of various external parameters on particle motion.

In the first part of this work, two investigations on the abrasive wear behaviour of steels using the DSRW test are carried out; firstly, the abrasion of three steels with an ash from a biomass power station are compared with that observed for abrasion with a conventional silica abrasive. In the burning of biomass in thermal power stations, ash is produced which commonly leads to damage of the powerplant through a combination of abrasion, erosion and corrosion [11] and can be

considered as an abrasive media. The aim of this investigation is assessment of wear behaviour of this type of ash in order to reduce its harmful effects on the powerplant components. The second investigation is a study on the motion of particles in the DSRW test with silica abrasive against a range of steels, both as a function of applied load, but also as a function of the hardness of the steels. The changes in behaviour are rationalised in terms of the mechanics governing particle motion. The aim of this work is achievement of a robust model in order to describe the motion of particles in contact in DSRW test which addresses the detail of the particle-rubber wheel contact mechanics.

Most engineering materials used for applications in which abrasive wear resistance is a major requirement, such as tool steels, white cast irons, cobalt-based alloys and metallic matrix composites, are multiphase materials formed of a metallic matrix reinforced by a dispersion of hard particles [12]. The reason for the success of this type of material in tribological applications can be explained, in a simplified form, by stating that the toughness of the matrix together with the hardness of the reinforcement particles enables optimal wear resistance to be achieved. The abrasive wear resistance of materials consisting of mixtures of hard and soft phases depends on several microstructural parameters, e.g. hardness, shape, size, volume fraction and distribution of the hard phase particles, the properties of the matrix and the interfacial bonding between the two phases. They are composite materials with a hard phase, normally WC that has a hexagonal crystal form and a binder phase which is normally cobalt. To increase the corrosion resistance of the materials other metallic or alloyed binders such as nickel are used.

The characteristic high hardness and fracture toughness of sintered WC cermets has made them materials of choice for use as abrasive wear resistant components in a variety of industrial applications. These composites combine the hard, brittle WC phase and a ductile metallic binder phase in different proportions to produce materials with a wide range of properties [13]. Tungsten carbide grain size distribution, as well as the content and composition of the cementing metal binder phase, play a decisive role in determining the fracture mode, mechanical properties, and wear resistance of these materials [14, 15]. Studies of WC-Co materials have shown that abrasion typically involves rounding, fragmentation, and pullout of WC grains and removal of exposed binder, and have suggested that the material removal process involves both plastic deformation and fracture [16, 17].

An alternative to the use of wear resistant bulk materials is surface engineering to produce materials that are wear resistant, with the objective of maximising the benefit/cost relationship. Surface engineering aims to produce composite materials where the substrate and the coating or surface modification provide superior performance to that which would be obtained by each of the parts individually. The performance obtained is always a combination of various physical, chemical, mechanical, metallurgical and thermal properties of the substrate and coating. In this context, the use of high velocity oxy-fuel (HVOF) thermal sprayed WC cermet deposits looks promising for wear protection due to the excellent combination of mechanical properties of these cermets [18].

HVOF spraying is one of many processes used for spraying coatings with tribologically attractive properties. In this process, the combustion reactions between oxygen and a fuel propel particles at high temperature and high velocity towards the substrate. The coatings produced have low porosity, high adhesion to the substrate and low oxide content due to the high velocities used. The coating is formed by particles of liquid and/or mushy materials that strike against the substrate where they form thin platelets called lamellae or “splats”, which cover the surface irregularities. The lamellae cool rapidly depending on the thermal spray process used, and solidify. Other particles that are projected over the already deposited material acquire the same lamellar shape, forming anisotropic structures parallel to the interface. The result of such a deposition process is a coating with a structure of splats, voids and oxides.

The properties and performance of WC cermet coatings are attributed to a complex function of size, shape and distribution of carbides, hardness and toughness of matrix, binder matrix composition and content, and microstructural changes which occur during the spray process. The investigations of the causal relationship between deposition process parameters, microstructure and wear performance have shown that to reach the best output, the coating should have high retained WC content which is finely dispersed [19, 20]. This depends essentially on minimising decarburisation and dissolution of WC during spraying, which is a function of the powder characteristics, flame temperature and particle velocity. The tungsten and carbon from the dissolving carbides diffuse into the matrix and react with binder and promoting the formation of amorphous phases that are hard and brittle. This change to the microstructure of the matrix has a

significant effect on the coating properties [19, 20]. These reactions have generally a negative effect on coating performance in wear.

In recent decades, the processing, properties and applications of the WC-Co coatings with different cobalt content have been extensively studied. There are also a considerable works on the characterisation and properties of thermally sprayed WC cermets with other binders such as CoCr and Ni. However, there is little information in the literature about the new WC cermet coatings with complicated alloyed binders (e.g., nickel base and iron base alloys) and their wear behaviour, especially in relation to abrasive processes. Therefore, the second part of this investigation focuses on characterisation and three-body abrasion of WC–NiMoCrFeCo and WC-FeCrAl coatings which were deposited using a Top Gun HVOF system. For comparison, three types of the WC-17 wt% Co powder feedstocks with different carbide grain sizes were also deposited. The aim of this study is characterisation of the new WC coatings (i.e. WC composite coatings with Ni base alloy and Fe base alloy binders) and their abrasive wear behaviour under “hard abrasion” and “soft abrasion” regimes.

This thesis comprises eight chapters. Chapter 2 presents a review of the literature about the main subjects presented in this thesis. In chapter 3 the methodology and the experimental equipments and materials which are utilised are described. Chapter 4 includes the results and discussion of abrasive wear of steel substrates whereas chapters 5 and 6 present results and discussions of the characterisation of the coatings and their abrasive wear behaviour respectively. The conclusions and future work are presented in chapters 7 and 8.

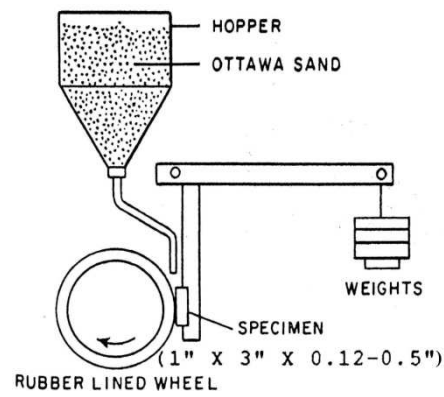


**Fig. 1.1** Schematic diagram of dry sand rubber wheel abrasion test apparatus [4].

# Chapter 2

---

## Literature Review

---

This chapter presents a review of the literature about the main subjects presented in this thesis. Keeping in view the themes of the thesis, the chapter is divided into following main parts; *i*) Abrasive Wear and *ii*) HVOF- Sprayed WC Cermet Coatings. Section 2.1 addresses abrasive wear process in general followed by reviews of abrasive wear in steels, abrasive wear ash from power-plants and abrasive wear in WC cermet materials and coatings. Section 2.2 comprises a brief background to HVOF process, WC cermet materials, and microstructural developments during spraying of these materials.

### 2.1 Abrasive Wear

#### 2.1.1 Introduction

In general, wear may be defined as the progressive loss of material from a solid surface by the mechanical action of a contacting solid, liquid, or gas [21]. Many wear studies have focused on surface damage in terms of material-removal mechanisms, including transfer layer formation, plastic deformation, brittle fracture and tribochemistry [22]. Wear has been classified in various ways; one of the usual classifications of wear is based on the fundamental mechanism that is operating. Wear can be divided into different modes such as adhesion, abrasion, erosion, surface fatigue and tribochemical reaction. Each wear mode can also be divided additionally into various wear mechanisms. In studying the wear

behaviour of materials, a specific mechanism of material removed may be dominant; however, commonly, several wear mechanisms operate at the same time [23].

Wear occurs in many different industrial situations, and results high costs due to equipment failure, replacement of worn parts and downtime during repairs. In addition, wear may influence the quality of the products involved. The cost of wear is high; findings have shown that the cost of wear to the U.S. economy was about \$20 billion in 1978 [24].

### **2.1.2 Types of Wear**

Wear encountered in industrial situations can be broadly grouped as: abrasive 50%, adhesive 15%, erosion 8%, fretting 8%, and chemical 5% [1].

#### **Abrasive Wear**

Abrasive wear is the displacement or detachment of material by the passage of hard particles or hard bulges which are forced against and slide along a solid surface [16]. In this type of wear, a material is seriously abraded or scratched by a counterbody harder than itself. Under a normal load, the asperities on the harder surface indent into the softer surface thus, producing plastic deformation. When a tangential motion is introduced, the material is removed from the softer surface by the combined action of micro-ploughing and micro-cutting.

#### **Adhesive Wear**

This type of wear occurs due to localised bonding or welding between contacting solid surfaces leading to material transfer between the two surfaces and loss from either surface.

### **Fatigue Wear**

Fatigue wear of a solid surface caused by fracture resulting from material fatigue.

This wear is caused by deformation sustained by the asperities and surface layers in contact. Contact between asperities accompanied by very high local stresses generate fatigue propagated cracks, hence the term fatigue wear [25].

### **Erosive Wear**

This type of wear occurs when individual solid particles impact with a surface.

This wear is defined as the process of material removal from a surface subjected to impingement attack by solid or liquid media, being particulate in nature for the former and in the form of droplet for the latter [21]. In erosion, several forces of different origins may act on a particle in contact with a solid surface [25].

### **Fretting Wear**

Fretting wear is defined as a type of wear which occurs as a result of slip by a small amplitude of two surfaces relative to each other. Like all tribological systems, the surfaces are loaded. As the amplitude is increased the material losses by fretting tend to be similar to that due to reciprocating sliding under comparable conditions of load and environment [21].

### **Chemical Wear**

Chemical or corrosive and oxidative wear occur in a wide diversity of situations with both lubricated and unlubricated surfaces. The main cause of this form of wear is a chemical reaction between the wearing material and a corroding medium which can be a chemical reagent, reactive lubricant or even air. This type of wear occurs when a film of material is formed by chemical attack of either contacting body and while this may provide some lubrication, this film is commonly readily removed by the mechanical action associated with one of the other mechanisms of wear [25].

### **2.1.3 Abrasive Wear Processes**

The abrasive wear process has been classified according to three factors [26]:

- The number of bodies involved in the contact, two or three body;
- The stress level; low if the abrasive does not fracture significantly and high if it does;
- Freedom of the abrasive; open if the abrasive is free to move in the direction of the normal load, closed if it is constrained.

Classifications such as two-body and three-body, high- and low-stress conditions have been developed over the years to describe abrasion processes in order facilitate meaningful discussion [27].

#### **2.1.3.1 Two and Three-body Abrasion Wear**

In abrasive wear, material is removed or displaced from a surface by hard particles, or sometimes by hard protuberances on a counterface (hard rough surface), forced against and sliding along a soft surface [3]. The nature of abrasive wear is determined by the way which particles traverse the worn surface. Particles

may roll and/or slide over the surface (Fig. 2.1). Therefore two basic modes have been identified: two-body and three-body abrasive wear.

Two-body abrasive wear involves the removal of material by abrasive particles which are held fixed (as in abrasive paper) while being moved across a surface. This process produces a grooving form of wear.

Three-body abrasion involves loose particles which may rotate as well as slide as they contact the wearing surface. Compared to two-body abrasion, three-body abrasion is much more common and also much more complicated than two-body abrasion. Plastic indentation wear will be much more important in three-body abrasion than that in two-body abrasion [28]. Furthermore, in three body abrasion, the movement patterns of abrasives are more complicated than in two body abrasion, since the abrasives not only slide, but also roll. Thus, a relatively wide range of wear rates have been variously reported for three-body abrasion conditions, which depend not only on the material being tested, but also on the testing apparatus. In three-body abrasion of metals, cutting wear and plastic deformation wear coexist [29]. As a consequence, two-body abrasion tests are said to produce wear rates one to three orders of magnitude higher than three-body abrasion under comparable loading conditions [30, 31].

### **2.1.3.2 Open and Closed Abrasive Wear**

Misra and Finnie [32] proposed a further subdivision of three-body abrasion into “closed” and ”open” groups. The closed group covers the cases of fine abrasives between closely mating surfaces. Open three-body abrasion covers cases where

there is a thick bed of abrasive, or the particles are so large, that the two-opposed surfaces are so far apart that the mechanical properties of one have no influence on the other.

### **2.1.3.3 High and Low stress Abrasive Wear**

Abrasive wear processes have also typically been grouped into two regimes: high or low stress [2]. When abrasive particles are compressed between two solid surfaces, high-stress or grinding abrasion occurs. The high pressure produces dents and scratching of the surfaces and fractures and crushes the abrasive particles [33]. Low-stress or scratching abrasion happens when lightly loaded abrasive particles move across the wearing surface, generating cutting and ploughing on a microscopic scale but with no damage to the abrasive particles. The distinction between low-stress and high-stress conditions is not sharp [27].

### **2.1.4 Mechanisms of Abrasive Wear**

Several mechanisms have been proposed to explain how material is removed from a surface during abrasion. These mechanisms include plastic deformation, fracture, fatigue, grain pull-out and corrosion [3, 23, 25, 34]. In order to understand abrasive wear in simple terms, these mechanisms shall be separated into the two main mechanisms: plastic deformation and fracture (Fig.2.2). Under some circumstances, plastic flow may occur alone, but because of the complexity of abrasion, rarely does one mechanism completely account for all the loss. Although the plastic deformation mechanism is often linked with ductile materials

and the fracture mechanism is linked with brittle materials, both can occur together.

#### 2.1.4.1 Plastic Deformation

Two major processes take place when abrasive particles contact the surface of a relatively ductile material [34]:

- The formation of grooves which do not involve direct material removal.
- The separation of material in the form of primary wear debris or microchips.

In both cases, material is deformed to the side of the grooves and can become detached to form secondary microchips. Ultimately, material is removed by fracture, but plastic deformation processes control the rate at which material is removed. If fracture did not occur, the material would continue to deform until it was able to elastically support the load on the contacting particles.

Robinowicz suggested a simple model for the abrasive wear process by plastic deformation [35]. This model is based on an abrasive particle, idealized as a sharp cone of semiangle  $\theta$ , being dragged across the surface of a ductile material which flows under an indentation load  $F$  (Fig. 2.3). It forms a groove in the material with hardness  $H$ , and wear is assumed to occur by removal of some proportion of the material which is displaced by the particle from the groove. The volume of groove  $V$  per unit length can be obtained:

$$\frac{V}{L} = \frac{2}{\pi} \frac{F}{\tan \theta H} \quad (2.1)$$

Therefore, the wear rate  $Q$  is defined as:

$$Q = K \frac{F}{H} \quad (2.2)$$

which is the well-known Rabinowicz equation [31].  $K$  is the wear coefficient and defined as:

$$K = \frac{2\eta}{\pi \tan \theta} \quad (2.3)$$

where  $\eta$  is the fraction of material displaced from the groove. According to the Rabinowicz model, wear in homogeneous materials only depends on the attack angle  $\theta$ , the normal load  $F$ , the hardness  $H$  of the material and the geometry of the indenter (in this case a conical indenter). This simple model suggests that the wear rate per length of sliding will be directly proportional to the load, and will vary inversely as the hardness of the surface.

#### **2.1.4.2 Fracture**

Although plastic deformation occurs during abrasive wear of brittle materials, fracture is often the rate controlling mechanism. Even during the wear of ductile materials, fracture may occur. For a ductile material, fracture is most likely to occur just behind a contacting abrasive particle since this region is subject to a tensile stress. The material removal in brittle materials is likely to be controlled by fracture rather than by plastic deformation except during wear by very lightly loaded blunt abrasive particles [36].

One model for the abrasive wear by fracture is based on the removal of material by lateral cracks which grow upwards to the free surface from the base of the subsurface deformed region and are driven by the residual stresses associated with

the deformed material (Fig. 2.4). Evans and Wilshaw developed a model using fracture mechanics to describe removal of material by lateral cracking [37]. In this model, the volume wear rate per unit sliding distance  $Q$  is given by:

$$Q = \alpha \frac{F^{5/4} d^{1/2}}{A^{1/4} K_C^{3/4} H^{1/2}} \quad (2.4)$$

where  $F$ ,  $d$ ,  $A$ ,  $K_C$  and  $H$  are load, diameter of abrasive particle, contact area, fracture toughness and hardness of material respectively.  $\alpha$  is a material-independent constant.

## 2.1.5 Variables Affecting Abrasive Wear

There are several factors which influence the wear of material during the abrasive wear process. These factors can be grouped under three main headings; particle, material and environment.

### 2.1.5.1 Properties of the Particle

#### Geometric properties (Particle shape, orientation and size)

Both theoretical predictions and experimental results confirm that the abrasive particle shape has an effect on the rate of wear [38]. This is because it influences the transition load from elastic to plastic contact and the critical indentation size for fracture. If particle load and surface hardness are constant, the projected area of plastic contact will be constant, but the cross-sectional area of a groove resulting from such a contact will depend on the particle shape. Moore showed that the ratio of cross-sectional to projected area of contact for pyramidal, conical and spherical indenter increase as the included angle, cone angle and radius,

respectively, decrease [39]. In addition, this ratio is generally less for a spherical than for a pyramidal or a conical contact. Thus, for both plastic and brittle mechanisms of material removal, it is expected that the wear rate will be higher for “sharp” pointed abrasives than for “blunt” round abrasives [40]. Fig. 2.5 shows a comparison of the wear rate obtained in abrasive wear testing for steel against two types of abrasive sands namely rounded and crushed silica sands. Both sands had the same particle size distribution and differed only in their shape. The sharp, crushed particles resulted in rates of wear typically two to five times higher than that produced by their rounded counterparts. Swanson and Klann [41] have reported a factor of ten in the volume loss of the plain carbon and low alloy steels examined using the wet and dry sand rubber wheel abrasion tests with round and angular silica abrasives.

The abrasive particle size also affects the wear rate of materials. When the materials and the abrasive type remain fixed, the wear rate increases with increasing particle size up to a certain size; above this critical size, the wear rate becomes almost independent of further size increases. This critical size is often cited as about 100  $\mu\text{m}$  (Fig. 2.6) [42].

### **Particle Hardness**

The hardness of abrasive particles can influence the rate of wear. Particles with lower hardness than that of the surface cause much less wear than harder particles. It has been found that the rate of material removal decreases significantly when the hardness of the surface  $H_s$ , approaches the hardness of the abrasive,  $H_a$  [43]. Fig. 2.7 shows the relative abrasive wear rates of a wide range of metals and

ceramics, abraded by two different types of abrasive particles. The wear rate becomes much more sensitive to the ratio of the abrasive hardness  $H_a$  to surface hardness  $H_s$  when  $H_a/H_s$  is less than  $\sim 1$ . The critical value of  $H_a/H_s$  has in fact been estimated as 1.2 [3, 44, 45]. Abrasive particles of any shape will cause plastic scratching only if  $H_a/H_s > 1.2$ . Abrasion under conditions where  $H_a/H_s < 1.2$  is sometimes termed soft abrasion, in contrast to hard abrasion when  $H_a/H_s > 1.2$ . The critical transition point between hard and soft abrasion appears to be the point at which plastic deformation in the form of grooves and scratches occurs [46].

### **Particle Strength**

Plastic deformation of the surface will occur as the normal load on the particle is increased only if the particle can sustain this contact pressure without deforming or crushing. Thus, the strength and toughness of an abrasive particle are important factors in abrasive wear. Gahlin and Jacobson [47] described abrasive with quartz and chert, which have similar hardness, but with chert having a greater resistance to fracture than quartz; wear generated by chert was between two and three times that quartz.

### **2.1.5.2 Properties of the Material**

#### **Microstructure of the Specimen**

The microstructure of materials affects their wear properties. For ferrous materials, various factors like retained austenite, carbide content and size, heat treatment regime and alloy content impact on the wear properties [48]. In heterogeneous materials like composites synthesized from two or more distinct components, the structural properties are important in abrasive particle contact.

Parameters such as volume fraction and distribution of a dispersed phase, its coherency and hardness all affect abrasive particle indentation, strain hardening, strain distribution, fracture, and recovery processes [49]. Fig. 2.8 shows that a finely dispersed hard second phase can result in homogeneous behaviour of a composite which leads, in general, to an increase in wear resistance.

### **Hardness of Specimen**

The relationship between wear resistance and material hardness is complicated [9], but it is generally recognized that hard materials exhibit lower abrasive wear rates than softer materials. Eq. 2.2 suggests that the wear rate varies inversely with the hardness of the material. Many pure metals do behave in this way, although alloys often exhibit more complex behaviour (Fig. 2.9) [50]. The loss of proportionality between hardness and the relative wear rate for hardened metals is the result of defining the wear resistance in terms of the undeformed hardness of the metal [25]. The materials at the worn surface will have been strain-hardened by plastic flow, and that hardness will generally be greater than that of the bulk. Moreover, the microcutting mechanism becomes more dominant as the hardness of the material increases. This was observed not only for abrasion with angular abrasives, but also for abrasives with a more rounded morphology [40].

#### **2.1.5.3 Characteristics of the Test setup and Environment**

##### **Load**

Eq. 2.2 predicts that the wear rate varies directly with the applied load. Although for many systems the wear rate varies proportionally with load over limited ranges, sudden transitions from low to high wear rate, (and sometimes back again)

are often found with increasing load associated with changes in mechanism of material removal [3, 51].

### **Temperature**

The temperature of a wearing surface is controlled not only by the ambient temperature, but also by the heat generated (and carried away) by the wear process itself. The difference between those is that in the first, the abrasives remain relatively cool due to the transient nature of abrasion. During wear, a surface is subject to applied stress and temperature rises. At least 90% of the energy expended in plastic deformation during wear must be dispersed as heat [1]. The temperature increase caused by plastic deformation during abrasion is associated with the speed of sliding [52]. This may cause plastic deformation, recrystallization, and phase changes, all of which affect the mechanical properties of the surface material and, consequently, the abrasive wear rate. In general, with increasing temperature there is a corresponding decline in the hardness of both the worn material and the abrasive. Increasing temperature influences materials such as metals in decreasing their hardness more significantly than for the non-metallic abrasive materials [53]. Therefore the ratio of abrasive hardness to metal hardness increases with increase in temperature leading to a higher wear rate. In addition, in three-body abrasive wear, contact between an abrasive and the worn surface would be particularly short compared with that in the two-body abrasive mode. Thus, in three-body abrasion, heat generated in the deformed material would not easily diffuse into the abrasive particles. This causes thermal softening of the surface material while the abrasive remains with its hardness virtually unaltered [25]. Another effect of high temperatures is to induce a form of wear which

depends on the combined action of oxidation and removal of oxide layers by abrasion. The oxidation of steels in air is much more rapid at 600°C than at 20°C , and as temperature rises, the removal of steel as oxide becomes more significant [54].

### **Moisture**

Moisture has a strong influence on abrasive wear rates. Usually, abrasive wear rates increase with moisture content in the atmosphere, but there are occasions when opposite effects have been observed [55]. The abrasive may either be just sufficiently weakened by moisture to produce a large number of new cutting edges, or severe grit weakening may occur causing disintegration of the grits into non-abrasive, fine particles. Both the worn material and the abrasive may be weakened by moisture [56]. Indeed, for the same abrasive and worn material, two body abrasive wear may increase with humidity while the three-body abrasive wear rate may either increase or decrease [25].

## **2.1.6 Abrasive Wear Tests**

### **2.1.6.1 Laboratory Abrasive Wear Tests**

In selecting and specifying laboratory wear tests, attention must be paid to the fact that wear performance is system related, depending not only on materials properties but also on the characteristics of the abrasive and the sliding and loading conditions. There are two major groups of laboratory test methods for abrasive wear:

- 1- Those in which the abrasive is fixed relative to the wearing specimen.

- 2- Those in which the abrasive is loose or free with respect to the wearing specimen.

In fixed abrasive tests, the type and size of abrasive is limited by the availability of bonded abrasive papers or cloths whereas in loose abrasive tests, there is (theoretically) complete freedom on the choice of abrasive which might even include abrasive material from a service environment. The load per unit area in some loose abrasive tests (particularly wheel tests and bin tests) is difficult to characterise and may vary widely throughout the duration of the test.

For fixed abrasive tests, the mechanics of abrasive particle-wearing surface contact is consistent over a wide range of loading conditions and material types. This can vary with load, counterface properties, abrasive shape and test material. In attempting to devise or specify a laboratory test to simulate a service wear environment, the following system parameters should be considered [57]:

- Test conditions such as: Abrasive type, size, shape and distribution, fixed or loose abrasive, sliding distance, abrasive path length, sliding speed, load, and properties of counterface.
- Test materials such as: chemical/ physical/ mechanical properties and microstructural dimensions of materials.

### **2.1.6.2 Standard Test of Abrasive Wear**

It is important to thoroughly characterize the test conditions, to determine the precision of the test technique, and to consider these as the results are interpreted. Reproducibility (an essential feature of any good test) can be achieved by careful

control of variables. The most commonly used laboratory tests for abrasive wear employ either a pin-shaped specimen sliding against fixed abrasive giving two-body wear (Figs. 2.10a to 2.10c), or a rotating (rubber or steel) wheel sliding against a plane specimen with loose abrasive particles being continually fed between the two, giving three-body wear (Fig. 2.10d).

Typical laboratory abrasive wear tests are [31]:

1. Dry/wet-sand rubber-wheel three-body (low-stress) abrasion;
2. Dry/wet-sand steel-wheel three-body (high-stress) abrasion;
3. pin-on-drum two body (high-stress) abrasion;
4. Jaw crusher (high-stress) gouging-abrasion;
5. High-speed, impeller–tumbler impact abrasion.

The dry-sand rubber wheel (DSRW) abrasion test apparatus has been used widely to simulate low-stress, three-body abrasive wear [58]. The pin-on-drum abrasive wear test (POD) involves high-stress, two-body abrasive wear. The jaw crusher test is a type of high stress wear test that may result in either two-body or three-body conditions [59].

### **2.1.6.3 Dry Sand Rubber Wheel Test**

The most commonly used test configuration for three-body abrasion is that of a specimen loaded against a rotating wheel with abrasive particles being entrained into the contact zone. This is the basic principle of the tests described by ASTM standard G65 [4]. The rubber wheel tester, which was standardized by ASTM, has been said to produce low stress three-body abrasion [5]. Even before the test

became an ASTM standard, it had been used by a number of laboratories for many years. The test is widely used to rank materials for components that will be subjected to low stress abrasion in service like agricultural tools, chutes and hoppers in ore processing plant, and construction equipment [60]. This test has a longer history, and has generated more data than other types of abrasion testing machines [61]. However, this test configuration has some limitations. For example, the abrasive particles may get embedded in the rubber wheel and scratch the test specimen in a manner similar to two-body abrasion [2].

The apparatus is shown schematically in Fig. 2.11. In the test, a plane specimen is loaded against the rim of a rotating rubber wheel; sand is fed into the gap between the wheel and specimen and is carried past the specimen and thus abrades it. The behaviour of a material in a rotating wheel abrasion test depends not only on the intrinsic properties of the test sample itself, but also on the conditions of the test, such as nature of the abrasive particle type, size, shape, brittleness, the wheel hardness, its stiffness and the nature of the environment. The rubber wheel abrasion test has been the subject of a large body of research [62].

#### **2.1.6.4 Rubber Wheel Variables**

In the sand-rubber wheel test, the rate of wear increases with rubber hardness, which is measured with a Shore A Durometer tester, as described in ASTM D-2240 [4]. It has been shown that the weight loss of some steels exhibits an exponential dependence on the rubber hardness (Fig. 2.12). This function could be linearized by means of a semi-log plot (Fig. 2.13). The plot represents results in the form of parallel straight lines displaced in a vertical direction. The effect of

rubber wheel hardness on wear rate can be explained in the way that particles groove or roll. It has been also suggested that the hard wheel tends to distribute the total load only over the largest grains, with particles too small to be loaded by the rubber probably being ineffective (Fig. 2.14) [62].

Avery [62] used concept of “opportunity vs. severity” to explain the independence of the wear rate on the sand feed rate. Sand feed rate is partly opportunity, but it also affects severity, and thus would not be altered to merely change weight loss. In a low feed rate condition, a few particles are in contact between the rubber wheel and the surface resulting in high load per each particle, whereas in the high feed rate of abrasive, a large number of articles are in contact causing a low load per particle. Therefore, the wear rate is independent of feed rate of abrasive [63]. The Rabinowicz [35] wear model (Eq. 2.2) show two wearing parameters ( $F$  and  $H$ ) that are obvious and others are concealed in the wear coefficient  $K$ , which has been given a physical definition but actually is a factor of ignorance.

It has been found that the velocity of the wheel (sliding speed) only slightly affects the wear rate. This is thought to be due to surface temperature changes. Stevenson and Hutchings [63] remark that in the rubber-wheel dry-sand abrasion test, the observed dependence of wear rate on sliding speed is more probably related to variations in the mechanical properties of the rubber with strain rate and temperature than with the properties of the test material. As the temperature of the rubber increases, its hardness declines (Fig. 2.15). A maximum was seen in the dependence of wear rate on sliding speed. This was attributed to a balance

between strain rate effects increasing the modulus of the rubber, and heating effects reducing the modulus.

### **2.1.7 Abrasive Wear Behaviour of Steels**

Many investigators [1, 50, 64] have shown that the abrasive wear resistance of steels increases with carbon content and with increase in hardness due to heat treatment. Studies also show that the wear behaviour of steels greatly depend on their microstructural features. The nature of phases present such as pearlite and martensite and changes in volume fraction of martensite in a ferrite matrix (dual-phase structure) have been observed to strongly control the overall wear response [48]. Fig. 2.16 shows that the abrasive wear ratio is a strong function of the carbon content and microstructure within a range from 0 to 0.8 wt%. However, the wear resistance does not increase with any hardening associated with work hardening [65]. Fig. 2.17 shows that the wear resistance of steel increases rapidly only when the surfaces being abraded exceeds some critical ratio of the hardness of the abrasive. Moreover, there is a direct correlation between carbide volume fraction in steels and their resistance to abrasive wear in which the wear rate of steel decreases as the carbide content increases [34]. Swanson and Klann [41] showed that the use of an angular abrasive produces a significant increase in the volume loss of the plain carbon and low alloy steels examined. The shape of the abrasive certainly is a significant factor; however the change in the number of particles that slid across the interface when the abrasive is changed from a round grain to a sharp grain sand is also a contribution factor to take into account.

## **2.1.8 Abrasive Wear with Ash Particles**

### **2.1.8.1 Introduction**

Due to sanitary and environmental problems and operational costs related to either the discharge, land disposal or re-use of wastes, the utilization of biomass as a fuel is significant issue [66, 67]. It is found that different types of biomass materials have a high heat content which can be classified as carbon-neutral energy content. Therefore as a renewable energy source, it can be employed for firing in power plants [68]. Recently its use as a fuel source for thermal power plants has increased, both as a main fuel, and for co-firing with coal.

In combustion processes, ash is produced in the form of fly ash and bottom ash. Both types of ash particles can result in mechanical and chemical damage to the related components. Depending on the system, this damage may be erosion or abrasion; and it may be complicated by corrosion [11].

There is a wide range of feedstock materials which are termed “biomass”; the ash produced from them is also different. The behaviour of the ash associated with these types of fuel sources is of concern, particularly in terms of their abrasiveness [66]. Ash associated with conventional coal burning plants has been seen to lead to significant abrasive wear of components of the power plant [69].

### **2.1.8.2 The Ash Originating From Combustion**

During combustion, the mineral matter present in fuels may undergo chemical changes, such as oxidation, loss of water or crystallization, decomposition of the

less stable compounds, and calcination of carbonates to oxides. It may also undergo physical changes: some particles may melt, others may soften allowing rounding the corners of the particles, and the mineral within the coal and biomass material may accrete during the combustion of the particles to form hollow spheres (agglomeration) [67]. The extent of these changes will depend on the combustion process itself, and in particular on the maximum temperature attained and the residence time of the mineral matter in the hot zone. Some of the ash may be present as large particles; some of it may form a liquid slag which may freeze on cooler parts of the system and eventually separate as large fragments. These parts of the ash generally fall to the bottom of the combustion system, where they are removed: collectively they are referred to as bottom ash. Other parts of the ash are present as relatively small particles, and are carried along with the combustion gas as it flows through the system. This is called the fly ash. The chemistry of the bottom ash and the fly ash may be different; the relative amounts depend on the chemistry of the mineral matter in the fuel, and on the detailed characteristics of the combustion system. The wastage process may involve both mechanical effects and chemical effects. The mechanical effects include erosion, (which involves the impact of particles on the wasting surface, with the particles moving freely before and after the impact) and abrasion (where the particles are loaded onto the surface and move in contact with it for some time) [11].

### **2.1.8.3 Coal Ash**

The coal used in thermal power plants for generating electricity may result in 30 to 40% ash and even more [70]. About 80% of the ash is entrained in the flue gas and is captured and recovered as fly ash. The remaining 20% of the ash is dry

bottom ash, a dark gray, granular, porous, predominantly sand-sized (< 12.7mm) material that is collected in a water-filled hopper at the bottom of the furnace [71]. The coal ash itself is extremely abrasive. The aggressive nature of this mixture leads to rapid wear of the components. The mechanism of wear has been found to be a combination of corrosion and abrasion acting synergistically [69]. The fly ash particles can result in mechanical damage to the boiler tubes [11] whereas bottom ash generated from fluidized bed combustion (FBC) boilers causes significant wear in ash cooling screws (Fig. 2.18) [72].

#### **2.1.8.4 Biomass Ash**

The wear of the equipment in power plants is associated with the hard particles present in the fuel and ash, particularly those that are harder than the steels and other materials which are used for construction. The only mineral species that is commonly found in clean biomass materials in significant levels which is in this category is quartz, and only high quartz biomass materials or those contaminated with significant levels of tramp materials are expected to present problems with erosion and abrasion in the fuel handling and firing equipment [73].

In general, biomass usually creates less ash than coal, and the composition of its ash tends to reflect the inorganic material required for plant growth [74]. For this reason, wear processes tend to be less important than they are in coal-fired plants.

There are however, some specific areas where wear can be significant issues:

- Some biomass materials such as rice husk have high quartz content [66].
- The formation fused ash materials, particularly the bottom ash from grate-fired systems.

- In biomass boiler systems which suffer severe convective section fouling problems, there are excessive rates of particle impact erosive wear of boiler tubes and erosive wear associated with the regular use of convective pass soot-blowers [73].

### **2.1.8.5 Abrasive Testing of the Ash**

Characterization of the abrasive wear resistance of the components against ash is best achieved by loose- abrasive testing, in which the particles are free to roll and or reorient themselves as they pass across a wearing surface. The most common tests which fall into this category utilize either the wet sand or dry sand rubber wheel abrasion tests.

## **2.1.9 Abrasive Wear of WC-Metal Coatings**

### **2.1.9.1 Introduction**

The abrasive wear properties of WC–Co composites in the coated [20, 75-80] and sintered [81-84] forms have been extensively studied for the last two to three decades in light of their high resistance to wear. There is also a large body of work on WC cermets with other metallic binders such as Ni and CoCr [85-89] which are used in order to improve the corrosion resistance of these materials. In many of these works, research has sought to compare the behaviour of sintered and sprayed WC cermet systems to understand the microstructure–performance relationships, to enable the performance of coated systems to be improved towards that of sintered materials.

### 2.1.9.2 Abrasive Wear of Sintered WC-Metal Cermets

Because of a favourable combination of hardness and toughness, cemented tungsten carbides are commonly used in applications where the material is exposed to abrasive wear conditions such as in cutting tools [90]. The abrasive wear resistance of materials consisting of mixtures of hard and soft phases depends on several microstructural parameters such as hardness, shape, size, volume fraction and distribution of the WC grains, the properties of the matrix and the interfacial bonding between the two phases [91]. The mechanism of abrasion depends on the hardness ratio of the abrasive particle and the cermet which controls the resistance of the cermet to penetration by the abrasive particle [82]. Studies of WC cermets have shown that abrasion typically involves rounding, fragmentation, and pullout of WC grains and removal of exposed binder, and have suggested that the material removal processes involve both plastic deformation and fracture [17].

### Wear Mechanisms

The mechanism of abrasion in ductile materials is plastic deformation (section 2.2.4.1) while for brittle materials such as ceramics, it is dominated by fracture (section 2.2.4.2). Cemented WC cermets made up of two distinct hard and soft phases are more complex than homogeneous materials and it has been shown that their abrasion typically occurs by different mechanisms and at different rates, depending on the hardness ratio of abrasive and cermet [17]. If the abrasive hardness  $H_a$  is more than 20% harder than the cermet hardness  $H_c$ , it is termed a hard abrasive. In this regime, the wear rate is relatively high, and material is

removed by plastic deformation and grooves formed in the surface. Surface deformation is primarily by plastic flow, assisted, occasionally, by microfracture in the binder phase. The scale of each removal event is typically one or more orders of magnitude greater than the WC grain size and bulk hardness is the property which best correlates with resistance to abrasion in this region of abrasion by relatively hard abrasives [92]. Relatively soft abrasives, on the other hand, give a much reduced rate of wear and the mechanism of material removal is preferential removal of the binder followed by fragmentation and pullout of carbide grains [44, 93].

Jia and Fischer [94] investigated wear behaviour of cemented WC-Co cermets under hard and soft abrasion. Under a hard abrasion regime, their results showed that material was being removed by plastic deformation of the binder and fragmentation of the WC grains. Moreover, the fracture resistance of WC grains increased with decreasing grain size. Under soft abrasion, low penetration of the abrasive particle into the cermet without clear grooving was observed, but instead binder removal was observed which left exposed WC grains which themselves were removed by cracking or pull out. It was also found that the abrasive wear resistance increased sharply with cermet hardness. They suggested that dependence of abrasion on the local fracture strength and therefore carbide grain size under the soft abrasion was less than that under the hard abrasion.

Larsen-Basse and Koyangi [44] studied what they termed the scale effect in cemented WC-Co cermets. They concluded that an abrasive particle like silicon carbide which is slightly harder than the WC grains themselves, but much harder

than WC-Co cermet overall, can act as either a soft or hard abrasive particle depending on the testing parameters such as abrasive particle size and the loading conditions. For example, if the contact zone of the individual abrasive asperity is so large that bulk behaviour controls deformation of the WC-Co material, then these abrasives act as hard abrasives. However, if the contact zone is small, so that it only includes one or a few WC grains, then the abrasives act as relatively soft abrasives and very little material is removed [95].

### **Microstructural and Mechanical Properties**

Correlation studies of abrasion and mechanical properties have established that abrasive wear resistance is strongly related to changes in hardness and fracture toughness of the cermets [17]. An approximation toward predicting wear resistance by using a relationship between abrasion and mechanical properties was presented by Baldoni et al. [96]. They showed that abrasive wear resistance of ceramic materials increases linearly with increase of the mechanical property parameter  $K_{IC}^{3/4}H^{1/2}$  while for cemented WC materials, the abrasive wear resistance increased with  $K_{IC}^{3/8}H^{1/2}$ , reflecting a decrease in dependence of abrasion fracture toughness for cemented WC materials compared with ceramic materials, and indicating the ability of cemented WC cermets to accommodate a degree of plastic deformation during abrasion. The dependence of  $K_{IC}$  and  $H$  on microstructural parameters (composed of parameters such as mean free path,  $\lambda$  and WC grain size,  $D_{WC}$ ), has been studied by Chermant and Osterstock [97]. They showed that the ratio of  $\lambda^2/\bar{D}_{WC}$  directly correlates to hardness and fracture toughness; with increases in this ratio, fracture toughness increased and hardness decreased linearly. Many studies on cemented WC cermets have reported that for

a given binder content, hardness decreases and fracture toughness increases as WC grain size or binder mean free path increase [82, 94, 98, 99]. Moreover, increases in carbide phase fraction results increase in hardness and decrease in fracture toughness of WC hard metals. Fig. 2.19 shows the effect of changes in the WC grain size and binder content on the mechanical properties of cemented WC-Co cements. Wayne et al. [82] developed a combined mechanical property/microstructural parameter relationship for abrasion of WC-based cermets and proposed that:

$$\text{Abrasion resistance} \propto \left( \frac{K_{IC}^{3/8} H^{1/2}}{D_{WC}} \right) \quad (2.5)$$

Increases in hardness and fracture toughness of a cermet (controlled by the binder content and composition), and decreases in WC grain size result in increased abrasive wear resistance. The dependence on hardness is seen to be greater than that on toughness. Gee et al. [100] investigated the abrasive wear behaviour of a group of cemented WC-Co cermets with different binder contents using ASTM G65 and ASTM B611 abrasive tests. Their results show that the abrasive wear rate of cemented WC-Co cermets for smaller WC grain size and lower binder phase content is lower (Fig. 2.20). Saito et al. [98] worked on a range of WC-Co cermets with different binder contents and carbide grain sizes and found the same behaviour. They also showed a strong relation between the hardness and the inverse of the mean free path. As such, their results show that wear resistance was proportional to hardness and wear rate was linearly proportional to the mean free path. Quigly et al. [99] also studied abrasive wear behaviour of WC-Co cermets with different WC grain size and binder content. They showed that when the binder phase content increases, the hardness and abrasive wear resistance

decreases. In addition, at each binder content, the hardness and wear resistance of material with smaller WC grain size was higher. They therefore concluded that the ultrafine WC grained cermet was the hardest and most wear resistant.

Larsen-Basse [91] studied effect of composition, microstructure and service conditions on the wear behaviour of different cemented carbides such as the WC-Co and WC-Ni and compared the results with several carbides and hardened steels. The results show that there is a critical level of hardness ( $\sim 1250$  HV) at which abrasive wear resistance with quartz increased dramatically (Fig. 2.21). He also measured abrasive wear resistance of the cemented WC cermets under soft and hard abrasion regimes, shown in Fig. 2.22a and Fig. 2.22b respectively. The results show that for a given mean free path the wear resistance of WC-FeNi under soft abrasion (with  $\text{SiO}_2$ ) is significantly lower than that for the WC-Co while the opposite is true under hard abrasion (with SiC). He finally concluded that cobalt is an excellent binder to produce cermets with high abrasion resistance for following reasons; (i) strong bond with WC grains, (ii) relatively good ability to deform and lubricate and (iii) ability to undergo transformation from metastable to stable phase during deformation. Pirso et al. [101] investigated the abrasive wear of three groups of cermets; the WC-Co, TiC-Ni and  $\text{Cr}_3\text{C}_2$ -Ni. They suggested that abrasive wear mechanisms of different cermets are similar and occur through surface elastic-plastic and plastic deformation (grooving). The fracturing of bigger carbide grains and carbide frameworks and the formation of sub-surface cracks by a fatigue process under repeated abrasion is followed by loss of small volumes of the material.

In summary, the abrasive wear resistance of cemented WC cermets is controlled by the composition of the binder, WC content and grain size. Higher WC phase content and smaller carbide grains typically give the greatest abrasive wear resistance since cermets with these have smaller binder mean free paths and hence less exposure of the soft and ductile binder. The wear mechanism depends on the abrasion regime; under soft abrasion, the mechanism of material removal is preferential removal of the binder followed by fragmentation and pullout of carbide grains while under the hard abrasion, the material is removed by plastic deformation (grooving) and fragmentation of the WC grains followed by microfracture of the binder. The effect of binder type is complex.

### **2.1.9.3 Abrasive Wear of Thermally Sprayed WC Coatings**

Since there are significant differences between composition and microstructure of thermally sprayed WC coatings and sintered WC cermets, the abrasive wear behaviour and mechanisms in the sintered cermets may not be directly applicable to thermally sprayed coatings. The microstructural features such as anisotropy in the coatings due to lamella splat formation and the presence of amorphous phases after spray process have a stronger influence on the abrasion resistance of thermally sprayed WC composites [102]. However, comparison of the thermally sprayed WC coatings with the sintered cermets may help in understanding the effect of changes in the microstructural parameters on the mechanical properties and wear behavior of these materials.

#### **2.1.9.4 Variables Affects on Abrasion Performance**

The microstructural parameters of thermally sprayed WC coatings affect mechanical properties and wear resistance [14, 91]. The starting powder properties along with spray parameters establish the microstructural characteristics of the coating. The thermal spray parameters largely govern *i*) the thermal history of the particles, *ii*) the particle deposition velocity (Fig. 2.23) and *iii*) the oxidation of the particles in flight. Such parameters strongly affect the microstructure of the coatings.

#### **Feedstock powder**

The properties of the feedstock powder have important role in determining the microstructure and properties of the coating. Properties such as porosity and amount of  $W_2C$  phase, which are strongly related to the density of the starting powder exert a strong influence on the coating hardness [103]. It has been observed that the reaction during spraying was greater for the powder with the high initial porosity level, which is attributed to more efficient heating and atmosphere penetration in flight [104]. The coatings deposited from powders with medium and coarse carbides generally had lower porosity than those deposited from the powder with fine carbides. In addition, some studies [102, 105-107] showed that a decrease in carbide size in the feedstock powder led to a higher amount of  $W_2C$  in the coatings due to the larger surface-to volume ratio between the carbide and binder. Furthermore, powders having a narrow powder size distribution result in coatings of higher quality than powders with wider grain size distributions [108]. This is explained by the differing melting behaviour of powder particles of different size; small particles are more easily overheated than

larger particles, and overheating may give phases with low wear resistance and therefore coatings of poor quality (Fig. 2.24) [109].

### **Decomposition of WC**

One of the most important attributes of thermal sprayed WC composite coating microstructure is the extent of decomposition of WC grains during spraying, which is a strong function of the particle temperature in the flame, and can result in  $W_2C$  and W phases and an amorphous binder phase, in addition to primary WC phase in the coating. The tribological behaviour of these sprayed coatings compared with bulk sintered WC cermets is complicated because of the inhomogeneous microstructure and the phase transformations of the starting material, which together lead to a wide variation in mechanical properties. Up to 50% of the WC in the starting material is reported to decompose and transform during the spraying process [110]. Hence, the resultant coating microstructures can have a much lower volume fraction of the wear resistant primary WC phase and a much higher volume fraction of the binder phase compared to the starting powder microstructure [20, 77, 106]. Greater levels of WC decomposition have generally been seen as undesirable. From the work of Usmani et al. [102], comparison of Figs. 2.25a and 2.25d shows that an increasing of  $W_2C$  phase in the coatings goes alongside a decrease in wear resistance. Stewart et al. [75] also showed that the effect of these phase transformations is generally deleterious to the abrasive wear performance of HVOF WC–Co coatings. More decarburisation results in a higher level of the harder and more brittle  $W_2C$  phase surrounding the WC particles and an enrichment of the binder phase in W and C. This enrichment increases its hardness and brittleness.

The effect of decomposition on abrasive wear behaviour of thermally sprayed WC coatings can be considered clearly by comparing different thermal spray techniques such as HVOF with a liquid-fuel (HVOLF), HVOF with a gas-fuel (HVOGF) and plasma spray systems. Barbezat et al. [18] studied abrasive wear behaviour (DSRW test with quartz) of the WC coatings with Co, Ni and CoCr binders by using APS, VPS and HVOF spraying systems. Their best results for abrasion resistance were obtained with a cobalt matrix and a low level of brittle carbides like  $W_2C$ ,  $M_6C$  and  $M_{12}C$ . Khan et al. [111] investigated wear resistance of WC-Co coatings produced by APS and VPS spraying systems and found that the decomposition reaction during APS was significantly higher than that during VPS, likely due to an absence of oxygen. Their results show that plasma power only has a secondary influence on the decomposition reaction and measured wear resistance were greatest for the VPS coating compared with that for APS. Di Girolamow et al. [112] worked on atmospheric plasma spraying of WC-Co coatings and showed that by using a high helium flow rate in an optimized argon–helium mixture and by optimizing the spraying parameters, the degree of decarburization may be significantly reduced. This results from an increase the velocity of sprayed particles. They concluded that the decrease of the decomposition degree enhances hardness, toughness, and wear resistance (ASTM G77 test), all resulting in coatings comparable to those sprayed by high velocity oxygen-fuel. Sanchez et al. [113] also worked on atmospheric plasma spraying of WC coatings, but with conventional and nanostructured WC-Co feedstock powders. They used two plasmogenous gases,  $H_2$  and He and showed that the plasma jet produced using He is less energetic, thus reducing decomposition degree and increasing the level of retained WC in the coating, resulting in the

highest hardness and toughness values and the best wear resistance. Legoux et al. [109] investigated abrasive wear behaviour( DSRW test) of a WC-10Co-4Cr coating which was sprayed by three different types of HVOF guns and one plasma gun. Their results indicated that the abrasion wear resistance are related primarily to the particle temperature at flight due to the carbide degradation (Fig. 2.24).

Since the HVOF systems which employ gaseous fuel (HVOGF system) such as hydrogen often yield comparatively higher particle temperatures and lower velocities than systems which employ a liquid fuel (HVOLF system) such as kerosene [114], the degree of decomposition of WC in coatings produced by HVOGF is expected to be significantly higher than that produced by HVOLF. Sudaprasert et al. [115] compared wear resistance of WC-12 wt% Co sprayed with HVOLF and HVOGF techniques using a conventional ball-on-disc sliding test. Despite the higher levels of decomposition in the HVOGF coatings, their results showed that the wear rate of the HVOLF-sprayed coating is significantly greater than that of the HVOGF-sprayed coating (up to ten times depending on the applied load). They suggested that in HVOGF-sprayed coatings, the thermal history causes full melting of the binder phase leads to dissolution of the carbides and the formation of a highly alloyed matrix which during solidification on impact with the substrate leaving carbides well bonded to the amorphous matrix phase. However, in HVOLF-spraying, the binder is molten only in the rim of the particle whilst in the core, the binder phase remains solid. They concluded that the low wear resistance of the HVOLF-sprayed coating is associated with mechanical damage to the WC-Co powder particles as they impact with the substrate resulting in carbide cracking and a reduction in the integrity of the bond between

the carbide particles and the matrix phase. Picas et al. [116] studied abrasive wear properties (ball on disk) of a WC-10% Co 4% Cr deposited using three different variants of the HVOF process in which the fuels were hydrogen and kerosene. The results show the highest degree of decomposition and also highest hardness for the coatings sprayed by HVOGF system. The greater degree of decarburisation associated with the elevated temperature achieved during gas-fuelled spraying resulted in the formation of more of the hard and brittle  $W_2C$  phase surrounding the WC grains and an enrichment of CoCr binder phase in W and C; however, it also produced a cohesion decrease in the WC particles within the coating and consequently a decrease in wear resistance. Khan et al. [104] in another work investigated abrasive wear behaviour of different WC-Co coatings produced by HVOF spraying of four powders using both hydrogen and propylene as fuel gas. Their measurements of hardness and Young's modulus indicate that chemical reactions generate brittle phases and also tend to result in fine scale microcracking, porosity and residual stresses. They finally concluded that there is a close correlation between high degrees of decomposition and poor resistance to abrasive wear. Marple and Lima [117] used three different HVOF systems (using hydrogen, propylene and kerosene as fuel) and a wide range of spray parameter settings to study the effect of in-flight particle characteristics on the abrasive wear resistance of WC-12Co coatings (DSRW test with silica abrasive). Their results indicate that there was generally a minimum in abrasive wear when the in-flight particle temperature was in the range of 1750 to 1950 °C. The XRD spectra and BSE images show increase in degree of decomposition with increasing in-flight particle temperature. They proposed that at low temperatures and velocities, particles are not sufficiently molten and have insufficient kinetic energy to

produce good bonding between the splats and only limited reaction between the constituents, leading to lower abrasion resistance with poorly bonded splats that can be relatively easily removed. At higher temperatures, reactions that degrade the carbide phase play an increasingly important role. While some dissolution of the carbide phase in the cobalt matrix may be beneficial, there is a point beyond which the reaction of the WC to produce increased levels of other species (e.g.,  $W_2C$  and W) is detrimental to the wear resistance of the coating. This offsets any improvements derived from increases in the cohesive strength of the coating or matrix hardening at higher particle temperatures and velocities.

Schwetcke and Kreye [118] reported spraying of WC-Co powders with various HVOF gun systems to study coating properties such as abrasive wear (grinding wheel test under 30 N load against 320 grit SiC abrasive paper). They found that the extent of the carbon loss depended strongly on the spray system used, whereas the degree of carbide decomposition increased with higher heating of the particles. Their results show that carbon loss in the spray process ranging from 30 to 60% does not adversely effect the wear resistance of the coatings (Fig. 2.26). Carbide decomposition decreases the volume fraction of the carbides, but its detrimental effect on the hardness and wear resistance is compensated by the hardening of the binder matrix due to the solution of tungsten and carbide and the formation of hard  $W_2C$  and eta phases. Only when the carbon loss exceeds 60% are the hardness and wear resistance reduced. Also at a carbon loss of less than 30% the hardness and wear resistance of the coatings are slightly lower. In this case the low carbon loss may indicate an insufficient heating of the particles.

Verdon et al. [119] studied the effect of decomposition on the erosive wear resistance of WC-Co coatings sprayed by HVOF system with two different fuel gases ( $H_2$  and  $C_3H_8$ ) and found that there is an optimum amount of decomposition which ensures an optimum wear resistance for given erosion conditions (Fig. 2.27).

In summary, the degree of decomposition depends on the history of particle in-flight which is controlled by many parameters like thermal spray technique, gun system and type of fuel. Chemical reaction during spraying in higher temperature causes new phases ( $W_2C$ , W and eta) to form and changes the crystalline metallic binder phase to a brittle amorphous phase. In general, optimum abrasive wear performance is achieved with coatings having a balance between hard carbide phases within hard matrix phase, good bonding of the carbides and binder and high binder toughness to resist cracking. The properties required depend on the type of abrasive wear test and abrasive particle employed. In the other words, the wear mechanism determines the optimum coating characteristics.

### **WC Grain Size and Content**

WC composites generally derive wear resistance from the presence of a high volume fraction of hard, wear resistant WC grains in a metal-based binder phase. General observations from HVOF thermally sprayed WC cermet coatings and sintered materials show that an increasing binder content reduces the hardness and abrasive wear resistance of the coating resulting from a reduction of hard carbide phases [101, 103]. In the coatings, the binder can exhibit some brittleness due to dissolution of W and C in binder during spraying. Khan et al. [104] studied

abrasive wear behaviour (DSRW test with silica) of HVOF sprayed WC-Co coatings with different binder content (9, 12 and 17wt%). Their results show that higher wear resistance is generally expected when the carbide content is higher, but the wear rate for coating with the highest carbide content is low due to extensive microcracking and fracture occurring during the test.

The effect of carbide grain size on the abrasive wear resistance for thermally sprayed WC coatings has been studied by many investigators. Usmani et al. [102] studied abrasive wear (two-body wet abrasion test with 120 grit SiC paper under 240 kPa) behaviour of HVOF sprayed WC-Co coatings with different carbide grain sizes (0.75, 0.88, 1.03, and 1.43  $\mu\text{m}$ ) and found that by increasing carbide size in the coatings, there is a decrease in hardness and  $\text{W}_2\text{C}$  phase, and an increase in fracture toughness and abrasion resistance (Fig. 2.25). Li et al. [120, 121] in two different works studied the effect of carbide grain size of WC-Co powder with different carbide sizes using an HVOF system and showed that the wear rate of cermet coating was observed to be proportional to the square root of carbide particle size in the coating and inversely to the volume fraction of carbide phase content.

The effect of both carbide grain size and content can be illustrated by mean free path parameter. For the cemented materials, it has been shown that there is a correlation between abrasion resistance and the mean free path in the binder phase between the carbide grains; a small mean free path, due to a high volume fraction of fine carbide grains, gives the highest abrasion resistance [91]. Kumara et al. [122] investigated abrasive wear (DSRW test with alumina) behaviour of WC-

10Co-4Cr coatings produced by using HVOF and pulsed combustion processes and found a liner relationship between abrasive wear loss of coatings and the binder mean free path (Fig. 2.28) showing the best abrasion resistance among the coatings tested for coating with lowest mean free path.

The effect of carbide grain size on abrasive resistance in HVOF coatings and sintered cermets seems to be opposite. Decomposition of the carbides during spraying is the main reason for this. The microstructure of thermally sprayed WC cermets must be consider in terms of bonded splats which contain WC,  $W_2C$  and W phases within an brittle amorphous W-C-metal binder. Large carbides tend to undergo less decomposition than fine carbides as reported by many authors [106, 123]. Higher decomposition leads to decreased volume fraction of retained WC grains and increased dissolution of W and C in the binder phase.

## **Porosity**

Porosity has an effect on wear in that coating collapse often occurs around pores [124, 125]. Moreover, open surface pores will serve as origins for wear scratches made by individual abrasive particles. Pores which have been formed during the deposition process and can be found within the coatings have an effect on some of the mechanical properties such as elastic modulus, shear modulus, and hardness that may affect the wear performance [123]. Nevertheless, when the pores appear on the surface of a coating or are generated on the surface due to cutting or polishing process, the contact condition will be changed which causes the change in wear performance.

In thermal spray processes, it is known that high impact velocity and high temperature are considered to be desirable to obtain dense coatings. Marpel and Lima [117] reported that thermally sprayed WC-12Co coatings deposited with different type of HVOF systems contain porosity level of 1% and lower when the average particle temperature was above 1850°C (Fig. 2.29). The particle temperature and particle velocity depend on the morphology of the feedstock powder, and it has been shown that the larger the particle size, the higher the particle density and heat capacity, the lower the highest particle temperature and velocity that are reached during flight in HVOF spraying [126]. These result in higher porosity in the coating with larger particles. The effect of porosity on binder hardness also becomes more pronounced with increasing WC volume fraction since porosity tends to increase with higher WC content as shown in Fig. 2.30. This effect is more sensitive for coatings with finer carbide sizes [126].

#### **2.1.9.5 Abrasive Wear Mechanisms**

Wear of WC cermet coatings occurs by the accumulation of damage, fracture and removal of single grains of WC; the basic wear mechanism of all WC-based cermet coatings is reported to be the local pulling-out of carbide particles from the binder phase [127]. There are additional mechanisms of wear described by authors who have measured the abrasive wear of thermally sprayed WC cermet coatings.

Stewart et al. [75] reported indentation-induced sub-surface cracking during abrasion of HVOF sprayed WC-Co with both hard (alumina) and also soft (silica) abrasives. Their work showed that the brittle, tungsten-rich areas of the binder phase (and possibly splat boundaries) were the favoured routes for crack

propagation. The scars on the coatings produced by hard abrasion were relatively flat with large amounts of grooving and pitting, whereas the scars produced by soft abrasion exhibited only limited grooving in areas which were devoid of carbides, and where original splat outlines could still be discerned. Kasparova et al. [88] studied the abrasive wear mechanism of WC-Hastelloy C when abraded with alumina and silica and reported plastic deformation, grooving, ploughing and cutting of the surface when abraded by alumina particles whereas, the main wear mechanism associated with abrasion by silica particles was smearing of the binder phase and extruding of large materials blocks in the wear track. Kumari et al. [122] investigated abrasion of thermally sprayed WC-10Co-4Cr with alumina (average 50 $\mu$ m) and reported preferential removal of the binder phase, followed by WC grain pullout. Kim et al. [128] reported a splat delamination mechanism for abrasion of thermally sprayed WC-Co coatings. This splat delamination resulted from subsurface microcracks, the formation of which were controlled by the material properties such as the intersplat cohesive strength. The cohesive strength of the thermally sprayed coatings generally is an important factor controlling material removal. Hartfield-Wunsch and Tung [125] argued that for thermal spray coatings, if a splat delamination mechanism was predominant, the splat direction and waviness would play important role in wear performance of coating with delamination in flat splats being easier than that in wavy splats.

#### **2.1.9.6 Abrasive Wear Resistance**

The complex behaviour of WC cermet thermally sprayed coatings illustrate clearly that wear resistance can never be regarded as an intrinsic material property. The wear rate, and the mechanisms of wear, depend not only on the

composition and microstructure of the material, but also to a very important extent on the conditions to which it is exposed [3]. Under certain conditions, the abrasive resistance of these type of coatings can be dominated by their fracture toughness rather than their hardness [110]. Another important element for the abrasion resistance of the coatings is the bond strength between the hard particles and the matrix. A strong bond between the matrix and the particles, will result in a higher resistance to abrasive wear [77].

In general, it is known that the wear resistance of a material depends on the material's resistance to penetration by abrasive particles or protruding asperities of mating material, and the resistance to material removal by fracture and plastic flow. This resistance to wear is, in part, reflected by properties such as hardness ( $H$ ) and fracture toughness ( $K_{IC}$ ) [129]. Wayne and Sampath [81] proposed following equation for abrasive wear resistance of thermally sprayed coatings which show the effect of hardness and fracture toughness along with binder content:

$$\text{Wear resistance} \propto (K_{IC}^{3/8} H^{1/2}) \left( \frac{V_f^{Co}}{1-V_f^{Co}} \right) \quad (2.6)$$

where  $V_f^{Co}$  is the volume fraction of cobalt. Although, they showed evidence in their work to confirm this relationship, it was believed that other mechanical parameters like residual stresses and cohesive strength would be required to improve the predictive capability of the relationship [102].

In sintered WC cements, the hardness decreases and the fracture toughness increases with increasing binder content. In thermally sprayed WC cermet coatings during the spraying process, the dissolution of WC decarburization and

results in the formation of an amorphous binder phase are considered to affect the mechanical properties of the binder phase. The intrinsic binder hardness has been estimated using a rule of mixtures [130] and exhibited significantly higher values than those reported for sintered materials. The hardening of binder phase increases the coating hardness and reduces the fracture toughness [103]. While the hardness of sintered WC cermets strongly depends on the WC volume fraction, the hardness of the coating depends more on the properties of binder and other new phases such as  $W_2C$  and  $W$  distributed in the binder ( $W_2C$  phase ( $H_v=3000$ ) is harder than the WC phase ( $H_v=1300-2300$ )) [90]. Therefore, the mechanical properties of the WC cermet coatings are a result of a balance of microstructure, phase make up (amounts of  $W_2C$ , amorphous phase), porosity, etc. Also, it has been observed that thermally sprayed WC coatings exhibit large anisotropy in mechanical behavior within the deposit; for example, the measured fracture toughness in the direction parallel to the substrate (perpendicular to the direction of spray) has been shown to be significantly lower than that measured in the direction perpendicular to the substrate (in the direction of spray) [131].

In summary, the abrasive wear resistance of thermally sprayed WC cermet coatings is controlled not only by the composition of the binder, WC content and grain size in starting powder, but also by the degree of chemical reaction during spray process. In general, lower degree of decomposition and higher retained WC phase content give the greatest abrasive wear resistance. On the other hand, the hard  $W_2C$  and brittle amorphous phases resulted from decomposition can enhance the bulk hardness of the coating and abrasive wear performance. There is an optimum point of decomposition for each coating which abrasive wear resistance

can be in maximum level. The wear mechanism in the thermally sprayed WC cermet coatings can be predicted based on the abrasion regime. Under soft abrasion, the mechanism of material removal is preferential removal of the binder, fragmentation and pullout of carbide grains while under hard abrasion, the material is removed by plastic deformation (grooving) and fragmentation of the WC grains followed by fracture in binder.

There are a considerable number of works on the characterisation and properties of thermally sprayed WC-Co coatings. New advanced materials include WC composite with complicated alloyed binders such as nickel or iron base alloys which can improve the properties and applications of these types of coatings. The properties and performance of these coatings are attributed to the microstructural changes which occur during the spray process. Therefore, the characterisation of the new coatings and investigation of the causal relationship between deposition process parameters, microstructure and wear performance of these coatings will be important.

## **2.2 HVOF- Sprayed WC Cermet Coatings**

### **2.2.1 Introduction**

Thermal spraying is a coating process in which melted and/or heated materials are sprayed onto a prepared surface. The feedstock material is typically heated by either plasma, arc or combustion flame. Coating materials available for thermal spraying include metals, alloys, ceramics, plastics and composites which are fed in powder or wire form, heated to a molten or semimolten state and accelerated

towards substrates in the form of micrometer-size particles. The resultant coatings therefore arise from the successive build-up of flattened particles commonly referred to as “splats” (Fig. 2.31). The metallurgical structure of splats may feature oxides, metastable phases, ultra-fine grained or even amorphous material [132]. Common thermal spraying systems are “flame spraying”, “wire arc spraying”, “plasma spraying”, “detonation spraying” and “High-velocity oxy-fuel (HVOF) coating spraying” [133]. The main differences between these types of spraying techniques are in the degree of heating and acceleration of the feedstock during spray process. In processes such as flame spraying and wire arc spraying, the particle velocities are generally low ( $< 150$  m/s), and particles must be molten to be deposited. Plasma spraying, developed in the 1970s, uses a high-temperature plasma jet generated by an arc discharge with typical temperatures  $>15000$  K, which makes it possible to spray refractory materials such as ceramic oxides. With the advent of vacuum plasma spraying systems (VPS) and low pressure systems (LPPS), materials which are prone to oxidation may also be deposited.

During the 1980s, a new class of thermal spray processes called high velocity oxy-fuel spraying was developed. In this process in which the degree of heating of the powder particles is lowered in favour of their acceleration, a mixture of gaseous or liquid fuel and oxygen are combusted continuously in a combustion chamber. The resultant hot gas at a pressure close to 1 MPa flows out through a converging–diverging nozzle. The jet velocity at the exit of the barrel typically exceeds 1000 m/s. A powder-feed stock is injected into the gas stream, which accelerates the powder up to around 800 m/s. The stream of hot gas and powder is directed towards the surface to be coated. The powder partially melts in the

stream, and deposits upon the substrate. The resulting coating has low porosity and high bond strength [134]. The resultant bonding is more the result of kinetic as opposed to thermal energy. Some of the important differences between combustion and plasma systems are highlighted in Table 2.1.

HVOF spraying is commonly used to deposit wear and corrosion resistant coatings. The process has been most successful for depositing cermet materials (e.g. WC-Co) and other corrosion-resistant alloys (stainless steels, nickel-based alloys, aluminium, hydroxyapatite, etc. [134].

### **2.2.2 HVOF Process Variables**

The HVOF process variables can be classified into primary and secondary parameters [135]. The primary parameters include the feedstock powder (composition, morphology, size and feed rate), the fuel gas (composition and flow rate), the oxygen-fuel gas ratio, the carrier gas (composition, flow rate and pressure) and the gun design (nozzle type and dimensions). The secondary variables include the spray distance, the rotational speed of sample, the gun traverse rate and substrate parameters (type, geometry, grit blasting or preheating prior to spraying and cooling during spraying). All of these variables can affect on the microstructural characteristics (i.e. phases present and porosity) and mechanical properties (i.e. hardness, ductility and wear behaviour) of the sprayed coating.

### **2.2.2.1 Feedstock Powder**

The structure and properties of coatings manufactured by thermal spraying depend strongly upon powder feedstock characterisation such as composition, morphologies, porosity, size distribution and flowability [133]. The powder feedstock morphology and particle size distribution are related to its manufacturing route. There are several manufacturing methods of thermally sprayed powder feedstock such as atomization, fusing and crushing, milling and sintering, cladding and spray-drying techniques [136]. Powders with the same chemical composition and size distribution produced by different manufacturing methods can have different morphologies which result in significant structural variations after thermal spray coating. The powder morphology, resulting from their manufacturing process, varies from spherical to irregular or blocky [137]. The effect of particle shape on their aerodynamic behaviour, different particle-specific masses (corresponding to particles with different porosity) result in different thermal conductivities and diffusivities. The capability of powder in flowing through the powder feeder and injection system, termed the flowability is extremely important in all thermal spray processes. Poor flowability results in fluctuations in powder feed rate and thus in inhomogeneous coating structures [136]. It is well known that spherical and homogeneous powder particles with a narrow size range are preferable to particles having faceted shapes, wide size distributions and non-uniform distribution of components [138].

### **Spray-Drying Technique**

For producing cermet particles like WC cermets, it is necessary to mix rather fine ceramic and metal or alloy particles and form granules of their mixtures. Spray-

drying is one of the most versatile techniques to manufacture of such powders. In spray-drying, agglomerated powders are produced from suspensions; particles are sintered in rotating furnaces where diffusion occurs within particles but not between them.

### **2.2.2.2 Fuel Gas**

A number of different fuel types may be employed in HVOF thermal spraying including kerosene, hydrogen, propylene, acetylene and natural gas [139]. Different types of fuel gas can change the combustion temperature of the system affecting the amount of thermal transfer to the powder particles and consequently changing in coating structure [114].

Oxygen to fuel gas ratio (stoichiometry) also influences the temperature of the flame and spray condition (reducing or oxidising atmosphere) [19]. By changing the stoichiometry, it is possible to change the temperature and exit velocity of the gas flow and the energy of the particles as they impact with the substrate which in turn affects their composition and the bond strength of the coating [140]. Microstructural decomposition in the coating is significantly influenced by oxygen-fuel ratio which then affects the microstructure and mechanical properties of the coatings [141].

### **2.2.2.3 Powder Carrier Gas**

In order to feed the powder into the flame stream, a carrier gas is needed; the carrier gas can act as a diluent to the oxygen-fuel gas and will cause a reduction in

the gas temperature as it absorbs a fraction of the heat of combustion energy [114]. The main parameters relating to a carrier gas which can influence the final coating properties are the composition, flow rate and the pressure.

#### **2.2.2.4 Gun Design**

The gun design is an important part of the spraying system. Many factors such as where the powder enters the system and components such as the nozzle have a significant effect on the final coating. Figs. 2.32a and 2.32b exhibit two different types of HVOF nozzle which use liquid and gas fuel respectively.

#### **2.2.2.5 Stand Off Distance**

The length of time the particles dwell in the flame zone and as such the temperature of the particles at the impact point are determined by the stand-off distance. The larger distance means that the particles are more time in the oxidizing environment and probably have a lower temperature upon impact. Fig. 2.33 shows the temperature and velocity of the particle in-flight as a function of stand-off distance for an HVOF system indicating stronger influence of particle size on the particle temperature than the particle velocity [105]. Apart from small particles, the dependence of velocity on stand-off distance is small.

#### **2.2.2.6 Traverse Speed**

Both the horizontal and vertical gun-substrate traverse speeds can affect the nature of each deposited layer of coating. Fig. 2.34a shows schematic diagram of a single

traverse of a spray stream across a substrate. Subsequent overlapping of successive passes of the gun will result in the build up of a coating layer [142]. The overlap of each pass should be less than half the width of the spray pattern to produce a coherent coating thickness (Fig. 2.34b). A thicker layer can result in overheating, cracking and possibly spallation. Thinner layers can increase the oxide content [142].

### **2.2.3 Sintered WC Cermet Materials**

WC-metal/alloy cermets (also known as hardmetals) are one of the important types of composite materials. The combination of hard carbide and tough, energy absorbing metal results in a material which has some of the best attributes of each phase. Two important aspects of the WC cermets which determine the characteristics of the composites are the composition and the WC grain size [13]. These factors describe the dispersion of the hard and brittle carbide phase within the ductile metallic matrix.

### **2.2.4 Thermally Sprayed WC coatings**

Many thermal spraying techniques such as air plasma spraying (APS) and high velocity oxy fuel (HVOF) spraying can be applied to deposit the WC cermet coatings; however, the properties of coatings strongly depend on spraying technique. Compared to other spraying techniques, HVOF spraying is one of the best methods for depositing WC cermet powders due to the higher velocities and lower temperatures experienced by the powder [2]. Tungsten carbide based powders are widely used in high-velocity oxygen fuel (HVOF) spraying system to

produce dense coatings of high hardness and wear resistance, used in a variety of conditions which include sliding, fretting, abrasion and erosion. In applications where higher demands on corrosion or oxidation resistance are made, the WC based powders are produced with advanced binder materials such as Ni based alloys [88]. However, the microstructure and the mechanical properties of the coatings not only depend on the composition of the powder, they are also considerably affected by phase transformations which have taken place during the spray process. Compared to sintered WC cermets, for which the sintering atmosphere, temperature and time are carefully controlled, HVOF-sprayed WC coatings still suffer from decomposition and decarburization during spraying process leading to formation of detrimental phases such as  $W_2C$ , W resulting from an oxidation of the spray material in the flame and from thermally activated reactions between WC and the binder matrix, respectively [119, 143, 144]. Furthermore, rapid solidification of the supersaturated binder (with tungsten and carbon in solution) matrix can cause the formation of an amorphous or nanocrystalline phase [20, 145, 146]. Phase transformations and the resulting coating characteristics are affected by the type and composition of the powder as well as by the spray system and the fuel used [102, 104, 147, 148].

#### **2.2.4.1 Feedstock Powder**

In the past few years, feedstock powders prepared by agglomeration (via spray drying) and subsequent sintering have been used for HVOF coatings. Improved flowability is one advantage of these powders. Other advantages of spray powder preparation are the predominance of equilibrium phases, a homogeneous microstructure for all powder particles, and a controlled hard phase grain size.

Porosity of the powders can be reduced and controlled by optimisation of the spray drying process [149].

#### **2.2.4.2 Phase Transformation during spraying process**

During thermal spraying of WC-based powders, phase transformations occur that determine the microstructure and chemistry of the coatings. In broad terms, these cover firstly the decomposition of carbide phase during time spent in the hot gas, and secondly the formation of new phases during the solidifications process within the rapidly cooled splats which form when powder particles impact the substrate (Fig. 2.35). The decomposition is directly linked to the temperature-time history and gaseous environment in the spray system; the degree of reaction determines not only the phases present within the coating, but also their quantities. The decomposition of the particles is dependent upon the reaction with oxygen in the hot gas resulting in a decarburisation process. The amount of decarburisation is affected by the flame oxidation potential, the local temperatures of the individual carbide particles and the relative solubility of the carbide into the binder phase [150].

The mechanisms of decomposition can be described as follows: With increasing the temperature of the particle in-flight, the metallic binder phase reaches the melting point and wets the WC grains thus preventing direct contact with the gas phase. However, as dissolution of the WC crystals in the molten metal proceeds the total amount of the tungsten and carbon dissolved into the binder phase increases considerably. At the same time, oxygen diffuses through the molten phase and reacts with the carbon to form CO. Carbon will be removed from the

melt either by reaction with oxygen at the melt/gas interface or through oxygen diffusion into the rim of the molten particle, leading to CO formation [105]. The depletion of carbon from the melt will thus be restricted to a shell region, the depth of which will depend on transport of carbon, oxygen and the reaction kinetics. However, removal of carbon, locally, from the melt will drive further dissolution of WC grains in this shell region as the system attempts to re-establish local equilibrium at the WC-melt interface. The overall result will be WC grains which are considerably less angular in the outer shell regions (due to dissolution), a reduced WC volume fraction compared with the central regions of the particles, and a W:C atomic ratio in the melt greater than unity. When the temperature decreases, new phases are formed due to the decreasing solubility of tungsten in the binder liquid phase [150]. As the total amount of carbon has been reduced by oxidising reactions, it is only possible to form phases with a lower amount of carbon (i.e.,  $W_2C$ , W). Therefore, the composition of new phases depends on the solubility degree of W and C in the binder and amount of carbon loss during decarburising process. Once it is assumed that higher concentration of tungsten and carbon must be located near to the original WC crystals, it is reasonable to believe that new phases grow near to these carbides or they use the WC structures as crystallising nuclei.

Stewart et al. [105] discussed the mechanisms associated with the production of the new phases in Co-W-C system and identified two points on the ternary phase diagram relating to possible melt compositions at ~2200 K (Fig. 2.36) although, they believed that  $W_2C$ , W and the binder (W, C) nanocrystalline/amorphous phase all form during rapid solidification of the splat. Since high splat cooling

rates exist during thermal spray deposition ( $\sim 10^6$ - $10^7$  K/s [151]), ternary phase diagrams can only aid in understanding how shell and core regions of splats, having different melt compositions as a result of decarburization, might behave. At approximately 2220 K the melt composition in equilibrium with WC at the core of a powder particle is shown by the solid circle in Fig. 2.36 (W:C atomic ratio=1). If, as in the shell region, carbon has been lost from the liquid then a possible melt composition would be indicated by the open circle. Higher spraying temperatures will result in large amount of W and C dissolution and as such will cause the composition at the periphery of a particle to change. In the presence of oxygen there have been several possible routes proposed which all result in the production of free carbon, liberated from WC during decarburisation [139, 152, 153]. The nanocrystallinity may be due to crystallization of an originally amorphous matrix as a consequence of reheating during successive gun passes to build up a thick coating.

There are two main methods for quantifying the amount of decomposition that occurs during spraying. Firstly, there is chemical analysis whereby the chemical composition of the coating is compared to that of the powder feedstock. Since carbon is the element most likely to be lost during spraying, the carbon value usually is the most informative. The second method by which phase content can be quantified is to use XRD techniques. In this method it is possible to quantify the amount of phases both in the coating and in the starting powder feedstock and compare these. There are number of methods whereby this comparison may be done; *i*) obtaining the ratio of same Miller index WC/W<sub>2</sub>C peak intensities [114,

138, 154], *ii*) comparison to normalised WC/W<sub>2</sub>C samples [102] and *iii*) the Rietveld analysis method [78].

### 2.2.4.3 Phase Content and Composition

The microstructure of thermally sprayed WC cermet coatings are characterised by special observable features. Depending on the degree of the dissolution and decomposition, the cross-sectional SEM backscattered electron (BSE) images of the coatings show quite clearly the layer by layer structure of the coatings, including carbide grains with different size, shape and distributions, binder matrix regions with various BSE contrast indicating different compositions, and a degree of porosity dispersed within the coating (Fig. 2.37).

Two types of carbides can be seen in the microstructure of the coatings, those that retain their morphology as in the powder feedstock (blocky or angular in nature) and those being more rounded in nature. It has established that these rounded carbides often comprise two phases, with the outer fringe usually being much brighter than the core (indicating higher mean atomic number). TEM investigations can confirm that the brighter surrounding phase is W<sub>2</sub>C [78, 105]. Formation of the new W<sub>2</sub>C and W phases is due to crystallization from tungsten-rich molten binder during high rate solidification; the new phases form as fringe shape around WC grain as an efficient nucleation substrate [105].

The matrix phase also generally includes at least two separate regions with variable contrast in the BSE image [145]. Variation in intensity within the binder material in BSE mode indicates different compositions due to the varying amount

of W and C dissolved into the binder [118]. Karimi et al. [145] showed the gray regions to be tungsten-rich in comparison with the dark regions (see Table 2.2). Schwetzke and Kreye [118] reported much higher amounts of W and C in the binder of an HVOF-sprayed WC-Co coating than those given in the equilibrium phase diagrams for Co-W and Co-C due to the binder phase being described as a super saturated solid solution. A number of workers have discussed the exact nature of the binder phase reporting amorphous [146], nanocrystalline [145] and even microcrystalline [155]. Grimberg et al. [155] suggested that amorphous or nanocrystalline binders result from rapid solidification rates whilst microcrystalline material would result from slower cooling rates. The cooling rate is also dependent on the particle size; smaller particles would reach higher temperatures and impact with the substrate at high speeds (Fig. 2.33) resulting in rapid solidification leading to more amorphous or nanocrystalline material.

Porosity is a prevalent feature in the microstructure of WC cermet coatings and affects a wide range of coating properties such as abrasive wear behaviour. Various methods are employed for quantitative measurement of porosity, which forms an important and integral part of microstructural characterization of thermal spray coatings. Image analysis (IA) has been known as a reliable method for characterization of porosity using microstructural images from thermally sprayed coatings [156]. The level of porosity in the HVOF coatings is generally very low (a few percentage). Due to the structural complexity of WC cermet coatings, great care must be taken in preparing the cross sections to achieve a true representation of the microstructure in order to measure the extent of porosity [157]. There are two main kinds of porosity in thermal spray coatings: gas porosity and shrinkage

porosity. The first is responsible for the development of the large pores in the coating and is formed as a result of the gas capture due to the roughness of the substrate (coating) surface and the molten droplet deformation during its impingement. The second is formed within the coating during the solidification [158]. Tekmen et al. [159] suggested that the free carbon content from the decomposition of WC can react with oxygen to form CO<sub>2</sub> gas porosity. In general, it is considered that the coating porosity decreases with the increase in spray particle velocity and an improvement in particle melting-degree. The combination of high temperature and velocity should facilitate the particle deformation upon impact, so that the solidifying splats will be able to conform to the surface of the previously deposited layer and fill the pores and defects [116]. Increasing binder contents also tended to reduce porosity of the coatings because compared to WC, metallic binder has lower melting point and easier to be melted, which can fill the pores in the coating [126]. However, the porosity of the coatings is also affected by the melting behaviour of the particles. Dense powders, produced by sintering or fusing, are difficult to melt in the HVOF process. Thus, coatings sprayed with these powders show higher porosity, especially when spray systems are used that provide rather low heating of the particles [118].

#### **2.2.4.4 Microstructure and Mechanical Properties**

The mechanical properties of the thermally sprayed coatings are a result of a balance of their composition, microstructure, phase contribution, porosity, etc. For thermally sprayed WC cermet coatings, the levels of decomposition affect on the mechanical properties such as hardness and fracture toughness [160]. The hardness and fracture toughness value can be influenced by many factors such as

binder content [161], binder composition [150], splat cohesion [162], the spraying system employed [163], the particle temperature and velocity during spraying [117], size of WC grains [106] and the degree of porosity present [103, 160].

Wide ranges of hardness value (between  $H_V = 800-1800$ ) have been reported for HVOF-sprayed WC cermet coatings by a large number of investigators [102, 104, 116, 126, 141, 160, 164, 165]. This is not only due to different powder feedstocks and spraying parameters, but also because of inhomogeneous nature of these materials. This variation basically depends on microstructural characteristics of coatings. General trends observed for sintered WC cermet materials are that increasing the binder content reduces the hardness of the cermet because a reduction of hard carbide phase [126] while for HVOF deposited coatings the hardness depends on many parameters like volume fraction of hard carbide phase [161], hardness of amorphous binder (W, C), formation of new phases and porosity of coating [166]. For example reduction of the carbide phase during the spraying process due to the decomposition leads to dissolution of W and C into the binder and increase its hardness after rapid solidification. Thus although decreasing the carbide phase content causes the hardness of thermally sprayed WC cermet coatings to decrease, amorphous binder saturated with W and C can increase the bulk hardness of coating.

In sintered WC cermets, it has been found that the toughness decreases as hardness increases [82, 98, 167]. This relationship is observed for most materials and is attributed to plastic deformation at crack tips that increases fracture energy.

O'Quigley et al. [168] showed that the relationship between hardness and fracture toughness of sintered WC hardmetals is of the following type:

$$H_v = -mK_{IC} + c \quad (2.7)$$

where  $H_v$  and  $K_{IC}$  are hardness and fracture toughness of hardmetal respectively whereas  $m$  and  $c$  are functions of the WC grain size (and possibly other microstructural parameters). In the sprayed WC cermet coatings (because of anisotropic laminated structure) the same flaws that decrease the hardness can also decrease the tensile strength and accelerate crack growth. Therefore, fracture toughness and hardness cannot essentially have inverse relationship. Qiao et al. [160] deposited a series of WC–Co coatings by the high velocity oxy fuel (HVOF) process and concluded that the hardness and toughness of the coatings increase together, in contrast to the behaviour observed in sintered WC cermets.

**Table 2.1** Attributes of different types of thermal spray systems [133].

Spray system	Heat source	Feedstock	Powder temp (°C)	Powder velocity (m/s)	Deposition rates (kg/hr)
Flame	Oxy-acetylene or hydrogen	Wire or powder	3000	40	2-6
APS	Plasma arc	Powder	12000	200-400	3-9
LPPS	Plasma arc	Powder	12000	200-400	3-9
Detonation	O <sub>2</sub> -acetylene-N <sub>2</sub> +gas detonation	Powder	4500	800	0.5
HVOF	Oxyfuel combustion	Powder	3000	800	2-4

**Table 2.2** A typical characterisation of binder phase composition [145].

Element	Dark binder (at%)	Light binder (at%)
W	32-35	34-52
C	36-48	24-38
Co	13-28	14-17
O	4-7	3-8

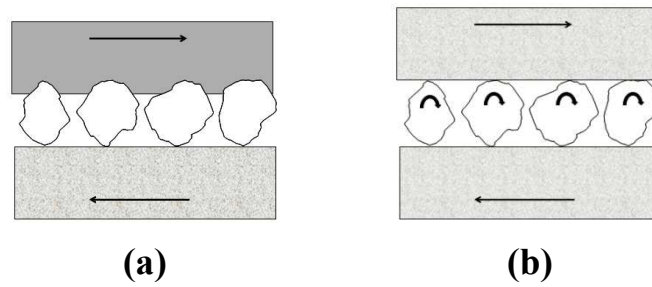


**Fig. 2.1** (a) two and (b) three-body abrasion mechanisms.

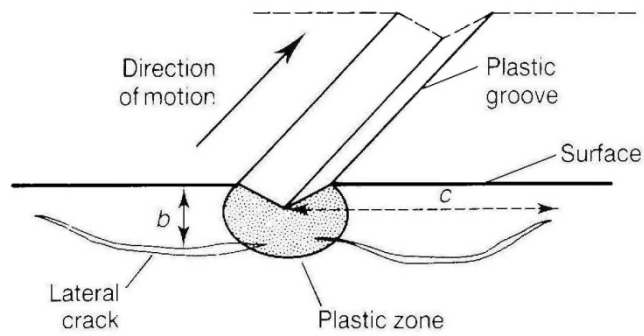


**Fig. 2.2** Schematic illustration of material removal in a brittle material by the extension of lateral cracks from beneath a plastic groove. c: sideways spread of the cracks and b: the depth of the lateral cracks [3].

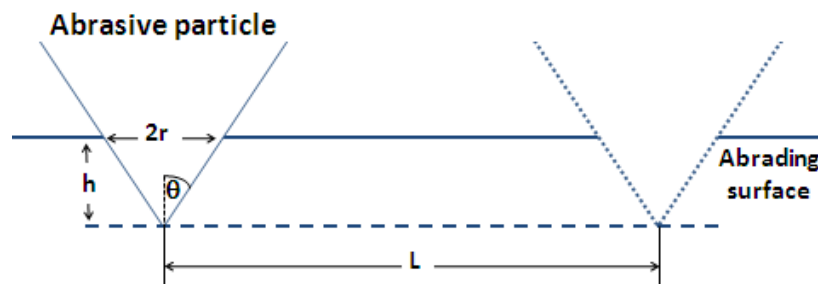


**Fig. 2.3** Schematic illustration of a conically-ended abrasive grain which is removing material from a metal surface.

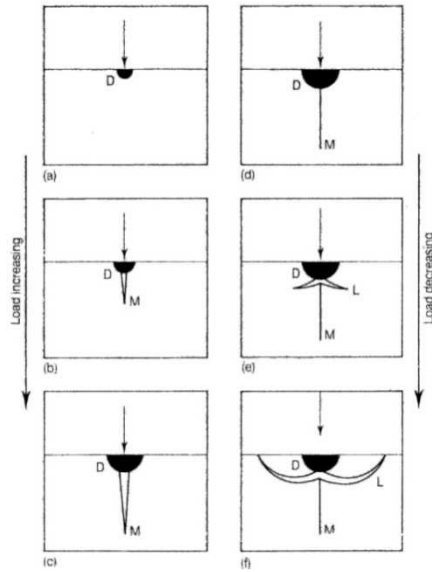


Fig. 2.4 Generation of cracks under an indenter in brittle solids [3].

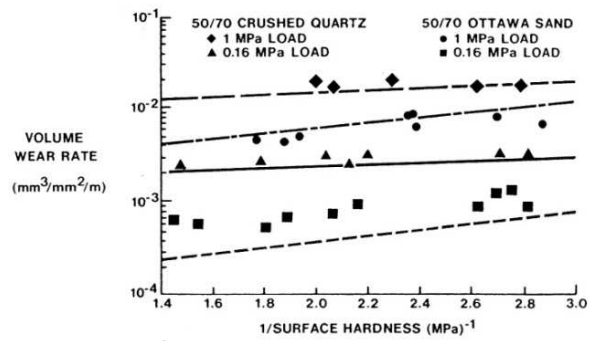


Fig. 2.5 Predicted and experimental volume wear versus 1/surface hardness for steel against two types of abrasive sands; rounded and crushed silica sands [38].

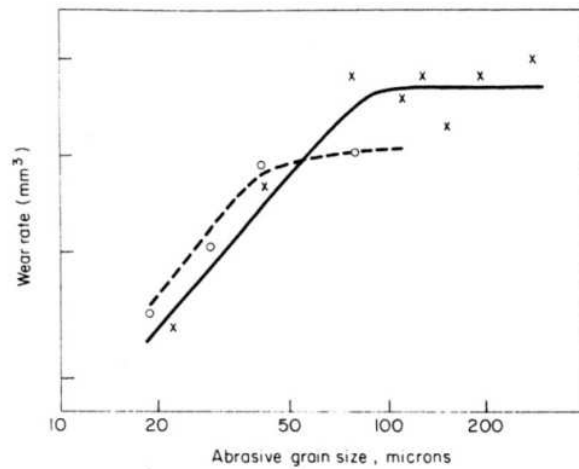
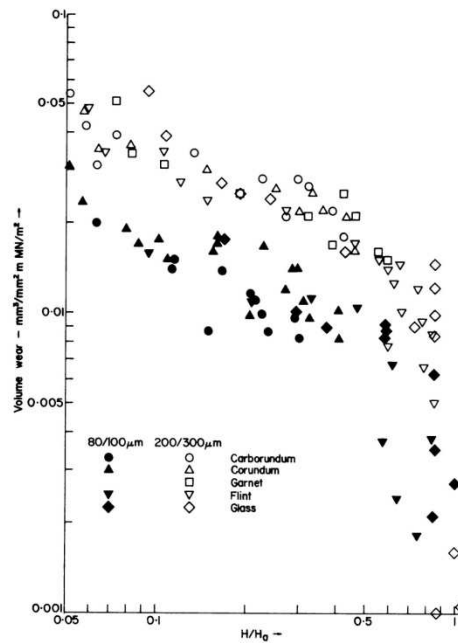
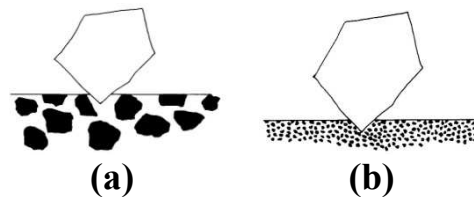


Fig. 2.6 Effect of abrasive particle size on wear of metals; × steel, ○ bronze [35].



**Fig. 2.7** Relative abrasive wear resistance versus hardness ratio of worn to abrasive material [34].



**Fig. 2.8** Schematic diagram illustrating effect of abrasive particle size on deformation of WC composite; (a) scale of deformation is comparable with size of reinforcement and deformation is heterogeneous; (b) scale of deformation is considerably greater than that of reinforcement and deformation is effectively homogeneous [49].

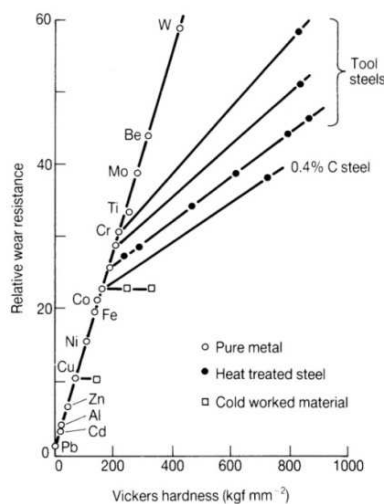


**Fig. 2.9** Relative wear resistance for pure metals and heat-treated and work-hardened steels under condition of two-body abrasion, plotted against indentation hardness [50].

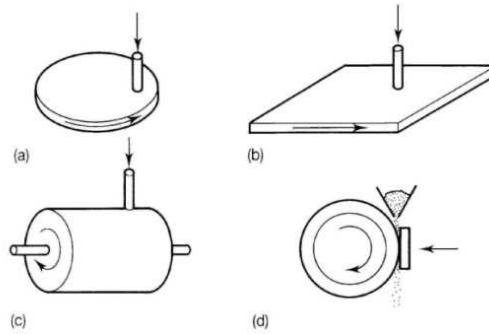


**Fig. 2.10** Schematic illustration of four common methods used to measure abrasive wear rates of materials: (a) pin on abrasive disc; (b) pin on abrasive plate; (c) pin on abrasive drum; (d) rubber/steel wheel abrasive test [3].

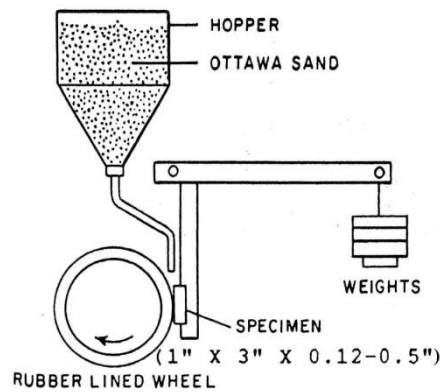


**Fig. 2.11** Schematic diagram of dry sand rubber wheel abrasion test apparatus [4].

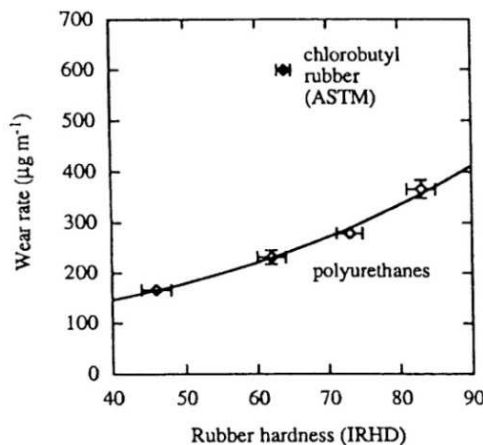


**Fig. 2.12** The effect of rubber hardness on the wear rate of 1020 steel [63]

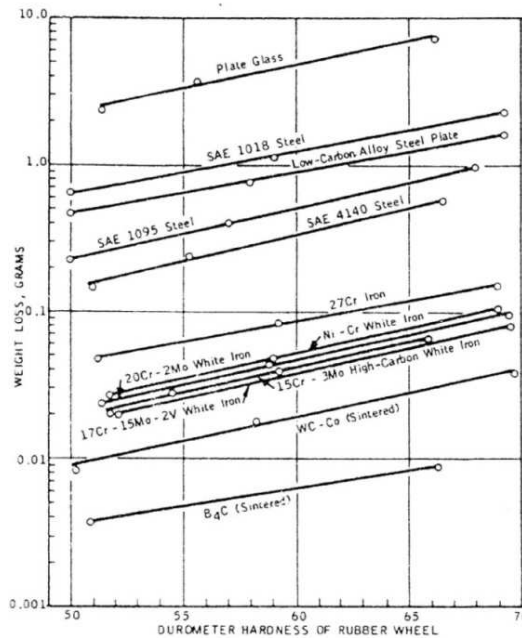


**Fig. 2.13** Weight loss of various materials as determined from the rubber wheel abrasive test at different levels of rubber hardness [61].

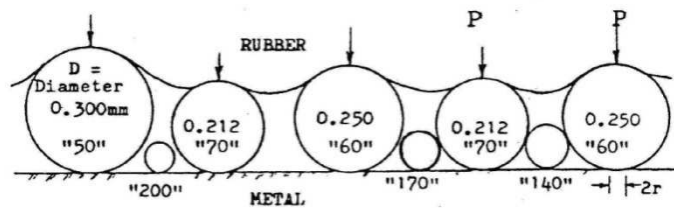


**Fig. 2.14** Idealized section of rubber wheel pressing on various size of spherical sand grains, to scale [62].

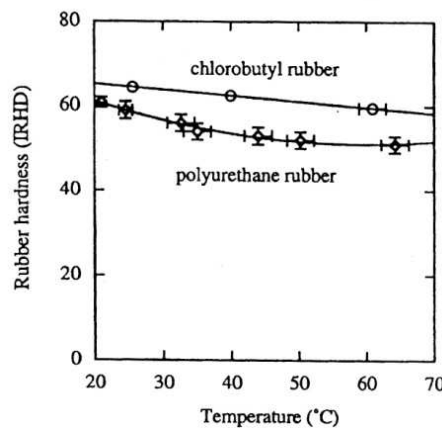


**Fig. 2.15** The effect of temperature on the hardness of a cast polyurethane rubber and a chlorobutyl (ASTM standard) rubber [63].

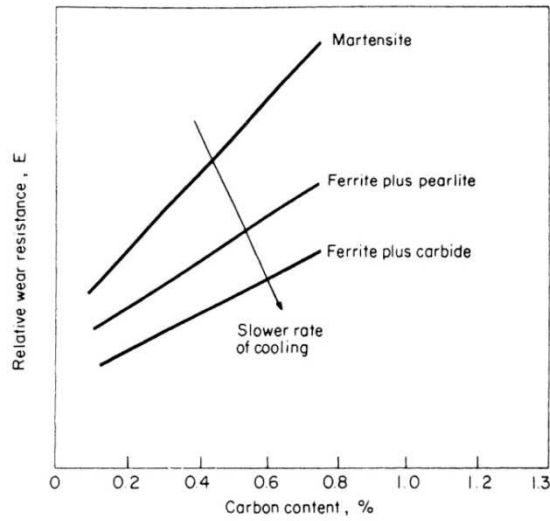


**Fig. 2.16** Effect of carbon content and microstructure on abrasive wear resistance of steels [1].

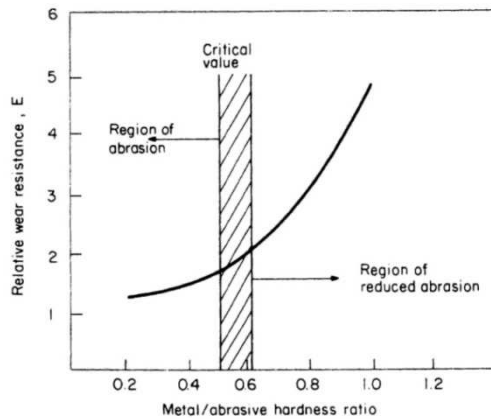


**Fig. 2.17** Effect of hardness ratio of steel and abrasive on wear resistance of steel [48].

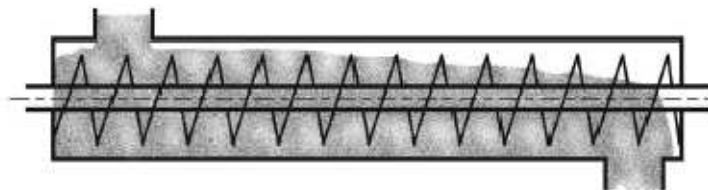


**Fig. 2.18** Ash distribution inside cooling screws equipments [72].

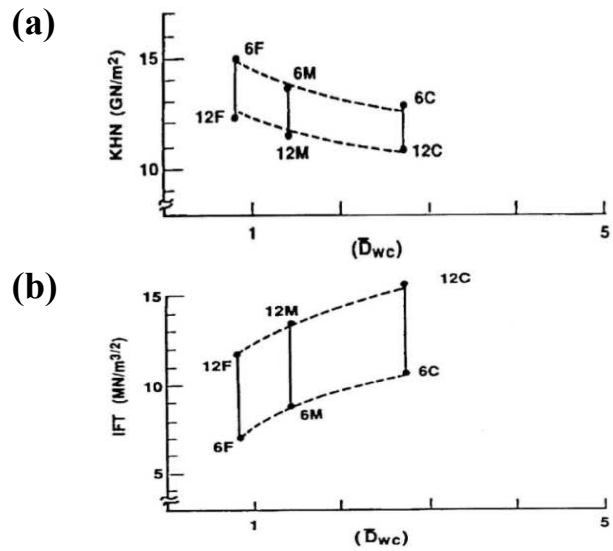


**Fig. 2.19** Effect of changes in the WC grain size and binder content on the mechanical properties of WC-Co cements (IFT: indentation fracture toughness, KHN: knoop microhardness, F: fine, M: medium, C: coarse size of WC grains, 6: 6 wt%Co, 12: 12 wt%Co) [82].

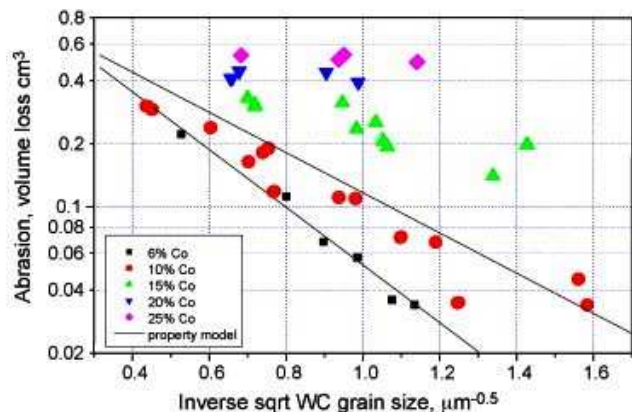


**Fig. 2.20** Dependence of abrasive wear on inverse square root WC grain size for sintered WC-Co cermets [100].

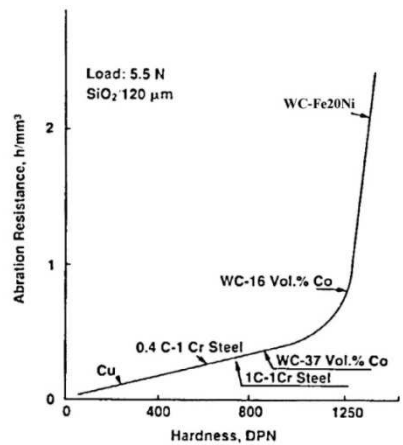


**Fig. 2.21** Effect of hardness on the abrasion of metals, alloys, and cemented carbides by quartz abrasives [91].

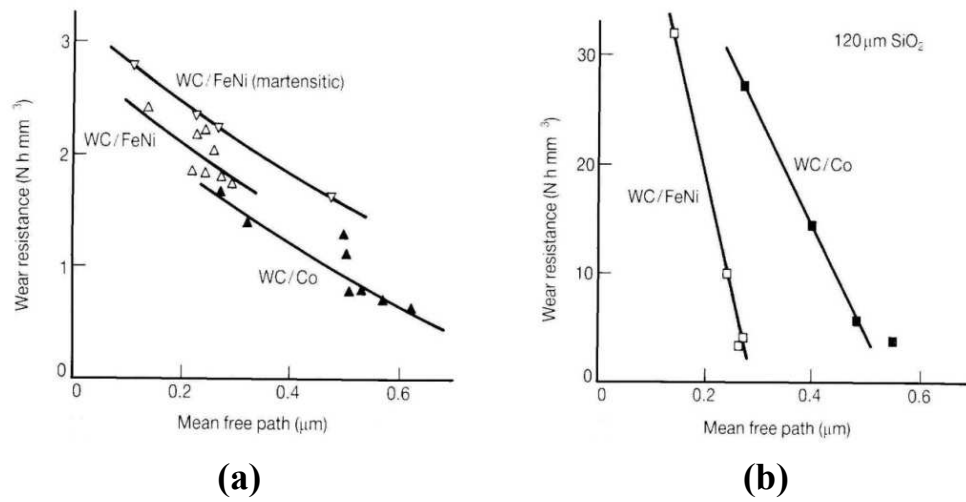


**Fig. 2.22** Abrasion resistance versus mean free path under; (a) hard abrasion by silicon carbide particles and (b) soft abrasion regime by quartz particles [91].

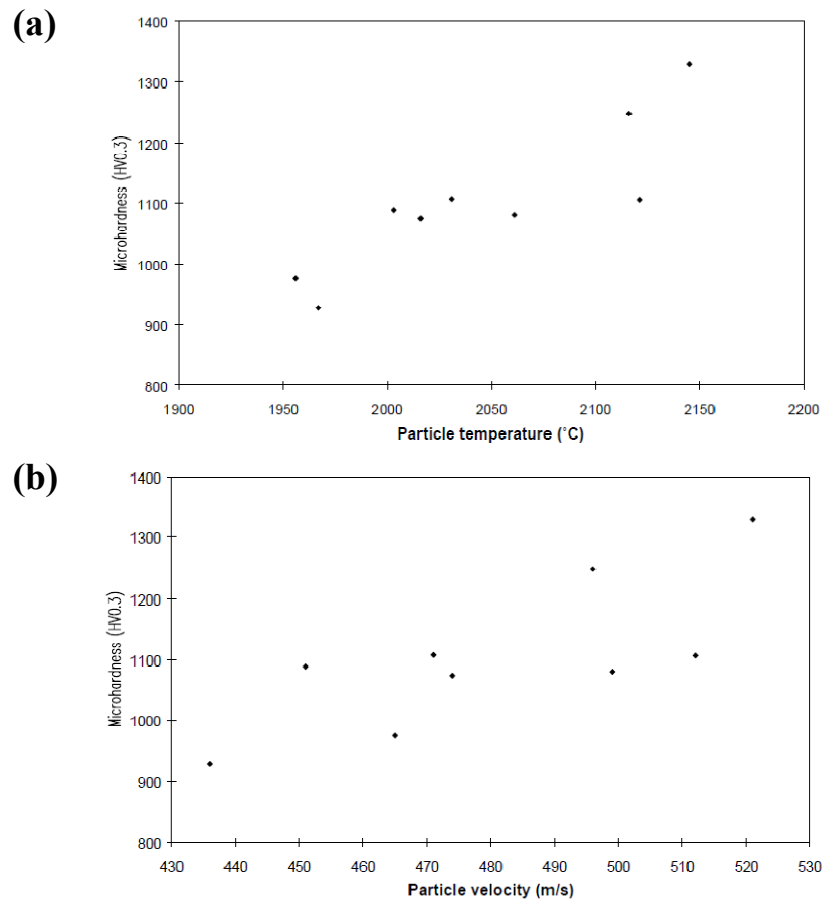


**Fig. 2.23** Relationship between coating hardness and the particle (a) temperature and (b) velocity during the HVOF spraying of WC-12Co powders for different spray parameters [80].

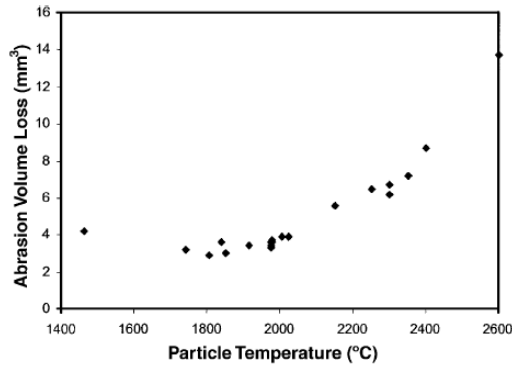


**Fig. 2.24** Abrasion volume loss as a function of the in-flight particle temperature [109].

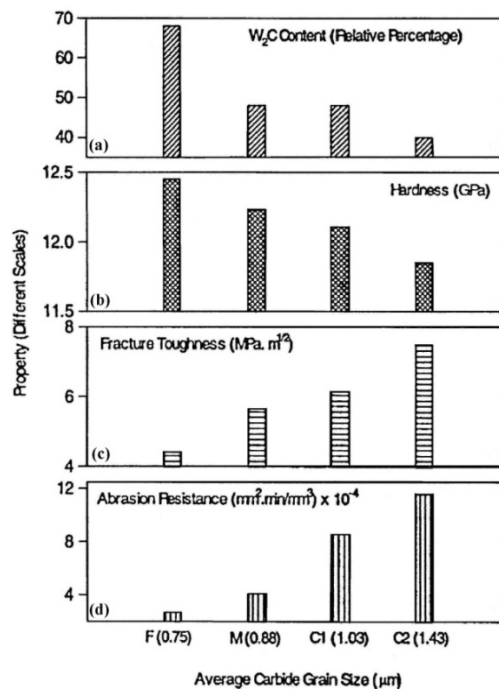


**Fig. 2.25** The W<sub>2</sub>C content, hardness, fracture toughness and abrasion resistance plotted as a function of carbide size of the HVOF WC sprayed coatings. ( F: fine, M: medium, C1 coarse1 and C2: coarse2) [102].

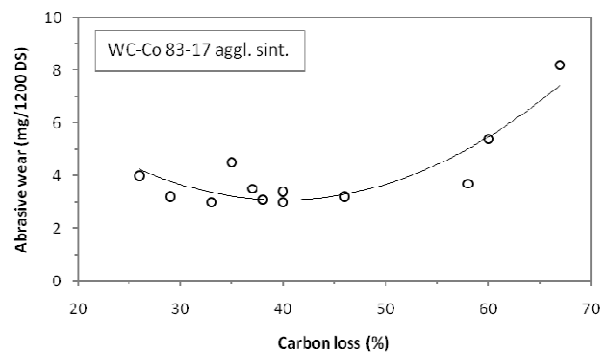


**Fig. 2.26** Effect of carbon loss in the spray process on the wear resistance of WC-Co coatings [118].

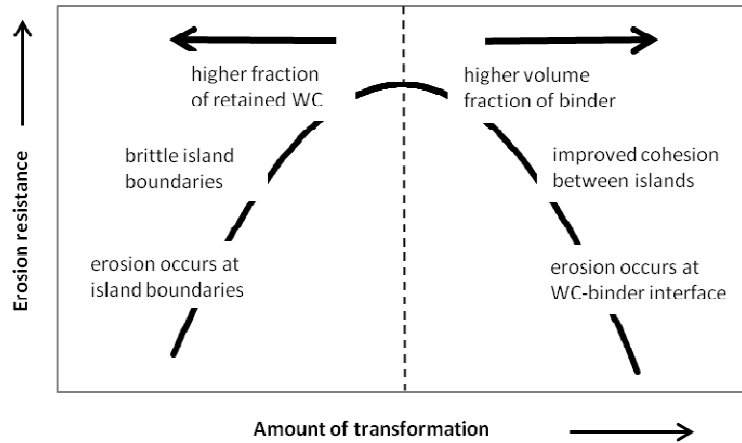


**Fig. 2.27** Schematics of the dependence of the erosion resistance of WC-Co coatings on the decomposition that occur during HVOF spraying [119].

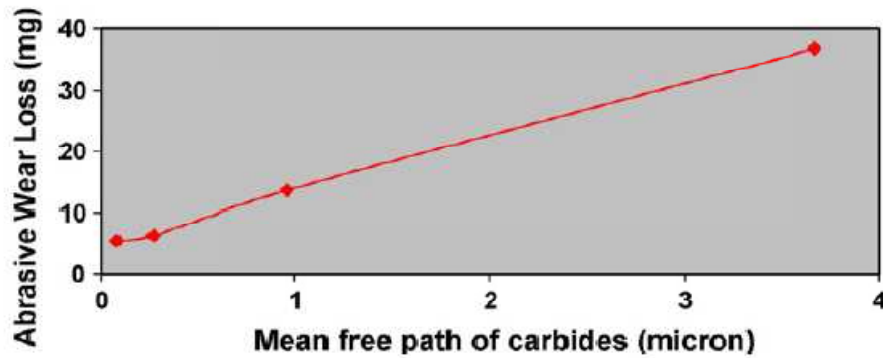


**Fig. 2.28** Relationship between abrasive wear loss of coatings and their calculated binder mean free path [169].

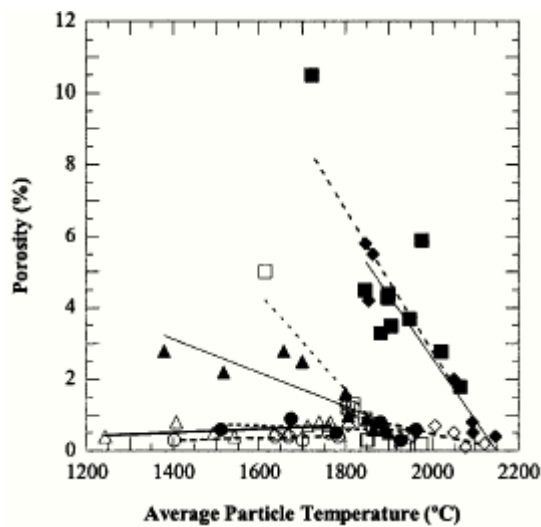


**Fig. 2.29** Levels of porosity in HVOF-sprayed WC-12Co coatings produced under a range of spray conditions [117].

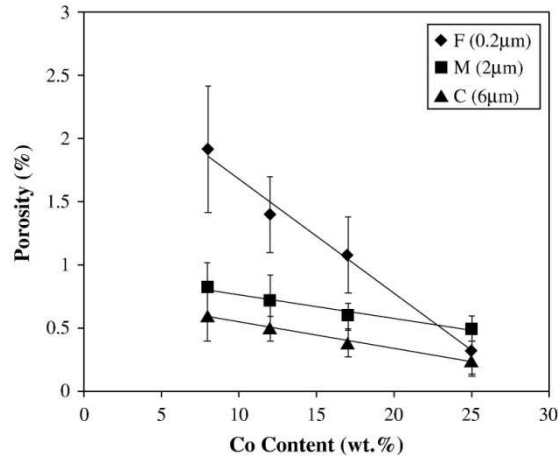


**Fig. 2.30** Effect of binder volume fraction and carbide size on the porosity of HVOF sprayed WC-Co coatings (F: fine, M: medium and C: coarse carbide size) [126].

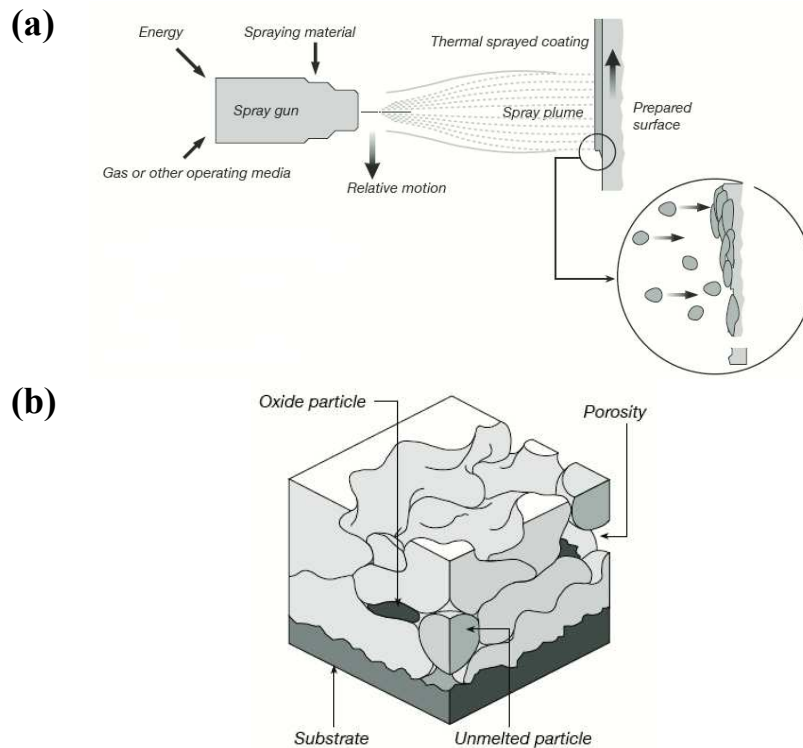


**Fig. 2.31** Schematic diagram of (a) thermal spraying process and (b) thermal sprayed coating [170].

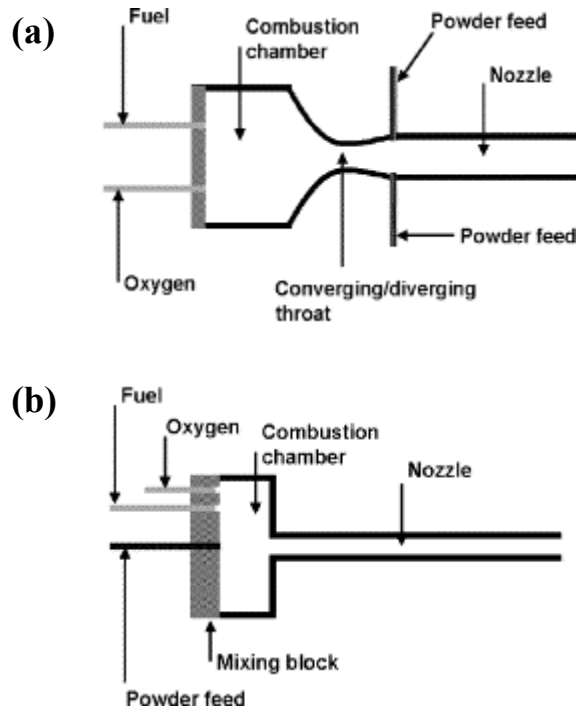


**Fig. 2.32** Schematic diagrams of the design of HVOF system: (a) liquid fuel (Met-jet) ; (b) gas fuel (Top Gun) [115].

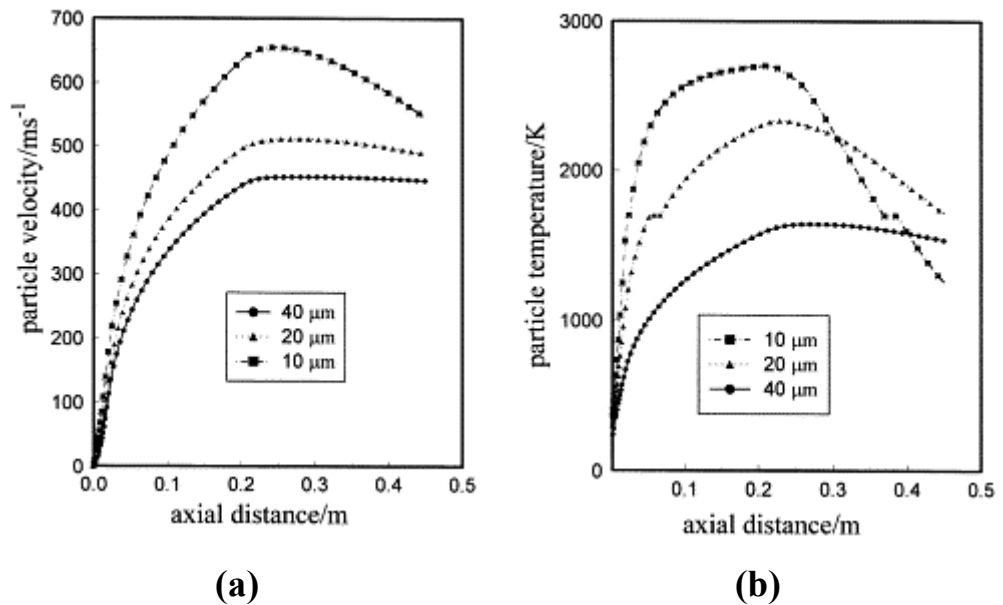


**Fig. 2.33** Profiles of (a) axial velocity and (b) temperature of different size particles injected at five different locations as a function of axial position [105].

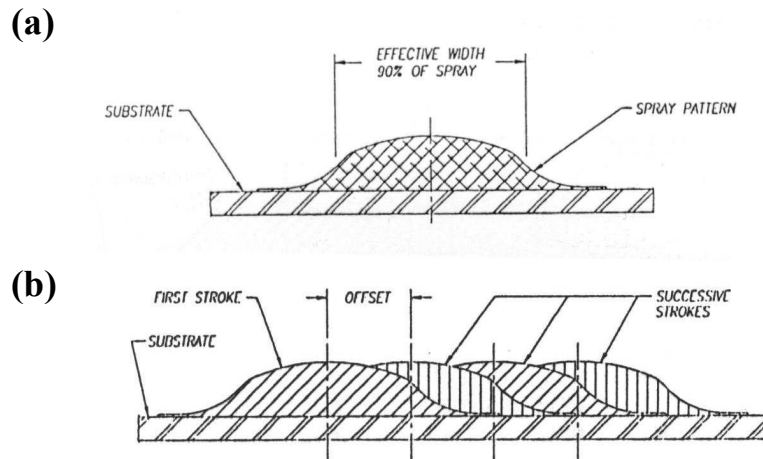


**Fig. 2.34** schematic diagram of (a) single traverse and (b) thicker layer of a spray stream across a substrate [142].

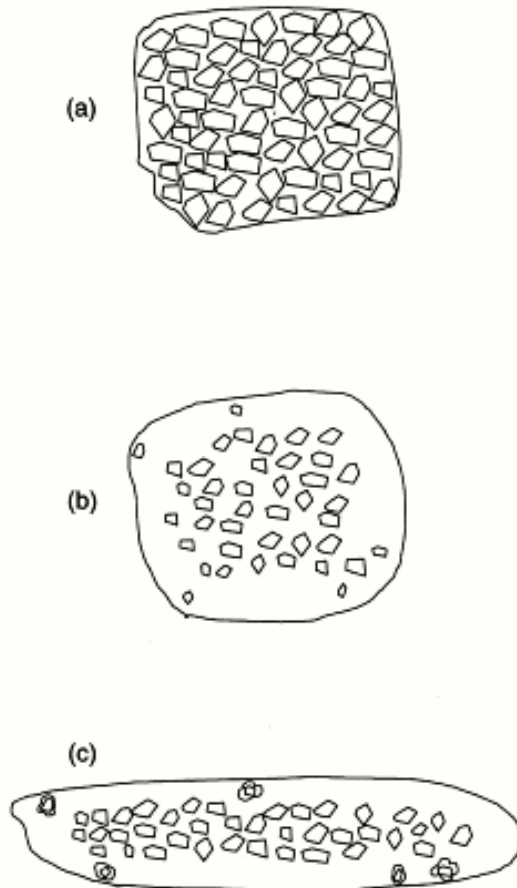


**Fig. 2.35** Schematic illustration of the processes involved in melting, WC dissolution and decarburization of a WC/Metal powder particle. The formation of a lenticular splat on impact with the substrate is illustrated in (c) [105].

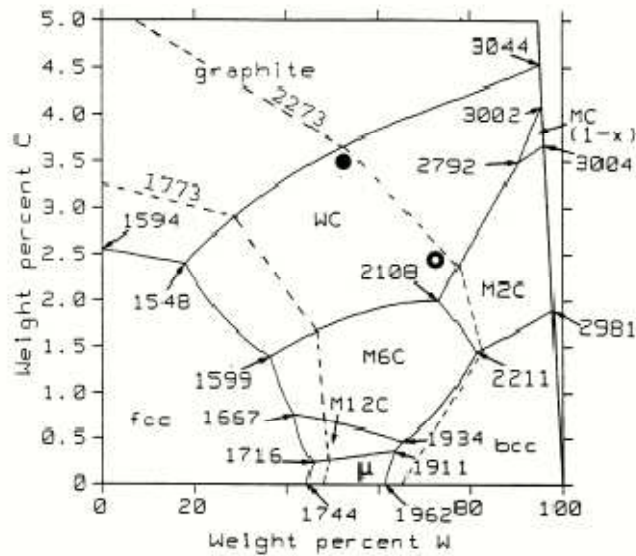


**Fig. 2.36** The liquidus surface projection of the Co-W-C system. The solid lines show calculated liquid phase compositions in simultaneous equilibrium with two solid phases, dotted lines represent approximate isotherms on the liquidus. The solid circle represents the approximate liquid composition at 2220 K in equilibrium with WC at the core of a particle; the open circle represents a possible liquid composition at the periphery of a particle (i.e. depleted in C) also in equilibrium with WC at 2200 K [105].

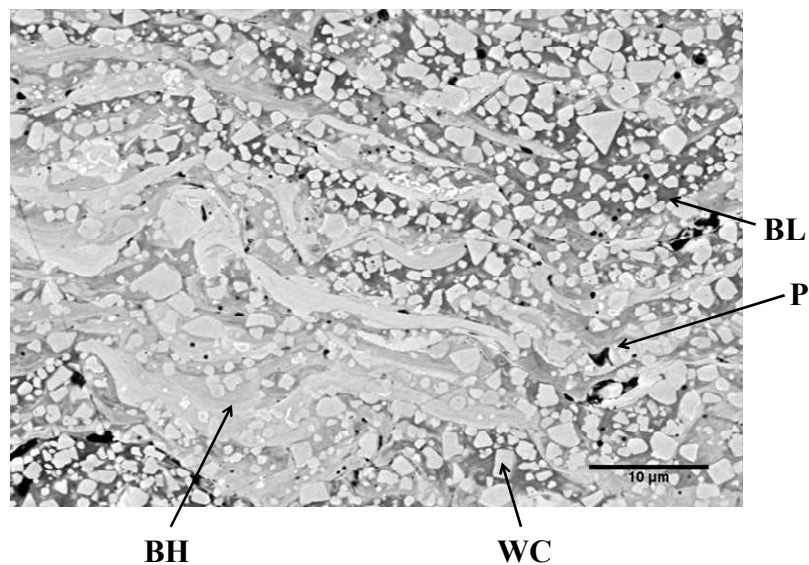


**Fig. 2.37** BSE cross-section image of a HVOF sprayed WC-17Co coating. P: porosity, WC: carbide grain, BH: binder phase with high dissolved WC and BL: binder phase with low dissolved WC.

# Chapter 3

---

## Experimental Procedures

---

### 3.1 Abrasive Wear Testing

#### 3.1.1 Introduction

In this work, the abrasive wear tests were carried out in three groups and the wear behaviour of materials under these conditions of abrasion were considered. These groups are:

- 1) The abrasion of three steels with different hardnesses with an ash from a biomass power station,
- 2) The abrasive wear of five types of steels with widely varying hardnesses with silica sand, and
- 3) The abrasion of five types of tungsten carbide coatings with different binders and carbide grain sizes deposited by using HVOF thermal spray system with silica and alumina sands.

The materials were abraded using a dry sand rubber wheel test (a variant on ASTM G65).

### 3.1.2 Test Method and Apparatus

In order to testing the materials under three-body low-stress abrasion condition, the samples were tested using a modified “dry sand rubber wheel” tester. This modified design is based on that reported by Stevenson and Hutchings [63]. The test apparatus used in this work, shown in Fig. 3.4 differed from that described in the ASTM standards as illustrated in section 2.2.6.3. In this test apparatus, the sample was held in a slot on top of the rotating wheel; in this way a controlled feed of abrasive could be passed between the wheel and the sample with the raised walls of the slot preventing any abrasive from not passing over the top surface. The rubber wheel consisted of a cast polyurethane elastomer (monothane A60; CIL, Preston, UK) around an inner steel wheel to give an overall diameter of 227 mm. The tyre had a width of 12 mm and an international rubber hardness of  $63 \pm 3$  degrees as measured with a Wallace Hardness Meter. It was rotated at 195 revolutions per minute, equivalent to a sliding speed of  $2.32 \text{ m s}^{-1}$  (in agreement with ASTM standard G65 [4]). The abrasive particles were fed via a chute onto the rubber wheel just before the contact region between the test specimen and the wheel. In this work, silica and alumina particles in medium distribution sizes as two usual abrasives which are used in the investigations on abrasive wear of materials were employed. The sand feed rates were maintained constant as follows: For bottom ash the feedrate was  $1.09 \text{ g s}^{-1}$ , for silica sand in the size ranges 180-250  $\mu\text{m}$  and 300-600  $\mu\text{m}$ , the feedrates were  $2.37 \text{ g s}^{-1}$  and  $0.85 \text{ g s}^{-1}$  respectively, and for alumina in the size range of 212-300  $\mu\text{m}$ , it was  $2.64 \text{ g s}^{-1}$ . The higher feed rates cause larger amounts of abrasive particles to move into the contact region where whole particles cannot pass through the gap, while in the

lower feed rates, wear rate is too low to measure. The abrasive is dragged through the wheel-specimen contact zone which is loaded by a dead weight on the sample.

The mass loss of the sample was measured before and after every test by a GF-200 balance (A & D Instruments Ltd., Tokyo, Japan) with a 210g capacity and 0.001 g resolution. Abrasion distances of 100, 200, 400, 600, 800 and 1000 revolutions were employed for the steel samples and 800, 1600, 2400, 3200 and 4000 revolutions for sprayed samples. The wear rate is taken as the gradient of the steady state part of the plot of mass loss versus sliding distance. Wear test were performed under five applied loads (19.6, 49, 68.6, 98, and 127.5 N). No recycling of the abrasive took place and all tests were performed dry. Before measuring the weight of samples, they were cleaned by washing in methanol and then dried.

### 3.1.3 Characterisation of Abrasive Particles

#### 3.1.3.1 Abrasive Materials

Three types of abrasives were employed in this work: (i) angular alumina (Abrasive Developments, Henley-in-Arden, UK), (ii) rounded silica (The David Ball Company, Bar Hill, UK) and (iii) the bottom ash particle from a waste-to-energy power station. The alumina and silica sands were in different size ranges; 212-300  $\mu\text{m}$  for alumina, 180-250  $\mu\text{m}$  and 300-600  $\mu\text{m}$  for silica. The bottom ash had a very wide range of particle sizes (some particles over 3 mm in size) and to allow the material to be used in the laboratory abrasion apparatus, the fraction of the ash with particle size less than 850  $\mu\text{m}$  was sieved out and used for the tests.

### **3.1.3.2 Analysis of Size**

Size analyses of particles were conducted using two different techniques: sieve and laser granulometry. The sieve analysis technique uses a test sieve shaker, Octagon 2000 (Endecotts, London, UK) and the latter uses the Malvern Instruments Master Sizer (Malvern Instrument Limited, Worcs, UK).

### **3.1.3.3 Morphology**

The morphology of the abrasive particles before and after an abrasive wear test was investigated by using a Philips XL30 (FEL Ltd, Cambridge, UK) scanning electron microscope in secondary electron (SE) mode. It was operated with an accelerating voltage of 20 kV and a working distance between 10 and 15 mm. The abrasive particles were sprinkled on to an aluminium stub and held in place through the use of an adhesive carbon tab. The ensemble was then sputter coated with gold by a Polaron sputter coater (Quorum Technologies Ltd. Company, East Sussex, UK) to make the particles conductive.

### **3.1.3.4 Hardness**

The hardnesses of the abrasive particles were measured using a LECO M-400 micro hardness tester with a 300 gf load. Abrasive particles were prepared by mounting in hot hardening resin and polishing so that a flat cross-section of the abrasive particle was exposed for indentation. Hardness measurements reported are an average of 5 indentations on different particles.

### **3.1.3.5 Fracture Strength**

The fracture strength of particles was measured by compression testing between very hard tungsten carbide ceramic platens. For each particle size range, ten individual particles were chosen and their strengths measure individually with an Instron Universal tester (Instron, Bucks, UK) fitted with a 45 N load cell. The machine was run in displacement control; when particles fractured, the load dropped. The load at first fracture and the maximum load borne by each particle were measured and the averages calculated.

## **3.1.4 Characterisation of Worn Surfaces**

### **3.1.4.1 Wear Scar Investigation**

In order to investigate the wear processes and mechanisms, the wear surfaces of samples were examined by scanning electron microscopy (Philips XL30, FEI Ltd, Cambridge, UK). The SEM was operated with an accelerating voltage of 20 kV in SE and BSE imaging modes. Also, energy dispersive X-ray EDX-SEM analysis was employed for qualitative compositional analysis where required (qualitative since analysis performed as non-plane surface).

### **3.1.4.2 Profilometry Assessment**

To measure the size, shape and depth of scars generated following wear tests, profilometry was employed. Stylus profilometry and surface roughness measurement of the samples were performed using two different machines for two and three dimensional profilometry. The former was a Surfcom Surface Texture Measuring Instrument supplied by advanced Metrology Systems Ltd ( Leicester,

UK). The latter was a Talysurf CLI 1000 Surface Profiling System (Taylor Hobson Limited, Leicester, UK) which can work with both stylus and laser surface detector.

### **3.1.4.3 Temperature of Sample during Wear Testing**

In some steel cases, the increase in temperature during wear testing was investigated. A thermocouple was attached to the sample surface close to the centre of the wear scar using a special heat resistance glue (see Fig. 3.5). The temperature was recorded as a function of the number of revolutions of the wheel (readily converted to sliding time) and the effects of load and abrasive type (silica 180-250  $\mu\text{m}$  and the bottom ash) were studied. The temperature of the rubber wheel was roughly monitored by pressing a fine thermocouple onto the wheel immediately at the end of each test.

### **3.1.4.4 Particle Fragmentation Following Wear Test**

In some cases, the size distributions of the abrasive following wear testing were measured by the sieve analysis technique. To allow separate collection of abrasive particles which had passed through the contact zone from that which had not, a pair of stationary brushes (one each side of the wheel) were placed along the vertical radius on the wheel up to the level of the test specimen; the brushes separated the two abrasive collection routes. Thus, abrasive particles that passed through the contact zone would be collected separately from those that fell away from the wheel before being passed through the contact. Following wear testing, the size distributions of the particles that had passed through the contact zone

were again measured by mechanical sieving. Each test was performed at least three times.

### 3.1.5 Abrasive Wear Testing of Steel Substrates

In this part of the work, the main purposes were to evaluate the abrasive wear behaviour of steels with a bottom ash abrasive from a biomass power station and to compare it with wear observed when abraded with silica. As part of this study, analysis of the motion of abrasive particles in the dry sand-rubber wheel abrasion test was conducted. The aim was to understand the mechanics controlling particle motion, and thus the dependence of particle motion upon external factors, focussing on the effects of testpiece hardness and applied load. For these purposes, wear behaviour of steels under conditions of abrasion were studied in two groups of materials: (i) the abrasion of three steels with an ash from a biomass power station and (ii) the abrasive wear of five types of steels with various hardnesses with silica sand.

Dry sand–rubber wheel testing was employed for abrasion test with bottom ash (0-850  $\mu\text{m}$ ) and silica sand (180-250  $\mu\text{m}$ ) as abrasive particles under five loads of 19.6 N, 49 N, 68.6 N, 98 N and 127.5 N.

#### 3.1.5.1 Test Materials

The compositions of the steels were determined by atomic emission spectroscopy (using a Foundry Master, Worldwide Analytical Systems AG, Germany). For abrasive wear testing, test pieces (59×25×12 mm) were produced and the surfaces to be exposed to wear (one of the largest faces on each sample) were ground with

successively finer silicon carbide abrasive papers and finally with a fabric pad loaded with 6  $\mu\text{m}$  diamond abrasive.

### **3.1.5.2 Hardness Testing**

The hardnesses of the steel samples were measured with a Vickers Hardness Tester with 10 kgf and 30 kgf indentation loads and a dwell time of 15 seconds. The block steel specimens were polished before testing. Hardness measurements reported are an average of five indentations, and the range quoted is the standard error in the mean.

### **3.1.6 Abrasive Wear Testing of Sprayed Coatings**

Five different types of tungsten carbide cermet powders with different binders and carbide grain sizes were sprayed on mild steel substrates (as usual and inexpensive material) using the HVOF system. To evaluate the abrasive wear performance of the coatings, the dry sand–rubber wheel test method, described in section 3.2.2, was employed. The test parameters used for both the steels and coatings were the same. Two abrasive particles including alumina and silica with the particle size range of 212-300  $\mu\text{m}$  and 180-250  $\mu\text{m}$  respectively were used. The wear experiments were performed with loads of 19.6 N, 49 N, 98 N, and 127.5 N.

## 3.2 Coating Properties and Characterizations

### 3.2.1 Materials

#### 3.2.1.1 Powders

In order to investigation on the properties of the new advanced thermally sprayed WC composite coatings, five different tungsten carbide based cermet powders were used as feedstock powders in this study. These powders had different average carbide grain sizes and binder compositions as follows: WC-15 wt% nickel alloy (NiMoCrFeCo), WC-15 wt% iron alloy (FeCrAl) and three types of WC-17 wt% Co with different carbide grain sizes. The materials have been labelled Ni, Fe, Co-I, Co-II and Co-III (indicating the Ni, Fe and Co respectively as basic elements in the binders). The mean grain sizes of WC in the Ni, Fe, Co-I, Co-II and Co-III powders were 0.7, 0.5, 1.0, 0.9, and 0.5  $\mu\text{m}$  respectively. All powders were agglomerated and sintered spheroids in the diameter range from 15 to 45  $\mu\text{m}$ . Details of the powders provided by two manufacturers (H.C.Starck, Laufenburg, Germany and Sulzer Metco, Hattersheim, Germany) are given in Table 3.1 whilst their compositions are given in Table 3.2.

#### 3.2.1.2 Substrates

The substrates used for coating deposition were mild steel (0.12% C, 0.7% Mn). The substrate sample dimensions used for wear testing were  $59 \times 25 \times 12$  mm whilst those used for characterisation of the coatings were  $59 \times 25 \times 3$  mm. Substrates were cleaned and grit blasted with  $\sim 250$   $\mu\text{m}$  brown alumina just before the coating process in order to degrease and roughen the surface.

## 3.2.2 Spray Systems and Parameters

Coatings were sprayed using a Praxair/UTP Top-Gun HVOF spray system shown schematically in Fig. 3.1. Hydrogen was employed as the fuel gas and nitrogen as the carrier gas. The powder is introduced axially in to the rear of the 22 mm combustion chamber, where gas was pre-mixed and burnt. The hot gas jet and powder were propelled along the nozzle (120 mm in length) to impact the substrate. The gun was attached to a traverse unit producing a vertical traverse at  $5 \text{ mm s}^{-1}$ . The specimens were mounted on the circumference of a horizontally rotating turntable with a radius of 140 mm giving a surface traverse velocity of  $1 \text{ m s}^{-1}$ . The specimens were cooled during spraying with compressed air jets. Fig. 3.2 shows the schematic diagram of the spraying set-up. The spray parameters for all coatings are shown in Table 3.3.

## 3.2.3 Characterisation of Powder Feedstock

### 3.2.3.1 Size Analysis

A Malvern Mastersizer S (Malvern Instruments Ltd, Worcestershire, UK) laser particle size analyser was used to measure the particle size distribution of the feedstock powders. By passing the powders in circulating water through a laser beam, the laser light is scattered, and collected by annular detectors. The scattering angle is proportional to the size of the particles, and thus the powder diameter can be calculated from the intensity of light scattered at each angle. For each powder, eight measurements were taken and the mean calculated.

### 3.2.3.2 X-ray Diffraction (XRD)

The phase composition of the powders were studied by X-ray diffraction (XRD) using a Siemens D500 diffractometer (Siemens Analytical X-ray Instruments, Sunbury-on-Thames, UK). The X-ray generator was operated at 40 kV and 25 mA generating monochromatic Cu K $\alpha$  radiation at a wavelength of  $\lambda = 0.15406$  nm. The diffraction data were collected over a  $2\theta$  range of  $30^\circ$ – $80^\circ$  with a step size of  $0.010^\circ$  and 4s dwell time per step.

### 3.2.3.3 Scanning Electron Microscopy (SEM) and EDX Analysis

Microstructural examination of powder particles was performed using a Philips XL30 (FEI Ltd., Cambridge, UK) scanning electron microscope (SEM) employing both secondary electron (SE) and back scattered electron (BSE) imaging to study the morphology and phase distribution of the powder particles. The morphology of powders was examined by sprinkling powder on to an adhesive carbon tab attached to an aluminium stub. Cross-sections of the powders were obtained by sprinkling the powders into the mould followed by hot mounting in conductive resin. The mounted powder was polished with SiC papers and diamond pads. All SEM investigations were performed at an accelerating voltage of 20 kV in both SE and BSE modes and with energy dispersive X-ray (EDX) analysis to determine phase compositions.

## 3.2.4 Characterisation of Coatings

### 3.2.4.1 XRD

X-ray diffraction (XRD) was used to characterise the as sprayed coatings. The procedure and parameters were as for XRD studies of the powders.

### 3.2.4.2 SEM

Microstructural examinations were performed on the cross-sections of the as-sprayed coatings using a Philips XL30 (FEI Ltd., Cambridge, UK) scanning electron microscope (SEM). Back scattered electron (BSE) imaging was used to study the phase content and carbide grain size and morphology in the coatings, as the differences in mean atomic number result in differences in contrast. All SEM investigations were performed at 20 kV. The specimens were prepared by sectioning normal to the coating-substrate interface with a precision ceramic blade on an automatic precision cut-off machine (Struers Accutom-5 Cutoff, Copenhagen, Denmark) operating at a slow cutting rate of  $0.005 \text{ mm s}^{-1}$  with a 3000 rpm wheel speed. After cutting, cross-sectional samples were hot mounted in conductive resin (Metprep, Coventry, UK) and were then ground with P1200 ( $\sim 14 \mu\text{m}$ ) grit size SiC paper and polished by a lapping procedure to a  $1 \mu\text{m}$  finish.

### 3.2.4.3 Microhardness

Vickers microhardness of the as-sprayed coatings was measured using a LECO M-400 microhardness tester with a 300 gf load and a dwell time of 15 s. The mean value of 10 indents taken along the mid-plane of a coating cross-section parallel to the coating/substrate interface is quoted as the hardness of the

materials. The error quoted is the standard error in the mean, i.e.  $\sigma/\sqrt{n}$  where  $\sigma$  is standard deviation of the individual hardness measurements and  $n$  is the number of measurements made.

#### **3.2.4.4 Chemical Analysis**

Chemical analysis was performed on the as-sprayed coatings by LSM Ltd. (London and Scandinavian Metallurgical Co. Limited, South Yorkshire, UK). The X-Ray Fluorescence (XRF) analysis technique was used for all elements. Oxygen and carbon contents were determined by XRF-HSS (quantitative), whilst the other elements were determined by XRF-Uniquant (semiquantitative). Coating samples were prepared by spraying onto thin mild steel substrates and then removing the coating from the substrate by bending the samples.

#### **3.2.4.5 Phase Volume Fraction and WC Grain Size Analysis**

The volume fraction of phases and the carbide grain sizes in the powders and coatings were estimated by the method of line analysis from BSE micrographs at magnifications of between 5000 and 10000 times. A series of random lines were drawn across micrographs of the cross-sections of both powders and coatings and the length of each carbide intersection measured. It was assumed that the volume fraction of carbide was equal to the intersection fraction. The carbide grain size was taken as the average of the intersection lengths.

### 3.2.4.6 Porosity

For measuring coating porosity level, image analysis (IA) was performed on SEM/BSE images at a magnification of 2500× obtained from polished cross-sections of coatings. Image analysis software (ImagJ 1.41) was employed to identify and measure porosity. Ten images were recorded to calculate the mean pore volume fraction.

### 3.2.4.7 Fracture Toughness

The fracture toughness of coatings was determined by an indentation method. Vickers indentation measurements were performed on the metallographically prepared cross-sections of the coating surfaces using a load of 5 kgf. Indents were positioned such that the two indent diagonals were parallel and perpendicular to the coating/substrate interface, respectively. The indenter was positioned carefully at approximately the mid-point of the coating. If the indents were placed too close to the outer surface of the coating, the cracks produced by indentation resulted in the coating fracturing while if the indents were too close to the coating/substrate interface, the values of Vickers hardness measured would not be representative the coating properties [171]. Due to the presence of splat boundaries in the coating parallel to the coating-substrate interface (see Fig. 3.3), the fracture toughness is lower in this direction, resulting in preferential fracture. The lengths of the cracks which were parallel to the substrate/coating interface were measured from optical micrographs at a magnification of 400× using the image analysis software (ImagJ 1.41). For each coating, at least 35 indentations were examined. The fracture toughness ( $K_{Ic}$ ) of the coatings was calculated according to the Evans and Wilshaw model [37]. These values were calculated using only the cracks parallel

to the substrate–coating interface. The equation for indentation fracture toughness as given by Evans and Wilshaw is:

$$K_C = 0.079 \left( \frac{P}{a^{3/2}} \right) \log \left( \frac{4.5a}{c} \right) \quad (3.1)$$

where  $P$  is the applied indentation load (N),  $a$  the indentation half diagonal (m), and  $c$  the crack length from the centre of the indent (m). The recommended  $c/a$  ratio for valid use of this equation is  $0.6 \leq c/a < 4.5$ . Fig. 3.3 shows a typical photograph of a 5 kgf indentation coating cross-section with the important variables.

**Table 3.1** The details of the commercially produced powders.

<b>Powder</b>	<b>Manufacturer</b>	<b>Commercial designation</b>	<b>Powder type</b>	<b>Nominal size (<math>\mu\text{m}</math>)</b>
WC-NiMoCrFeCo (85-15%wt)	H.C.Starck	Amperit 529	Agglomerated and sintered	-45 +15
WC-FeCrAl (85-15%wt)	H.C.Starck	Amperit 618	Agglomerated and sintered	-45 +15
WC-Co (83-17%wt)	H.C.Starck	Amperit 526	Agglomerated and sintered	-45 +15
WC-Co (83-17%wt)	Sulzer Metco	Woka 3202	Agglomerated and sintered	-45 +15
WC-Co (83-17%wt)	Sulzer Metco	Woka 3202 FC	Agglomerated and sintered	-45 +15

**Table 3.2** The measured compositions of the feedstock powders.

<b>Designation</b>	<b>Powder designation</b>	<b>Composition (wt%)</b>								
		<b>W</b>	<b>Ni</b>	<b>Mo</b>	<b>Cr</b>	<b>Fe</b>	<b>Co</b>	<b>Al</b>	<b>C</b>	<b>O</b>
Ni	Amperite 529	80.04	8.48	2.24	2.15	0.84	4.05	-	5.65	0.06
Fe	Amperite 618	79.16	-	-	3.41	10.81	-	1.03	5.59	0.16
Co-I	Amperite 526	78.14	-	-	-	0.05	16.83	-	5.03	-
Co-II	Woka 3202	78.01	-	-	-	0.04	16.83	-	5.16	-
Co-III	Woka 3202 FC	77.88	-	-	-	0.03	17.02	-	5.10	-

**Table 3.3** Spray parameters employed for coating depositions.

<b>Spray parameter</b>	<b>Ni</b>	<b>Fe</b>	<b>Co-I</b>	<b>Co-II</b>	<b>Co-III</b>
O <sub>2</sub> flow rate (l min <sup>-1</sup> )	240	240	240	240	240
Fuel gas (H <sub>2</sub> ) flow rate (l min <sup>-1</sup> )	640	640	640	640	640
Carrier gas (N <sub>2</sub> ) flow rate (l min <sup>-1</sup> )	17	17	17	17	17
Spray distance (mm)	250	250	250	250	250
Number of pass	51	40	40	40	40
Length of pass (mm)	76	77	77	77	77
Carousel diameter (mm)	280	280	280	280	280
Substrate velocity (m s <sup>-1</sup> )	1	1	1	1	1
Gun transverse speed (mm s <sup>-1</sup> )	5	5	5	5	5
Coating time (s)	924	729	733	674	669
Consumption of powder (g)	555	635	665	710	711
Coating thickness (μm)	260	436	350	445	460
Powder feed rate (g min <sup>-1</sup> )	36	52	54	63	63

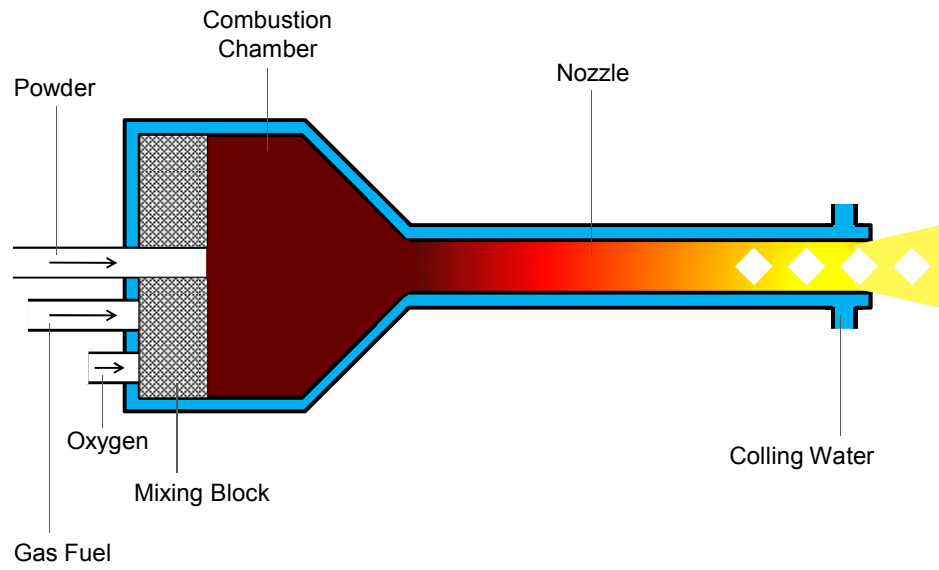


**Fig. 3.1** Schematic diagrams of the design of Top-Gun thermal spray system.

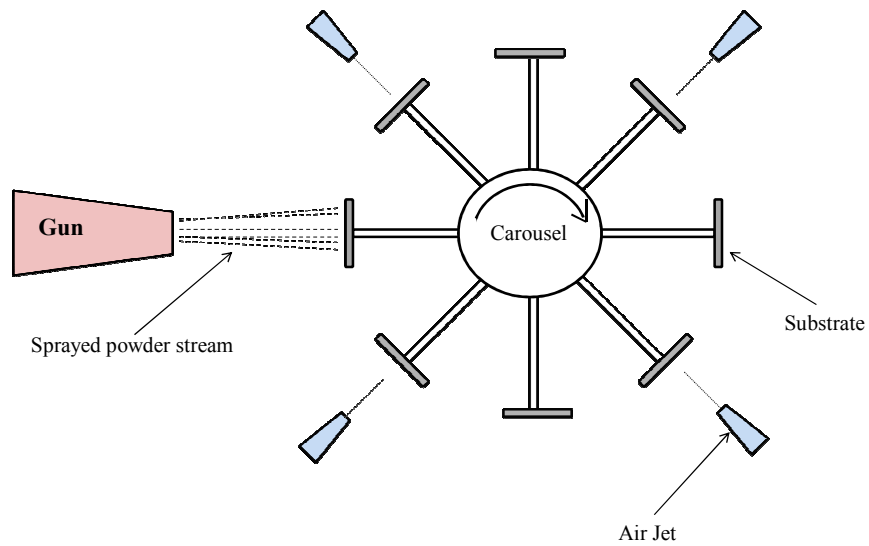


**Fig. 3.2** Schematic diagram of spray set-up in plan view.

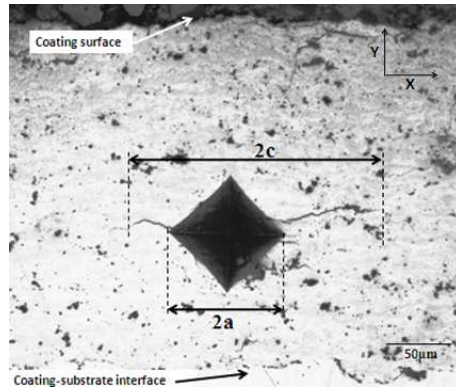


**Fig. 3.3** Optical photomicrograph of 5 kg indentation illustrating crack growth.

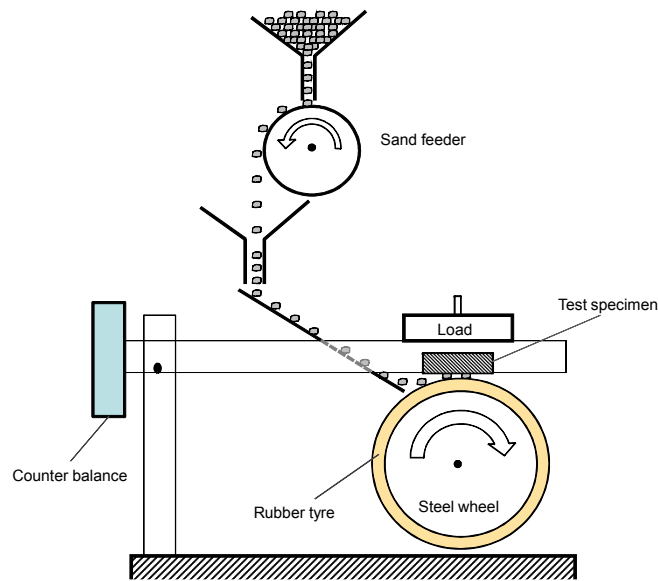


**Fig. 3.4** The dry sand rubber wheel abrasion test apparatus

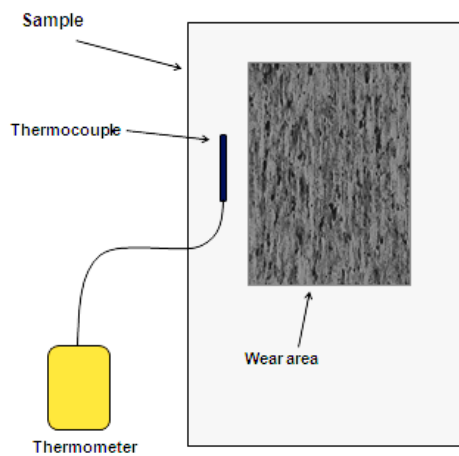


**Fig. 3.5** Schematic diagram of the inserted thermocouple on the sample surface close to the centre of the wear scar.

# Chapter 4

---

## Abrasive Wear of Steel Substrates: Results and Discussion

---

### 4.1 Introduction

In this part of the work, the wear behaviour of different types of steel under condition of abrasion was investigated. For this purpose, five steels with widely varying hardnesses and two abrasive particle types were chosen. Abrasive wear tests were carried out in two groups; *i*) the abrasion of three steels with a bottom-ash from a biomass-fired power station and, *ii*) the abrasive wear of five steels with conventional silica sand. To further assess the behaviour with silica abrasive, wear tests were also performed on two of the five steels using the same silica sand with a different size range. All materials were abraded using the dry sand rubber wheel abrasive test (a variant on ASTM G65) with five different loads. Finally, wear behaviour of the steels with the friable ash was compared with that observed when abraded with silica abrasive particles under the same test conditions.

## 4.2 Results

### 4.2.1 Characterisation of Abrasive Particles

#### 4.2.1.1 Abrasive Materials

Three types of abrasive were employed in this work, namely an ash abrasive and two conventional silica sands in two different size ranges. The ash was produced by a power station where the primary feedstock was meat waste streams. The composition of the ash was measured by an outside contractor and found to be composed of 50 wt% CaO, 39 wt% P<sub>2</sub>O<sub>5</sub>, 2.5 wt% Na<sub>2</sub>O, 1.2 wt% MgO with the balance made up of a wide range of materials in lesser fractions. The pH of the ash was measured to be ~12.1. Two silica sands (David Ball, Bar Hill, UK) which were used in the work had two nominal particle sizes ranging from 180 to 250 µm and 300 to 600 µm.

#### 4.2.1.2 Morphology and Particle Size Analysis

Fig. 4.1 shows the morphology of the abrasive particles taken using scanning electron microscopy (SEM). The bottom ash particles which were used in the work had a very wide range of particle sizes (some particles over 3 mm in size) and to allow the material to be used in the laboratory abrasion apparatus, the fraction of the ash with particle size less than 850 µm was sieved out and used for the tests (Fig. 4.1a). To compare with the ash, two types of silica sand with different particle sizes ranging from 180-250 µm (Fig. 4.1b) and 300-600 µm (Fig. 4.1c) were used. SEM micrographs of the particles show rounded silica sands in contrast to angular shapes of the ash particles. Also, it can be seen that the size distribution for the ash is much wider than that of the silica sands. Higher

magnification SEM morphology images of the silica and ash are shown in Fig. 4.2. The images demonstrate the spongy and agglomerated structure of the ash (Fig. 4.2 a) while the structure of silica shows less porosity (Fig. 4.2 b).

The particle size distribution of the abrasive particles used for testing was determined by both passing the abrasives through a stack of wire-mesh sieves on a mechanical sieve shaker and by a laser granulometry technique (Malvern Instruments). In the sieve method, the mass proportions of the particles on each sieve were measured. Fig. 4.3 shows size distribution results for each particle type obtained using two techniques. The particle diameter,  $d_p$ , below which 50% of the volume lay in the sieve method was taken as the nominal particle diameter of the particles in any further analysis. The results indicate that for silica sands, the particle sizes are in a limited range of size while for the ash that is in a wide range of size.

#### 4.2.1.3 Mechanical Properties

It was found that the measured Vickers hardness of some larger and less porous ash particles (which allowed hardness measurements to be made upon them) exhibited a wide range between  $550 \text{ kgf mm}^{-2}$  and  $720 \text{ kgf mm}^{-2}$  when measured with a 50 gf load. This hardness is much higher than the value of  $160 \text{ kgf mm}^{-2}$  quoted for calcium oxide (the main constituent of the ash) [11], and indicates that the complex phases present in the ash yield a much more abrasive material than the individual constituents would indicate. The Vickers hardness of both the silica sands was measured as  $1116 \pm 46$  and  $1151 \pm 59 \text{ kgf mm}^{-2}$  for silica 180-250  $\mu\text{m}$

and silica 300-600  $\mu\text{m}$  respectively with a 300 gf indentation load. The Vickers microhardnesses of the abrasives are displayed in Table 4.1.

The fracture strength of particles in each of the sieved size fractions was measured by uniaxial compression testing. Typical examples of compression test data for  $\text{SiO}_2$  and bottom ash particles are presented in Fig. 4.4. The results indicate that firstly, the load for the silica sands increases monotonically with displacement and at a critical load (at particle fracture) sharply decreases, whereas for the ash particles, the curve shows a large number of fracture events. Because of the importance of particle size in compression strength, the particles of each abrasive type were categorized in smaller ranges of size by sieving. The expectation was that for each abrasive, similar particles in a given size range should have similar compression strength. Table 4.2 shows those groups of size and average fracture load of the abrasive particles related to each particle size. Fig. 4.5 shows the data of Table 4.2. It can be seen that both the silica abrasives have much higher crushing load than the ash abrasive. Furthermore, for silica sands, the compression load rises significantly with increasing particle size.

#### 4.2.1.4 Particle Density

To enable estimates of the loads on particles during the abrasion test to be made requires a knowledge of the particle density. Silica sands are composed of solid particles, whereas the ash particles are in an agglomerated or spongy form. Estimating the density of ash particles was done by measuring its bulk density and comparing it to the bulk density of the two other silica sands with known real density. The true particle density of the silica sand was assumed to be  $2650 \text{ kg m}^{-3}$

and the bulk densities measured. Table 4.3 shows the bulk and true densities of two different size fractions of the silica sands together with the ratio of the densities. For these two fractions, the bulk density was shown to be 0.63 and 0.65 respectively of the true particle density. It was then assumed that this ratio of bulk to true particle density was applicable to the bottom-ash abrasive. For average ash particle size of 425  $\mu\text{m}$ , the ratio will be 0.65 and since the measured bulk density of the bottom ash was 1116  $\text{kg m}^{-3}$ , an estimate of the true density of the bottom ash particles of 1720  $\text{kg m}^{-3}$  was made.

## 4.2.2 Characterisation of Steel Substrates

### 4.2.2.1 Analysis of Elements

The wear behaviour of five types of steels was examined in this work. These were Armco Iron, a low carbon steel, a mild steel (with a ferrite-pearlite structure), Hardox 400 (with a bainitic structure) and a ground flat stock (GFS) (with a quenched martensitic structure). In this work these steels have been designated C02, C04, C12, C18 and C99 respectively (utilising the two numbers to represent the first two decimal places in the weight percentage of carbon in the alloys). The compositions of these steels determined by atomic emission spectroscopy are shown in Table 4.4. The C02, C04, C12 and C18 steels were used in the as-received state. The C99 was austenitized for 1 hour at 810°C (from a 500°C preheat) before being quenched into oil where it remained for 30 minutes followed by tempering at 150°C for 30 minutes; 0.5 mm was then ground from its surface to remove any decarburized material.

### 4.2.2.2 Hardness

The hardnesses of the steels measured using a Vickers hardness tester are presented in Table 4.5. The hardness is seen to increase with increasing the carbon content.

## 4.2.3 Characterisation of Wear Performance

### 4.2.3.1 Abrasion of Steels

The abrasive wear rates of the steel samples were measured with the dry sand rubber wheel abrasion test (DSRW) technique. For the silica 180-250  $\mu\text{m}$  abrasive, all of the five steels were tested while for bottom ash abrasive, only the C12, C18, and C99 steel samples were examined and finally, for silica sand 300-600  $\mu\text{m}$  only two types of steels (C12 and C18) were tested. Fig. 4.6 exhibits an example of the raw mass loss data for one of the abrasive wear tests performed; the wear rate has been determined from the data that is in the linear (steady state) mass-loss regime. A typical graph showing the mass loss of C18 steel as a function of abrasion distance for five applied loads is shown in Fig. 4.7. It can be seen that for all five loads, the progress of mass loss was linear with abrasion distance. Moreover, there is a monotonic increase in wear rate with applied load. Figs. 4.8a through 4.8c show the steady state wear rates as a function of load for all steels with silica 180-250  $\mu\text{m}$  (Fig. 4.8a), silica 300-600  $\mu\text{m}$  (Fig. 4.8b) and the bottom ash particles (Fig. 4.8c).

Eq. 2.2 represents the relationship between the abrasive wear rate and the other relevant parameters. According to Eq. 2.2 for a given substrate, the abrasive wear rate is directly proportional to the applied load as may be broadly seen for both

the silica abrasives in Figs. 4.8a and 4.8b over the range of loads examined for all steel types. The wear rates are also observed to increase as the steel hardness is reduced (from C99 to C02) as expected. In contrast, the wear rates observed for the steels abraded with the bottom ash abrasive (Fig. 4.8c) are clearly not proportional to the applied load; moreover, over certain load intervals for all three of the steel types examined, as the load was increased, the wear rates were observed to decrease, in some cases quite substantially. For the harder steels, the wear rates are generally lower than those observed for the silica abrasives, despite the ash being an angular abrasive and the silica being a rounded abrasive. The distribution of wear across the surface can be measured by employing profilometry. Figs. 4.9a and 4.9b show depths of wear on the surfaces of C12 samples following wear with silica 180-250  $\mu\text{m}$  and bottom ash particle abrasives respectively. The images indicate that the wear scar increases in both depth and width with silica sands with increasing applied load. However, this trend is not observed following wear with the ash particles.

After abrasive wear testing, the worn surfaces of all samples were examined by SEM. Fig. 4.10 shows the plan view SEM images of the five grades of steel before abrasion while Fig. 4.11 shows the plan view SEM images (of the same magnification) of the central zone of the wear scars on the five grades of steel following abrasion at the lowest and highest loads utilised (19.6N and 127N respectively). In all cases the sliding direction of the wheel across the sample has been in the vertical direction. Some of the worn surfaces (e.g. Fig. 4.11a) show evidence typical of particle rolling, with significant indentation of the surface and little directionality. In contrast, Fig. 4.11j shows evidence typical of particle sliding (grooving) across the surface of the sample. There is evidence for particle

rolling through the contact for the C02 steel under both 19.6 and 127 N loads and the C04, C12 and C18 steels under a 19.6 N applied load only; however, the abrasion of C99 at the both loads was via a grooving mechanism. Moreover, for C04, C12 and C18 steels, as the load was increased, a transition in behaviour took place so that under a load of 127 N, only particle grooving through the contact was observed for these steel types. It is obvious that in the steels with lower hardness, the particle rolling mechanism is dominant while in the steels with higher hardness grooving is dominant. Moreover, increasing load causes to transition in behaviour from rolling to grooving.

The plan view images of the central zone of the wear scars on the two steels C12 and C18 following abrasion with silica 300-600  $\mu\text{m}$  are shown in Fig. 4.12. There is evidence that more particles roll through the contact for both C12 and C18 steels with silica 300-600  $\mu\text{m}$  compared to where abraded with silica 180-250  $\mu\text{m}$ .

Fig. 4.13 shows the plan view images of the central zone of the wear scars on the three steels following abrasion with bottom-ash at the lowest and highest loads utilised (19.6 N and 127 N respectively). It can be seen that in all cases, the mechanism of abrasion is that of grooving of the particles through the metals with very little evidence for particle rolling.

#### **4.2.3.2 Temperature of Wear Samples during the Test**

For selected cases, the effect of increasing applied load on the temperature of a sample during the wear test was investigated. The samples were instrumented with thermocouples which were inserted into holes drilled to within 1 mm of the

contact surface in the test specimens, and the temperature measured during the wear test. Fig. 4.14 shows the effects of load on the evolution of specimen temperature at a constant sliding speed for C12 and C99 samples with silica 180-250  $\mu\text{m}$  and for C12 with the bottom-ash particles. In each case, the temperature of the specimen rose rapidly at first; the rate of increase then decreased and in some cases a steady state was reached. The rate of increase and the final temperature increased with load. The temperature of the rubber wheel was also monitored by pressing a thermocouple on the rubber surface immediately after the wear testing. The steady-state sample temperatures during abrasion of the C12 and C99 steels are shown in Table 4.6 as a function of the applied load along with the temperature of the rubber wheel immediately following testing.

For all loads, the temperature reached was higher with the lower specimen hardness (compare Fig. 4.14a with 4.14b). Moreover, the temperature of samples reached with silica abrasive (which is harder) was higher than that with bottom ash abrasive (compare Fig. 4.14a with Fig. 4.14c).

### **4.2.3.3 Particles Fragmentation during Wear Test**

The load applied to each abrasive particle during the wear test may cause the particle to fracture. This depends on the particle strength and the applied load. Fig. 4.15a shows SEM images of the bottom-ash abrasive after wear of C12 steel under the lowest applied load of 19.6 N while Fig. 4.15b shows SEM images of the silica 180-250  $\mu\text{m}$  particles following wear test with C12 steel, but under the highest applied load of 127.5 N. Comparison the SEM micrographs with Fig. 4.1a and 4.1b revealed that significant fragmentation has occurred for the bottom ash

particles whereas no change can be seen in the silica sands. Crushing of the large particles of the ash following wear testing is apparent. Fig. 4.16a shows an ash particle with a highly porous (spongy) structure which will result in a low particle crushing strength. Fig. 4.16b also shows that many of the particles are indeed agglomerates of still smaller particles.

To quantify particle crushing during wear testing, the particles that had passed through the contact zone were collected and mechanically sieved in order to find the particle size distribution. This was performed using a C99 steel sample abraded with ash under different applied loads. The results of the sieve analyses can be seen in Fig. 4.17. A significant shift in the size distribution of the ash to lower sizes is observed, which has only a small dependence upon the applied load employed during testing. The  $d_{50}$  value (the particle size for which 50 wt% is above that size) is 415  $\mu\text{m}$  for the abrasive before testing, and drops to 294  $\mu\text{m}$  and 308  $\mu\text{m}$  respectively following abrasion under applied loads of 19.6 N and 127 N. Further tests showed that as well as being insensitive to applied load in the range considered, particle fragmentation is also independent of the three steels types being abraded with the bottom ash abrasive.

Fig. 4.18 presents the same data in another format, and shows the percentages of the bottom-ash abrasive within each of the size fractions both before testing and following abrasion of C99 under the lowest applied load of 19.6 N. It can be seen that the fractions in the larger size ranges (above 425  $\mu\text{m}$ ) have all decreased significantly, but that the fractions in the smaller sizes have increased considerably.

#### 4.2.3.4 Particles in Contact Zone during Abrasion

The magnitude of load in the dry sand rubber wheel abrasive test exerts an influence on the number of particles passing through the gap between the rubber wheel and the sample and also on the wear contact length. Not all of the abrasive fed towards the contact actually passed through the contact zone, with some falling off the wheel to the sides. To allow separate collection of abrasive particles which had passed through the contact zone from that which had not, a pair of stationary brushes were placed along the vertical radius on the wheel up to the level of the test specimen (one each side of the wheel); the brushes separated the two abrasive collection routes. Thus, abrasive particles that passed through the contact zone would be collected separately from those that fell away from the wheel before being passed through the contact. As such, the actual feedrate of abrasive through the contact could be measured. The ratio of the actual to the metered feedrate of particles was termed the flow fraction,  $f$ ; this was measured as a function of applied load,  $P_{app}$ , and the results for silica 180-250  $\mu\text{m}$  abrasive shown in Table 4.7. Fig. 4.19 also shows the fraction of abrasive particles passing into the contact zone during abrasion of C18 steel with the bottom ash as a function of applied load. It can be seen that the fraction decreases significantly as the applied load for the abrasion test is increased.

The worn surfaces were examined after a small sliding distance and at full sliding distances for all loads examined. The length of the wear scar was measured, which was primarily a function of applied load (indicating that the primary influence on wear scar length was the load-dependent elastic deformation of the rubber tyre) and it is not dependent on abrasive type. For each load, an average

contact length,  $L_c$ , was determined, as shown in Table 4.7. The Young's modulus of the rubber can be estimated from the rubber hardness of 61 IRHD to be around 3.5 MPa [172] and the Poisson's ratio estimated to be 0.5 (typical for a rubber). Using simple contact mechanics for a line loaded contact, contact lengths of 13 mm (loaded under 19.6 N) and 36mm (loaded under 127 N) are estimated. These are reasonably correlated with the experimental values in Table 4.7, but show a larger range of values than those observed experimentally. The measured average wear scar lengths (contact lengths) between the rubber wheel and the test sample under different applied loads are presented in Fig. 4.20. The contact length is observed to increase significantly with increasing applied load.

#### 4.2.3.5 Particle Loading During Abrasion testing

To estimate the loads on an individual particle during the abrasion test for a material with a wide particle size distribution is complex. It requires knowledge of the number of particles of a given size in the contact zone, along with knowledge of how the total applied load is shared over the different particle size ranges. In the current analysis, only the applied force is considered (i.e. the tractional forces on the particles are neglected). The number of particles of a given size in the contact zone at any one time ( $N_s$ ) is given by:

$$N_s = \frac{W_s L}{v m_p} \quad (4.1)$$

where  $W_s$  is the mass flow rate of that particular particle size fraction passing through the contact zone,  $L$  is the wheel-specimen contact length,  $v$  is the sliding speed between the wheel and specimen and  $m_p$  is the mass of a particle in that size fraction.

The estimate of  $N_s$  is made more complex by the fact that  $L$  is a function not only of the applied load, but also of the time for which the test has been running. It was found experimentally that the average contact length,  $L$ , varied with applied load as shown in Fig. 4.20. It was also found that the fraction of the abrasive fed which actually passes through the contact zone is a function of the applied load in the test (Fig. 4.19); thus

$$W_s = f_p f_s W_T \quad (4.2)$$

where  $W_T$  is the total mass feedrate of the abrasive,  $f_p$  is the fraction of the abrasive which passes through the contact zone and  $f_s$  is the fraction of the abrasive which lies in the size range being considered, because not all particles which pass through the contact zone are under load. It is found that for the bottom ash,  $f_p$  varies as shown in Fig. 4.19. The fraction of particles in a given size range are determined by sieve analysis and are shown in Fig. 4.18. Therefore, the Eq. 4.1 can be written as

$$N_s = \frac{f_p f_s W_T L}{v m_p} \quad (4.3)$$

The mass of a particle is given by its volume and density. Assuming that the particles are spheres, the particle mass,  $m_p$ , can be estimated as

$$m_p = \frac{1}{6} \rho_p \pi d_p^3 \quad (4.4)$$

where  $d_p$  is the average particle diameter in that size fraction and  $\rho_p$  is the true density of the particle.

To estimate the fraction of the total load borne by each individual size fraction is difficult. Avery [62] suggests that due to the low elastic modulus of the rubber wheel, it can be assumed that for an abrasive feedstock with a narrow size

fraction, the load per particle can be assumed to be the same for all particles within the contact. The assumption of a tightly graded abrasive is clearly not the case in this work, certainly for the bottom ash abrasive. As such, it was assumed that the larger particles will bear the whole load and then fracture, whereupon the next fraction down will bear the load and then fracture, and so on until the load per particle in a given fraction is below the crushing load for the size. As such, the load per particle in each fraction assuming that all the larger abrasive particles have been crushed (i.e. assuming that the total load is borne by this fraction alone),  $P_p$ , is given by:

$$P_p = \frac{P}{N_s} \quad (4.5)$$

where  $P$  is total applied load. The values of  $N_s$  and  $P_p$  for each of the size fractions are shown for an applied load of 68.7 N in Table 4.8. It should be noted that although  $L$  and  $f_p$  are functions of applied load, their effects counter each other, and the overall dependence of  $P_p$  on applied load varies almost in proportion to  $P$  within each size fraction. Fig. 4.21 shows the results of Table 4.8 as a graph. It is clear that the load per particle increases significantly with particle size.

In addition to the load per particle, Stevenson and Hutchings [63] showed data for the packing fraction of the particles. The packing fraction,  $f_{pack}$ , was defined as

$$f_{pack} = \frac{W_T f}{v d_p b \rho_p} \quad (4.6)$$

where  $b$  is the breadth of the wheel. The packing fraction under the various test conditions are also shown in Table 4.7.

## 4.3 Discussion

### 4.3.1 Abrasive Wear of steels with Ash

#### 4.3.1.1 Abrasive Particle Characteristics

The hardness of the both silica particles are higher than all the steels examined. They both exhibit a rounded morphology and a narrow size range (Fig. 4.1b and 4.1c). However, as can be seen from Tables 4.1 and 4.5, the hardness of the silica abrasive is less than 1.2 times the hardness of the C99 steel, and, as such, particle blunting is likely during abrasion which will result in a lower rate of wear than might be observed with a harder abrasive particle [3]. The hardness of the ash particles (550 - 720 kgf mm<sup>-2</sup>) is soft compared to the silica sands. As such, the ash is relatively hard compared to the mild steel (C12), has a hardness range which spans that of 1.2 times the hardness of the C18 steel, and is soft compared to the C99 steel (see Table 4.5). The ash particles are also relatively angular in morphology (Fig. 4.1a) with a wide range of size (Fig. 4.3a).

Many workers have used compression testing to measure the load-bearing capability of particles. Sikong et al. [173] employed this type of test to assess the breakage behaviour of fine particles of brittle minerals and coal. They used Eq. 4.8, as given by Hiramatsu and Oka [174], to calculate the stress,  $\sigma_f$ , required to initiate fracture in a spherical particle of radius  $R$  from the crushing load,  $F_0$ :

$$\sigma_f = \frac{0.7 F_0}{\pi R^2} \quad (4.7)$$

Other workers have estimated the elastic strain energy required to cause fracture in a uniaxial crushing test; however, this method will only be valid if the fracture of the particles is governed by crack propagation rather than initiation, since in the

latter case the elastic strain energy may far outweigh the energy required to cause fracture. It is notable that for the ash particles, the strength does not significantly increase with particle size (Fig. 4.5). Moreover, the silica particles are observed to be much stronger in compression than the ash; this is not unexpected as the ash particles are commonly spongy or agglomerated (Fig. 4.16) whereas the silica particles are dense and solid (Fig. 4.2b).

#### **4.3.1.2 Wear Behaviour**

With both silica abrasive types, the wear rate (Figs. 4.8a and 4.8b) generally increases with higher applied load and decreases with harder steel. At lower applied loads and lower specimen material hardness, the dominant abrasion mode for the silica abrasives is rolling. As the sample hardness and applied load increases, the controlling mode changes to grooving (sliding) (Figs. 4.11 and 4.12). The rounded shape of the silica particles primarily is reason of the rolling motion of the particle through the contact. With increasing the hardness of the sample material towards that of the abrasive particles themselves (for the case of C99), the wear rate is seen to decrease significantly, more than would be predicted assuming an inverse dependence upon substrate hardness. This occurs as the abrasive particles are no longer able to sufficiently indent the sample material, and are instead deformed themselves under the applied load. In spite of this, very little silica abrasive crushing was observed under any of the applied loads or against any of the sample types. Moreover, surface grooving of the C99 samples is still observed (Figs. 4.12 and 4.13) indicating that some indentation does still occur.

The wear rate of the steels with the bottom ash particles did not steadily increase with applied load for any of the materials examined (Fig. 4.8c). In this case, since the hardness of the abrasive particles is higher than the two softer steels examined (C12 and C18), the grooving of these two materials (Figs. 4.13a through 4.13d) is not unexpected. However, despite the fact that the abrasive is significantly softer than the hardest of the steels (C99), grooving wear can still be observed for in this case (Figs. 4.13e and 4.13f). The ratios of the wear rate with silica 180-250 $\mu$ m abrasive to the wear rate with the ash abrasives shown in Fig. 4.22. It can be seen that in all cases but one, the wear rate with silica is higher than that with the ash abrasive. Moreover, Fig. 4.22 shows that in broad terms the ratio of the wear rate with silica to that with ash abrasive particles tends to increase as material hardness increases. Gates et al. [175] suggest that the greatest benefits of harder materials in providing abrasive wear resistance is seen as the abrasive particles themselves become softer, since the softer abrasives are less able to damage the harder sample materials (Fig. 4.23). Fig. 4.22 also shows that for any material type, the ratio of wear with the silica to that with the abrasive ash particles is a function of load. The anomalous dependence of the wear rate on applied load with ash particles is again seen in this figure.

The unusual relationship between wear rate and applied load for abrasion of the steels with the ash observed in Fig. 4.8c may depend on the following: (i) the relative softness of the ash particles, being between the hardness of the C18 and the C99 steels; (ii) the low level of compression strength of ash and (iii) the wide distribution size of ash particles in comparison with silica sands. These two latter factors cause the very high levels of fragmentation of these particles during

abrasion testing. It is well known that there is a particle size effect in abrasion, where below around 100 $\mu\text{m}$ , the wear rate decreases as the particle size is reduced [176]. However, the increase in the fraction of particles below around 100 $\mu\text{m}$  is relatively small (around 5% as seen in Fig. 4.18) and thus cannot be the cause of the behaviour observed. Shipway and Hutchings [177] have argued that particle crushing at high impact velocities in erosion results in a reduction in erosion rate with increasing particle impact velocity for erosion of a material much harder than the erodent itself. However, Fig. 4.17 shows that the particle size distribution in the abrasive following testing is insensitive to the applied load during the test, and this indicates that particle crushing at the higher loads cannot explain the low wear rates of the steels at these loads. Comparison of Fig. 4.21 with the single particle crushing test results (Fig. 4.5) has been presented as a graph in Fig. 4.24 showing ratio of the load per particle,  $P_p$  and maximum load to fracture,  $P_f$  for bottom ash abrasive particles versus particle size. This shows that the loads experienced by particles above around 425  $\mu\text{m}$  will be sufficient to cause particle crushing, but that the smaller particle sizes will be broadly unaffected. This assessment is substantiated by the results presented in Fig. 4.18.

In contrast to the silica sands, the low hardness of the ash abrasive causes low wear rates (especially for the C18 and C99 steels). Moreover, the fact that its hardness is significantly higher than the mild steel, results in the large differences in wear rates of the steels as a function of their hardness. However, the hardness of the abrasive cannot be responsible for the dependence of wear rate on load as observed in Fig. 4.8c. It seems that the large particles of ash cause much of the damage to the steel samples during the wear test. Over the range of loads

employed, the force per particle on these larger particles is limited not by the overall applied load, but by the crushing strength of the particles themselves. When these large size particles are crushed, the load will be carried by the smaller particles. This means that when the particle size is reduced, the load per particle rapidly decreases (Table 4.4) and it seems that these more lightly loaded particles do less damage than the more heavily loaded larger particles. The wide particle size distribution of the ash affects the number of particles which are in contact with sample under load at the beginning of the wear test process in the contact zone. Furthermore, the loads on the larger particles is limited by the crushing strength of the particles themselves, and not on the applied load explaining why the observed wear rates are not a strong function of applied load (see Fig. 4.8c).

## 4.3.2 Abrasive Wear of Steels with Silica

### 4.3.2.1 Wear Rate and Mechanisms

Fig. 4.8a shows the wear rates of the steels with silica 180-250  $\mu\text{m}$  as a function of applied load. It can be seen that the wear rates for the three steels with lower hardness (C02, C04 and C12) increase linearly with load at the lower loads, with the rate of increase of wear rate with load increasing at higher applied loads. Similar behaviour has been reported in the literature [178]. Also, it was observed that in general, with increasing hardness, the wear rate of the steels decreased. However, this was not always the case; for example, the C04 steel (with a hardness of  $117 \text{ kgf mm}^{-2}$ ) exhibited a higher wear rate than the C02 steel (with a hardness of  $80 \text{ kgf mm}^{-2}$ ), indicating that other factors (such as other materials properties or the mode of material removal) were affecting the wear rate.

SEM plan view micrographs of scar surfaces (Fig. 4.11) show clearly that the motion of particles through the contact zone depends upon both the material type and the applied load. For steel samples with low hardness and under low applied load, a particle rolling mechanism dominates, whereas a particle sliding (grooving) mechanism is favoured by samples of high hardness and by high applied loads. For the two hardest steels (C18 and C99), the particle sliding (grooving) mechanism is observed across the range of applied loads (see Fig. 4.12 g, h, i, and j). However, for the steels of lower hardness (C02, C04 and C12), the rolling mechanism is observed at the lower loads and grooving at the higher loads. This change in mechanism may be the cause of the non-linear dependence of wear rate with applied load for these softer steels as observed in Fig. 4.8a.

### 4.3.2.2 Particle Motion during Abrasion

Fang et al. [10] have proposed a model of particle motion in abrasion testing with loose abrasives. In that work, the forces acting on the particle were analysed. A modified version of the diagram from the work of Fang et al. [10] is shown in Fig. 4.25. It is proposed that the particle will move through the contact by sliding (grooving) if the clockwise moment is less than the anticlockwise moment, i.e.

$$F_p h < P_p e \quad (4.8)$$

where  $F_p$  is the lateral force on the particle and the dimensions  $e$  and  $h$  are as defined in Fig. 4.25. If the inequality in Eq. 4.8 is not satisfied, the particle will roll through the contact.

### Effect of Sample Hardness

It has been shown for a given applied load on a particle that a high sample hardness favours particle sliding (grooving) whilst a low sample hardness favours particle rolling. According to Eq. 4.8, grooving will occur if:

$$\frac{F_p}{P_p} < \frac{e}{h} \quad (4.9)$$

The coefficient friction in grooving,  $\mu_p$ , is defined as:

$$\mu_p = \frac{F_p}{P_p} \quad (4.10)$$

By examination of Eq. 4.9, the change in particle motion with hardness implies that the ratio of  $F_p$  to  $P_p$  changes with sample hardness, assuming that for a given particle type and particle geometry, the ratio of  $e$  to  $h$  is independent of sample hardness. This latter assumption can be shown to be reasonable since the largest metal–particle contact area in the cases considered in this work (given by the highest load per particle of 190 mN on the metal with the lowest hardness of 80 kgf mm<sup>-2</sup>) is given by the ratio of the load to the hardness which is of the order of 240 μm<sup>2</sup>. If this area is assumed to be semicircular in plan view, it gives an estimate of the contact dimension of around 12 μm. Thus any changes over dimensions of this order of magnitude will tend to be insignificant compared to the dimensions of the particle size itself, these being of the order of 250 μm.

To allow a simple model of particle motion to be developed requires that the shape of the particle in contact with the metal (and also in contact with the rubber wheel) be considered. Torrance [179] addressed the variation of attack angle with depth of penetration of an abrasive particle in machining (where sharp particles

such as alumina are employed). In this case, he employed a hyperbolic profile for the abrasive tip shape since he argued that modelling of particles as spheres provided attack angles which were too low. In contrast, other workers have modelled abrasives as sphere-ended cones or pyramids, allowing the radius of the tip to be decoupled from the abrasive particle size [180, 181]. Pintaude et al. [182] conducted two-body abrasion tests against abrasive papers. They observed that friction was higher as the metal being tested became softer, indicating that higher penetration of the abrasive particle into the surface leads to an increase in ploughing friction. However, they indicated that these observations cannot be explained if a model which employs a geometry which is independent of indentation depth is employed. Similarly, work by Goddard and Wilman [183] has shown that for indenters for which the shape is independent of depth of indentation, there can be no change in the ratio of  $F_p$  to  $P_p$  as the hardness changes. However, if the indenter has a spherical shape, the ratio of  $F_p$  to  $P_p$  does change with depth of indentation (and thus with sample hardness under a given indentation load).

In light of the above, if a grooving spherical contact is assumed, it can be argued that the load on each particle is borne by contact over half of a spherical cap (see Fig. 4.26). Assuming that the pressure exerted by the steel surface on the particle is given by its hardness, then the following may be shown [183]:

$$P_p = \frac{\pi r^2}{2} H_v \quad (4.11)$$

and

$$\mu_g = \frac{F_g}{P_p} = \left[ \left( \frac{R^2}{r^2} \right) \sin^{-1} \left( \frac{r}{R} \right) - \sqrt{\left( \frac{R^2}{r^2} \right) - 1} \right] \quad (4.12)$$

where  $\mu_g$  is known as the coefficient of friction in plastic resistance to grooving,  $F_g$  is the force required to overcome the plastic resistance to grooving and the dimensions  $r$  and  $R$  are as defined in Fig. 4.26. It must be noted that the radius of the spherical cap contact,  $R$ , in Fig. 4.26 is not the same as the particle radius. For a grooving contact, the force  $F_p$  indicated in Fig. 4.25 has two main origins; (i) that associated with overcoming the plastic resistance to grooving ( $F_g$ ) and (ii) that associated with normal adhesive friction,  $F_a$ , and as such the total lateral force,  $F_p$ , is given by

$$F_p = F_g + F_a = \mu_g P_p + \mu_a P_p \quad (4.13)$$

which thus yields

$$\mu_p = \mu_g + \mu_a \quad (4.14)$$

where  $\mu_p$  is the observed coefficient of friction in grooving and  $\mu_a$  is coefficient of friction in normal adhesion. Whilst no values for  $\mu_a$  have been measured in this work, values of  $\mu_p$  of around 0.4 have been quoted by Stevenson and Hutchings [63] for similar tests (although it is not reported as to whether these values were from rolling or grooving motion of particles, nor what the hardness of the sample steel was). Although the loads in the work of Stevenson and Hutchings were not dissimilar to those used in the current work, the packing fraction ( $f_{pack}$ ) was much higher in that work and thus the loads per particle in the work were all less than 25 mN, which is less than the lowest load per particle utilised in the current work (see Table 4.7). Knowing that the contribution of  $\mu_g$  reduces as the contact radius  $r$  becomes smaller (associated with a reduction in applied load), it is thus assumed that the value of  $\mu_p$  of around 0.4 measured by Stevenson and Hutchings can be reasonably used as the value for  $\mu_a$  in this work.

Fig. 4.27 shows the calculated values of observed coefficient of friction ( $\mu_p$ ) for the lowest and highest values of load per particle employed in the experiments over the range of hardnesses of the steels examined (see Tables 4.5 and 4.7). The data are presented for two values of  $R$  (see Fig. 4.26), namely 126  $\mu\text{m}$  and 12.6  $\mu\text{m}$ . The former value represents the case when the radius of the spherical cap in contact with the metallic surface is the same as that of the particle itself, whilst the latter case represents a case where the radius of the contacting asperity is much smaller than the particle radius. It can be seen that in both cases, for a given load per particle, the value of  $\mu_p$  decreases with increasing hardness of the metal sample. (The trends in  $\mu_p$  with applied load per particle will be considered separately in the next section.) According to Eq. 4.9, this decrease in the ratio of  $F_p$  to  $P_p$  with increasing sample hardness will tend to promote particle sliding (grooving) as the sample hardness increases, as is observed in the experiments. As such, the change in particle motion associated with sample hardness under conditions of constant applied load can simply be attributed to changes in the grooving friction coefficient associated with particle indentation depth (and thus the overall observed friction coefficient).

Consideration of Eq. 4.9 indicates, therefore, that the observed coefficient of friction must be greater than the ratio ( $e/h$ ) to promote particle rolling. An estimate for the maximum value of ( $e/h$ ) for the particles can be given by the particle aspect ratio ( $AR_p$ ). The particle aspect ratio ( $AR_p$ ) was defined as the ratio of the maximum Feret diameter to the minimum Feret diameter. Feret's diameter is used to get an average value of particle size using microscopic measurements; the distance between two tangents on opposite sides of the particle profile, that are

parallel to some fixed direction (Fig. 4.28). A back-lit optical micrograph is presented in Fig. 4.29 which allowed image analysis of the projection of the particle shape to be conducted; the average value of  $AR_p$  for the silica 180-250  $\mu\text{m}$  particles was measured to be 1.51 with the maximum and minimum values being 1.70 and 1.28  $\mu\text{m}$  respectively. Consideration of simple geometry indicates that the maximum apparent coefficient of friction ( $\mu_p$ ) will be realised when the grooving coefficient of friction ( $\mu_g$ ) is at a maximum; from Eq. 4.12, it can be seen that this is achieved when the depth of indentation of the spherical indenter is equal to its radius, whereupon the observed coefficient of friction ( $\mu_p$ ) will be  $(1 + \mu_a)$ . Earlier in this section, it was argued that a sensible value of  $\mu_a$  was 0.4 and thus it can be seen that the maximum value of  $(1 + \mu_a)$  is less than the value of the particle aspect ratio ( $AR_p$ ) of 1.51 required to cause particle rolling. Given that particle rolling has been experimentally observed indicates that there are a number of assumptions which are not valid, such as the simple view that complex particle shapes can be expressed by the value of  $AR_p$ .

### **Effect of Applied Load**

In the previous section, the effect of changes in the sample hardness were considered, with no assessment of what was occurring at the rubber wheel–particle interface (since it was assumed that since situations of constant load were being considered, changes at the particle–rubber interface would be limited to effects of changes in the lateral force). However, it was clear from Fig. 4.27 that the observed friction coefficient would increase with increasing load per particle. Fig. 4.30 shows the calculated values of observed coefficient of friction ( $\mu_p$ ) for the lowest and highest values of hardness of the steels examined over the range of

applied load per particle employed in the experiments (see Tables 4.5 and 4.7). As in Fig. 4.27, the data are presented for two values of  $R$  (see Fig. 4.26), namely 126  $\mu\text{m}$  and 12.6  $\mu\text{m}$ . The reasons for the trends observed are the same as they were for the trends in hardness, namely that for a spherical indenter, the ploughing friction coefficient increases as the depth of indentation increases. A similar increase in observed coefficient of friction ( $\mu_p$ ) with increasing applied load has been observed in the DSRW tests reported by Dube and Hutchings [178].

Since it has been argued that low observed coefficients of friction favour particle sliding (grooving), particle sliding is thus shown to be favoured by low applied loads per particle. This prediction is in contrast to the observed phenomena, where quite the opposite is observed, namely that for low applied loads, particle rolling becomes more favoured. These apparent inconsistencies can be resolved by consideration of the equation which governs the transition between sliding (grooving) and rolling behaviour (Eq. 4.9). Sliding will occur when the observed friction coefficient ( $\mu_p$ ) is less than that of the ratio ( $e/h$ ) as shown in Fig. 4.25. As the observed friction coefficient for particle sliding ( $\mu_p$ ) increases with applied load, then this implies that the ratio ( $e/h$ ) must be increasing with load more quickly so that the transition between rolling at low load and sliding at high load observed for the lower hardness steels in Fig. 4.11 can be rationalised.

It has been shown that when there is adhesion between a rubber and a rigid body with tangential motion between them, there will be a non-symmetric distribution of contact forces across the contact area [184]. Such asymmetry of contact between a stiff sphere and a rubber surface in sliding has also been shown by a

number of workers [185-190]. Fig. 4.31 (adapted from Barquins [187]) shows the type of asymmetrical contact that might be expected. With this in mind, as the load is increased, it can be seen that  $e$  increases in size and that  $h$  decreases in size, both of which result in an increase in the ratio  $(e/h)$ . This increase in  $(e/h)$  with load must be more rapid than the increase in  $\mu_p$  with load, and as such the observation of particle motion changing from rolling at low loads to sliding at high loads can be qualitatively understood. However, the change in shape of the contact with applied load (as shown schematically in Fig. 4.31) needs to be described quantitatively to allow a fuller understanding of the particle motion in such contacts to be developed.

The change in shape of the contact between the particle and the rubber wheel associated with increases in load may be more significant than might be expected by a consideration of the loads themselves due to temperature effects in the rubber. Fig. 4.15 shows the steady temperature of sample during abrasive wear test which increase with increasing load. Increasing sample temperature will be associated with increases in the temperature of the rubber (Table 4.6). The increase in temperature of the rubber will cause a decrease in the measured rubber hardness [63], and thus to a decrease in elastic moduli [172] and to higher strains associated with the lateral and normal forces on the particles as shown in Fig.4.31.

### **General Observations**

Using a range of steels with a wide range of hardness has shown that under a standard set of conditions, particle motion through the rubber wheel–testpiece contact depends upon the testpiece properties. Such a dependence must be of

concern to users of the test, since a robust test methodology will expose all materials to the same conditions which themselves are independent of the material properties. In light of this, it is recommended that observation of wear scars following exposure to the DSRW test and identification of the mode of particle motion through the contact is a routine part of this test methodology.

Having highlighted the differences in the motion of particles, it is also noted that the wear coefficients observed are not strongly dependent upon the mode of particle motion through the contact. This is in contrast to the very different wear coefficients commonly associated with three-body abrasion and two-body abrasion, with the latter producing wear coefficients an order of magnitude higher than the former. In the DSRW test, even if the particles groove through the contact, they are able to orient themselves so that their attack angles on the testpiece are not high, thus resulting in ploughing and wedging. This is in contrast to two-body abrasion with fixed abrasives (such as abrasive papers) where some of the particles will have very high attack angles on the testpiece, producing cutting wear with its associated high wear coefficients. As such, there is a need to distinguish between “fixed-particle grooving abrasion” and “free-particle grooving abrasion”.

#### **4.3.2.3 Effect of Silica Particle Size and Shape on Wear**

Fig. 4.32 shows comparison of two different sizes of silica sand in wear rate. The results indicate that the smaller abrasives cause more wear than the larger. Moreover, the SEM images of the C12 sample following wear with silica 180-250  $\mu\text{m}$  and 300-600  $\mu\text{m}$  under the highest load (shown in Fig. 4.11e and Fig. 4.12b

respectively) indicate that rolling of particles occurs for the larger abrasive, whereas sliding (grooving) effects are evident for the smaller abrasive.

However, despite the fact that the hardness of silica 300-600  $\mu\text{m}$  abrasive is slightly higher than that of silica 180-250  $\mu\text{m}$  (Table 4.1), and also that the particle size of silica 300-600  $\mu\text{m}$  is considerably larger than that of silica 180-250  $\mu\text{m}$  (Fig. 4.1b and 4.1c), the wear rates with the former are lower and a rolling wear mechanism can be observed for this abrasive more than that for the silica 180-250  $\mu\text{m}$  in the corresponding samples (see Fig. 4.11 and 4.12).

There is a size effect in abrasion which leads to decreasing wear rate with decreasing particle size [176], although for particles larger than about 100  $\mu\text{m}$  wear rates are often found to be independent of size [191]. The distribution size of the abrasive particle in this work (180-250  $\mu\text{m}$  and 300-600  $\mu\text{m}$ ) is above of the critical size ( $\sim 100$   $\mu\text{m}$ ) and therefore, the size of abrasive particles is not expected to affect the wear rate.

The shape of abrasive particles has an important role in determining the wear mechanism and wear rate. SEM images of the particles indicate different morphologies of the abrasives. Figs. 4.33a and 4.33b show a typical particle micrograph of silica 180-250  $\mu\text{m}$  and silica 300-600  $\mu\text{m}$  respectively. It is clear that silica 180-250  $\mu\text{m}$  are angular in contrast with silica 300-600  $\mu\text{m}$  particles. The shape of the particle protrusions contributes to the severity of wear. ‘Sharp’ protrusions promote rapid material removal. Both theoretical predictions and experimental results confirm that the abrasive particle shape has an effect on the

rate of wear [38]. It has been confirmed in laboratory tests by many researchers that increase in particle angularity results in a significant increase in abrasive or erosive wear rates, although it is difficult to define a quantity which describes particle shape well in this context. It is generally true that the more sharp and angular the particles are, the greater the wear rate will be.

Moore and Swanson [38] indicated that abrasive particle angularity can produce significant differences between the relative wear resistance determined under fixed and loose abrasive conditions. The differences are only minor when rounded abrasive are used. Fig. 2.5 shows a comparison of the wear rate obtained in abrasive wear test for steel against two types of abrasive sands; rounded and crushed silica sands. Both sands have the same particle size distribution and differ in their shape.

Swanson and Klann [41] studied abrasive wear behaviour of five different type of steels using the dry sand rubber wheel abrasion test. They used AFS 50/70 test silica sand and a crushed quartz sand with a more angular shape but approximately the same particle size distribution. They found that particle shape had a significant effect on the abrasive wear rate. The more angular abrasive not only produced more wear but also affected the relative wear resistances of the steels.

Kašparová et al. [88] studied the effect of particle angularity on carbon steel in the term of abrasive efficiency. They evaluated the wear resistance of the steel using dry sand rubber wheel test with silica and alumina sands. The abrasive particles

used in the first test were employed for next test and so on. They showed that the wear rate decreased significantly after first test. Comparing the SEM images of the used sands in the different tests indicated that the particles lost their high abrasive ability and their abrasive efficiency decreased rapidly; however, further use has no considerable effect on their abrasive efficiency. This result shows the effect of angularity of abrasive particles on abrasive wear rate for the same particles.

In summary, abrasion of steels in the DSRW test has shown that not only the ratio of abrasive to sample hardness is a significant factor in controlling the wear rates, the fracture of the abrasive particles can also influence wear rates. Abrasion of the steels with an ash from a biomass-fired power station showed that significant fragmentation of the ash abrasive was observed during the wear test which seems to be almost independent of the applied load in the wear test. In another work, the abrasion of a range of steels with conventional silica sand showed that the movement patterns of abrasive particles through the gap in the DSRW test is a function of both applied load and hardness of the material under test. A model of the particle motion in the contact was proposed which well predicted the effect of hardness on particle motion.

**Table 4.1** Vickers hardness of the abrasive materials.

<b>Abrasive</b>	<b>Range of size (<math>\mu\text{m}</math>)</b>	<b>Hardness (<math>\text{kgf mm}^{-2}</math>)</b>	<b>Indentation load (<math>\text{kgf}</math>)</b>
Silica	180-250	$1116 \pm 46$	300
Silica	300-600	$1151 \pm 59$	300
Bottom-Ash	0-850	550 - 720	50

**Table 4.2** Average fracture load of the bottom ash (0-850 $\mu\text{m}$ ), Silica sand (180-250  $\mu\text{m}$ ) and, silica sand (300-600  $\mu\text{m}$ ) for different ranges of particle size.

<b>Range of size (<math>\mu\text{m}</math>)</b>	<b>Bottom Ash (0-850<math>\mu\text{m}</math>)</b>		<b>Silica (180-250 <math>\mu\text{m}</math>)</b>	<b>Silica (300-600 <math>\mu\text{m}</math>)</b>
	<b>First peak (N)</b>	<b>Max. Load (N)</b>	<b>Max. Load (N)</b>	<b>Max. Load (N)</b>
180-212	0.45	0.84	6.47	-
212-250	0.97	2.66	7.18	-
250-300	0.79	1.72	-	-
300-355	1.45	1.89	-	7.72
355-425	0.91	1.51	-	14.05
425-500	1.51	2.64	-	20.12
500-600	2.49	4.64	-	24.78
600-850	1.26	1.70	-	-

**Table 4.3** Mean diameter, bulk and real densities of silica (180-250  $\mu\text{m}$ ) and silica (300-600  $\mu\text{m}$ ) sands.

Abrasive particle	Mean diameter ( $\mu\text{m}$ )	Real density, $\rho_r$ ( $\text{g cm}^{-3}$ ) [88]	Bulk density, $\rho_b$ ( $\text{g cm}^{-3}$ )	$\rho_b/\rho_r$
Silica sand (180-250 $\mu\text{m}$ )	215	2.65	1.68	0.63
Silica sand (300-600 $\mu\text{m}$ )	450	2.65	1.72	0.65

**Table 4.4** Chemical analysis of the five steels examined (results given in wt %).

Steel	Fe	C	Si	Mn	Cr	Mo	Ni	Cu
C02	Bal.	0.020	<0.005	0.046	0.012	0.006	0.020	0.012
C04	Bal.	0.047	<0.005	0.17	0.020	0.007	0.020	0.007
C12	Bal.	0.12	0.22	0.77	0.067	0.021	0.113	0.373
C18	Bal.	0.18	0.32	1.20	0.227	<0.005	0.009	0.006
C99	Bal.	0.99	0.27	1.09	0.485	0.160	0.524	0.162

**Table 4.5** Vickers hardness of the steels employed in the wear tests.

Sample	Hardness ( $\text{kgf mm}^{-2}$ )	Indentation load (kgf)
C02	80	10
C04	117	10
C12	242	30
C18	473	30
C99	830	30

**Table 4.6** Temperature of rubber wheel immediately after the abrasive wear tests of C12 and C99 steels with silica 180-250  $\mu\text{m}$  abrasive.

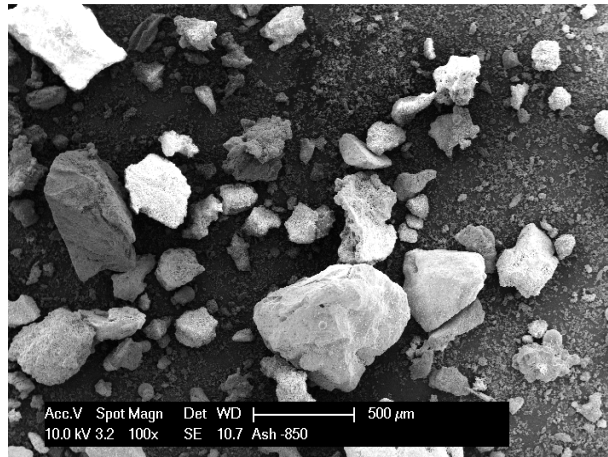
Sample	C12	C12	C12	C12	C99	C99	C99
Load (N)	19.6	68.6	98	127.5	19.6	68.6	127.5
Rubber wheel Temp. ( $^{\circ}\text{C}$ )	31.9	42.3	69.0	72.0	26.2	35.8	41.3
Specimen Temp. ( $^{\circ}\text{C}$ )	42	98	136	167	36	87	108

**Table 4.7** Particle parameters associated with wear of C12 steel with silica 180-250  $\mu\text{m}$  abrasive as a function of applied load; applied load,  $P_{app}$ ; measured wheel-specimen contact length,  $L_c$ ; flow fraction,  $f$ ; number of particles in contact zone,  $N$ ; average load per particle in the contact zone,  $P_p$ ; particle packing fraction in contact zone,  $f_{pack}$ .

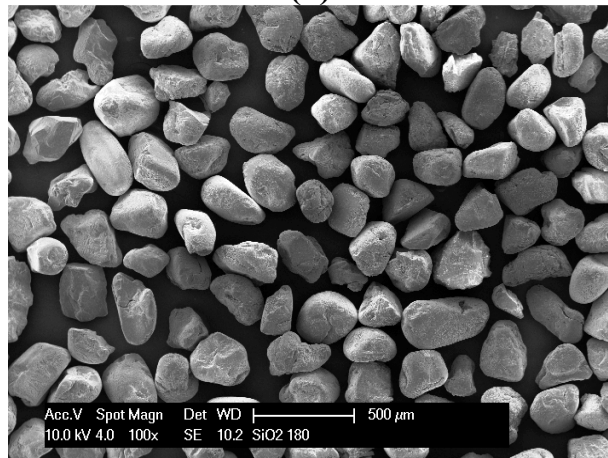
$P_{app}$ (N)	$L_c$ (mm)	$f$	$N$	$P_p$ (mN)	$f_{pack}$
19.6	20	0.8	745	26.3	0.097
49.1	25	0.71	826	59.4	0.086
68.7	27	0.71	893	76.9	0.086
98.1	30	0.67	936	104.8	0.081
127.5	32	0.45	670	190.2	0.054

**Table 4.8** Estimates of the load carried per particle within each size range for abrasion with bottom ash under an applied load of 68.7 N.

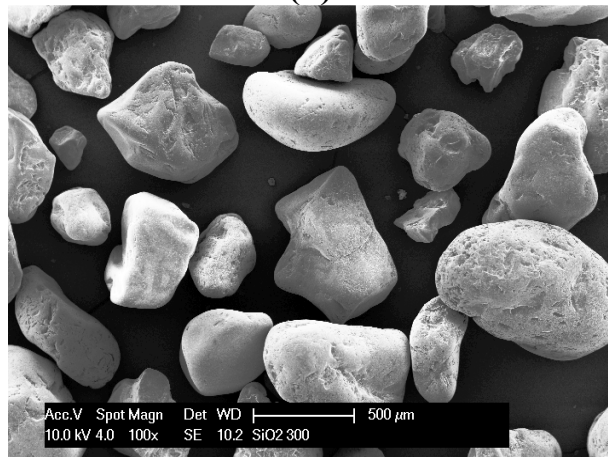
Size fraction ( $\mu\text{m}$ )	850-710	710-600	600-500	500-425	425-300	300-212	212-106	106-53	53-0
$d$ ( $\mu\text{m}$ )	780	655	550	462.5	362.5	256	159	79.5	26.5
$N_s$	3.01	3.66	6.95	8.61	37.4	71.7	251	1060	12900
$P_p$ (N)	22.8	18.7	9.9	8.0	1.8	0.96	0.27	0.065	0.0053



(a)

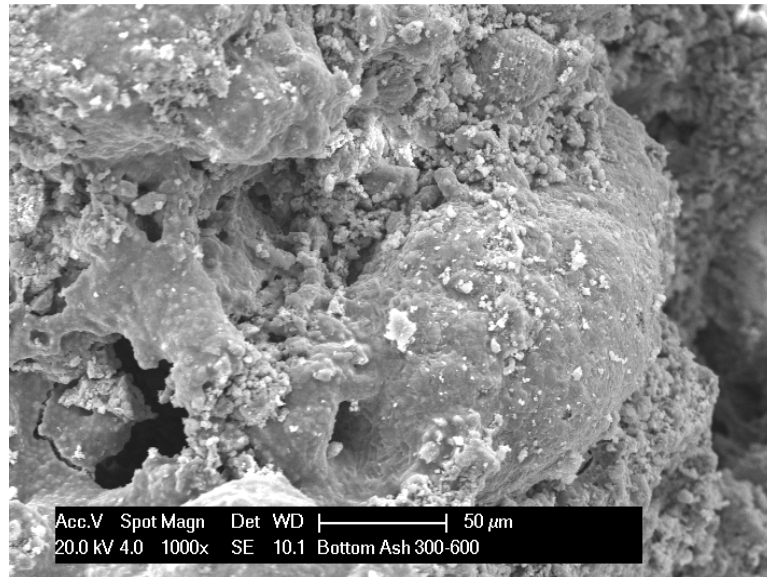


(b)

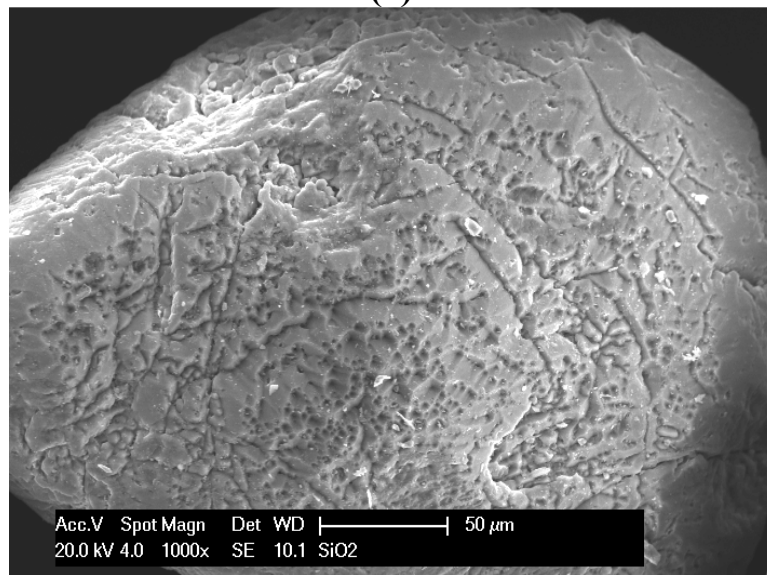


(c)

**Fig. 4.1** SEM morphology images of the abrasants employed for abrasion testing on steels; (a) bottom ash 0-850 $\mu\text{m}$ ; (b) silica sand 180-250  $\mu\text{m}$ ; (c) silica sand 300-600  $\mu\text{m}$ .



(a)



(b)

**Fig. 4.2** SEM images of a particle: (a) ash (spongy and agglomerate) and (b) silica.

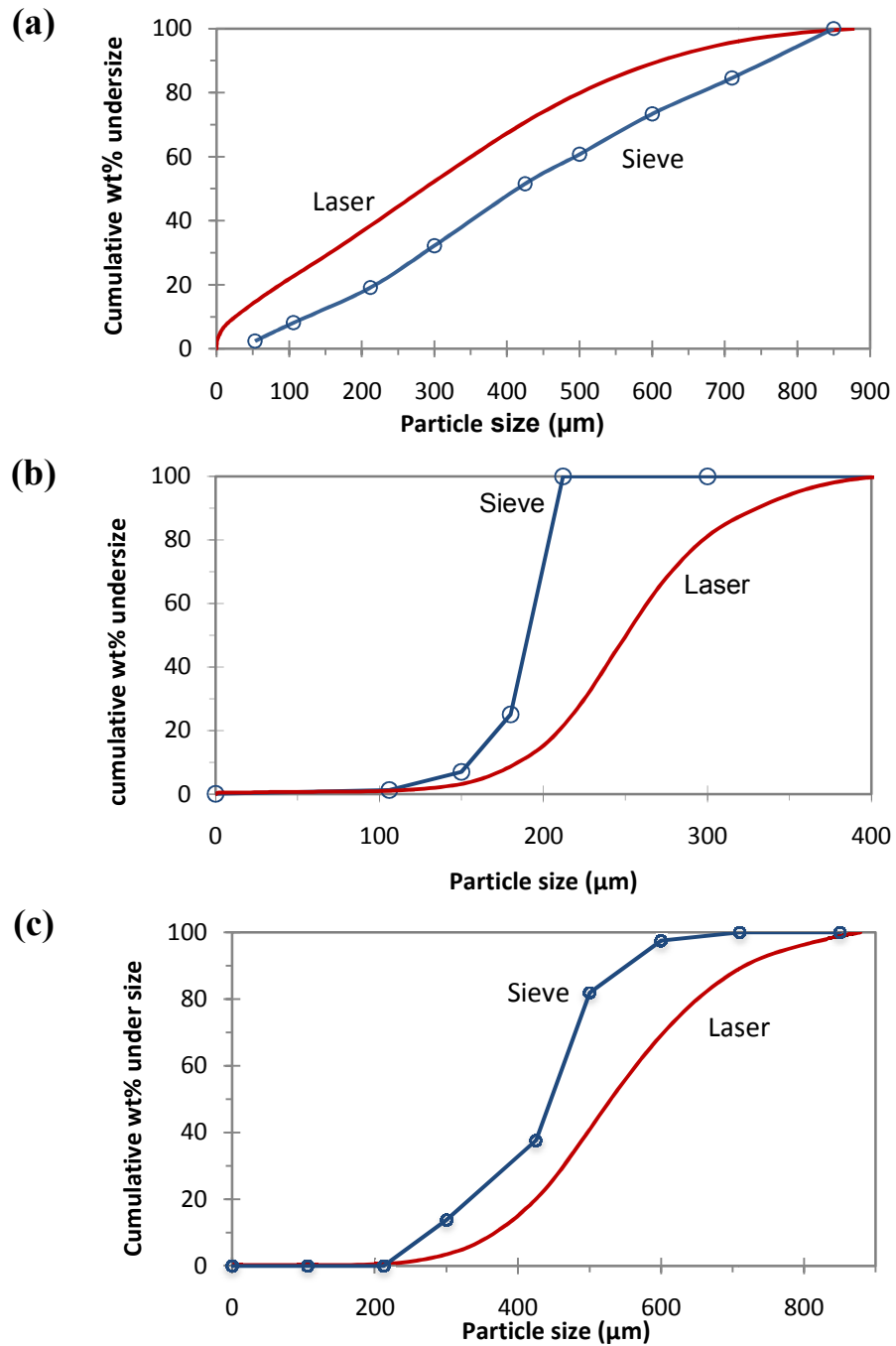


**Fig. 4.3** Size distribution results for (a) bottom ash; (b) Silica sand 180-250 μm; and (c) Silica sand 300-600 μm particles.

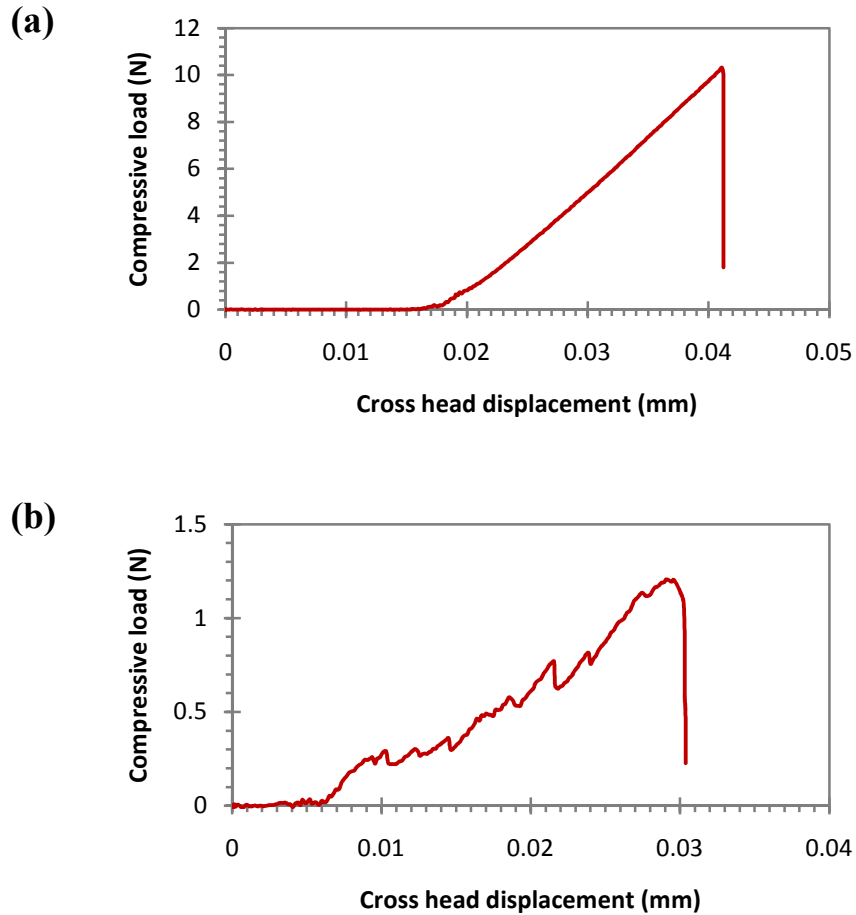


**Fig. 4.4** Typical graph obtained by compression strength test on (a) silica sand and; (b) bottom ash particles.

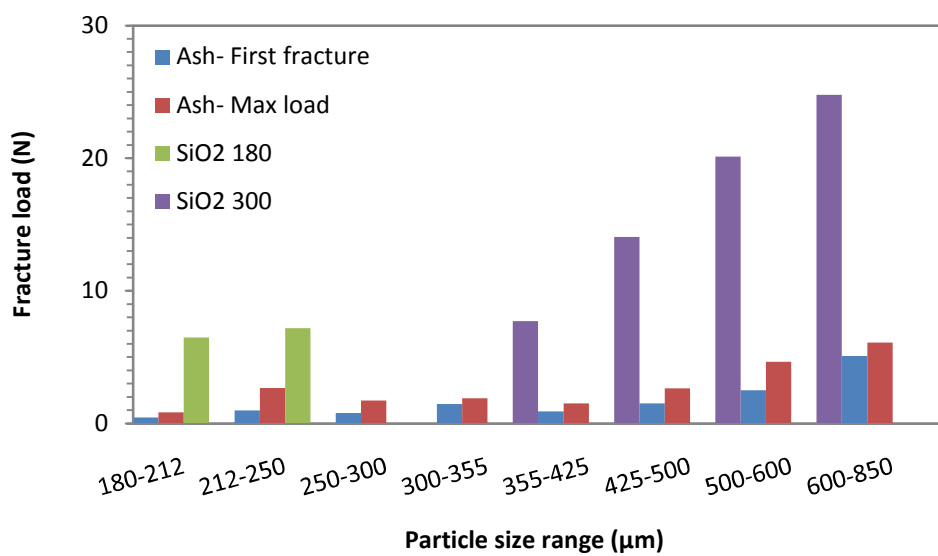


**Fig. 4.5** Average fracture loads of the abrasive particles employed as a function of particle size. For bottom ash, both first fracture and maximum load are shown; for silica sands, the first fractures were always at the maximum load.

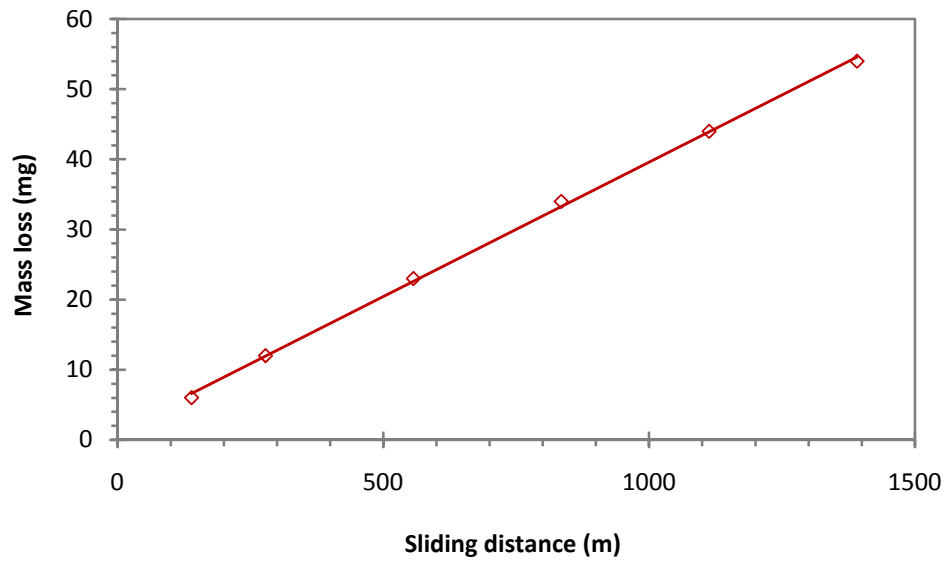


**Fig. 4.6** Plot of mass loss of steel against sliding distance for the C99 steel with ash under 127.5 N load.

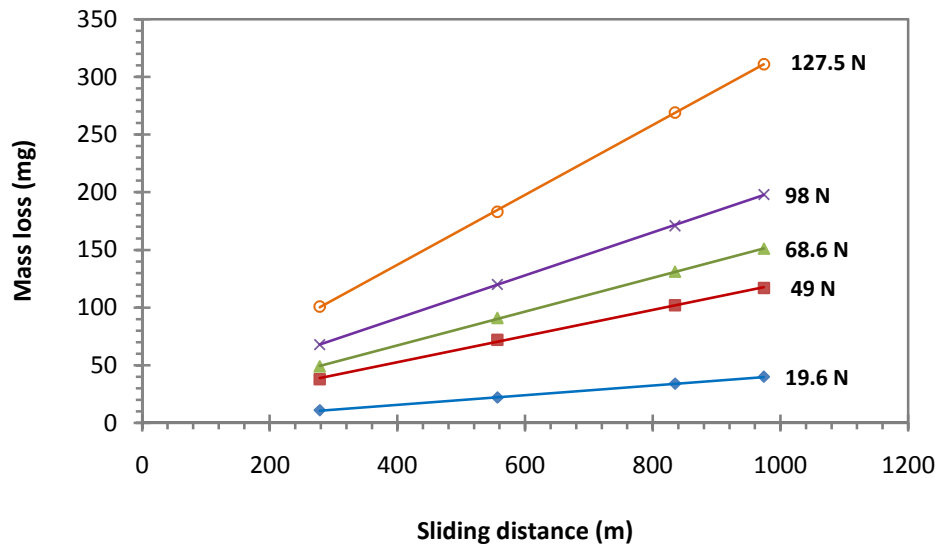


**Fig. 4.7** Mass loss of C18 steel as a function of distance for abrasion with bottom-ash as a function of applied load.

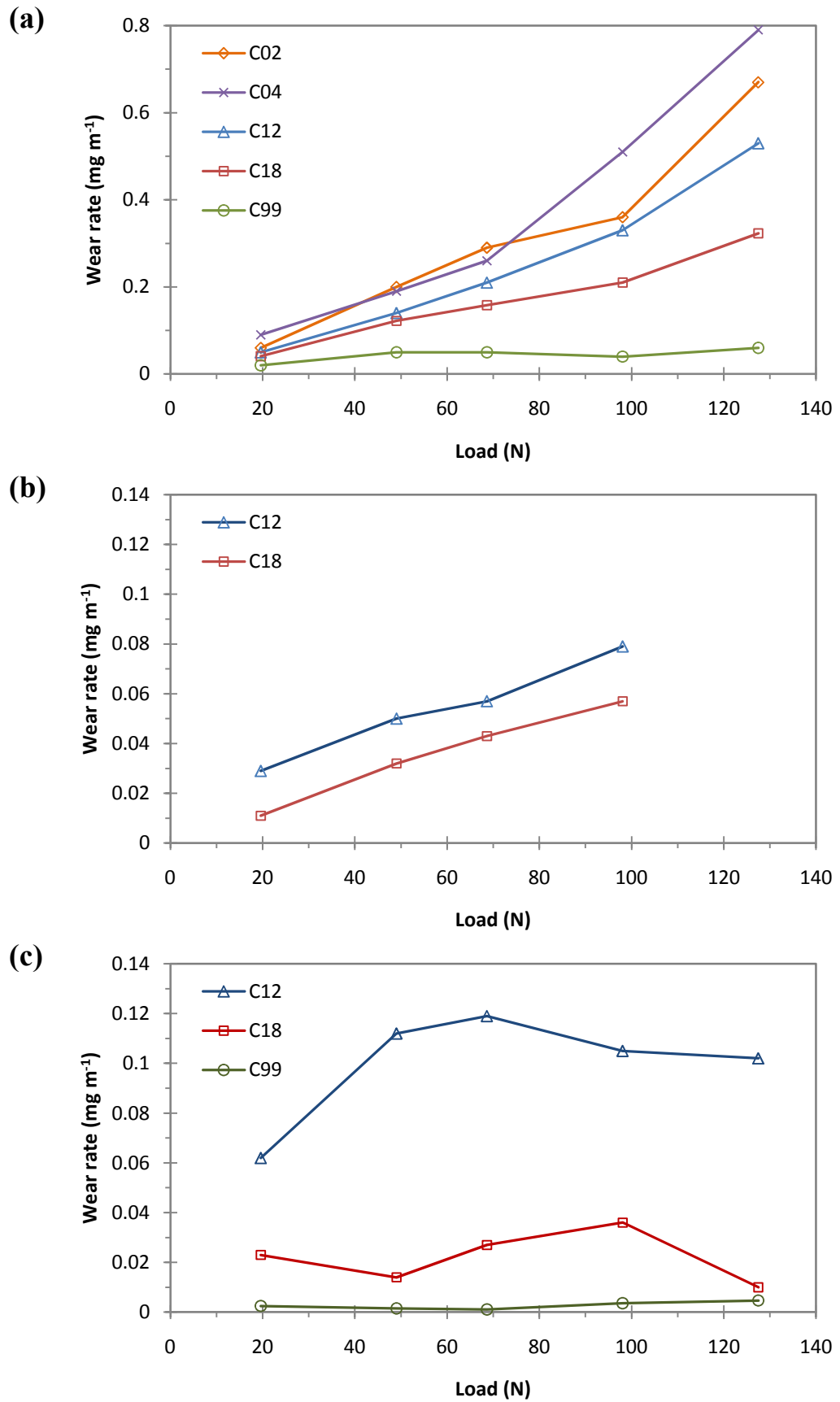


**Fig. 4.8** Steady state wear rates as a function of applied load with: (a) silica 180-250µm; (b) silica 300-600µm; and (c) the bottom ash particles.

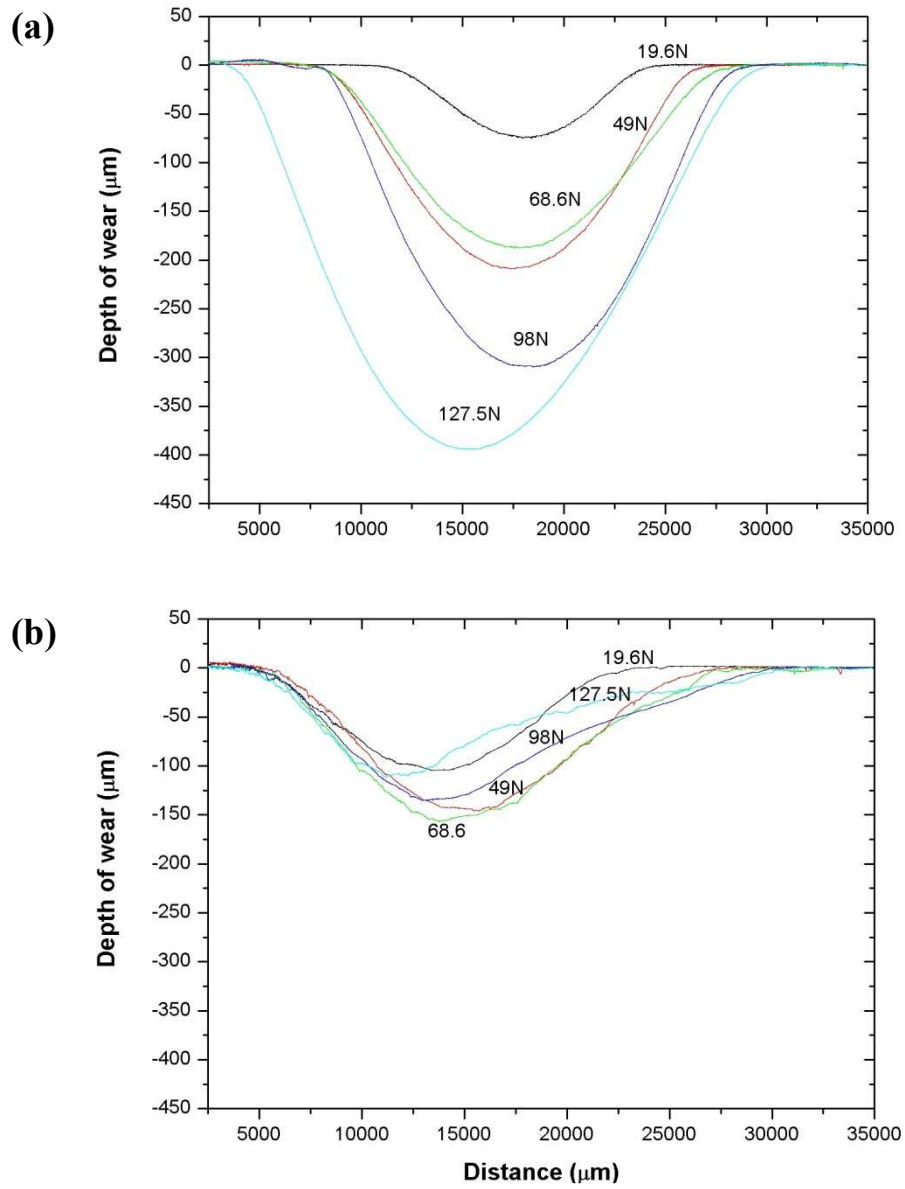


**Fig. 4.9** Depth of wear on the worn surfaces of C12 sample with (a) silica 180-250  $\mu\text{m}$  and (b) the bottom ash particle abrasives.

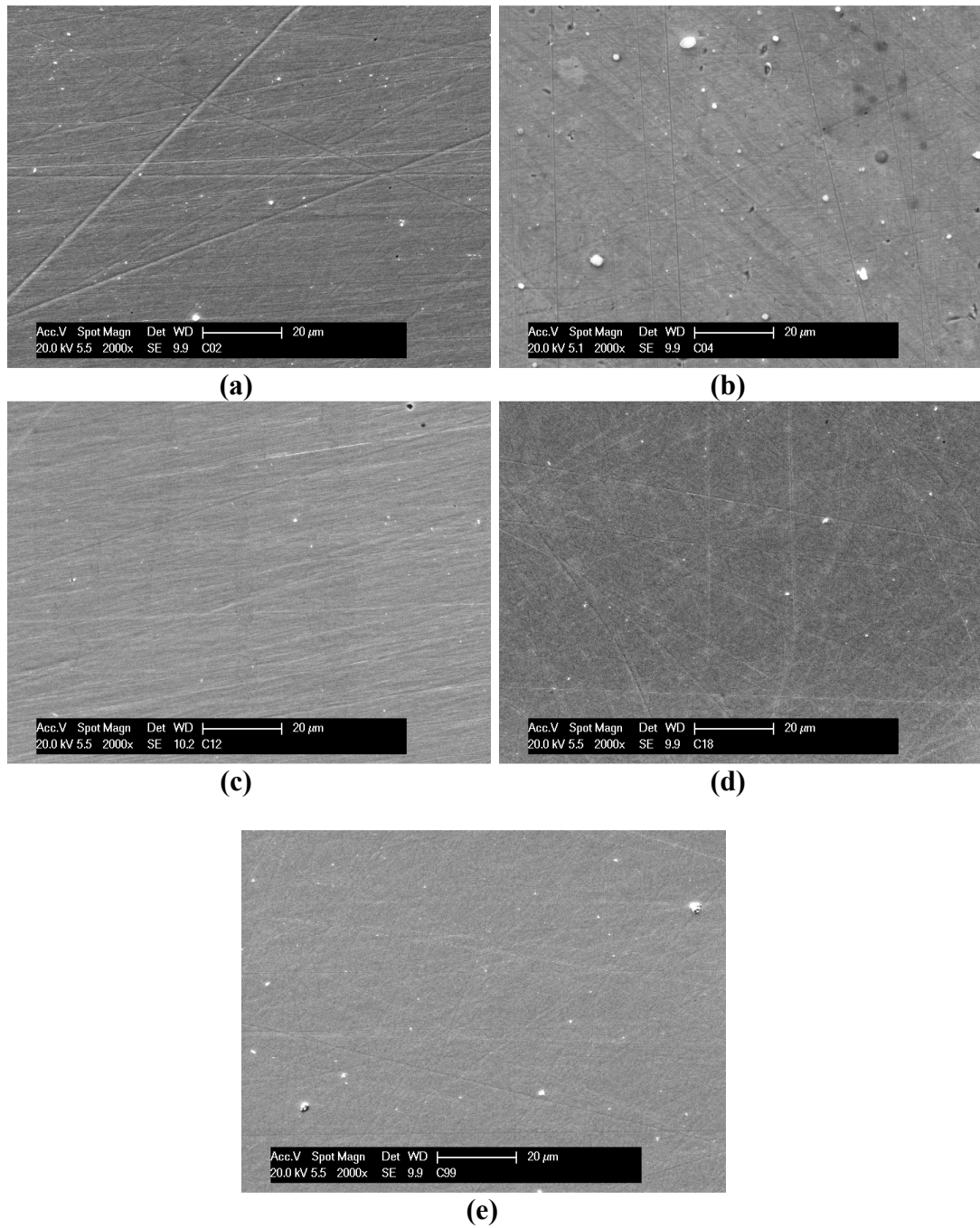


**Fig. 4.10** SEM plan view image of the five grades steel before abrasion; (a) C02, (b) C04, (c) C12, (d) C18, (e) C99.

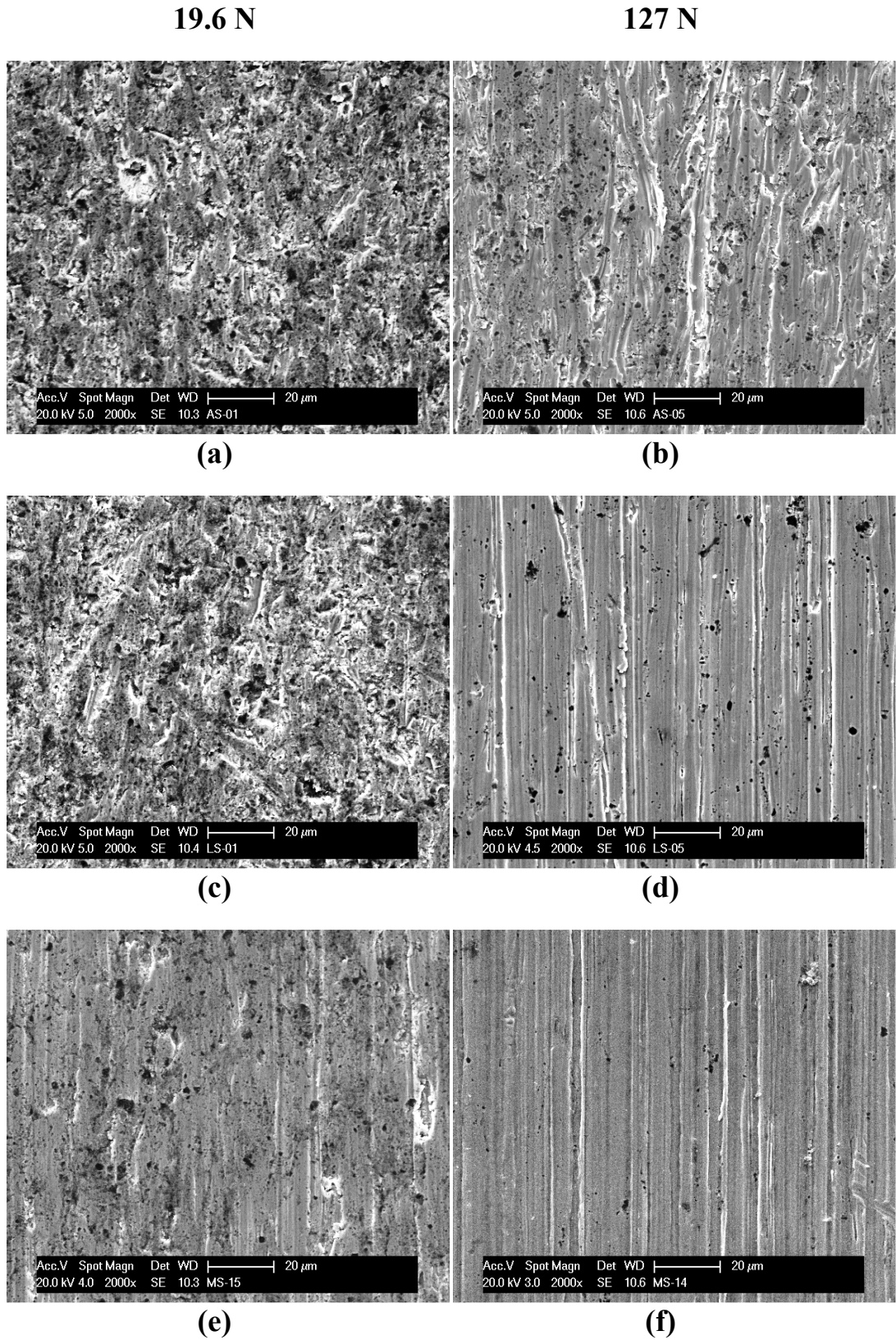
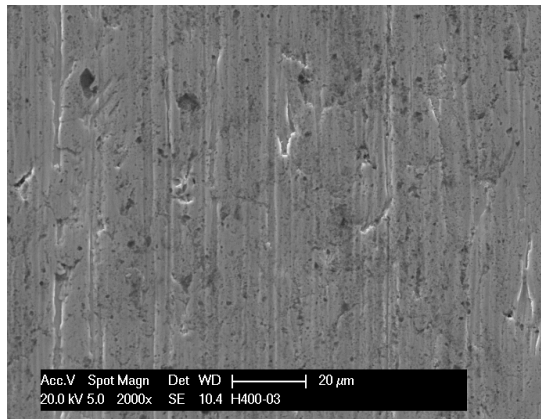


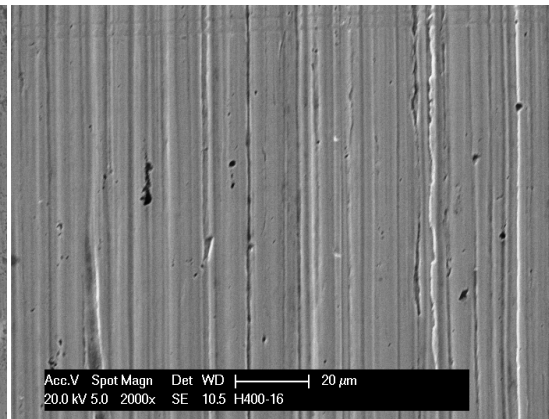
**Fig. 4.11** SEM micrographs of the central regions of the wear scars on the five grades of steel with Silica 180-250 μm for both the minimum and the maximum applied loads: (a) and (b) C02; (c) and (d) C04; (e) and (f) C12.

19.6 N

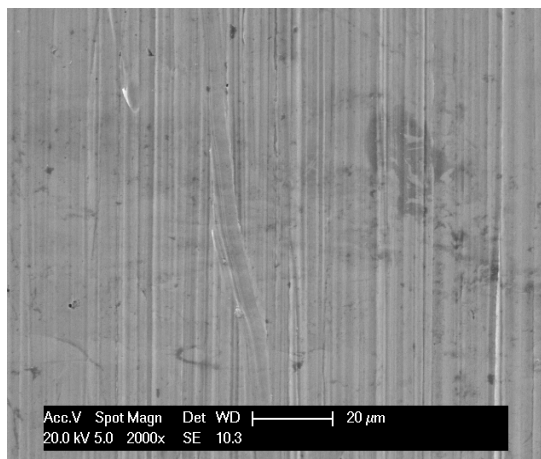
127 N



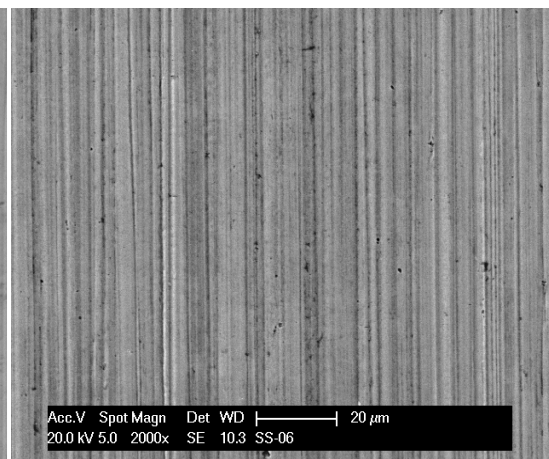
(g)



(h)



(i)



(j)

**Fig. 4.11** (continued) SEM micrographs of the central regions of the wear scars on the five grades of steel with Silica 180-250  $\mu\text{m}$  for both the minimum and the maximum applied loads: (g) and (h) C18; (i) and (j) C99.

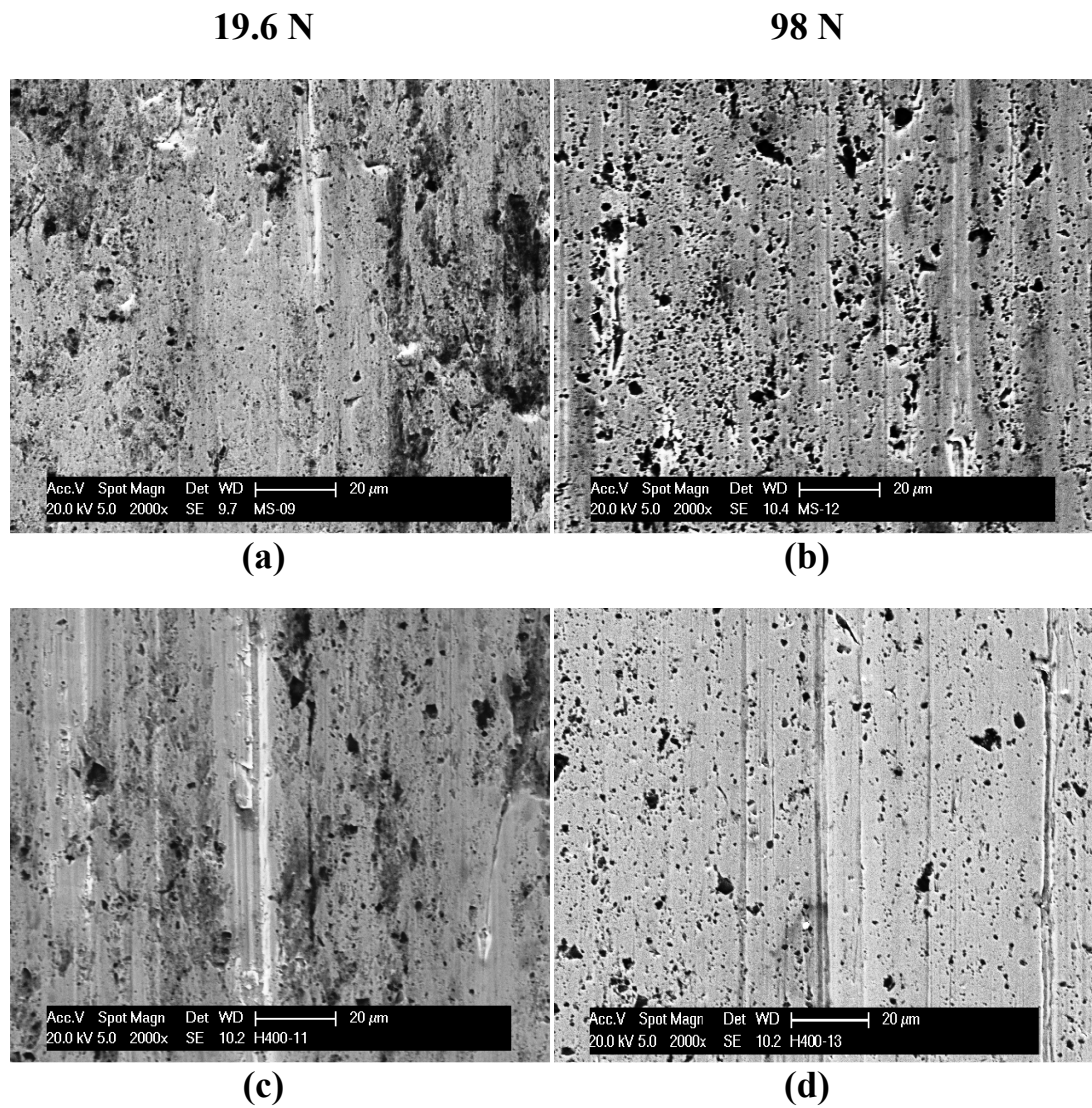


**Fig. 4.12** SEM images of the worn surfaces of the two steels following wear test with silica 300-600 μm under two lowest and highest applied loads as indicated: (a) and (b) C12; and (c) and (d) C18.

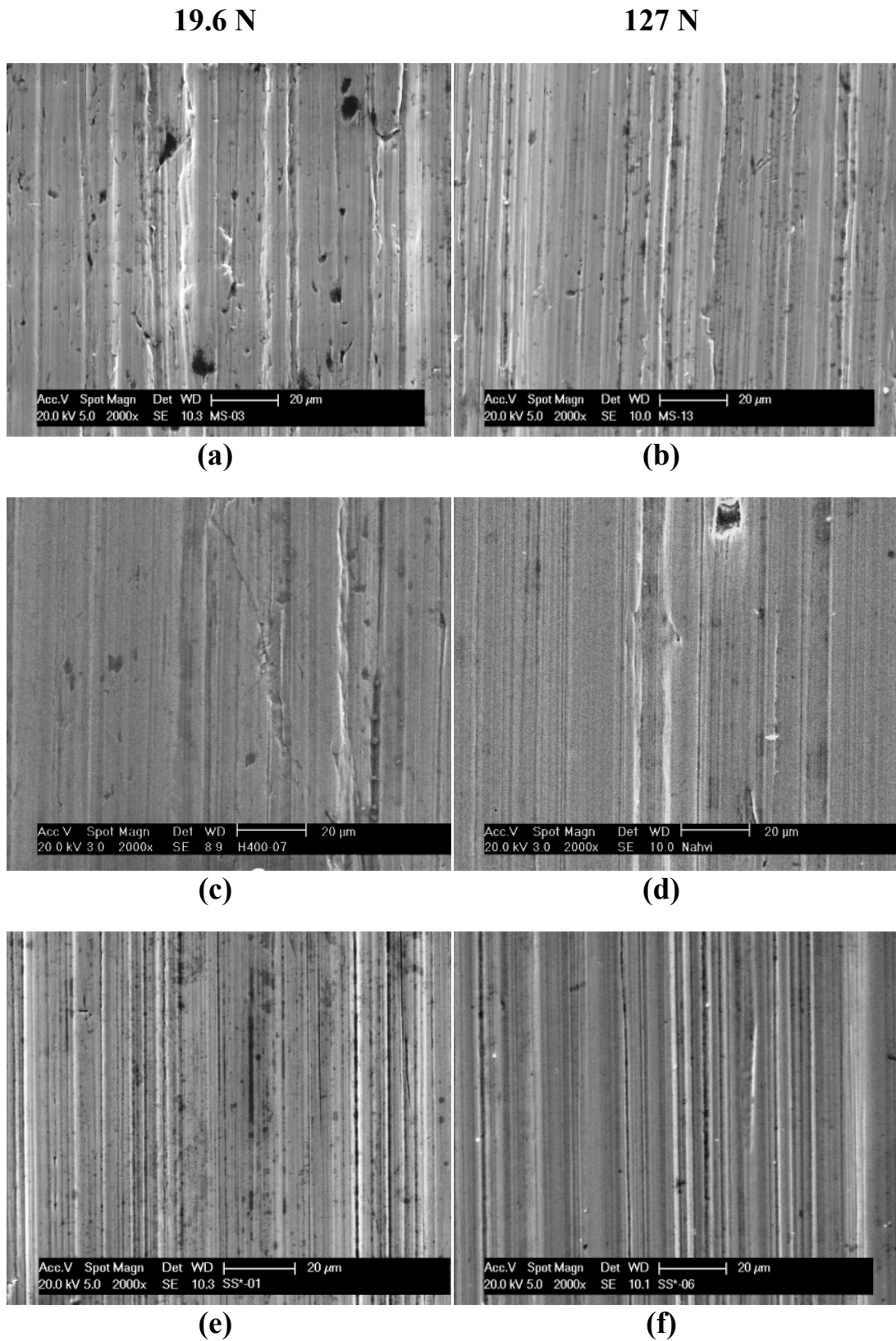


**Fig. 4.13** SEM images of the worn surfaces of the three steels following abrasion with bottom ash under the lowest and highest applied loads as indicated: (a) and (b) C12; (c) and (d) C18; and (e) and (f) C99.

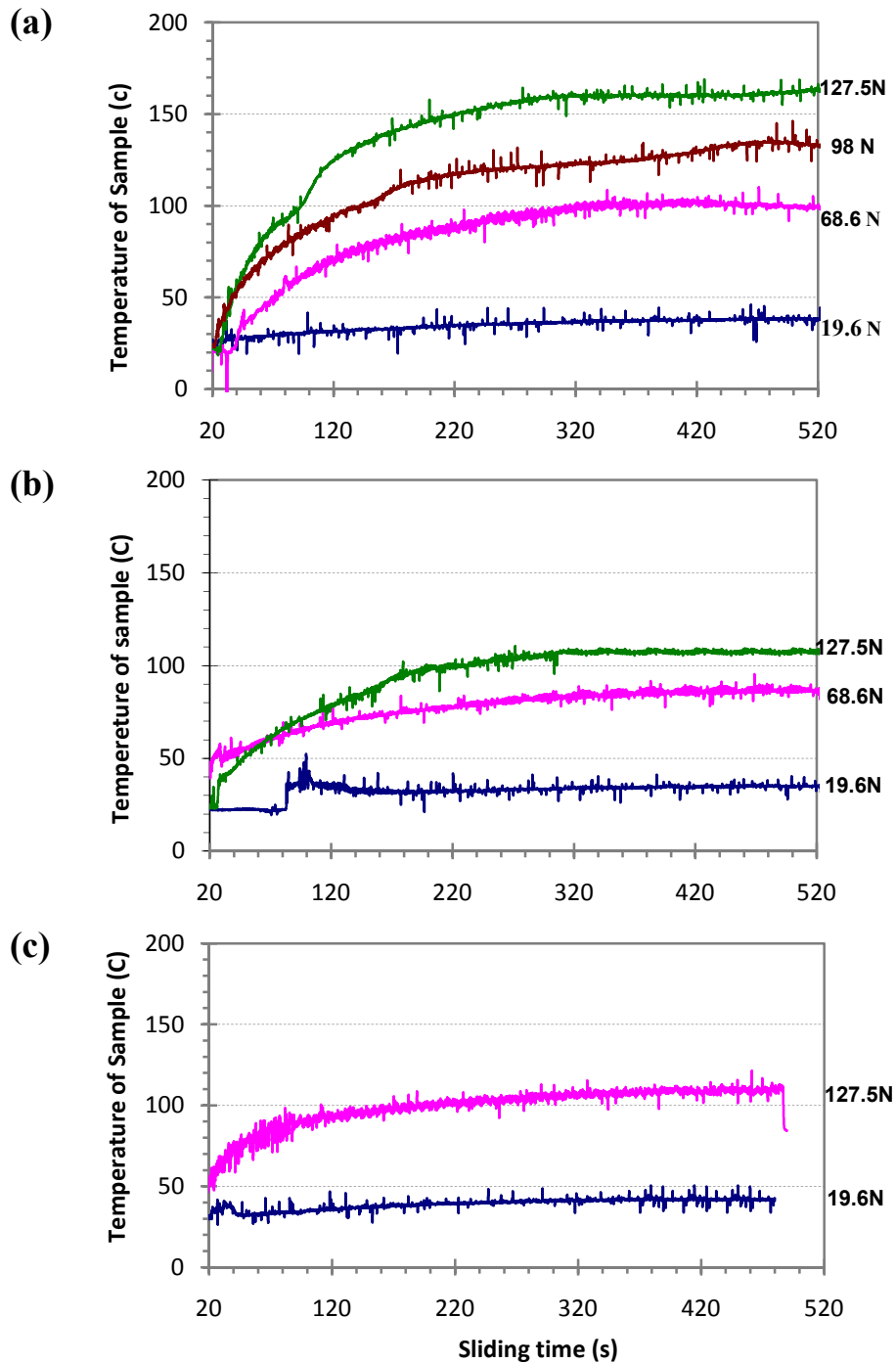


**Fig. 4.14** Changing of sample temperature during the abrasion wear test: (a) C12 with silica 180-250 $\mu\text{m}$ ; (b) C99 steel with silica 180-250 $\mu\text{m}$ ; and (c) C12 with the bottom ash particles.

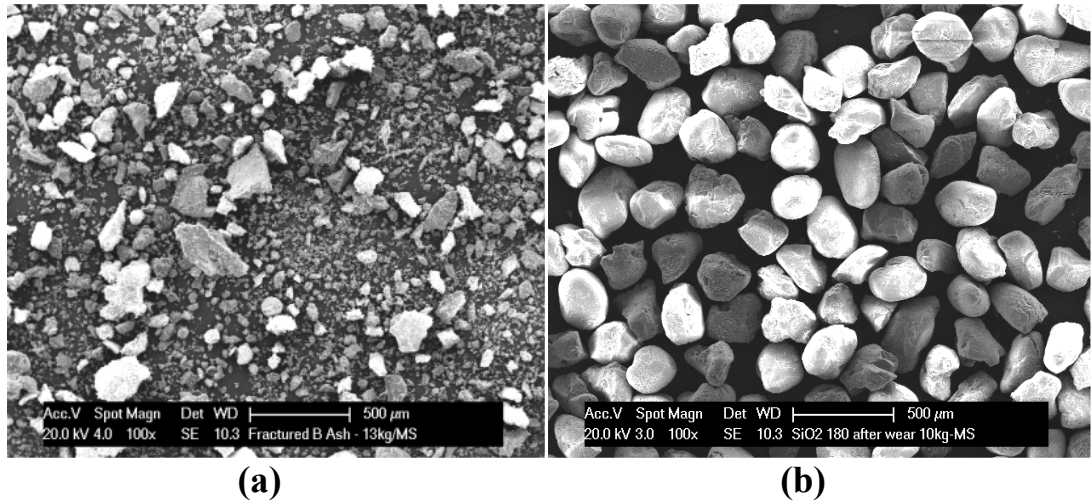


**Fig. 4.15** SEM images of (a) the bottom ash under 19.6 N applied load and (b) the silica 180-250 μm under 127.5 N applied load after passing through the contact zone following abrasion of the C12 Steel.

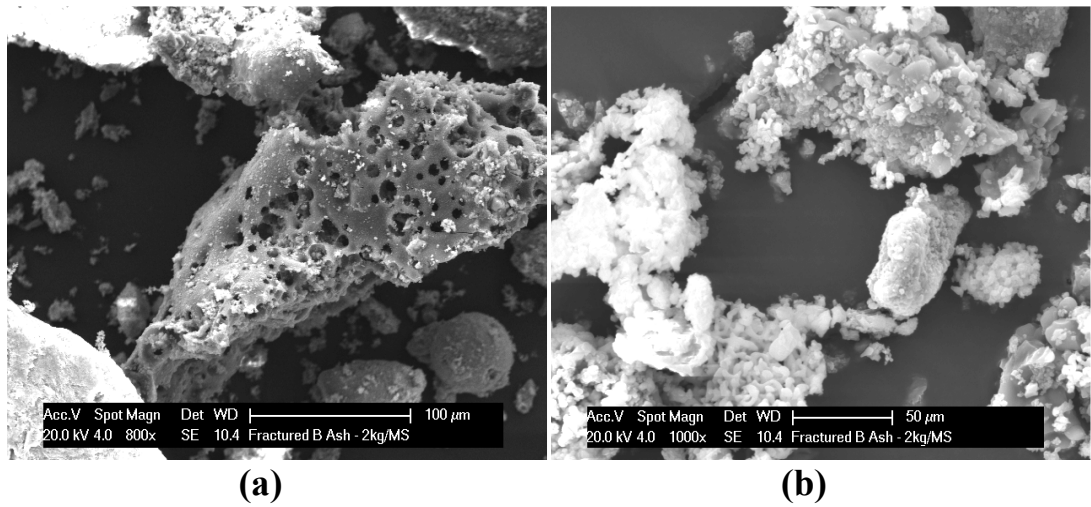


**Fig. 4.16** High magnification of the bottom-ash SEM images: (a) spongy nature of the particles and; (b) fine agglomerated particles.

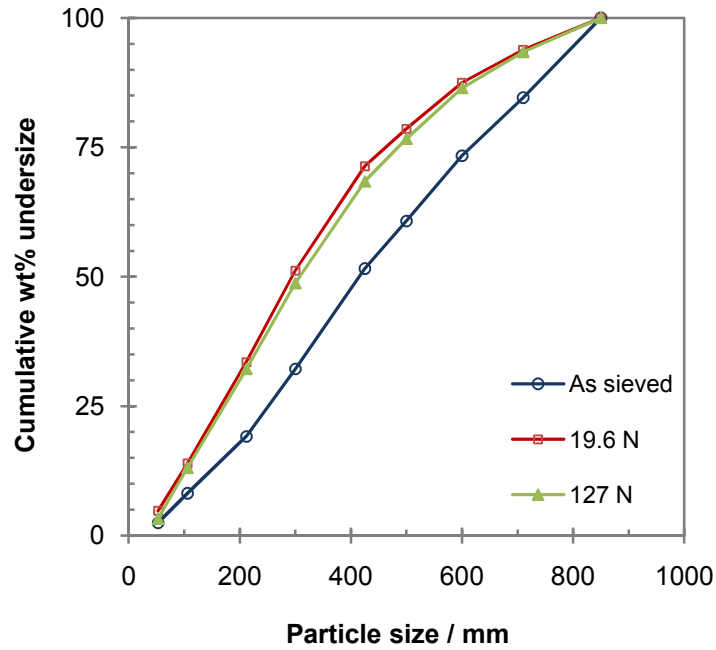


**Fig. 4.17** Particle size analysis (plotted as cumulative weight percentage under a given particle size) of the bottom ash. Ash particle size distributions plotted for the as-sieved ash (before abrasion testing) and then following abrasion of C99 at the two applied loads indicated.

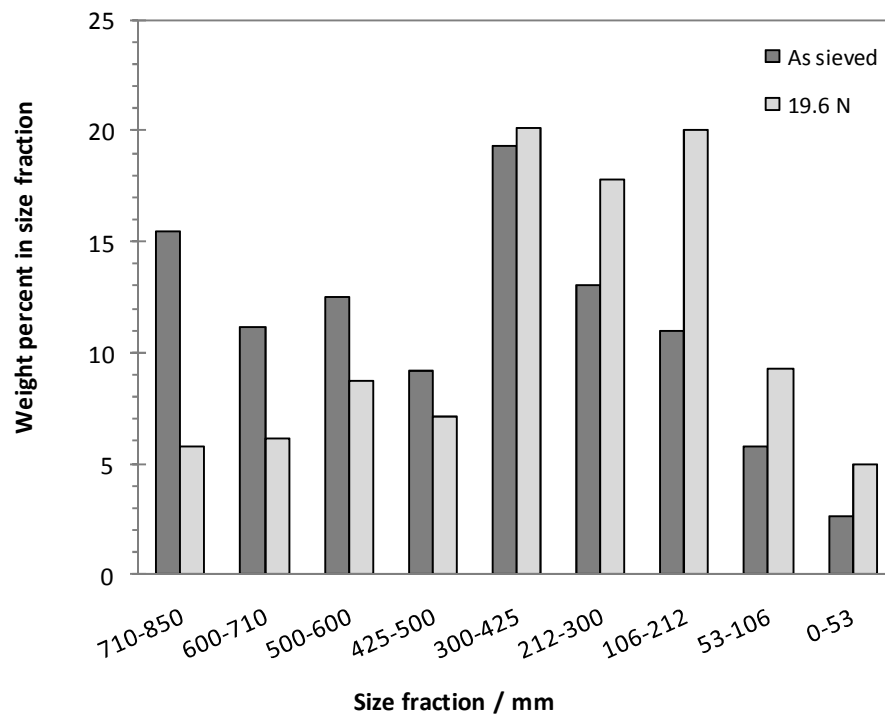


**Fig. 4.18** Particle size analysis (plotted as weight percentage in a particular particle size range) of the bottom-ash. Ash particle size distributions plotted for the as-sieved ash (before abrasion testing) and then following abrasion of C99 under a 19.6N load.

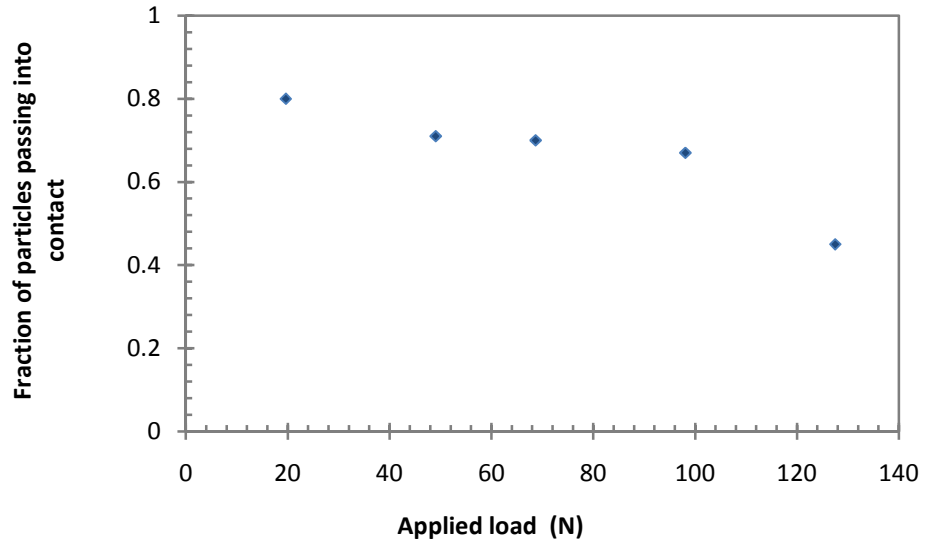


**Fig. 4.19** Fraction of the bottom-ash particles passing into wear contact during abrasion of C18 steel as a function of applied load.

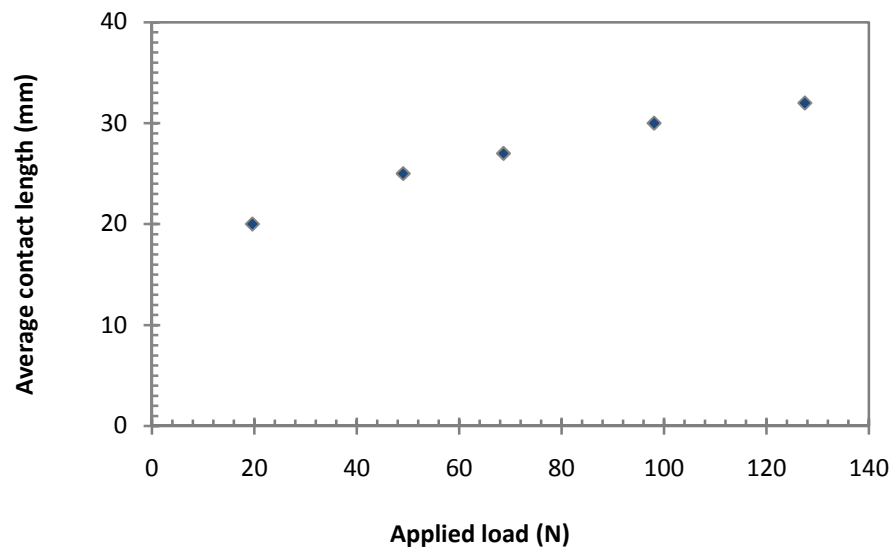


**Fig. 4.20** Measured average contact length of rubber wheel and steel sample as a function of applied load.

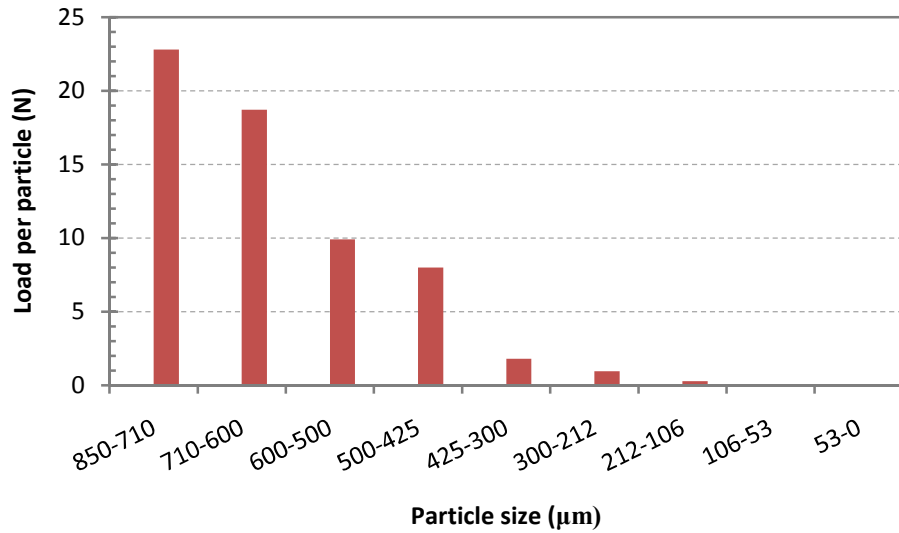


**Fig. 4.21** The load per particle for bottom ash abrasive versus particle size obtained by Equation 7.6 and Table 7.8 (the total load is 68.6 N).

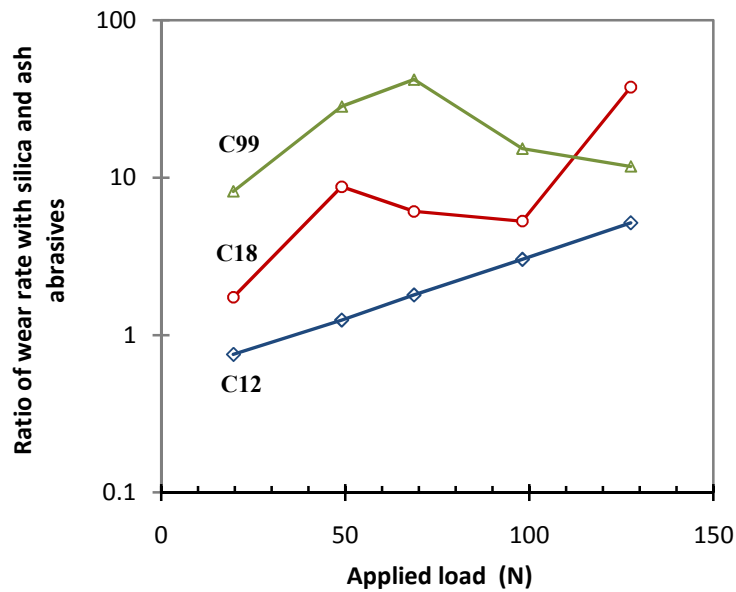


**Fig. 4.22** Ratio of wear rates with silica 180-250μm and ash abrasives as a function of applied load and test material type.

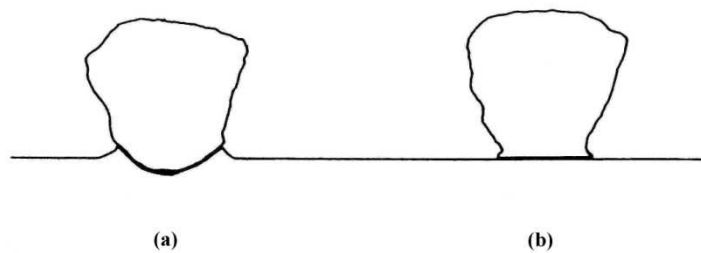


**Fig. 4.23** Illustration of contact between a grit particle under normal load and a plane surface. (a) Hard particle and (b) soft particle [3].

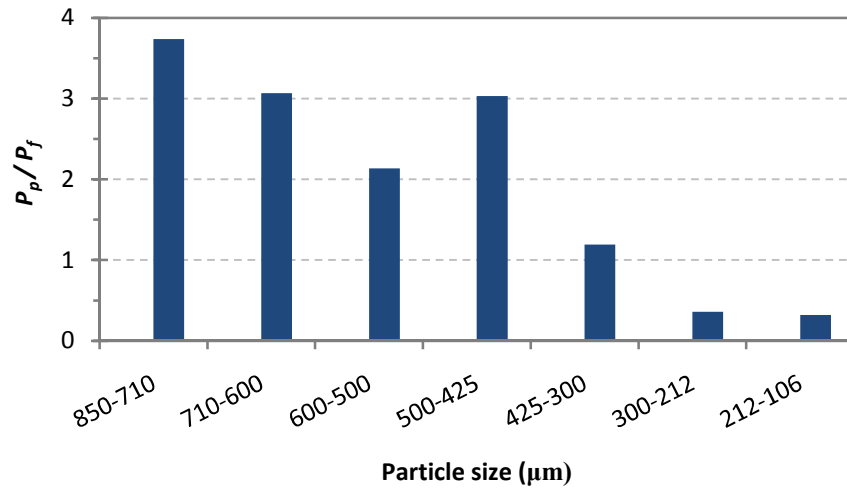


**Fig. 4.24** Ratio of the load per particle,  $P_p$  and maximum load to fracture,  $P_f$  for bottom ash abrasive particles versus particle size. The load per particle was obtained by Equation 7.6 and Table 7.8 (the total load is 68.6 N). The maximum load to fracture was obtained by Fig. 4.5.

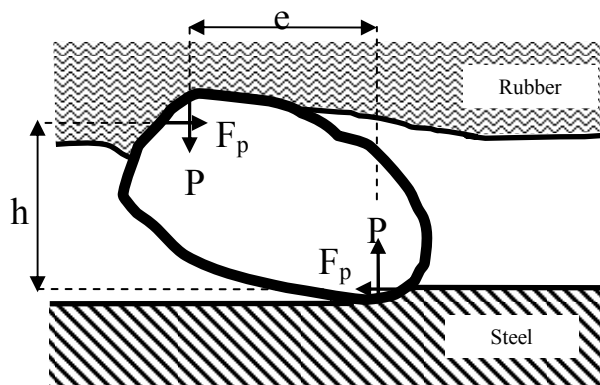


**Fig. 4.25** Model of forces on particle in contact.

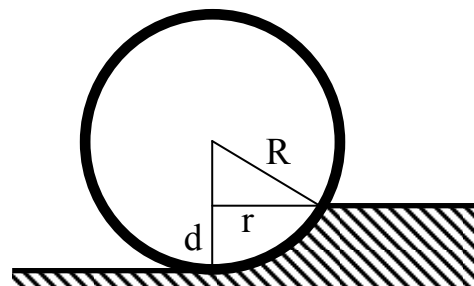
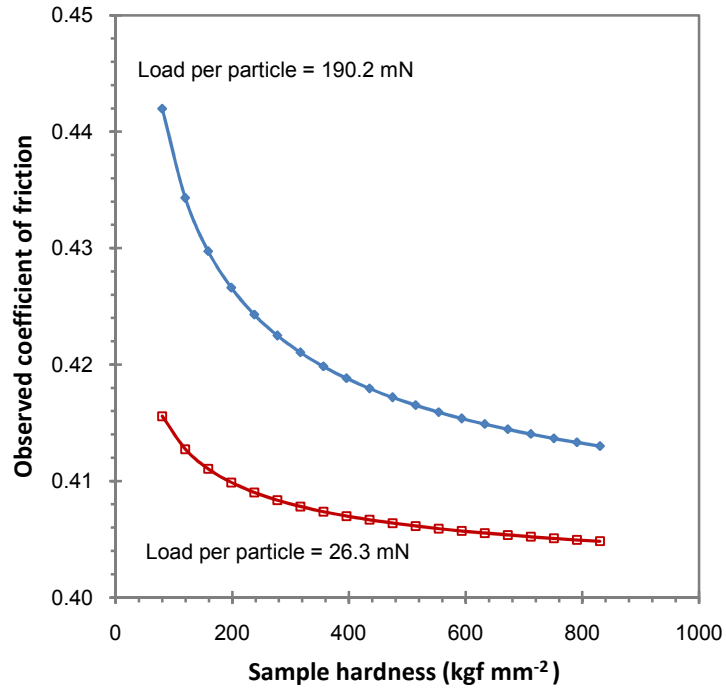
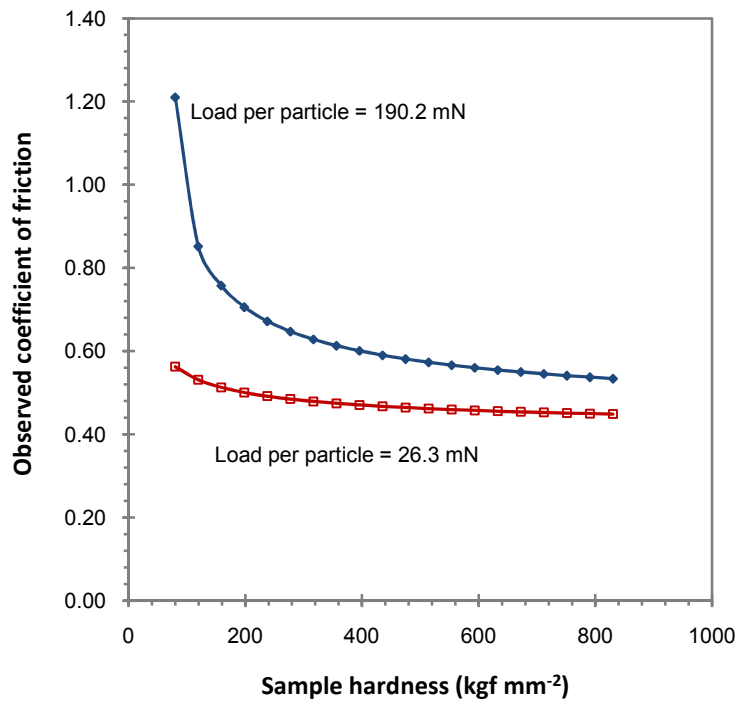


**Fig. 4.26** Schematic diagram showing the various geometrical features of a hard rigid sphere being loaded against a plastic counterbody.



(a)



(b)

**Fig. 4.27** Observed coefficient,  $\mu_p$ , of friction as a function of metal surface hardness for a sphere grooving through a metallic surface for two applied loads as shown; (a) tip radius = 126  $\mu\text{m}$ ; (b) tip radius = 12.6  $\mu\text{m}$ .  $\mu_a$  assumed to be 0.4 in all cases.

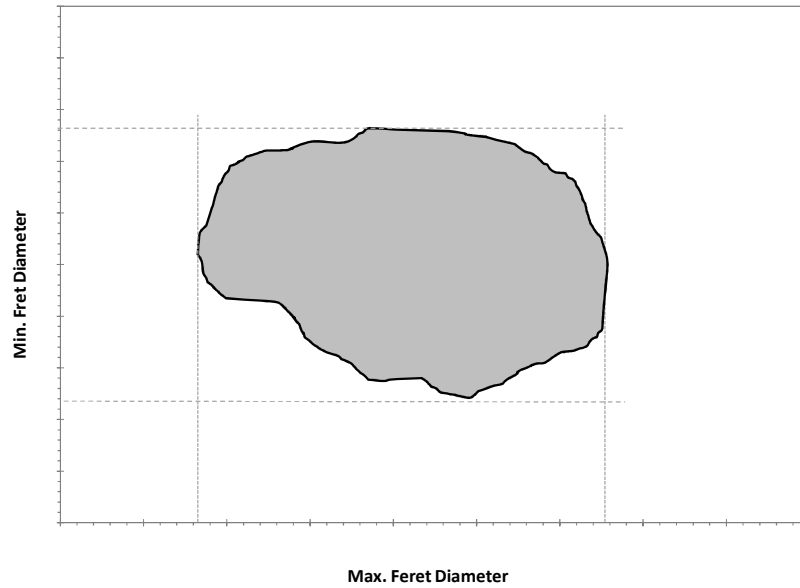


**Fig. 4.28** The ratio of the maximum Feret diameter to the minimum Feret diameter of particle was defined the particle aspect ratio ( $AR_p$ ).

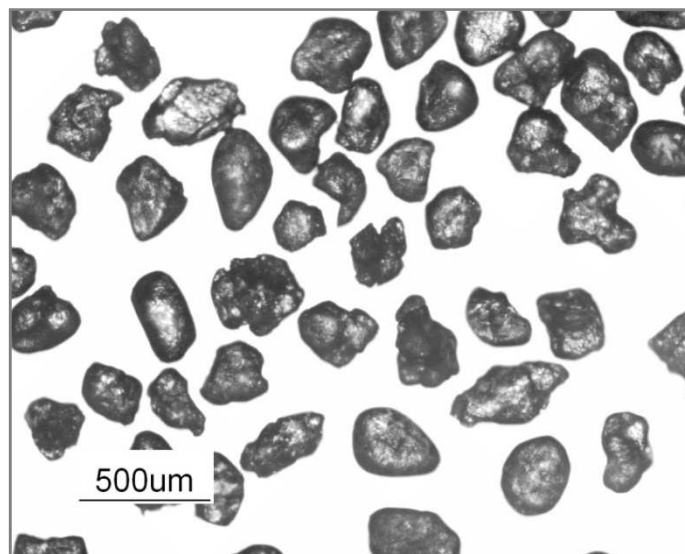
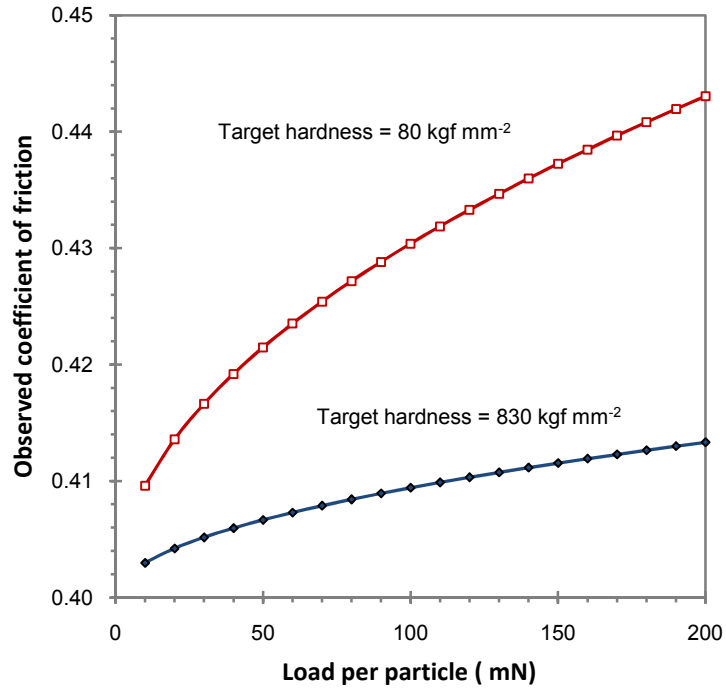
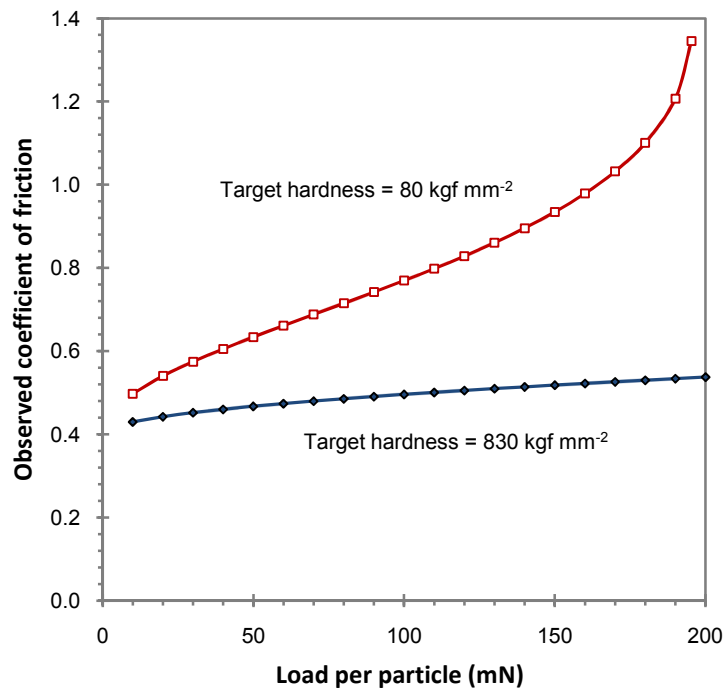


**Fig. 4.29** Optical micrograph of the silica 180-250  $\mu\text{m}$  particles for assessment of particle shape.



(a)



(b)

**Fig. 4.30** Observed coefficient,  $\mu_p$ , of friction as a function of applied load for a sphere grooving through a metallic surface for two metal surface hardnesses as shown; (a) tip radius = 126  $\mu\text{m}$ ; (b) tip radius = 12.6  $\mu\text{m}$ .  $\mu_a$  assumed to be 0.4 in all cases. As the particle size increases, the load per particle increases which promotes rolling.

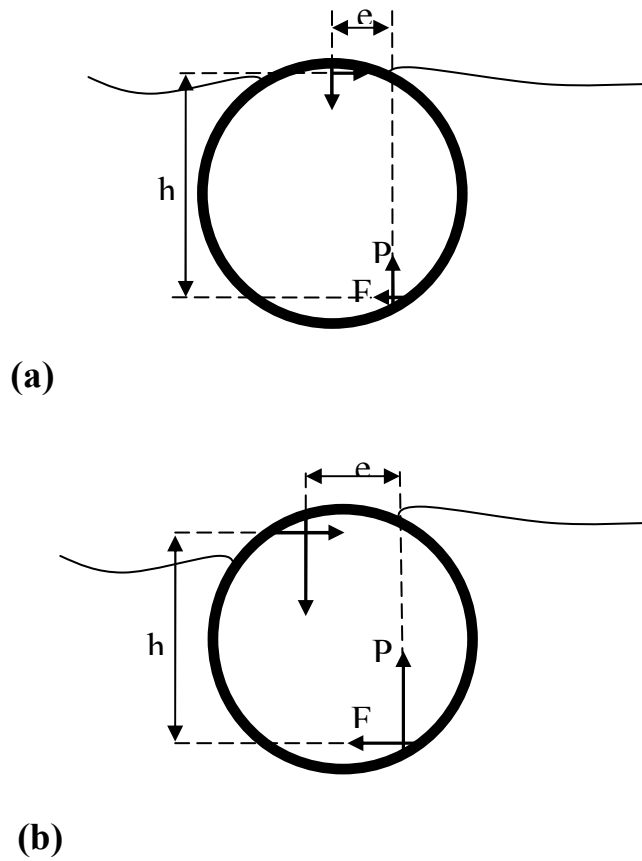


**Fig. 4.31** Schematic diagram of the shape of the contact between a rubber and a hard sphere in the presence of a tractional load; (a) low load per particle; (b) high load per particle.

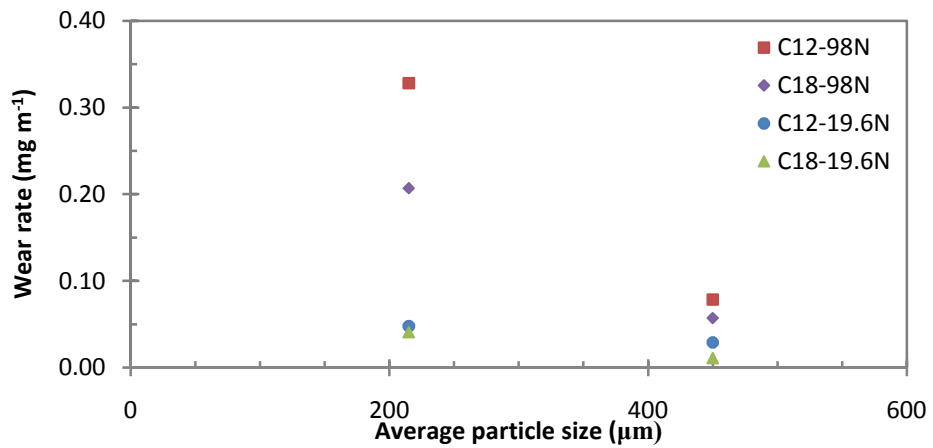
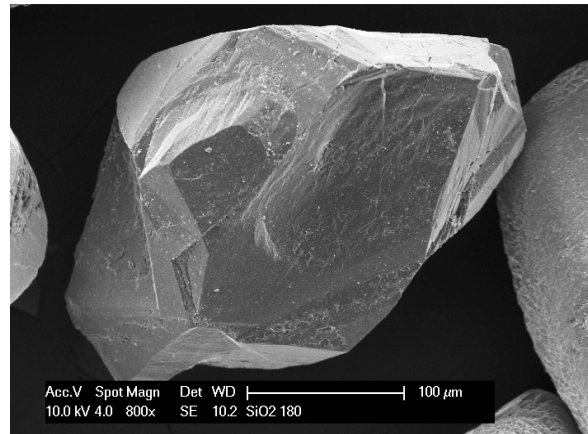


**Fig. 4.32** Effect of abrasive particle size on wear rate of two types of steel (C12 and C18) under lowest and highest loads for silica abrasive.



(a)



(b)

**Fig. 4.33** Typical micrograph of (a) silica 180-250  $\mu\text{m}$  and (b) silica 300-600  $\mu\text{m}$ .

# Chapter 5

---

## Characterisation of Coatings: Results and Discussion

---

### 5.1 Introduction

Five different WC-metal cermet powders were used as feedstock materials in this study. These powders had different average carbide grain sizes and binder compositions as follows: WC-15% nickel alloy (NiMoCrFeCo), WC-15% iron alloy (FeCrAl) and three types of WC-17% Co with different carbide grain sizes. The materials have been labelled Ni, Fe, Co-I, Co-II and Co-III (the Ni, Fe and Co respectively indicating the basic elements in the binders). The mean grain size of WC in the Ni, Fe, Co-I, Co-II and Co-III powders were 0.7, 0.5, 1.0, 0.9, and 0.5  $\mu\text{m}$  respectively. All powders were agglomerated and sintered spheroid shapes in the size range from 15 to 45  $\mu\text{m}$ . The powders were sprayed using a Praxair/UTP Top-Gun HVOF spray system on to mild steel substrates. The spray parameters for all coatings are shown in Table 3.3. A wide range of methods were used for characterising the powders and their sprayed coatings. This chapter describes the characterisation of these powders and coatings and compares the results.

## 5.2 Results

### 5.2.1 Characterisation of Powders

#### 5.2.1.1 Chemical Analysis

The chemical composition of the feedstock powders quoted by the manufacturers is shown in Table 3.2. The X-ray diffraction patterns of the powders are shown in Fig. 5.1. It can be seen that for all coatings, the main peaks correspond to the WC phase while other peaks correspond to the metallic binder phases for each powder. The XRD pattern did not indicate the presence of any other carbide phases such as  $W_2C$  which may be seen in some feedstock powders. Therefore it can be assumed that all the tungsten content existed in the form of the WC phase. Having made this assumption, the composition of elements in the binder phases for each coating can be deduced from the overall powder composition shown in Table 3.2. The results for the binder of the feedstock powders are presented in Table 5.1.

#### 5.2.1.2 Morphology and Particle Size Analysis

Fig. 5.2 shows the result of powder size distribution analysis for the powders measured using the laser diffractometry technique. The median sizes of particles ( $d_{50\%}$ ) and the size distribution ranges ( $d_{5\%} - d_{95\%}$ ) for all powders are presented in Table 5.2. It can be seen that there are only small differences in the size range and median size of particles among the powders.

SEM images of the powders at two different magnifications are shown in Fig. 5.3. As shown in the images, agglomerated and sintered particles in the all powders

have spherical morphology and are highly porous, with large holes within the spherical particles.

### 5.2.1.3 Microstructure and Phase Analysis

Fig. 5.4 shows BSE cross-sectional images of the powder particles at high magnification. Two phases with different contrasts are visible: the WC particles (light contrast) and the metallic binder phases (dark contrast). The blocky shape of the WC grains in all three types of the WC-Co powders are clear (Figs. 5.4c, 5.4d and 5.4e) whereas in the Ni and Fe powders, the WC grains seems to be more rounded (Figs. 5.4a and 5.4b). The large size of the WC grains in the powder particle for the Co-I and Co-II compared with the Ni, Fe and Co-III is also apparent.

Carbide grain size and volume fraction of the phases measured on the cross-section BS images of the powders (utilising the line analysis method) are given in Table 5.3. Table 5.3 also shows the calculated volume fraction from the basis of mass fractions quoted by the manufacturers (Table 3.2) and assuming WC density of  $15.63 \text{ g cm}^{-3}$  [192] and binder densities of  $8.87 \text{ g cm}^{-3}$  for the Ni powder (density of Hastelloy with similar composition [193]),  $7.2 \text{ g cm}^{-3}$  for the Fe powder (density of Kanthal with similar composition [194]) and  $8.90 \text{ g cm}^{-3}$  for the cobalt binder powders. The results from this estimate and from the measured area fractions compare reasonably and accordingly, confirm their accuracy.

## 5.2.2 Characterisation of As-Sprayed Coating

### 5.2.2.1 Chemical Analysis

Tables 5.4-5.8 present chemical analysis results of the starting powder and as-sprayed coating for all material samples. It can be seen that there has been a considerable loss of carbon upon spraying process for all coatings. Table 5.9 exhibits the carbon loss percentage of the coatings during spraying from Tables 5.4-5.8. Whilst the highest carbon loss was observed for the Co-I (42%) and Ni (36%), the carbon loss for the Fe (16%), Co-II (30%) and Co-III (29%) were significantly lower. In addition, there has been no significant pick-up of oxygen for the Co coatings; however, a small increase (0.14%) of oxygen was observed following spraying of the Ni coating, with a large increase of 0.46% for the Fe coating.

### 5.2.2.2 Microstructure and Phase Analysis

Fig. 5.5 shows comparative X-ray diffraction patterns of the coatings sprayed under the conditions given in Table 3.3 for the five powders. It is clear that the decomposition of tungsten carbide occurred during the spray process with all type of powders. However, the degree of decomposition of carbide is different. The tungsten carbide has dissolved in the molten binder during spraying; some of dissolved carbon reacted with oxygen in gas stream of HVOF flame and is lost as carbon monoxide; some of the remaining dissolved W and C have recrystallized as  $W_2C$  and W during solidification with the remainder being retained in the binder. For the all coatings, XRD peaks corresponding to the phases  $W_2C$  and W which formed during deposition are detected. Fig. 5.5 reveals that in the Co coatings there are small amounts of  $W_2C$  compared to that in the Fe coating; the

highest level of  $W_2C$  is observed in the Ni coating. There is a broad diffraction halo between  $2\theta$  values of approximately  $37^\circ$  and  $47^\circ$  for each coating which indicates the presence of an amorphous phase in the deposits. Although this broad halo exists for the all coatings, it is narrower and less high for the Fe and Ni coatings in contrast with that in the Co coating. In none of the coatings are crystalline peaks corresponding to the binder phases apparent.

The average diameter of WC grains and the volume fraction of the binder were measured on the all coating cross-sections by the metallographic technique of line analysis. The mean free path of the binder ( $\lambda$ ) was also measured from the BSE images using the following equation [195]:

$$\lambda = \frac{(1-f)}{N_L} \quad (5.1)$$

where  $N_L$  is the number of non-continuous grains intersected on a metallographic plane by a line of unit length and  $f$  the volume fraction of dispersed phase. For each coating, the results from 5 measurements were averaged to obtain an average value. Table 5.10 presents the result of the mean volume fractions of binders, WC grain sizes and mean free paths of the binders for the all coatings. The results indicate that the Co-I coating has the lowest amount of carbide phase and the highest value of mean free path. The results for other coatings are approximately comparable. Table 5.11 shows the grain size and volume fraction of carbides in both the powders and coatings. Table 5.11 indicates that the most significant change in carbide phase volume fraction (51%) occurs during spraying of Co-I while the least significant change (18%) is observed for Co-II. The results also show that at lower degrees of carbide phase reduction for the Co-II (18%), Ni (19%) and Fe (25%) with increasing decomposition, there was the greatest

decrease in carbide grain size while at higher degrees of carbide phase reduction, for the Co-I (51%) and Co-III (33%), the average size of carbides remained approximately constant (0% for the Co-III) or even slightly increase (10% for Co-I). this may result from whole decomposition of small carbide grains during spray process which leads to elimination of those grains and thus to an increase the value of the average carbide grain size.

Fig. 5.6 shows the BS cross-section microstructural images of the sprayed coatings. The images exhibit typical splat-like microstructures associated with thermal spraying with dark and bright contrast matrix layers, corresponding to regions of lower and higher mean atomic number respectively. In the darker matrix areas of the all coatings, angular particles (WC) can be seen whereas in the brighter regions, the tungsten carbide particles have a more rounded appearance and are often partially or wholly enclosed by bright contrast shells or fringes of another phase. The different levels of dissolved W are primarily responsible for the different contrast levels of the matrices. Although the size of the shells surrounding WC particles precluded accurate SEM/ EDX analysis, it is clear that they had significantly lower carbon levels than the particle centres (higher mean atomic number as observed in BSE imaging). It is probable therefore that the shells around the WC particles are the  $W_2C$  and W phases identified by XRD. There is evidence that bright shells surrounding WC grains are much more prevalent for the Ni coating (Fig. 5.6a) while, the amorphous (high tungsten) regions of binder are much high for the Co-I coating which exhibited the greatest of reduction in carbide content. Moreover, it can be seen that the number of WC particles in the coatings were very different; the carbide grain sizes in the Fe, Ni

and Co-III are small compared with that in the Co-I and Co-II as they were in the powders. In addition, carbide grains in the Ni, Fe and Co-III are numerous and dispersed within the coatings (Fig. 5.6a, 5.6b and 5.6e) while in the Co-I and Co-II there are some large regions in the bright matrices with no carbides (Fig. 5.6c and 5.6d). It is obvious that significant amounts of the bright phase ( $W_2C$ ) in the form of fringes form and small round grains can be seen in the Ni and Fe coatings in comparison with the Co coatings. The carbide grains in the Co coatings are mostly angular whereas the grains in the Ni and Fe coatings have a more rounded morphology; this observation was also made for the powders (Fig. 5.4) indicating that it is a feature of the precipitation processes in the different binder phases. The micrographs corresponding to the Co coatings show evidence of a greater degree of particle melting and flow after impact than those corresponding to the Ni and Fe coatings since a more splat-like microstructure is observed.

The deposit porosity of the coatings was measured using image analysis of BSE micrographs of the coating cross-sections. Fig. 5.7 shows a typical image of the coating cross-section following porosity analysis for all coatings. Table 5.12 also presents the volume fraction of the porosity along with the mean pore size of the coatings obtained from the analysis. It can be seen that the highest level of porosity occurs in the Fe coating with 5.1 vol%. The porosities of the three Co coatings are similar, with lower values than those of the Ni and Fe coatings. This is in accord with the higher degree of melting and flow of splats observed in the Co coatings in Fig. 5.6.

### **5.2.2.3 Mechanical properties**

The hardnesses of the coatings measured by using a Vickers microhardness tester are shown in Table 5.13. The hardness of the Co-III coating was found to be the lowest while the hardness for the Fe coating with similar WC grain size was the highest. The microhardnesses of the three Co coatings were very different. There was also a considerable difference between hardnesses of the Fe and Ni.

The fracture toughness values of the coatings were calculated by measuring the indentations from Vickers hardness tester under 5 kgf load by using the equation of Evans and Wilshaw [196] (section 3.1.4.7). For each coating, the measured fracture toughness was ordered from low toughness (long cracks) to high toughness (short cracks). It was supposed that for any indentations where cracking was not observed, the toughness value was above that of the highest toughness measured for that coating. Fig. 5.8 shows the plots of the cumulative distribution of the fracture toughness data for the coatings that were obtained by using this approach. The results indicate that fracture toughness of the five coatings can be classified in two groups; the Co coatings with high fracture toughness and the non Co coatings (Fe and Ni) having low fracture toughnesses. To quantify these differences, the median values of fracture toughnesses for the all coatings were determined and the values are displayed in Fig. 5.9.

## **5.3 Discussion**

### **5.3.1 Characterisation of Powders**

SEM and XRD results of the five powder feedstocks indicated that all powders consisted solely of tungsten carbide grains in a binder matrix (Figs. 5.1 and 5.4).

The XRD pattern did not indicate the presence of  $W_2C$  phases in any of the feedstock powders; however, it did indicate detected different crystal phases for each powder structure; NiCrFe and Mo for the Ni powder with Ni base Hastelloy binder, AlFe and  $Fe_3W_3C$  for the Fe with FeCrAl alloy binder and Co with crystal structure of fcc for the cobalt powders. SEM images of the all powders show that the agglomerated and sintered particles in the all powders have similarly spherical morphology and seem to be highly porous (Fig. 5.3). The size distribution analysis results for the powders (Fig. 5.2) shows some differences in the size range and median size of particles among the powders (Table 5.2). These results indicate similarity of the powders in morphology and particle size although they have different binder phase and/or carbide grain size.

### 5.3.2 Characterisation of As-Sprayed Coating

Despite the similarity of the feedstock powders in morphology and particle size (section 4.3.1) and the similar conditions of the spraying process for all materials (Table 3.3), a range of considerable differences can be seen in the microstructures and mechanical properties of the coatings.

SEM images of the all powders at high magnification show that the carbide grains were completely surrounded by metallic binders (e.g. see Fig. 5.10). During spraying, the metallic binder melts and wets the carbide grains and thus the oxygen in the HVOF flame cannot react directly on the carbides resulting in the decomposition of carbide phase under the second mechanism (section 2.1.4.2). In this circumstance, the formation of the coatings can be described in the following stages:

### **1. Melting of Binder**

When the powder particles are exposed to the hot gas jet, the temperature of particles increase until the metallic binder phase reaches to its melting point. Melting point of tungsten carbide is 3143 K while the melting point of a metallic binder, for example Co, is 1768 K. The temperature of gas jet in HVOF system is around 2000 K (Fig. 2.2).

### **2. Dissolution of WC in the Binder Phase**

At this stage, carbides begin to be dissolved by the molten binder phase and the metallic matrix increases the carbon and tungsten percentage present in the liquid phase. The binder phase of sprayed coatings shows a wide range of compositions depending on the temperature reached by the powder particles.

### **3. Decarburization**

At the same time, due to the high temperature involved in the spraying process, oxygen diffuses quickly through out the melting phase and reacts with the carbon to form  $\text{CO}_2$ . Carbon will be removed from the melt either by reaction with oxygen at the melt/gas interface or through oxygen diffusion into the rim of the molten particle, leading to CO formation.

### **4. Solidification**

Final stage is rapid solidification of sprayed particle. It may occur during the particle flight, when the particles are near to the substrate or when the particles reach the substrate. When the temperature decreases, new phases precipitate due to the decreasing solubility of tungsten in the binder liquid phase. As the

total amount of carbon has been reduced by oxidising reactions in the previous stage, it is only possible to form new phases with a lower amount of carbon ( $W_2C$ , W) and also nanocrystalline/amorphous phase of the binder (W, C). Growth of pre-existing WC grains would be most likely for melt compositions in the core which had not suffered carbon loss. Clearly, though, carbon loss brings the melt composition much closer to the  $W_2C$  (and/or W) phase field. Nucleation of  $W_2C$  and subsequent  $W_2C$  growth might well be kinetically favoured particularly if WC acted as an efficient nucleation substrate for  $W_2C$ . Therefore, the coating structure includes retained WC grains which remained in solid state during spraying, new precipitated phases (WC,  $W_2C$  and W) depending on the local composition of binder, along with the formation of a nanocrystalline/amorphous binder phase containing dissolved W and C.

Table 5.9 exhibits the carbon loss percentage for the all coatings indicating the highest value of decarburisation for the Co-I (42%) and Ni (36%). The high value of decarburisation in these coatings is due to high degree of decomposition of WC by its dissolution into the molten binder phase and the reaction of a significant fraction of dissolved carbon with oxygen resulting in high decarburisation. Larger amount of W and C dissolution was due to higher temperatures of particle in-flight. Since the spray parameters for the all coatings were nearly the same (Table 3.3), the size of the powder particles may be responsible for that. Fig. 2.23b illustrates the temperature of particles in-flight during HVOF spraying indicating higher temperatures being attained for smaller particles. Fig. 5.2 and Table 5.2 also show the size distribution and median size of the feedstock powders respectively revealing the smallest size of 32  $\mu\text{m}$  for the Ni and Co-I powders.

Table 5.11 on the other hand, shows the most significant change in carbide phase volume fraction (51%) on deposition of Co-I while a much smaller change (19%) is observed for the Ni. The results show that the Ni and Co-I had the same behaviour in the highest dissolution of W and C into their binders and the highest carbon removal from the binders but different behaviour in the solidification stage. In solidification, when the temperature decreases, new phases are formed due to the decreasing solubility of tungsten and carbon in the binder liquid phase. The higher volume fraction of carbide phase in the Ni compared with that in the Co-I coating must result from easier crystallisation of new carbide phases in the Ni due either to lower solubility of W and C in this binder or to more rapid crystallisation kinetics. Shaw et al. [150] compared HVOF sprayed WC cermet coatings with Co and NiAl binders and reported lower solubility of WC in the NiAl in contrast with that in the Co binders. Their results also showed greater extent of  $W_2C$  and W formation in the WC-NiAl coating than that for WC-Co coating; this lower solubility was cited as the reason for its easier precipitation at higher temperature on coating.

A cross-sectional BSE image of the Ni coating in Fig. 5.11 shows the formation of new phases as fringes around WC grains acting as an efficient nucleation substrate. On the other hand, higher solubility of W and C in the Co binder after cooling results in the binder phase rich in W and C in a solution state and consequently, the precipitation of new carbide phases will be insignificant. Table 5.14 shows the ratio of  $W_2C/WC$  for the all coatings indicating that in the Co coatings there are small amounts of  $W_2C$  compared that in the Ni coating, with the latter having much the highest level of  $W_2C$  (Fig. 5.5). The BSE cross-section

microstructural images of the sprayed coatings also show that bright shells surrounding WC grains are much more prevalent for the Ni coating (Fig. 5.6a) while, the amorphous (high tungsten) regions of binder are much high for the Co-I coating (Fig. 5.6c).

The volume fraction of porosity along with the mean pore size of the coatings is shown in Table 5.12. It can be seen that the highest level of porosity occurs in the Fe coating while the porosities of the other coatings are more similar. Table 5.9 presents the carbon loss percentage for the coatings indicating the lowest decarburisation degree for the Fe. This implies the lowest extent of dissolution of W and C into the binder probably due to lower temperature of the particle in-flight. Under such a circumstance, the binder had no chance to be wholly melted (melting point of the binder is equal or above that of the particle temperature) and consequently the porosity significantly increases as can be seen for the Fe coating (Fig. 5.7 and Table 5.12). The XRD pattern for the Fe coating indicates lower extent of  $W_2C$  compared with that for the Ni and also a narrower and less high broad halo (indicating only a minor presence of amorphous phase in the deposits) in contrast with other coatings.

The fracture toughness values of the coatings were calculated by measuring the indentations and associated cracking analysed by the method of Evans and Wilshaw [196] from Vickers hardness indentations. In HVOF coatings, cracks mostly propagate parallel to the substrate, because weak intersplat interfaces are preferred crack propagation paths. Depending on the microstructural characterisations of binder, cracks typically propagate in the metal matrix, going

round carbide particles. The amorphous metal matrix is therefore the preferential propagation path, probably because it is embrittled by WC dissolution [105]. A weak cohesion in the metal-carbide interface also can cause cracks to propagate in coating [197]. The median fracture toughness of the all coatings is presented in Fig. 5.9 showing two distinct groups of coatings; the non-cobalt group with low fracture toughness and the cobalt coatings having high fracture toughness. Higher cohesion between the WC grains and binder and strong intersplat interfaces in the cobalt coatings appear to be responsible for this significant difference. This is probably due to a good wetting property of cobalt binders with WC grains compared with those for the Ni and Fe coatings [198]. Cobalt is the most commonly used binder because it has excellent carbide wetting and adhesion properties [138, 199]. High WC wettability of cobalt binders in thermally sprayed WC-Co coatings results in improvement of their mechanical properties [200]. The micrographs corresponding to the Co coatings also show evidence of a greater degree of particle melting and flow after impact than those corresponding to the Ni and Fe coatings since a more splat-like microstructure is observed (Fig. 5.6).

The hardness of the thermally sprayed WC cermet coatings depends on the volume fraction of retained hard phase of WC, the volume fraction of new phases (e.g.,  $W_2C$  and W), the hardness of binder phase and microstructural properties of coating (i.e., porosity, mean free path of binder and WC grain size). From the measured hardness of the five coatings presented in Table 5.13, it can be seen that although the extents of coating hardnesses are in a high level of hardness in contrast with the other works (section 2.1.4.4), some variations in hardness values within the coatings are evident. The Ni and Fe coatings both with the high volume

fraction of carbide phases (Table 5.10) have different hardness. The ratio of  $W_2C/WC$  peaks for the Ni was significantly higher than that for the Fe coating (Table 5.14). This reveals that the volume fraction of carbide in the Ni includes retained WC and newly crystallised  $W_2C$  phases, whereas for the Fe coating with the lowest decarburisation (Table 5.9) and a low amount of  $W_2C$  (Table 5.14), the volume fraction of carbide phase is mostly associated to the retained WC phase from starting powder. The important role of the retained carbide phase in determining the hardness of thermally sprayed WC cermet coatings is well known and thus efforts have been exerted to control the decomposition of the carbide phase during spraying process. Many investigators reported that a decrease of the decomposition enhances hardness of thermally sprayed WC cermet coatings [112, 113]. Usmani et al. [102] showed that an increase of  $W_2C$  phase in an HVOF sprayed WC cermet coatings goes alongside a decrease in the hardness of coating. The formation of the more hard and brittle  $W_2C$  phase surrounding the WC grains produces a cohesion decrease in the WC particles within the coating and consequently a decrease in mechanical properties like hardness [115, 116].

In contrast, more decomposition of tungsten carbide during spraying can result in an enrichment of the binder phase in W and C. This is due to high solubility of these elements in the binder phase during rapid solidification [150]. This enrichment results in enhancement of both the hardness and brittleness of coating. Although decarburization decreases the volume fraction of the carbides, its detrimental effect on the hardness is compensated by the hardening of the cobalt matrix due to the solution of tungsten and carbon into the binder phase [118]. This is what occurred for the Co-I coating with a high degree of hardness (Table 5.13).

The highest decarburisation and a low  $W_2C$  fraction for the Co-I imply the high enrichment of W and C in the binder and the increase in the hardness of coating. A cross-section BSE image of the Co-I coatings (Fig. 5.6c) exhibits large gray regions within the binder phase indicating the high enrichment W in the matrix.

In the cobalt coating group, the Co-II and Co-III with the approximately same degree of decarburization (Table 5.9) exhibit different hardnesses. The volume fraction of carbide for the Co-II is higher than that for the Co-III (Table 5.3) while its ratio of  $W_2C/WC$  is lower than that for the Co-III (Table 5.14) indicating more retained carbide phase for the Co-II coating compared with the Co-III coating. This may be responsible for the difference in their hardnesses.

In summary, since the oxygen in the HVOF flame cannot react directly on the carbide grains, the formation of the coatings can be described in the following four stages: i) melting of binder in the hot gas jet, ii) dissolution of WC in the molten binder phase, iii) decarburization of binder and iv) precipitation of new phases ( $W_2C$  and W) and formation of amorphous phase of the binder during rapid solidification. High decarburisation of the Ni and Co-I coatings was likely due to their smaller powder feedstock particle. The results show different solubility of W and C in binders for coatings in the Co and non-Co groups during the solidification stage. In the Co coatings, higher solubility of W and C after cooling results in the binder phase rich in W and C in a solution state while in the non-Co coatings lower solubility of W and C leads to precipitate significant new carbide phases. The fracture toughness testing results presents low fracture toughness for the non-Co coatings and high fracture toughness for the Co

coatings. This is because higher cohesion between the WC grains and binder and strong intersplat interfaces in the cobalt coatings probably due to a good wetting property of cobalt binders with WC grains compared with those for the Ni and Fe coatings. The results also imply that two important factors results in enhancement of the hardness of the coatings are the volume fraction of retained hard phase of WC (e.g. for the Fe coating) and enrichment of the binder phase in W and C (e.g. for the Co-I coating).

**Table 5.1** Estimated composition of elements in the binders of the powder feedstocks using Table 3.2 and assuming all carbides are in the form of WC.

Designation	Composition of binder (starting powder stock) (wt%)							
	Ni	Mo	Cr	Fe	Co	Al	C	O
Ni	57.31	15.14	14.53	5.67	4.05	-	2.87	0.004
Fe	-	-	21.75	68.94	-	6.57	2.74	0.01
Co-I	-	-	-	0.3	99.70	-	-	-
Co-II	-	-	-	0.24	99.37	-	0.39	-
Co-III	-	-	-	0.18	99.70	-	0.12	-

**Table 5.2** Particle median size of the powders resulted from laser particle size analyser.

Powder	Median size of powder particle, $d_{50\%}$ ( $\mu\text{m}$ )	Particle size distribution range, $d_{5\%}$ - $d_{95\%}$ ( $\mu\text{m}$ )
Ni	32	15-65
Fe	36	18-65
Co-I	32	17-58
Co-II	38	22-59
Co-III	34	17-55

**Table 5.3** WC grain size with volume fraction of WC phases in the powders measured both by line analysis and calculated from the chemical composition of the powders.

<b>Powder</b>	<b>Measured volume fraction of WC (%)</b>	<b>Calculated volume fraction of WC (%)</b>	<b>WC Grain size (<math>\mu\text{m}</math>)</b>
Ni	73	76	0.7
Fe	77	71	0.5
Co-I	72	74	1.0
Co-II	67	74	0.9
Co-III	71	73	0.5

**Table 5.4** Measured chemical composition of the Ni powder and as sprayed coating.

<b>WC-Ni</b>	<b>Composition (wt %)</b>							
	<b>W</b>	<b>Ni</b>	<b>Mo</b>	<b>Cr</b>	<b>Fe</b>	<b>Co</b>	<b>C</b>	<b>O</b>
Powder	79.98	8.48	2.24	2.15	0.84	0.6	5.65	0.06
Coating	81.58	8.65	2.28	2.20	0.86	0.61	3.61	0.2

**Table 5.5** Measured chemical composition of the Fe powder and as sprayed coating.

<b>WC-Fe</b>	<b>Composition (wt %)</b>					
	<b>W</b>	<b>Fe</b>	<b>Cr</b>	<b>Al</b>	<b>C</b>	<b>O</b>
Powder	79.16	10.81	3.41	1.03	5.59	0.16
Coating	79.44	10.80	3.42	1.03	4.69	0.622

**Table 5.6** Measured chemical composition of the Co-I powder and as sprayed coating.

WC-Co (I)	Composition (wt %)				
	W	Co	Fe	C	O
Powder	78.14	16.83	0.05	5.03	-
Coating	79.84	17.16	0.05	2.89	0.071

**Table 5.7** Measured chemical composition of the Co-II powder and as sprayed coating.

WC-Co (II)	Composition (wt %)				
	W	Co	Fe	C	O
Powder	78.01	16.83	0.04	5.16	-
Coating	79.23	17.09	0.04	3.61	0.063

**Table 5.8** Measured chemical composition of the Co-III powder and as sprayed coating.

WC-Co (III)	Composition (wt %)				
	W	Co	Fe	C	O
Powder	77.88	17.02	0.03	5.10	-
Coating	78.99	17.29	0.03	3.63	0.050

**Table 5.9** Carbon loss percentages after spraying obtained from Tables 5.4 through 5.8.

Coating	Carbon loss (%)
Ni	36
Fe	16
Co-I	42
Co-II	30
Co-III	29

**Table 5.10** Volume fractions of carbide, WC grain sizes and mean free paths of the binders for the all coatings by use of a line analysis method on the BS cross-section images.

Coating	Volume fraction of WC (%)	WC grain size ( $\mu\text{m}$ )	Mean free path ( $\mu\text{m}$ )
Ni	59	~0.6	0.40
Fe	58	~0.4	0.31
Co-I	35	~1.1	2.03
Co-II	55	~0.8	0.68
Co-III	49	~0.5	0.54

**Table 5.11** Comparison of volume fractions and grain size of carbide in the powder and coating.

Material	Volume fraction of Carbide phase (%)			Carbide grain size ( $\mu\text{m}$ )		
	Powder	Coating	Changes	Powder	Coating	Changes
Ni	73	59	19 %	0.7	0.6	14 %
Fe	77	58	25 %	0.5	0.4	20 %
Co-I	72	35	51 %	1.0	1.1	-10 %
Co-II	67	55	18 %	0.9	0.8	11 %
Co-III	71	49	33 %	0.5	0.5	0 %

**Table 5.12** Deposit porosity and mean pore size of the coatings measured by image analysis on BS micrographs of the coating cross-sections.

Coating	Average Size ( $\mu\text{m}$ )	Porosity (vol %)
Ni	0.30	2.2
Fe	0.25	5.1
Co-I	0.27	1.6
Co-II	0.36	1.8
Co-III	0.42	1.2

**Table 5.13** Vickers microhardness of the coatings.

Coating	Micro hardness ( $\text{kgf mm}^{-2}$ )
Ni	1255 $\pm$ 38
Fe	1499 $\pm$ 82
Co-I	1418 $\pm$ 61
Co-II	1306 $\pm$ 71
Co-III	1203 $\pm$ 57

**Table 5.14** The ratio of  $\text{W}_2\text{C}$  to WC XRD-peak height for the all coatings ( $\text{W}_2\text{C}$  peak at  $d= 2.275 \text{ \AA}$  and WC peak at  $d= 1.882 \text{ \AA}$ ).

Coating	XRD peak height ratio ( $\text{W}_2\text{C}/\text{WC}$ ) $\times 100$
Ni	40.42
Fe	12.48
Co-I	15.58
Co-II	9.14
Co-III	14.96

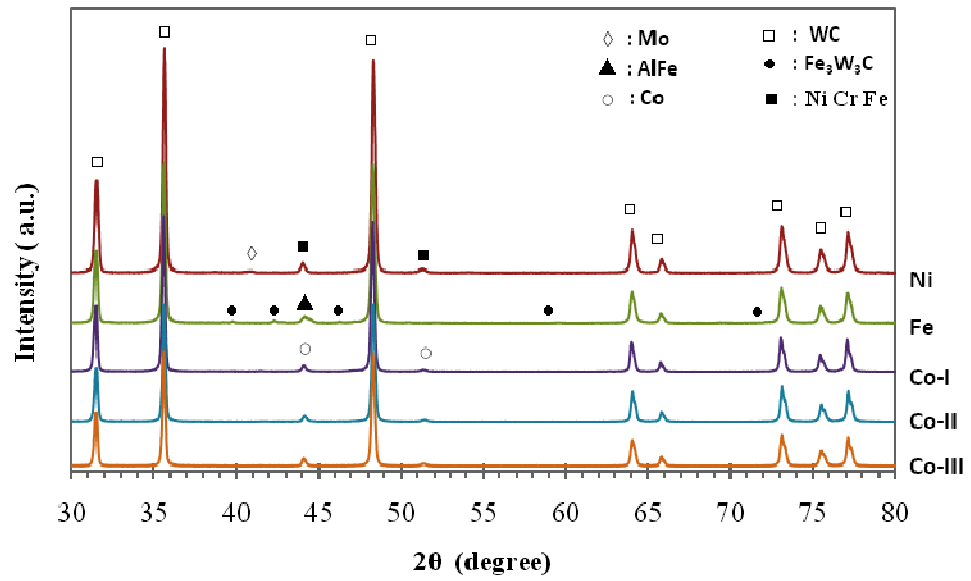


Fig. 5.1 XRD spectra of the feedstock powders.

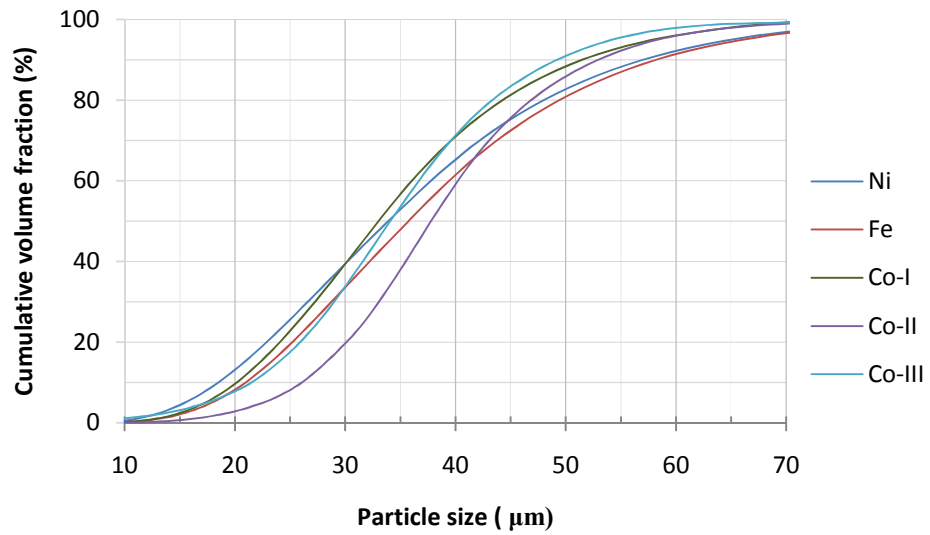
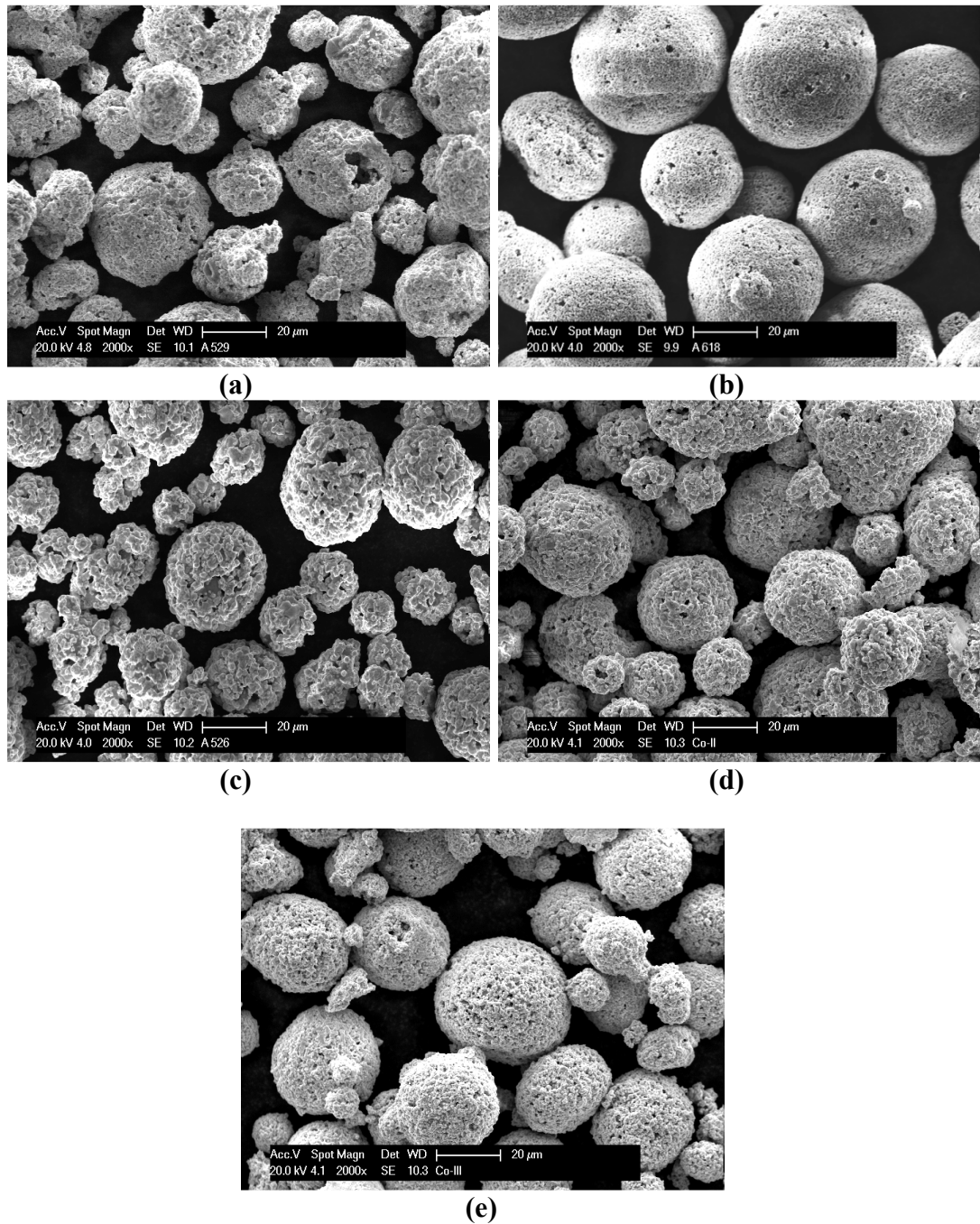
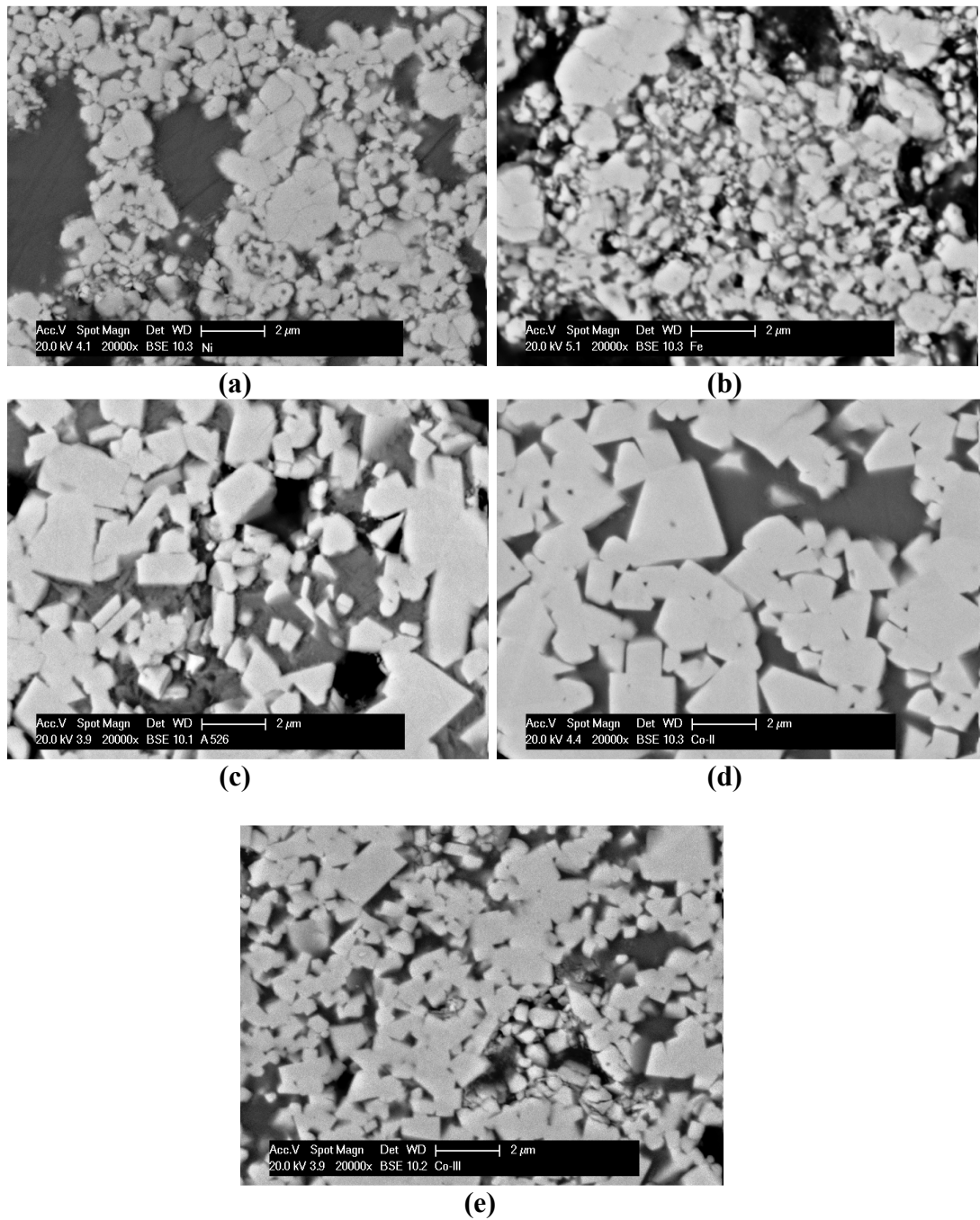


Fig. 5.2 Size distribution analysis of the powder particles.



**Fig. 5.3** Feedstock powder morphologies of: (a) Ni, (b) Fe, (c) Co-I, (d) Co-II, and (e) Co-III



**Fig. 5.4** BSE feedstock powder cross-sections of: (a) Ni, (b) Fe, (c) Co-I, (d) Co-II, and (e) Co-III.

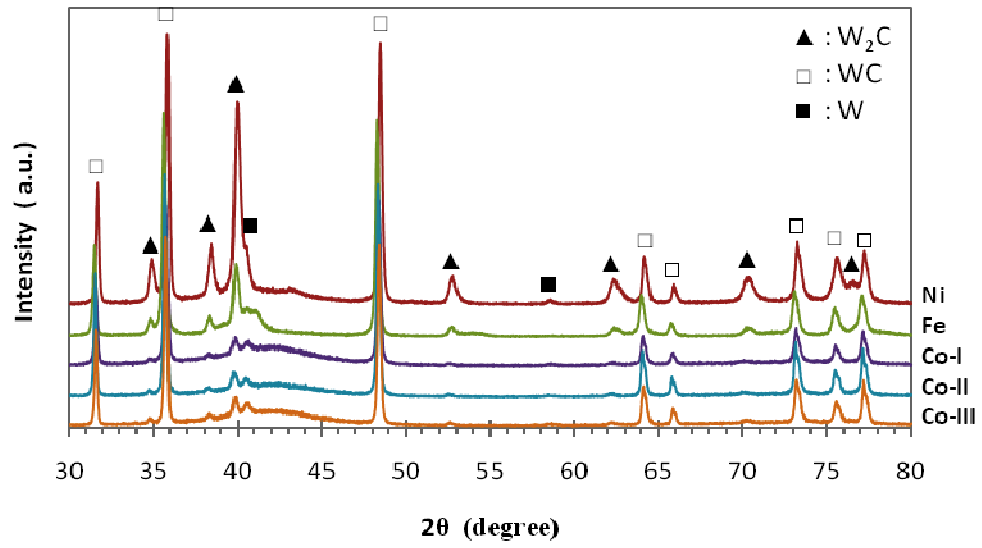
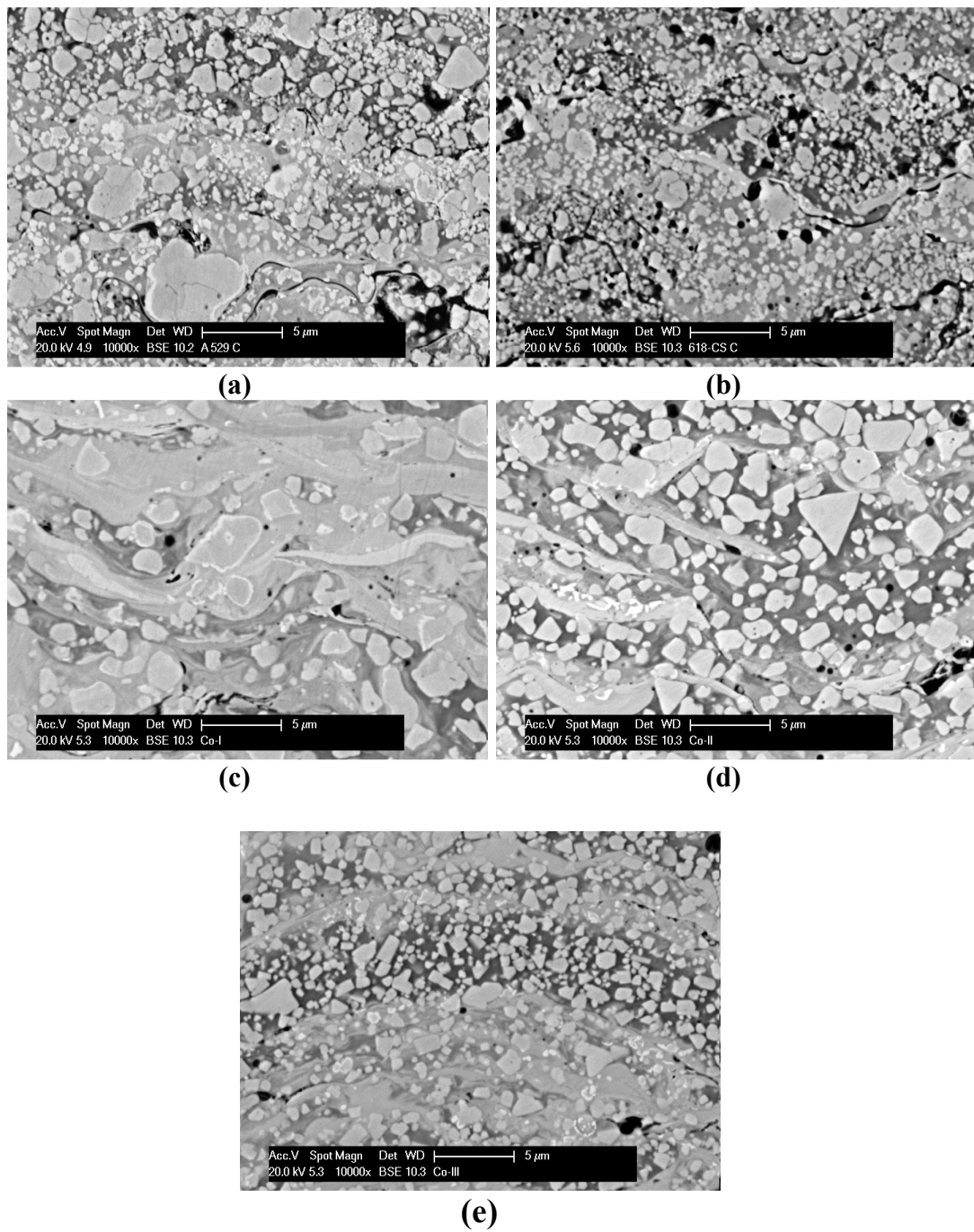
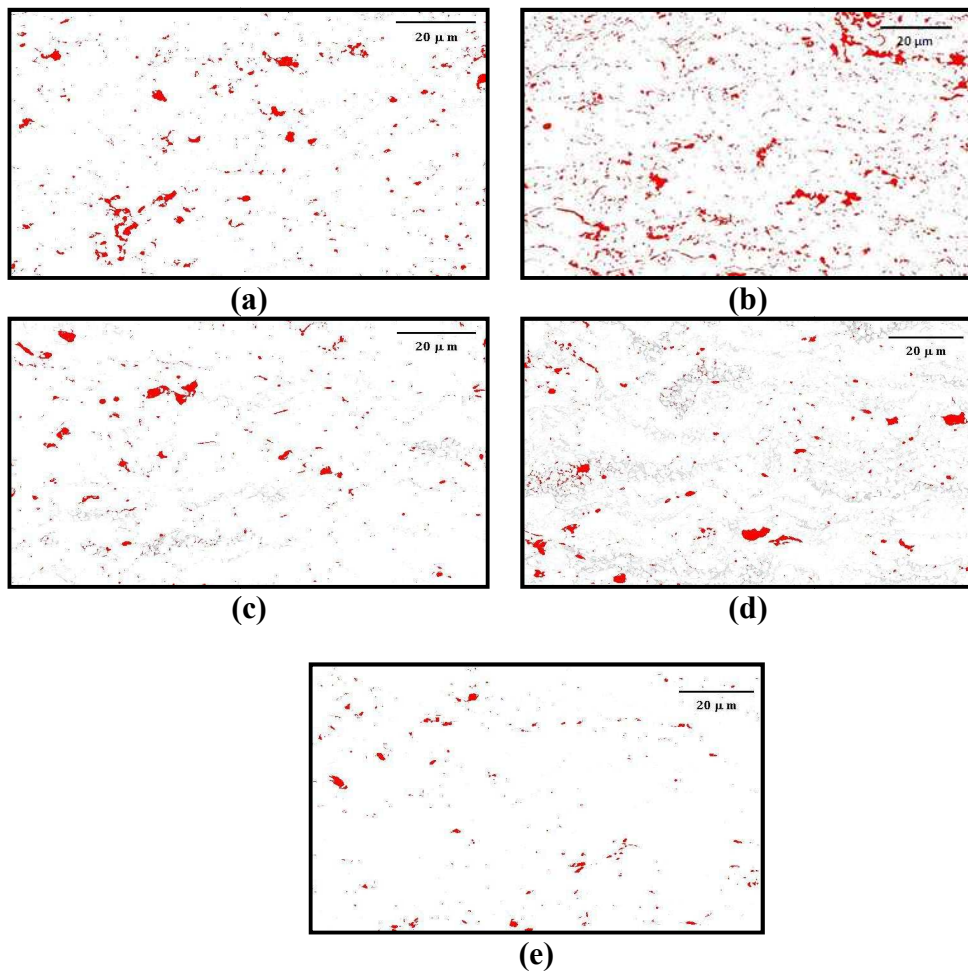


Fig. 5.5 Comparative XRD spectra results for the as-sprayed coatings.



**Fig. 5.6** Cross-section BS images of the sprayed coatings of: (a) Ni, (b) Fe, (c) Co-I, (d) Co-II, and (e) Co-III.



**Fig. 5.7** BSE images of the as-sprayed coating cross-sections after analysing the porosity by use of Image Analysis software: (a) Ni, (b) Fe, (c) Co-I, (d) Co-II, and (e) Co-III.

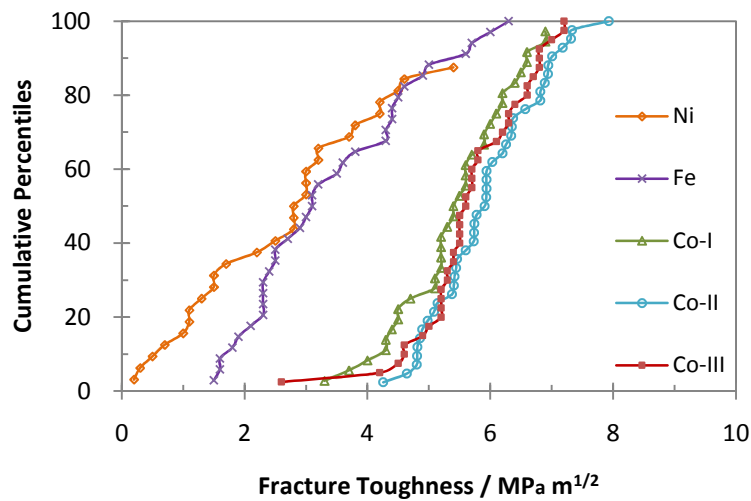


**Fig. 5.8** Cumulative percentiles corresponding to the indentation fracture toughness for the five coating types under 5 kgf load.

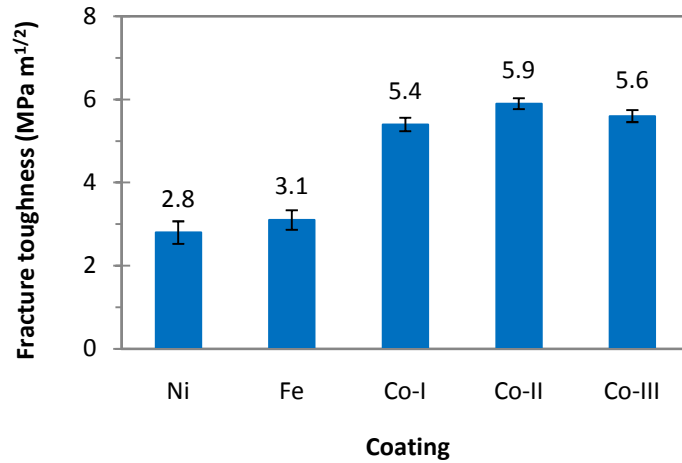


**Fig. 5.9** Median fracture toughness of the five coatings measured by use of Vickers indenter under 5kgf load.

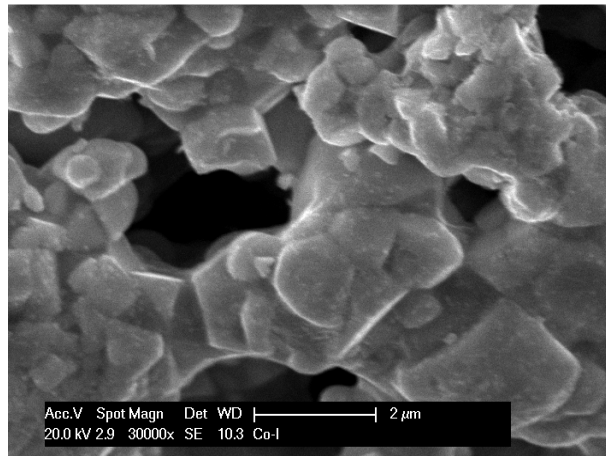


**Fig. 5.10** SEM image of the Co-I powder in high magnification ( $\times 30000$ ).

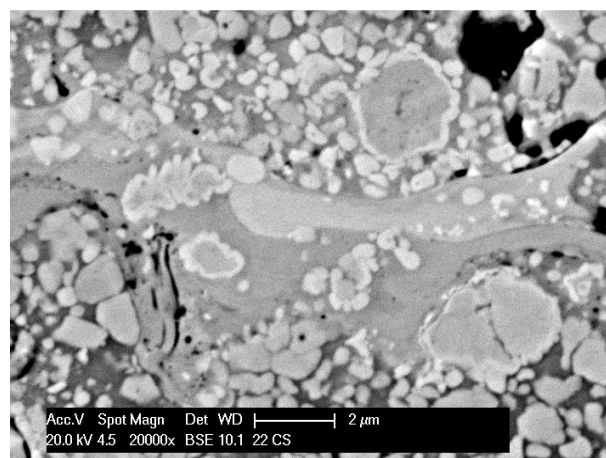


**Fig. 5.11** Cross-section BSE image of the Ni coating shows the formation of new phases as fringe shape around WC grain as an efficient nucleation substrate.

# Chapter 6

---

## Abrasive Wear of HVOF Sprayed Coatings: Results and Discussion

---

### 6.1 Introduction

Five different types of tungsten carbide cermet powders with different binders and carbide grain sizes were sprayed using an HVOF system and their abrasion behaviour was investigated. The details of the starting powders, spray parameters and coating properties are presented in chapter 5. To evaluate the abrasive wear performance of the coatings, the dry sand–rubber wheel test method (a variant on ASTM G65), described in section 3.2.2, was employed. The parameters used in the wear test were the same as were employed for the steels samples (section 3.2.2). Two abrasive particles, namely alumina and silica with the particle size ranges of 212-300  $\mu\text{m}$  and 180-250  $\mu\text{m}$  respectively were used as abrading media. The wear experiments were done with loads of 19.6, 49, 98, and 127.5 N. Finally, the abrasive wear behaviour of coatings with the two different abrasives was compared, and understood in terms of their mechanical and microstructural properties presented previously (chapter 5).

## 6.2 Results

### 6.2.1 Characterisation of Abrasive Particles

#### 6.2.1.1 Abrasive Materials

In order to assess the wear behaviour of the coatings, two types of abrasive particles were employed. The abrasive particles used in this work were rounded silica (The David Ball Company, Bar Hill, UK) and angular alumina (Abrasive Developments, Henley-in-Arden, UK). The abrasive size used for silica was F70 grit size (180-250  $\mu\text{m}$ ) and for alumina was F60 grit size (212-300  $\mu\text{m}$ ), both obtained by a sieving technique.

#### 6.2.1.2 Morphology and Particle Size Analysis

Fig. 6.1 shows the morphology of the abrasive particles. The micrographs of the particles show rounded silica abrasive particles in contrast to the angular shapes of the alumina particles.

The size distributions of the abrasive particles were measured by passing the abrasives through a stack of wire-mesh sieves on a mechanical sieve shaker. Fig. 6.2 shows the size distribution for each particle type. The results indicate that for silica 70 and alumina 60 the distribution sizes are similar, although the alumina abrasive had a larger fraction of larger particles. The particle diameter,  $d_p$ , below which 50% of the volume lay was taken as the nominal particle diameter of the particles in any further analysis. This is  $\sim 190$   $\mu\text{m}$  for silica 70 and  $\sim 200$   $\mu\text{m}$  for alumina 60.

### 6.2.1.3 Hardness

The Vickers hardnesses of the silica 70 and alumina 60 abrasives were measured on polished cross-sections with a 300 gf indentation load and are  $1116 \pm 46$  kgf mm<sup>-2</sup> and  $2103 \pm 25$  kgf mm<sup>-2</sup> respectively.

## 6.2.2 Characterisation of Worn Surfaces

### 6.2.2.1 Abrasion of Coatings

The wear rates of the coatings were measured using the dry sand rubber wheel abrasion test (DSRW) technique. Two types of abrasives under four different loads were employed for wear testing. Fig. 6.3 shows examples of the raw data for the abrasive wear tests performed on one of the coating materials, namely the mass loss of the Co-I coating as a function of abrasion distance (with silica 70 abrasive) for four applied loads. It can be seen that for all four loads, the progress of mass loss was linear with abrasion distance. Also, it is notable that in general, the rate of wear increases as the applied load increases. Table 6.1 exhibits the parameters of abrasive wear test for the five coatings along with the wear rate at each applied load for each series of coating-abrasive tests.

The wear rate has been determined from a least squares fit of the data that is in the linear (steady state) regime. Steady state wear rates of coatings were measured under four applied loads of 19.6, 49, 98, and 127.5N with both silica and alumina abrasives. Steady state wear rates with silica 70 and alumina 60 abrasives for each coating type as a function of load are shown in Figs. 6.4 and 6.5 respectively. In all cases, the wear rates of the coatings are observed to be significantly higher

with alumina 60 than silica 70 abrasive. It can be seen that the wear rate with the alumina abrasive is nearly between  $\sim 1.2$  and  $7.8$  times larger than that with the silica abrasive. The wear rate is sensitive to the ratio of abrasive hardness  $H_a$  to the surface hardness  $H_s$ . Abrasion under conditions where  $H_a/H_s > 1.2$  is sometime termed “hard abrasion”, in contrast to “soft abrasion” when  $H_a/H_s < 1.2$  [3]. Fig. 6.6 shows the values of  $H_a/H_s$  for each coating-abrasive combination. It is evident that for all coatings, the abrasive wear with alumina should be “hard” abrasion whereas that with silica should be “soft” abrasion.

Figs. 6.4 and 6.5 also indicate that for coatings with high wear rates, increasing applied load results in a significant increase in wear rate, whereas for coatings with low wear rates, the effect of applied load on wear rate is less. For example, wear rate with silica (Fig. 6.4) is highest for the Co-II coating and lowest for the Fe coating. The wear rate observed under 98 N load compared to that under 19.6 N for the Co-II coating is about 4 times as much whereas for the Fe coating is around 1.5 times. Similar behaviour is observed for wear with the alumina abrasive.

The wear test results with silica (Fig. 6.4) can be classified into two groups; the Co coatings with high wear rate and the non-Co coatings with low wear rate. On the other hand, the wear test results with alumina (Fig. 6.5) show that the highest wear rate is associated with the Co-III coating, whilst the Co-I coating had the lowest wear rate.

### 6.2.2.2 Wear Scar Investigation

After abrasive wear testing, the worn surfaces of all samples were examined by optical and SEM microscopies. Images of the central zone of the worn areas at the lowest and highest applied loads utilised were chosen. Fig. 6.7 shows optical microscopy images of the Fe coating following wear with silica 70. The surfaces show evidence typical of particle rolling, with significant indentation of the surface. In contrast, Fig. 6.8 shows evidence typical of particle sliding (grooving) and also evidence typical of small particle rolling across the surface of the sample following abrasion with the alumina particles. Optical microscopy images of all the coatings indicated that in the all cases and under all applied loads, silica 70 abrasive resulted in evidence of particle rolling while with alumina 60 abrasive resulted in grooving. Figs. 6.7 and 6.8 also show that the size of indentations and grooves increase with increasing applied load.

Figs. 6.9 through 6.18 present the plan view and cross-sectional micrographs of the wear scars for the five coatings following abrasive wear with silica 70 and alumina 60 abrasives under the lowest and the highest applied loads.

#### The Ni Coating

Fig. 6.9 shows the SEM images of the central zone of the wear scars on the Ni coating following abrasion with silica 70. The plan view images under the lowest and highest applied load (19.6 N and 127.5 N) are exhibited in Fig. 6.9a and 6.9b respectively, with the cross-sectional image of the worn surface at the highest load being shown in Fig. 6.9c. Carbide cracking and pullout can be seen in both top views of the worn surfaces. The metal matrix seems to wear at a higher rate

leaving unprotected carbide particles obviously visible in the plan view of wear scar at the higher load (Fig. 6.9b). Also there is some carbide pull out despite the small size of some of the carbide grains. The cross-sectional image (Fig. 6.9c) shows sub-surface cracking which will result in the formation of large pits. However, good adhesion of carbide grains at the wearing surface is evident. SEM images of the Ni coating abraded with alumina 60 are presented in Fig. 6.10. The plan view images under 19.6 N and 127.5 N loads show cutting and grooving of both the binder and carbide uniformly, with the grooves being larger and deeper under the higher load condition. Moreover, large material loss can be seen in the worn surface as dark regions under the higher applied load. The cross-sectional image of the worn surface (Fig. 6.10c) shows sub-surface cracking propagating through the binder phase. Vertical cracks can also be seen within the coating.

### **The Fe Coating**

Figs. 6.11a and 6.11b show the SEM plan view images of the central zone of the wear scars on the Fe coating following abrasion with silica 70 at the lowest and highest applied loads (19.6 N and 127.5 N ) respectively. Large cracks and a large amount of voiding are evident on the worn surface under both applied loads. Because of high level of the porosity in the coating, the pullout process cannot be distinguished easily. The metal matrix also seems to wear at a very slightly higher rate leaving unprotected carbide particles visible in the plan view image (Figs. 6.11a and 6.11b). A cross-sectional image of the worn surface at the highest load is shown in Fig. 6.11c. Sub-surface cracks can be seen propagating through the coating with high level of porosity within the coating. However, good adhesion of carbide grains and matrix is apparent. Figs. 6.12a and 6.12b show SEM plan view

images of the Fe coating abraded with alumina 60 under 19.6 N load and 127.5 N loads respectively. Grooves with large voids are apparent under both loads but at the higher load; the grooves are larger and deeper along with some cracks and a number of small holes probably due to material loss or open porosity on the coating surface (Fig. 6.12b). A cross-section of the worn surface under the highest load is shown in Fig. 6.12c. Sub-surface lateral cracking with a number of vertical cracks running through the coating and also a large area of porosity can be seen.

### **The Co-I Coating**

The plan view images of the wear scars on the Co-I coating after abrasion with silica 70 at the lowest (19.6 N) and highest (127.5 N) applied load are shown in Fig. 6.13a and 6.13b respectively. Wear scars produced under the both loads exhibited removal of matrix at a higher rate leaving unprotected carbide particles, along with carbide cracking and pullout which are more significant under higher applied load. The cross-sectional image under the highest load (Fig. 6.13c) although revealing no significant sub-surface cracking, shows the carbide grains are standing proud of the matrix indicating preferential wear of the matrix phase. Carbide cracking and voids due to pullout of carbide grains are also evident. Fig. 6.14a and 6.14b show SEM plan view images of the Co-I coating abraded with alumina 60 under 19.6 N and 127.5 N applied load respectively. Two distinct regions, one with a high density of carbide grains and one with a lower density of carbides are apparent under both loads. Fractured carbide grains and voids due to pullout carbide also can be seen. Under the higher load, more voids and cracked carbides can be seen (Fig. 6.14b). Fig. 6.14c shows a cross-sectional image of the

worn surface of the coating under the highest load. This exhibits some small surface pits; however, no sub-surface cracks can be seen.

### **The Co-II Coating**

SEM plan view images of the wear scars on the Co-II coatings following abrasion with silica 70 at the lowest (19.6 N) and the highest (127.5 N) applied loads are shown in Figs. 6.15a and 6.15b respectively. These wear scars exhibit three distinct features: regions with a high density of carbide grains; regions with a low density of carbide grains, and carbide pull out voids which appear as dark regions. At higher load (Fig. 6.15b), cracking of some carbides and a number of furrows due to removal of matrix leaving carbides unprotected can be seen. The cross-sectional image of the wear surface under the highest load (Fig. 6.15c) shows no sub-surface cracks propagating through the coating. Figs. 6.16a and 6.16b show SEM plan view images of the Co-II coating following abrasion with alumina 60 under 19.6 N and 127.5 N loads respectively. Carbide pull out voids and a number of furrows due to removal of matrix can be observed. Under the higher load, cracked carbides and a higher density of voids can be seen. Fig. 6.16c shows a cross-sectional image of the worn surface revealing apparently no sub-surface cracking in the coating.

### **The Co-III Coating**

Figs. 6.17a and 6.17b show the plan view images of the central zone of the wear scars on the Co-III coating after abrasion with silica 70 at the lowest and highest applied loads (19.6 N and 127.5 N) respectively. The wear scars include; regions with a high density of carbide grains, regions with low density of carbide grains

and a small number of voids due to carbide pull out. Moreover, a number of furrows by the sides of carbide grains due to removal of matrix at a higher rate are evident. A BSE cross-sectional image following wear at the highest load (Fig. 6.17c) shows sub-surface cracks propagating through of the bright binder phase. Also, unprotected carbide grains due to preferential wear of the binder are evident at the surface. SEM plan view images of the Co-III coating following abrasion with alumina 60 at the lowest (19.6 N) and highest (127.5 N) applied loads are shown in Figs. 6.18a and 6.18b respectively. The worn surfaces produced by alumina under both applied loads show two distinct regions of high and low density of carbide grains and with a low applied load (Fig. 6.18a), a large number of scratches and some narrow grooves in different directions are visible while at the highest applied load (Fig. 6.18b), wide and deep grooves along the direction of sliding flow are evident. The cross-sectional image of the worn surface under the highest load (Fig. 6.18c) shows sub-surface cracking with cracks running in the bright binder phase region.

## 6.3 Discussion

### 6.3.1 General Observations

The abrasive wear test results of the five coatings exhibited increases in wear rate with applied load when abraded with both silica and alumina sands (Figs. 6.4 and 6.5). There is an exception for wear rate under 127.5N load for some coating cases, where the wear rate unexpectedly reduced. In the DSRW test, both the sample and wheel temperatures increase during testing. The magnitude of these increases under a given test parameters, depend on abrasive type, sample material

and applied load [201]. Increasing the rubber temperature will result in a decrease in its hardness. Accordingly, it may result in a decrease in wear rate as the applied load is increased [63].

The ratio of abrasive particle hardness to coating hardness indicates that for all coatings, the abrasive wear by alumina is “hard” compared to that by silica which is “soft” (Fig. 6.6). For all the coatings and test conditions examined, the wear rate with the silica particle was significantly lower than that by the alumina particle. Low magnification optical microscopy images of all the coatings (Figs. 6.7 and 6.8) also indicate that in all the cases, silica 70 abrasive showed evidence for particle rolling with significant indentation of the surface while with alumina 60 abrasive, grooves along the direction of abrasive flow are apparent. Increasing applied load leads to an increase in the size of indentations and grooves (Figs. 6.7b and 6.8b). The angular nature of the alumina, in comparison with the more rounded silica particles (Fig. 6.1) and its greater hardness are the cause of these very significant differences in wear behaviour for the all coatings.

The results show that the wear rates of the coatings did not necessarily decrease with coating hardness. Figs. 6.19a and 6.19b display the wear rate of the five coatings with silica 70 and alumina 60 abrasives under different applied loads versus the coating hardness respectively. It can be seen that in some cases, coatings with higher hardness also exhibit higher wear rate compared with coatings with lower hardness. This is because of the complicated mechanism of abrasive wear in thermally sprayed cermet coatings and importance of other parameters.

The five coatings can be classified in to two groups of Co and non-Co with distinct characteristics. The coatings in each group have a number of similar properties in the feedstock powder and in the coatings after spraying process. In the starting powders, the WC content is 85 wt% for non-Co coatings compared with 83 wt% for the Co coatings (Table 3.1). Also, the carbide shape in the non-Co group seems to be rounded compared with angular carbide grains in the Co group (Fig. 4.4) and finally, the binder material in the starting powder is a pure metal (cobalt) for Co group whereas in the non-Co group there were two complicated alloys (Hastelloy type C for the Ni and Kanthal for the Fe coating) as binder materials (Table 3.2, see also section 4.2.3). For the coatings, the similar properties in each group are: *i*) low fracture toughness in non-Co coatings and high fracture toughness for the Co coatings (Fig. 6.20), *ii*) high porosity for the non-Co and low porosity for the Co coatings (Fig. 4.11), *iii*) higher amounts of  $W_2C$  and less amorphous phases in the non-Co and lower fractions of  $W_2C$  with more amorphous phases for the Co coatings (Fig. 4.5), *iv*) low mean free path for the non-Co and higher mean free path for the Co coatings (Table 4.9), and *v*) the high volume fractions of the carbide phase for non-Co and lower carbide volume fractions for the Co coatings (Table 4.9). The above data are summarized in Tables 6.3 and 6.4. These significant differences in the material properties of the two groups imply that the comparison of abrasive wear behaviour of the two groups in detail is difficult.

### 6.3.2 Abrasive Wear with Silica

The hardness of silica 70 particles ( $1116 \pm 46 \text{ kgf mm}^{-2}$ ) is lower than all the five coatings examined (Fig. 6.21). This abrasive particle exhibits a rounded

morphology (Fig. 6.1) and a narrow size range (Fig. 6.2). Moreover, as can be seen from Fig. 6.6, the ratios of abrasive hardness  $H_a$  to the hardness of coating surfaces  $H_s$  for all coatings are less than 1.2 indicating “soft wear” regime and, as such, particle blunting is likely during abrasion which will result in a lower rate of wear under three-body (rolling) abrasion mechanism (Fig. 6.7) than might be observed with a harder abrasive particle.

The selective binder phase removal from the near-surface layers seems to be an important step in wear process of composite materials by soft abrasives [93]. Cyclic indenting contact of abrasive particles during three-body abrasion process causes compressive stresses in the surface of coating. The binder is initially compressed out of the surface by these stresses ahead of and to the sides of the indenter. The next stage is probably damage to those WC grains which are in heavily loaded locations because the binder has flowed plastically. The WC grains break into small fragments and are gradually pulled out from the surface. The WC grains which are at the edge of a defect (a crack or an area of surface damage) will experience greater load as the abrasive particles indent than will grains away from the defect. These grains will be the first to be damaged, resulting in growth of the defect. Microcracks form around the pits and propagate through the coating preferentially in the tungsten rich binder phase or along splat boundaries. Elastic-plastic indentation of the abrasant into the coating can also cause sub-surface cracks to form close to surface of the coating resulting in detachment of fragments of the surface material [75]. The BSE cross-section images of the coatings clearly show that generally cracking starts at the end of an empty space resulting from

removal of binder material or carbide grains and then propagates through the coating (e.g., Fig. 6.17c).

From SEM plan view images of wear scars of the all coatings (Figs. 6.9, 6.11, 6.13, 8.15 and 8.17) it can be seen that the metal matrix wears at a higher rate leaving unprotected carbide particles. For the all coatings, removal of matrix can be seen to be more extensive under higher applied load (Figs. 6.13b, 8.15b and 8.17 b) with micro-grooves being formed by the sides of carbide grains and also, a number of fragmented carbide grains and voids due to pulling out of the carbides which are significantly higher for the cobalt coatings. Cross-section images of wear scars show also sub-surface cracking close to the surface (Figs. 6.9c, 6.11c and 6.17c) although this effect for the Co-III is low (Fig. 6.17c) and for the Co-I and Co-II is not significant (Figs. 6.13c and 6.15c). Finally, the wear scar images show that the preferential wear mechanism followed by WC fragmentation and pullout is predominant wear mechanism for the all coatings although, sub-surface cracking has also been observed as a mechanism for removal of materials in some cases (Figs. 6.9c and 6.11c). In these cases the removal of material occurs by both preferential removal matrix phase and sub-surface cracking processes. Pullout of the carbide grains is promoted by preferential wear of the softer phase (matrix) which exposes the already fractured carbides. Carbide cracking in the Co group of coatings was observed following abrasion under both loads especially near the surfaces within the carbide phase and along the splat boundaries whereas in the non-Co group coatings, the sub-surface cracking, induced primarily by elastic contact is the main mechanism of removal of materials.

The abrasive wear results of the Co group and non-Co group coatings showed two distinct wear behaviours with silica particles; the wear resistance for non-cobalt group is considerably higher than that for cobalt group. For the cemented materials, it has been shown that there is a correlation between abrasion resistance and the mean free path in the binder phase between the carbide grains; a short mean free path, due to a high volume fraction of fine carbide grains, gives the highest abrasion resistance [91]. A similar result has been reported for HVOF thermally sprayed WC coatings when abraded using the DSRW test showing the best abrasion resistance among the coatings tested for coating with lowest mean free path [122]. Comparison of the cross-section BSE images (Fig. 4.6) and the measured extent of WC volume fraction, the WC grain size and mean free path for the five coatings (Table 5.10) shows a lower mean free path for the non-Co coatings compared with that for the Co coatings. This considerable difference may be responsible of difference in wear behaviour of these two groups of coatings.

In the Co group coatings, similar wear rates are observed until higher applied loads are reached (Fig. 6.4). In this group, the Co-I coating with largest WC grains and low volume fraction of carbide phase (due to high degree of decomposition during spray process) has a high mean free path. In spite of that, the wear rate of the Co-I coating is lower than that for the Co-II and Co-III probably because of higher degree of its bulk hardness ( $1418 \pm 61 \text{ kgf mm}^{-2}$ ) compared with that for the Co-II ( $1306 \pm 71 \text{ kgf mm}^{-2}$ ) and Co-III ( $1203 \pm 57 \text{ kgf mm}^{-2}$ ) (see Table 4.12). The high hardness of a thermally sprayed composite carbide with relatively low carbide content results from the high hardness of the brittle amorphous phase

formed after spraying. The higher hardness of the binder in abrasion results in its preferential wear to be limited, causing a decrease the wear rate. Lee and Gurland [130] suggested an equation to estimate the hardness of binder phase in cemented WC materials. The following equation is a simplified form of that equation which has been used to estimate binder hardness of thermally sprayed WC coatings [126]:

$$H_C = H_{WC}V_{WC} + H_b(1 - V_{WC}) \quad (6.1)$$

where  $H_C$ ,  $H_{WC}$  and  $H_b$  are the hardnesses of the composite, carbide and binder respectively and  $V_{WC}$  is volume fraction of carbide phase. Assuming that the hardness of the WC phase ( $1800 \text{ kgf mm}^{-2}$ ) is the same for the all materials, the hardness of binder can be calculated to be 1212, 702 and  $629 \text{ kgf mm}^{-2}$  for the Co-I, Co-II and Co-III respectively. These values are an estimate and only useful for comparing the binder hardnesses of materials with similar characteristics; a significantly higher hardness of binder phase is estimated for the Co-I coating.

In the non-Co group, although abrasive wear behaviour of the both Ni and Fe coatings with silica 70 lay in the soft wear regime with low wear rates, the Ni wore more quickly than the Fe coating. The lower mean free path (Table 4.9) and higher hardness (Table 4.12) of the Fe coating compared with those for the Ni coating probably is main reason for this difference.

A comparison of the rate of wear for the five steels (chapter 4) and the five coatings with silica 70 is shown in Fig. 6.22. From Fig. 6.22 it is notable that in general, for all the materials the rate of wear increases as the applied load increases. The wear rates of the steels are observed to be significantly higher than

that for the coatings. There is an exception for wear rate of the C99 steel where the wear rate was the lowest. This was close to the wear rate of the Co-II coating. Fig. 6.22 also indicates that for steels with high wear rates, increasing applied load results in a significant increase in wear rate, whereas for all the coatings and the C99 steel with low wear rates, the effect of applied load on wear rate is less. This is due to different wear mechanisms of the steels and coatings.

### 6.3.3 Abrasive Wear with Alumina

The hardness of alumina 60 particles ( $2103 \pm 25 \text{ kgf mm}^{-2}$ ) is higher than all the five coatings examined (Fig. 6.21). This abrasive particle exhibits an angular morphology (Fig. 6.1b) and a narrow size range (Fig. 6.2). Moreover, as can be seen from Fig. 6.6, the ratios of abrasive hardness  $H_a$  to the hardness of the coating surfaces  $H_s$  for all coatings are more than 1.2 indicating the “hard wear” mechanism. Under hard abrasive conditions, plastic deformation can be caused by abrasive particles; this plastic deformation occurs mostly by plastic ploughing and cutting and followed by some local associated fracture in the more brittle composites [3].

The wear scars on the all coating surfaces produced by alumina abrasive (Figs. 6.10, 6.12, 6.13, 6.16 and 6.18) show grooving, pitting and cutting of the coating surfaces. Cross-sectional images of the wear scars also reveal significant sub-surface cracking for the Ni and Fe coatings (Figs. 6.10c and 6.12c) while for the Co coatings no significant cracking (for the Co-I and Co-II coatings) or a small number of shallow cracks (for the Co-III coating) can be seen (Figs. 6.14c, 6.16c and 6.18c). This latter effect is due to high fracture toughness of the Co coatings

in contrast with low fracture toughness of the non-Co coatings (Fig.6.20). These results imply that two main wear mechanisms are involved in material removal namely plastic deformation and fracture. The passage of the hard and sharp abrasive causes plastic deformation of the surface, resulting in the formation of grooves with material pile up at the groove edges in the first stage. Fatigue of the surface layers most probably occurs through mechanical deformation of those layers and results in a spalling type of failure, while sub-surface material deformation leads to cracking, which propagate into the coating as can be seen for some cases at the second stage (for example see Fig. 6.10c).

In the wear scars from the all coatings abraded with the alumina, two-body abrasion can be clearly observed. The optical microscopy images of the wear scars show grooves with an average width of around 50  $\mu\text{m}$  (Fig. 6.8) while the high magnification BSE images show grooves with average width of about 5  $\mu\text{m}$  (e.g. see Fig. 6.10b). Fig. 6.23 displays profiles of wear tracks across the wear scratch, perpendicular to the wear direction for the Ni coating following wear by alumina 60 under the highest load. The two scales of grooving can be observed in Fig. 6.23b and 6.23c. Since the carbide grain sizes in the five coatings are in the range of 0.4 and 1.1  $\mu\text{m}$  (see Table 5.9), in the first group of grooves (named macro-grooves), the dimension of deformation caused by individual abrasive particle is substantially greater than the size of the carbide grains whereas in the second group (named micro-grooves), the carbide grains are comparable in size with the scale of the abrasion damage or larger. In the first group, the behaviour of coatings against deformation is very much like a homogeneous solid while in the

second, the coatings respond heterogeneously [49]. Fig. 6.24 shows schematic image of these two modes of deformation for cobalt and non-cobalt groups.

In the macro-scale mode, when the coating behaves homogeneously (like a solid material), plastic deformation of the both matrix and carbide phases occurs simultaneously, with macro-grooves being formed parallel to the sliding direction (see Fig. 6.8). The displacement and removal of material in this mode depends on the depth of grooves and consequently the bulk hardness of the coatings. To remove material by abrasion, penetration of abrasives into the material and high enough shear force (parallel to the surface) acting on the penetrating particle are necessary.

In the micro-scale mode, where the coatings respond heterogeneously during abrasion, grooves were formed parallel to the sliding direction in the micro-scale mode for the all coatings (Figs. 6.10, 6.12, 6.14, 6.16 and 6.18). Although wear under both loads is generally by a cutting mode, the obvious clean cutting across the carbide particle and metal matrix together with some cracks, delamination and large grooves are seen in the higher load whilst the lowest load shows less effective cutting (Figs. 8.10 and 8.12). SEM plan view of wear scars for the Co coatings also reveals a number of fragmented carbides and voids resulting from pull out of carbide grains (Fig. 6.25).

Porosity has an important role in formation of grooves and consequent removal of material by the micro-scale mode. In the case of hard abrasive particles moving in between the soft rubber wheel and hard coating surfaces, entrapment of the corner

of an abrasive particle (which is sharp) into the surface pores can occur [123] or coating collapse may take place near the pores [125]. In these cases, a corner of abrasive particle can start to scratch from a deep indentation (Fig. 6.26). Therefore, open surface pores will serve as origins for wear scratches made by individual abrasive particles. However, penetration of abrasive particle into the dense region of coating will be more difficult. Thus, a bigger portion of pores leads to more grooves and results in a higher wear rate. Formation of grooves in the Fe coating (Figs. 6.12b) with much smaller width than the actual abrasive particle size (average groove width 5  $\mu\text{m}$ , median abrasive particle size 368  $\mu\text{m}$ ) provides evidence of the suggested mechanism which is based on entrapment of a corner of abrasive particle into the surface open porosities. Table 5.11 shows the porosity percentage of the coatings measured by the image analysis software (Image J 1.41) on the BSE cross-sectional images, indicating higher porosity for the non-cobalt coatings compared with that for the cobalt coatings. Higher porosity leads to more grooves which are apparent in Figs. 6.10b and 6.12.b for the Ni and Fe coatings respectively. Fig. 6.27 shows measured profiles of wear tracks with alumina under the highest applied load across the wear track for all coatings indicating that the Fe coating with the highest magnitude of porosity has the highest number of deep grooves. Higher loads cause an increase in both the number of grooves emanating from porosity and also depth of those grooves.

In the second stage of the wear, fracture is the predominant source of material degradation. At the first stage of wear when a sharp particle embeds into the surface and slides, a plastic groove forms. The penetration of the surface by the abrasive particles is observed to be different for each coating. Lateral cracks grow

upwards to the free surface from base of the surface indented region, driven by the residual stresses associated with the deformation. SEM cross-sectional images of the wear scars for the coatings (except the Co-I and Co-II) along the direction of abrasive flow reveal that sub-surface cracks propagate parallel to the coating top surface, through the coatings (Figs. 6.10c, 6.12c and 6.18c). In the Ni and Fe coatings with low fracture toughness, BSE micrographs of cross-sections of wear scars with alumina particles show a number of vertical cracks along with the horizontal cracks. As seen in Figs. 6.10c and 8.12c, two types of cracks are formed: lateral cracks parallel to the surface, and median cracks perpendicular to the surface. Stewart et al. [75] argued that formation of the vertical cracks is the initial stage of the material loss procedure and is caused by the indentation of the abrasant into the coating. These cracks run down through the coating and end when they reach either a region of tungsten-rich binder phase or a splat boundary. Immediately after, they propagate parallel to the coating surface until they find a path that leads back to the surface. Generally this process results in a high material removal rate in the coatings with low fracture toughness. Fig. 6.20 presents the median fracture toughness of the coatings showing significantly higher value of the toughness for the Co group coatings compared with the non-Co coatings while in each group the magnitude of the toughness is nearly the same. Therefore, it seems that at the second stage of wear, the fracture mechanism has a significant role in wear of the non-cobalt coatings in contrast with the cobalt coatings.

Although plastic deformation and fracture are the primary material removal mechanisms with alumina abrasive, the wear mechanisms for the all coatings are

not the same. Since the hardness of the alumina particles is higher than that all of the coatings, plastic deformation is the dominant wear mechanism in the first stage of abrasion. Under two-body abrasion (when abrasive particles temporarily embedded in the rubber wheel), ploughing and grooving marks appear. The depth of the grooves depends on the bulk hardness of the coating. At this stage, the penetration degree of abrasive into the coating is important. For the Co group of coatings, wear was observed to involve plastic deformation of the surface along with fracture of large carbide grains and carbide skeleton. The material loss is caused by the material displaced from the grooves and pullout of small carbide grains or fragments of larger fractured carbide grains. For the non-Co group of coatings, wear was observed to be plastic deformation followed by sub-surface cracking. In the first stage of wear, the higher porosity of the coatings has an important role in creating more grooves and consequently more material removal. The second stage of wear is the formation of sub-surface cracks followed by delamination of the surface layers. In this stage, fracture toughness of coating is much more important. For the Ni and Fe coatings, the low fracture toughness results in a high rate of material removal. While the bulk hardness controls wear rate in the first stage, the fracture toughness has significant role in the final stage of the wear.

In this work, the wear rate of the Co-I coating with highest level of decomposition and the largest carbide grain size is minimum. This is due to its high hardness, high fracture toughness and low porosity. There is no evidence of cracking in the BS cross-section of the coating indicating that no fracture mechanism has operated for this coating. Moreover, the high hardness of coating causes a

decrease in the rate of wear under the first stage of abrasion. The low porosity also protects the coating surface from grooving.

The characterisations of the Co-II coating are similar to those in the Co-I with a slight decrease in the hardness and increase in the fracture toughness. The prediction is for higher material removal during plastic deformation in the first stage of wear in comparison with the Co-I coating due to the lower hardness.

The Co-III, despite exhibiting high fracture toughness and a low degree of porosity has the highest wear rate by a large factor. This high wear rate can be associated with the very low hardness of this coating. Fig. 6.28 shows the optical microscopy plan view images of wear scars of the all coatings following abrasive wear with alumina 60. From Fig. 6.28e and also from SEM images of the wear scar (Fig. 6.18) along with profile of the wear tracks (Fig. 6.27), it can be seen that the worn surface of the Co-III with alumina is characterized by a huge number of deep parallel grooves, which are formed as the abrasive particles plough across the surface and eventually remove or push material into ridges along the sides of the grooves.

For the Ni coating, the low hardness results in wear in the first stage and the low fracture toughness results in a high rate of wear in the second stage. High porosity causes an increase in the wear rate at the first stage. In spite of the similar hardness in the Ni ( $1255 \pm 38$ ) and Co-III ( $1203 \pm 57$ ) coatings, their wear rates were very different; the wear rate of the Co-III under 127.5 N load is approximately four times more than that of the Ni coating. Due to high porosity of

the Ni, the measured microhardness is less than its real hardness. Therefore, the real resistance of the Ni coating to deformation during first stage of wear is significantly more than that in the Co-III coating.

The Fe coating, despite its high hardness, has much higher level of porosity and low fracture toughness which results in a large number of grooves in the first stage and a high level of cracking in the second stage and consequently higher wear rate.

In summary, the angular nature of the alumina and its greater hardness in comparison with the more rounded silica particles result in significant differences in wear behaviour for the all coatings. The five coatings can be categorized in to two groups of Co and non-Co with distinct characteristics. With silica particles, the wear resistance for non-cobalt group is considerably higher than that for cobalt group. A considerable lower mean free path for the non-Co coatings compared with that for the Co coatings may be responsible of difference in wear behaviour of these two groups of coatings. The wear scars of the all coatings with alumina show two-body abrasion in two micro and macro-scales. The wear results with alumina also imply that two main wear mechanisms are involved in material removal namely plastic deformation and fracture, thus while the bulk hardness control wear rate in the first stage, the fracture toughness has significant role in the final stage of the wear. Porosity has also an important role in formation of grooves and consequent removal of material by the micro-scale mode. In comparison with the Co coatings, the higher porosity and low fracture toughness

of non-Co coatings are generally the cause of their high material removals during the two wear stages.

**Table 6.1** Result of abrasive wear test for the five coatings.

Coating	Abrasive	Load (N)	Total distance (m)	Total mass loss (mg)	Wear rate (mg m <sup>-1</sup> )
Ni	Silica 70	19.6	2721.6	23	0.007
		49	2721.6	34	0.0107
		98	2721.6	52	0.0158
		127.5	2721.6	50	0.0129
	Alumina 60	19.6	2721.6	136	0.0423
		49	2721.6	188	0.0568
		98	2721.6	229	0.0698
		127.5	2721.6	202	0.0573
Fe	Silica 70	19.6	2695.2	19	0.0069
		49	2674.8	28	0.0088
		98	2674.8	49	0.0116
		127.5	2695.2	45	0.0104
	Alumina 60	19.6	2674.8	117	0.0374
		49	2674.8	201	0.0573
		98	2674.8	277	0.0804
		127.5	2674.8	256	0.0815
Co-I	Silica 70	19.6	2695.2	30	0.0091
		49	2674.8	66	0.0217
		98	2674.8	122	0.0327
		127.5	2721.6	85	0.0239
	Alumina 60	19.6	2674.8	78	0.0245
		49	2674.8	112	0.0348
		98	2674.8	153	0.0404
		127.5	2674.8	143	0.0417
Co-II	Silica 70	19.6	1314	18	0.0114
		49	1314	32	0.0209
		98	1314	70	0.0449
		127.5	1314	80	0.0449
	Alumina 60	19.6	2628	102	0.0339
		49	2628	168	0.054
		98	2628	175	0.0546
		127.5	2628	167	0.0512
Co-III	Silica 70	19.6	1314	26	0.016
		49	1314	33	0.0228
		98	1314	55	0.035
		127.5	1314	67	0.0415
	Alumina 60	19.6	2102.4	150	0.0628
		49	1314	216	0.1484
		98	1314	276	0.1865
		127.5	1314	281	0.191

**Table 6.2** General comparison of the non-Co and Co powder characterisations.

<b>Powder characterisation</b>	<b>Non-Co</b>	<b>Co</b>	<b>Ref.</b>
WC content	85 wt%	83 wt%	Table 3.1
WC shape	Rounded	Angular	Fig. 4.4
Binder material	Alloy	Pure metal	Table 3.2

**Table 6.3** General comparison of the non-Co and Co coatings properties.

<b>Coating property</b>	<b>Non-Co</b>	<b>Co</b>	<b>Ref.</b>
Fracture toughness	Low	High	Fig. 6.25
Porosity	High	Low	Fig. 4.11
W <sub>2</sub> C phase	High	Low	Fig. 4.5
Mean free path	Low	High	Table 4.9
WC content	High	Low	Table 4.9

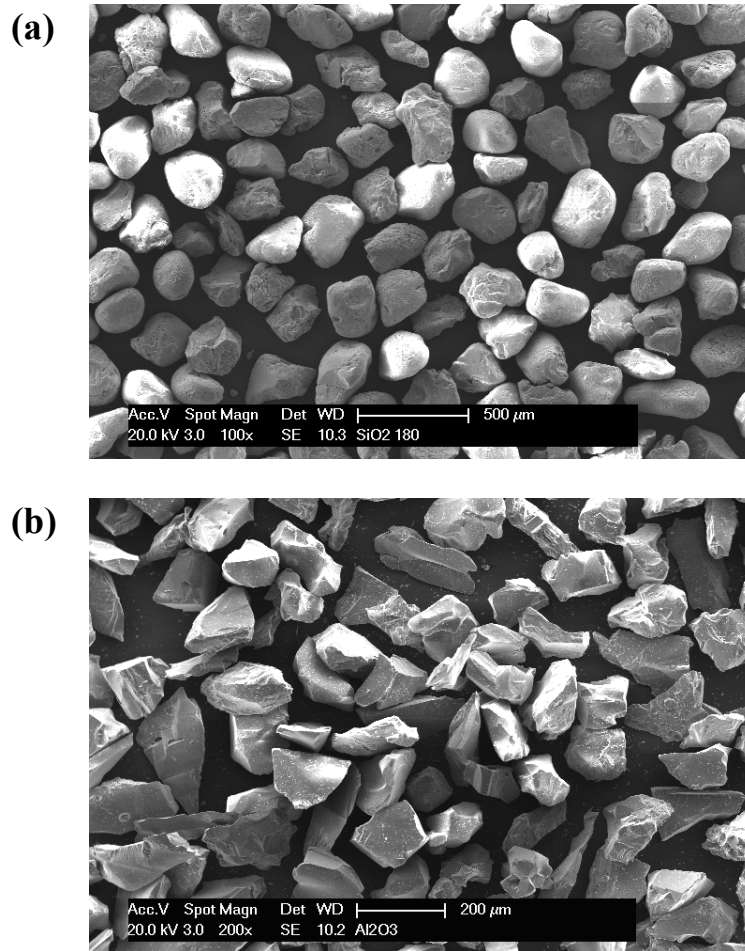


Fig. 6.1 SEM micrograph of (a) silica 70 and (b) alumina 60 abrasive particles.

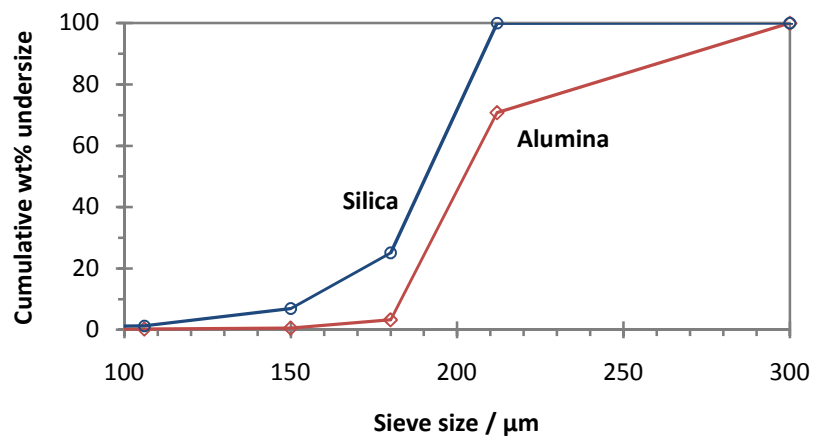
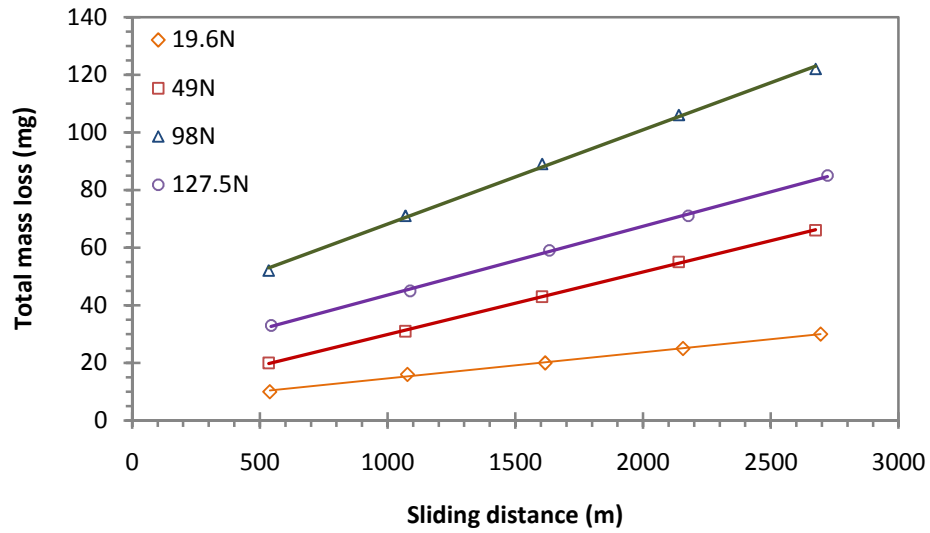
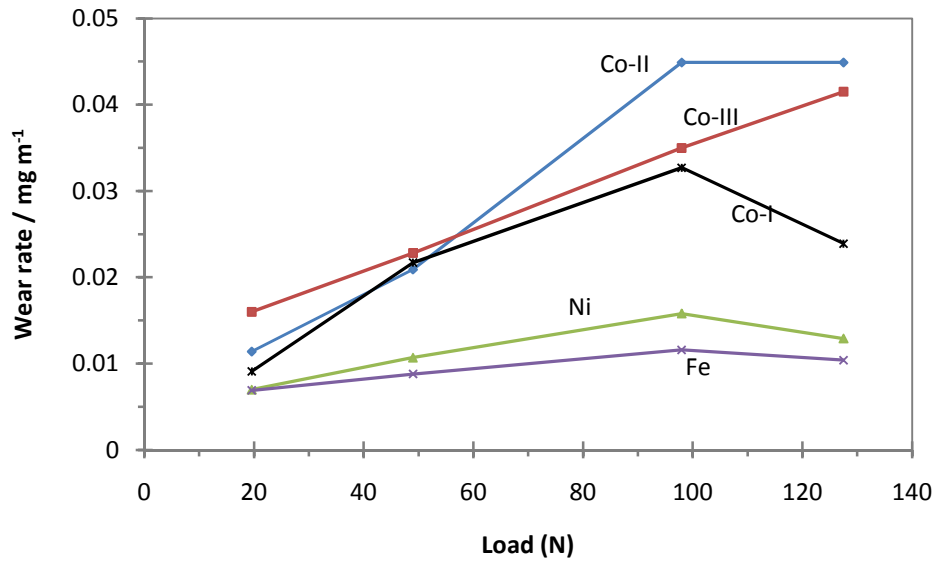


Fig. 6.2 Size distribution results for silica70 and alumina 60 particles.



**Fig. 6.3** Mass loss of the Co-I coating as a function of distance with silica 70 under different applied loads.



**Fig. 6.4** Wear rates of the coatings with silica 70 as a function of applied load.

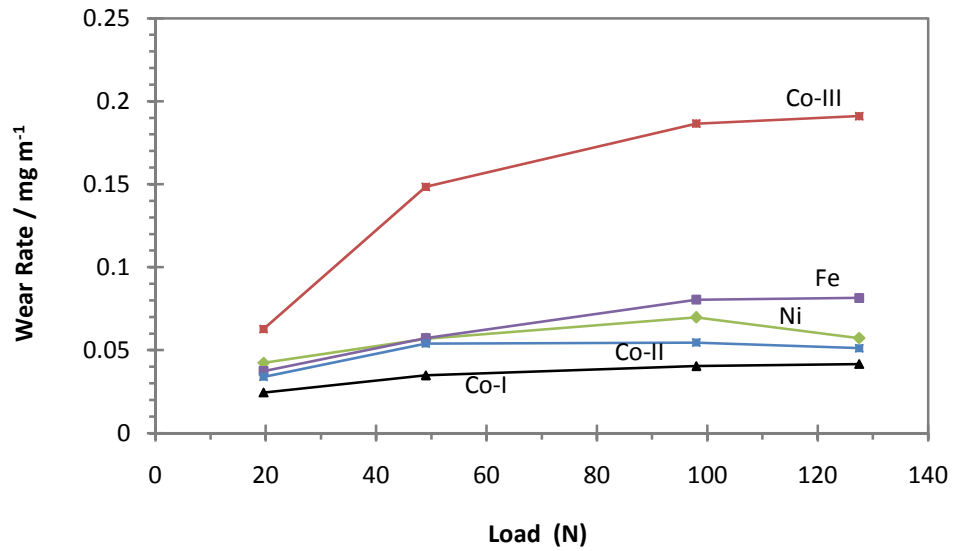


Fig. 6.5 Wear rates of the coatings with alumina 60 as a function of applied load.

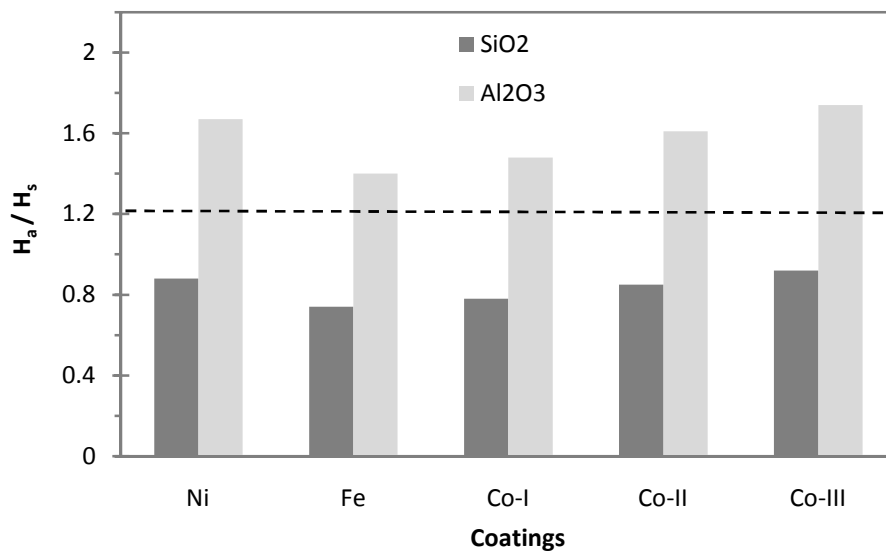
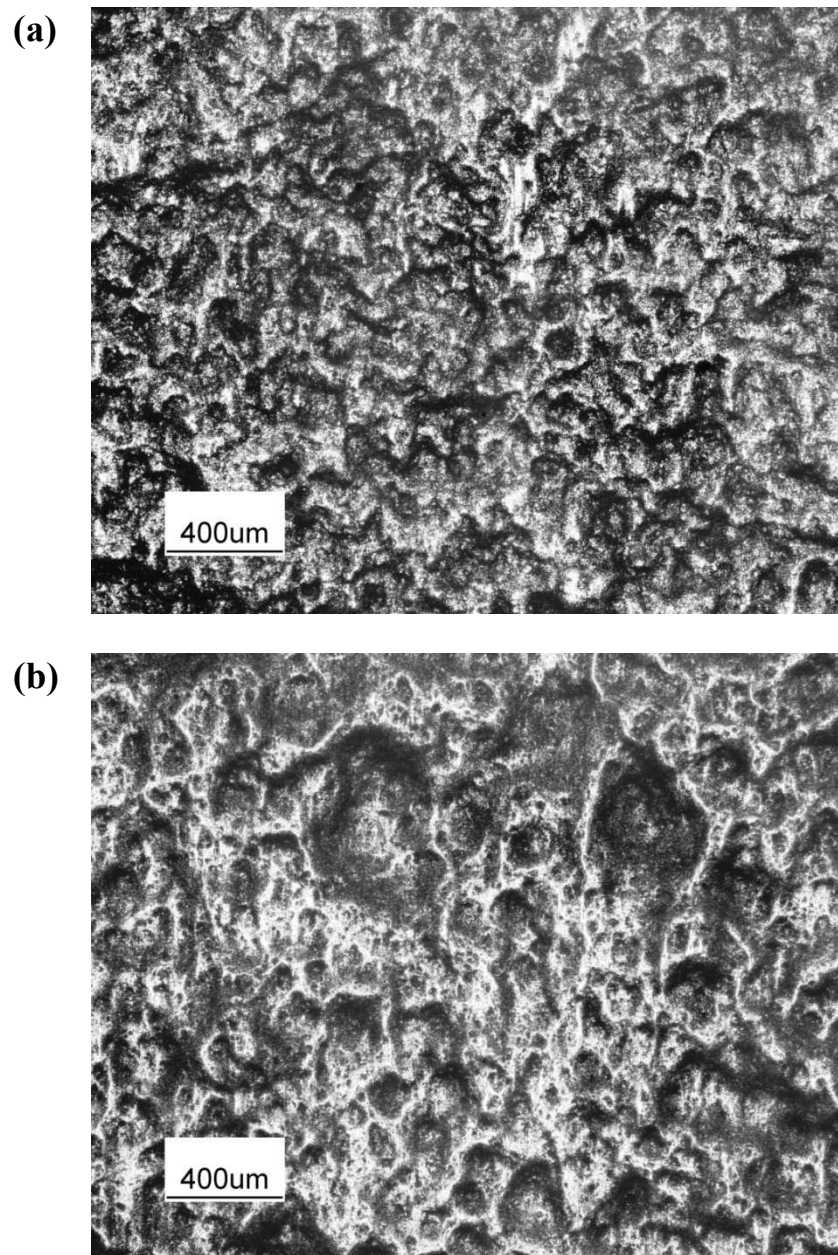
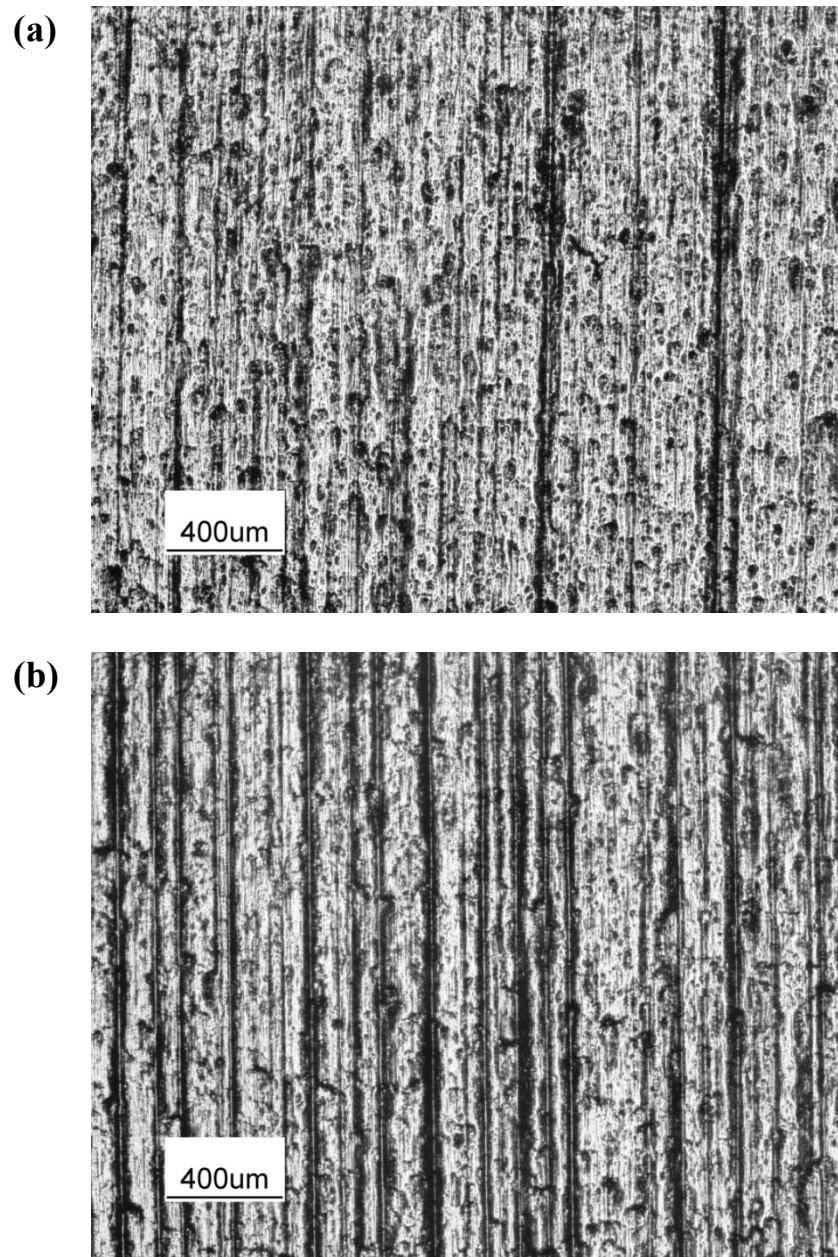


Fig. 6.6 Plot showing transition between “hard” and “soft” wear mechanisms ( $\frac{H_a}{H_s} = 1.2$ ) for the coatings with silica 70 and alumina 60 abrasives.



**Fig. 6.7** Optical microscopy plan view images of wear scars of the Fe coating following abrasive wear test by silica 70 at (a) the lowest load (19.6N) and (b) highest load (127.5N).



**Fig. 6.8** Optic Microscopy plan view images of wear scars of the Fe coating following abrasive wear test by alumina 60at (a) the lowest load (19.6N) and (b) highest load (127.5N).

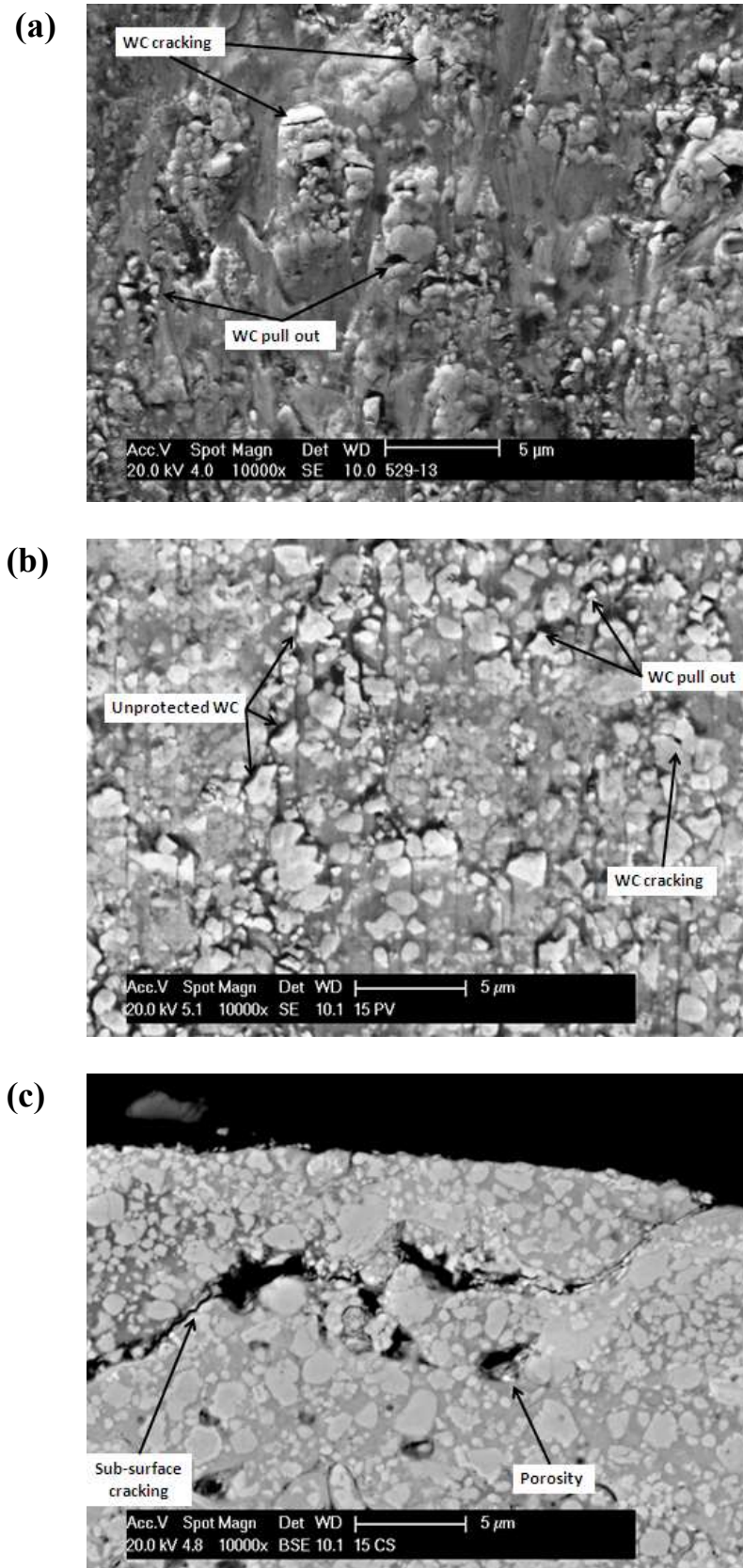


**Fig. 6.9** SEM images of the Ni coating surface following abrasive wear test by silica 70 showing (a) plan view image at the lowest load (19.6N), (b) plan view image at the highest load (127.5N) and (c) cross-sectional image at the highest load.

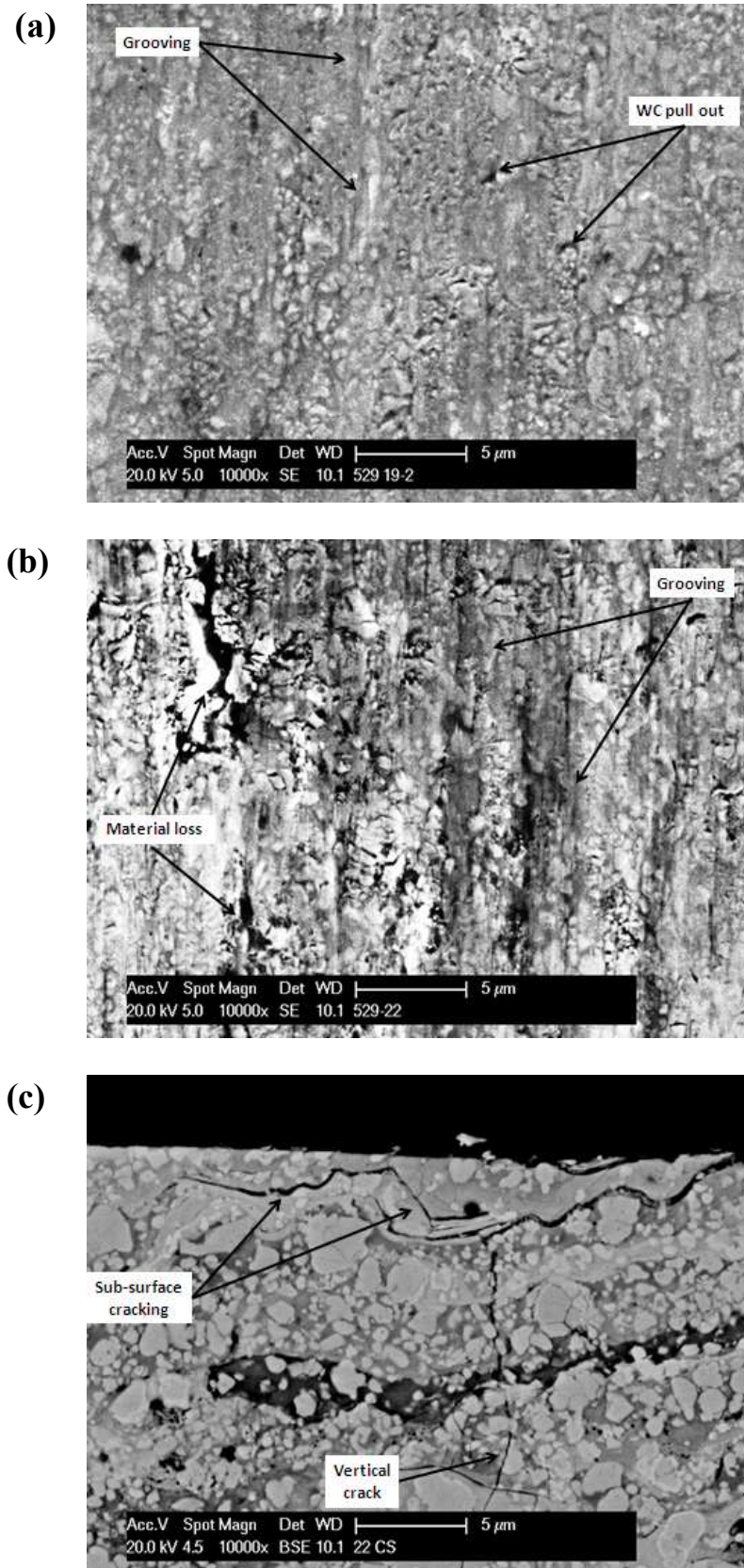


**Fig. 6.10** SEM images of the Ni coating surface following abrasive wear test by alumina 60 showing (a) plan view image at the lowest load (19.6N), (b) plan view image at the highest load (127.5N) and (c) cross-sectional image at the highest load.

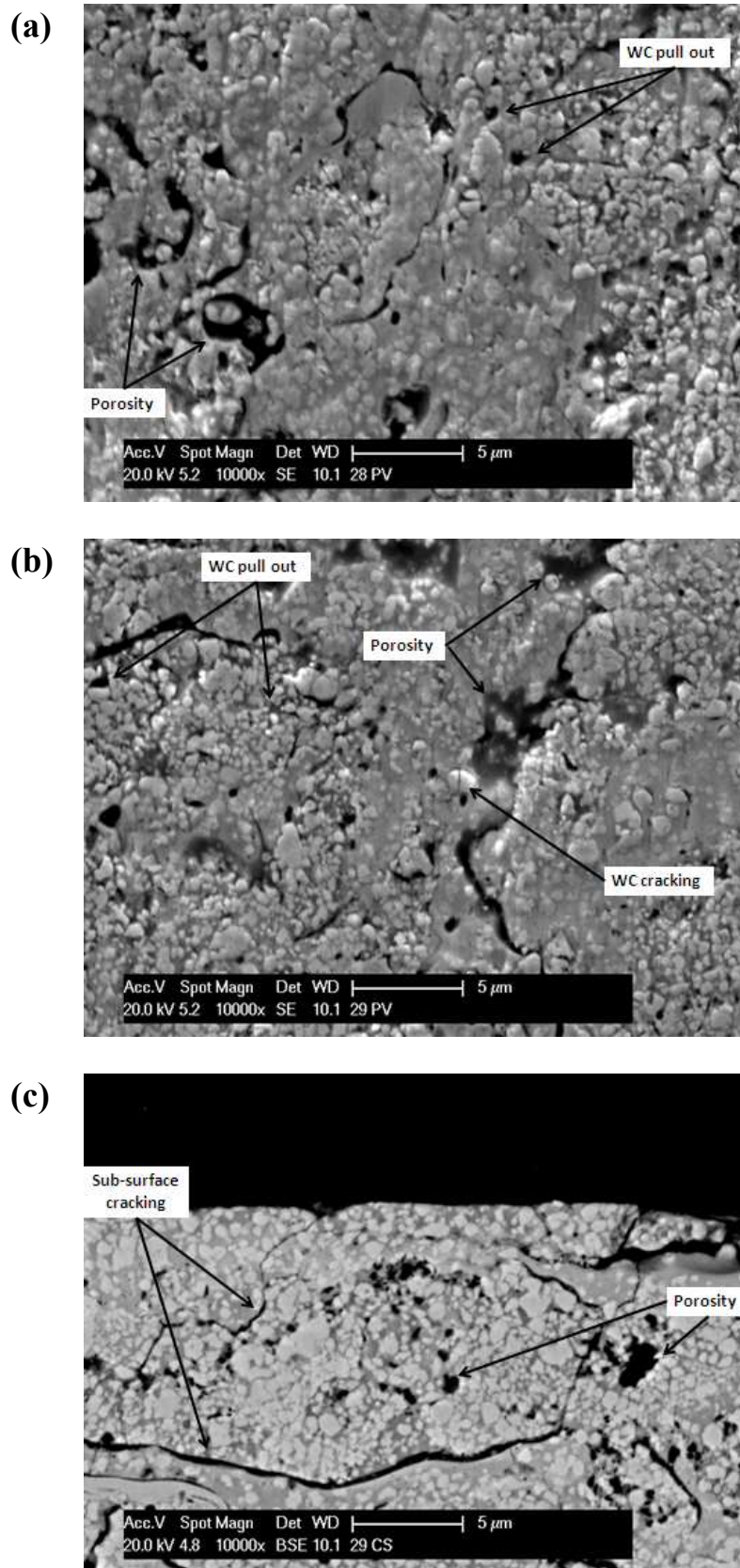


**Fig. 6.11** SEM images of the Fe coating surface following abrasive wear test by silica 70 showing (a) plan view image at the lowest load (19.6N), (b) plan view image at the highest load (127.5N) and (c) cross-sectional image at the highest load.

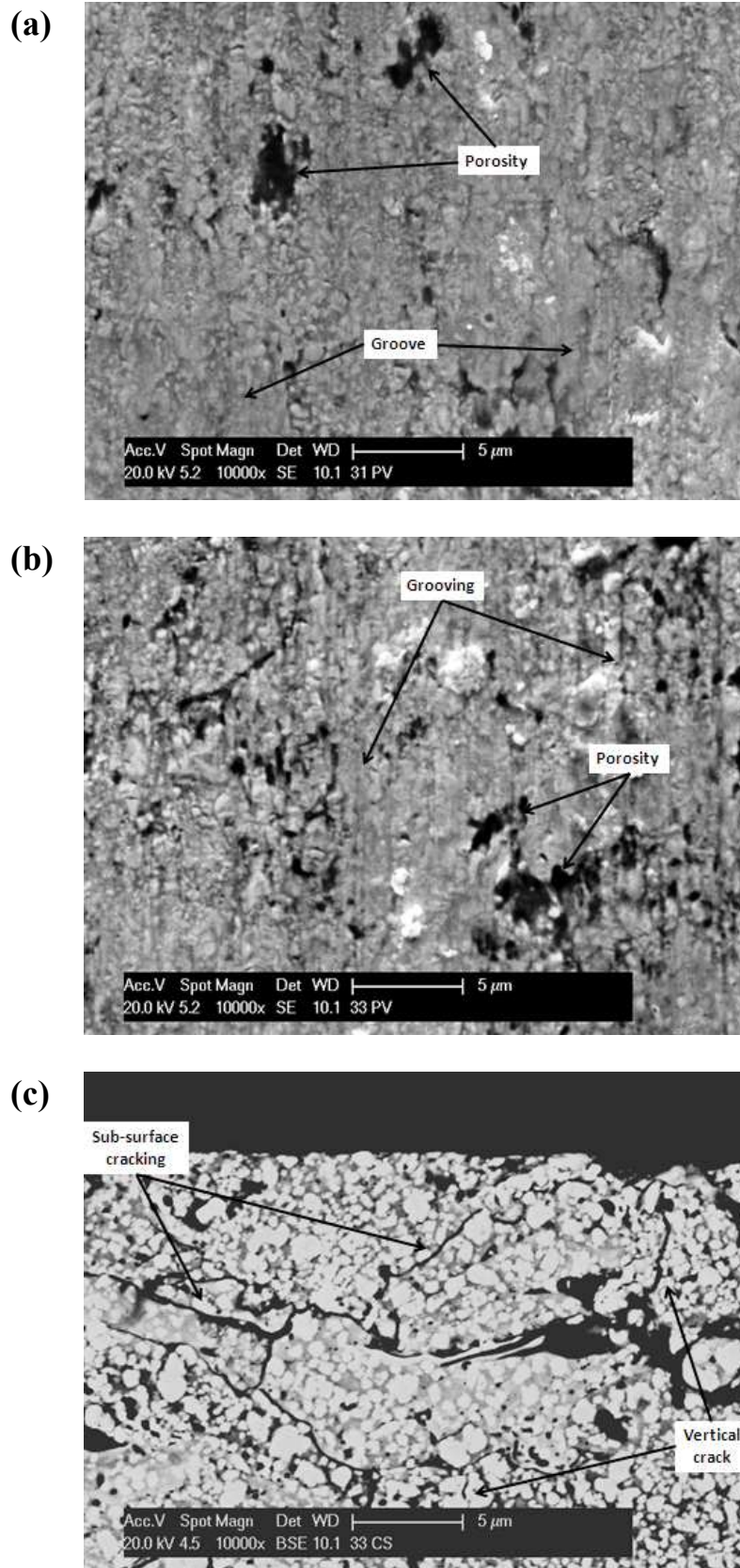


**Fig. 6.12** SEM images of the Fe coating surface following abrasive wear test by alumina 60 showing (a) plan view image at the lowest load (19.6N), (b) plan view image at the highest load (127.5N) and (c) cross-sectional image at the highest load.

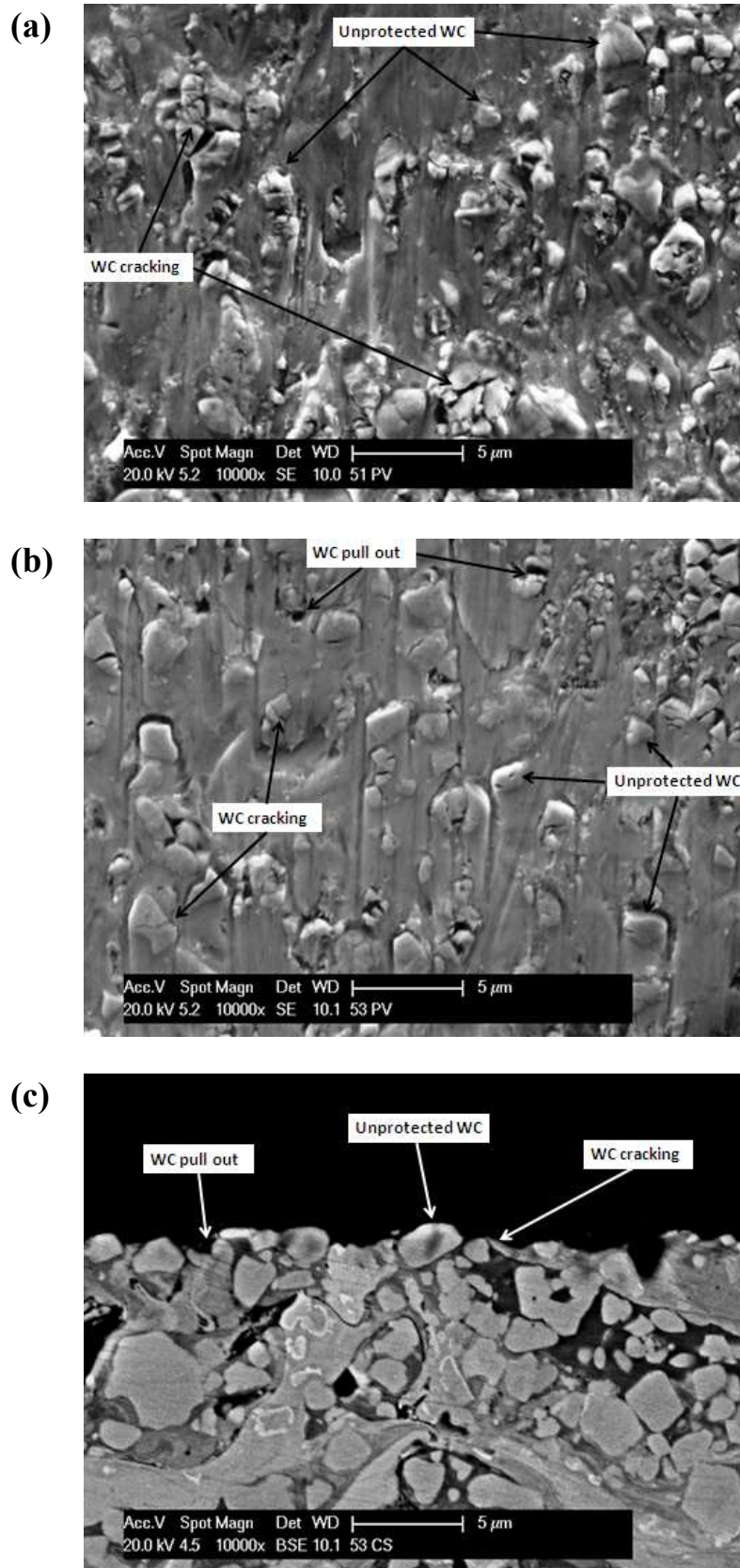


**Fig. 6.13** SEM images of the Co-I coating surface following abrasive wear test by silica 70 showing (a) plan view image at the lowest load (19.6N), (b) plan view image at the highest load (127.5N) and (c) cross-sectional image at the highest load.

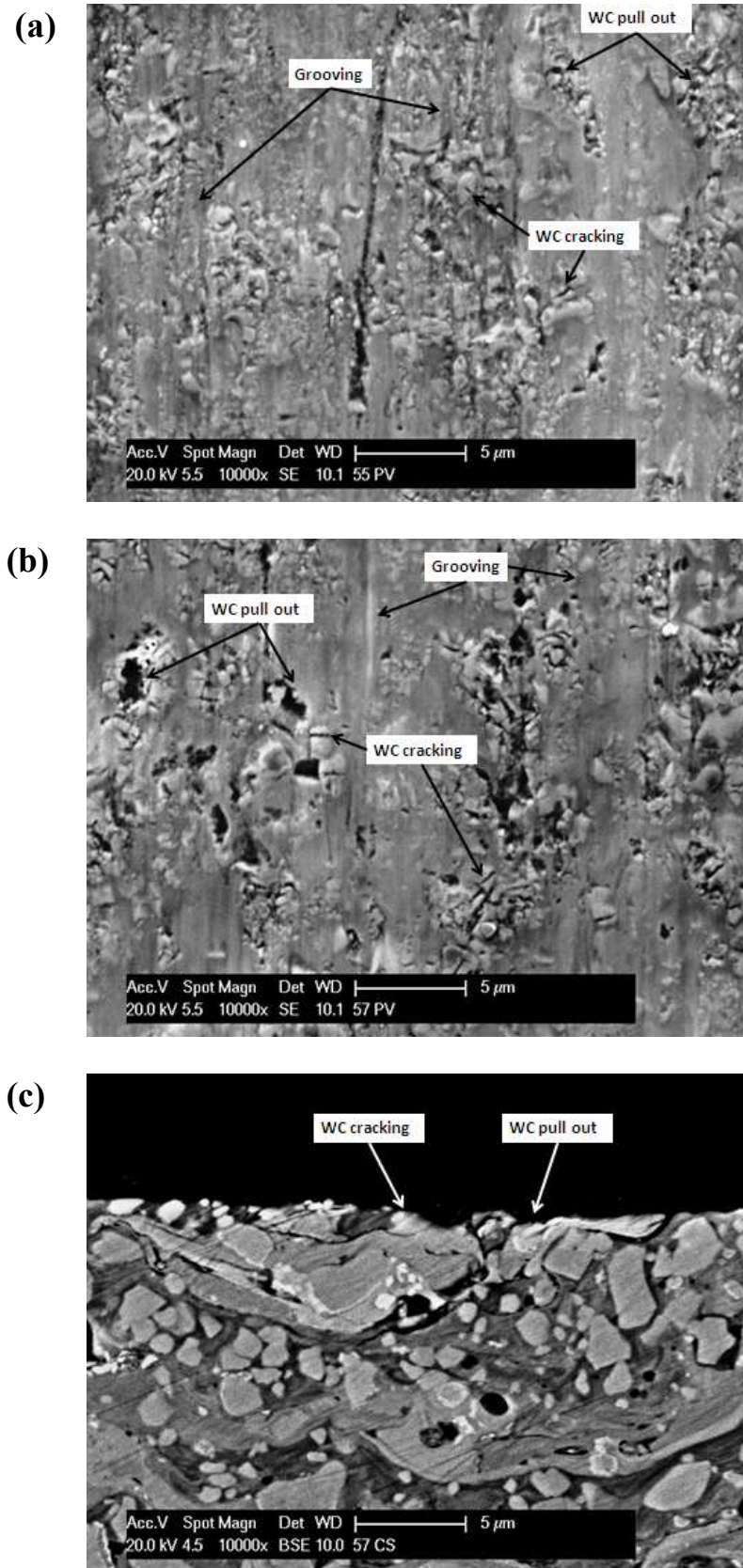


**Fig. 6.14** SEM images of the Co-I coating surface after abrasive wear test by alumina 60 showing (a) plan view image at the lowest load (19.6N), (b) plan view image at the highest load (127.5N) and (c) cross-sectional image at the highest load.

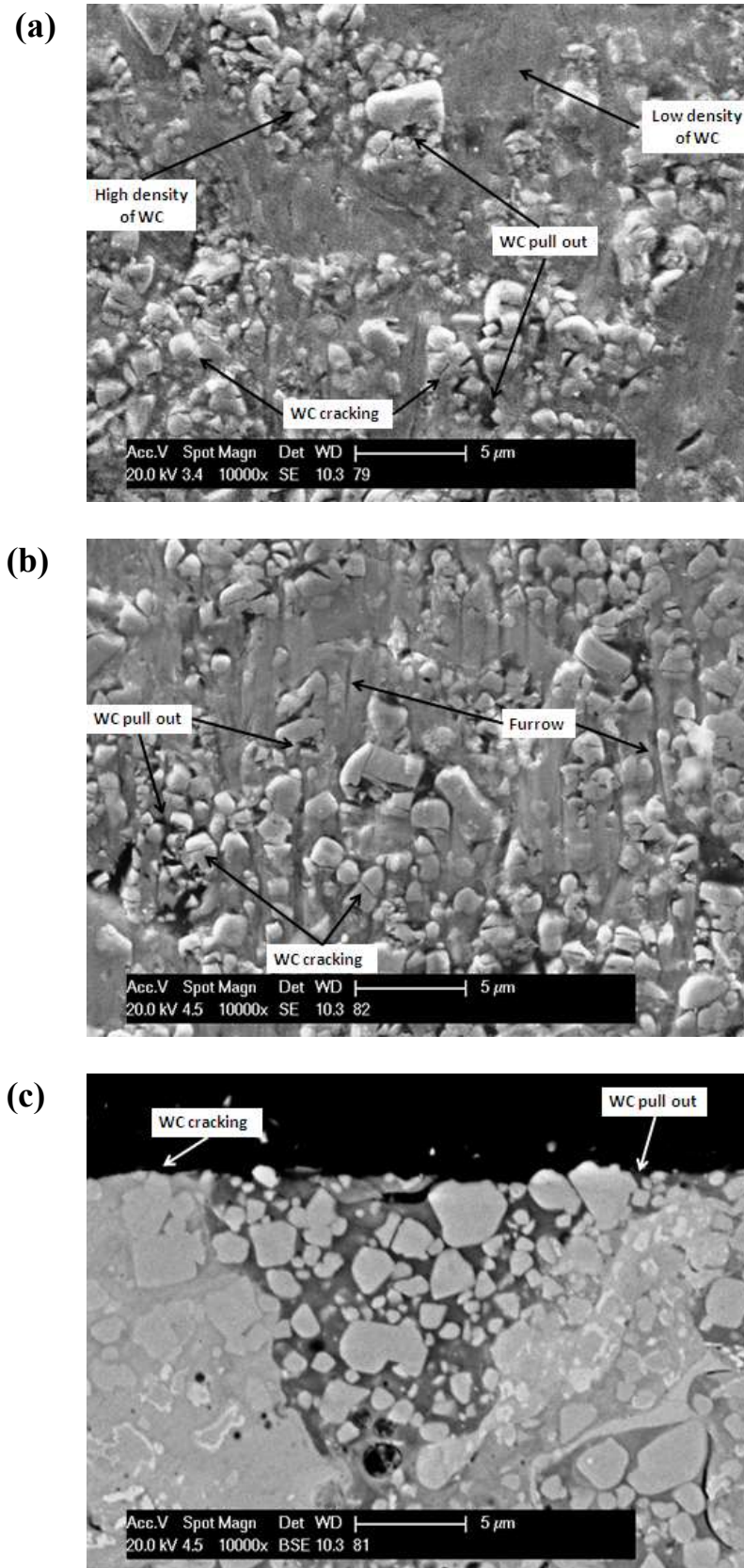


**Fig. 6.15** SEM images of the Co-II coating surface following abrasive wear test by silica 70 showing (a) plan view image at the lowest load (19.6N), (b) plan view image at the highest load (127.5N) and (c) cross-sectional image at the highest load.

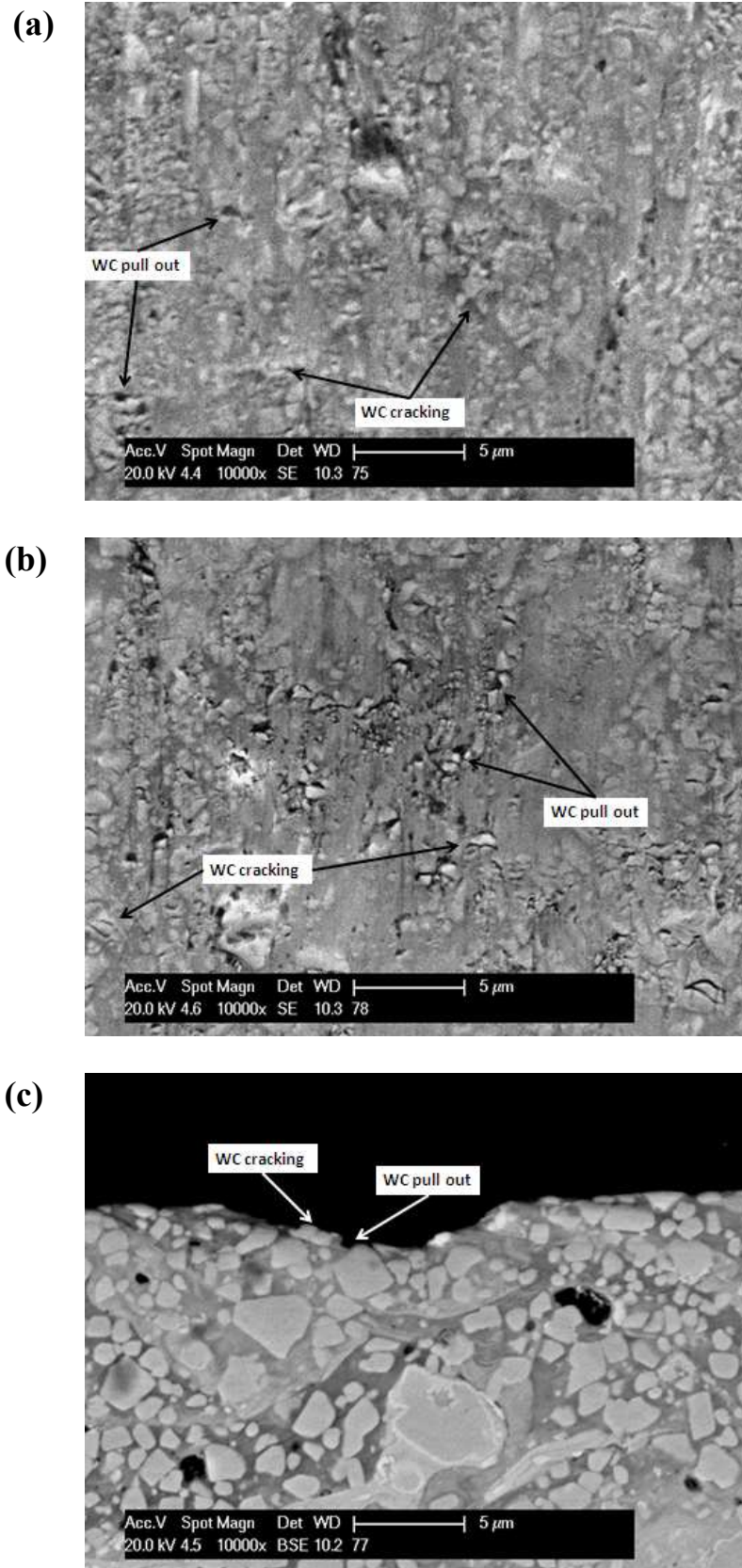


**Fig. 6.16** SEM images of the Co-II coating surface after abrasive wear test by alumina 60 showing (a) plan view image at the lowest load (19.6N), (b) plan view image at the highest load (127.5N) and (c) cross-sectional image at the highest load.

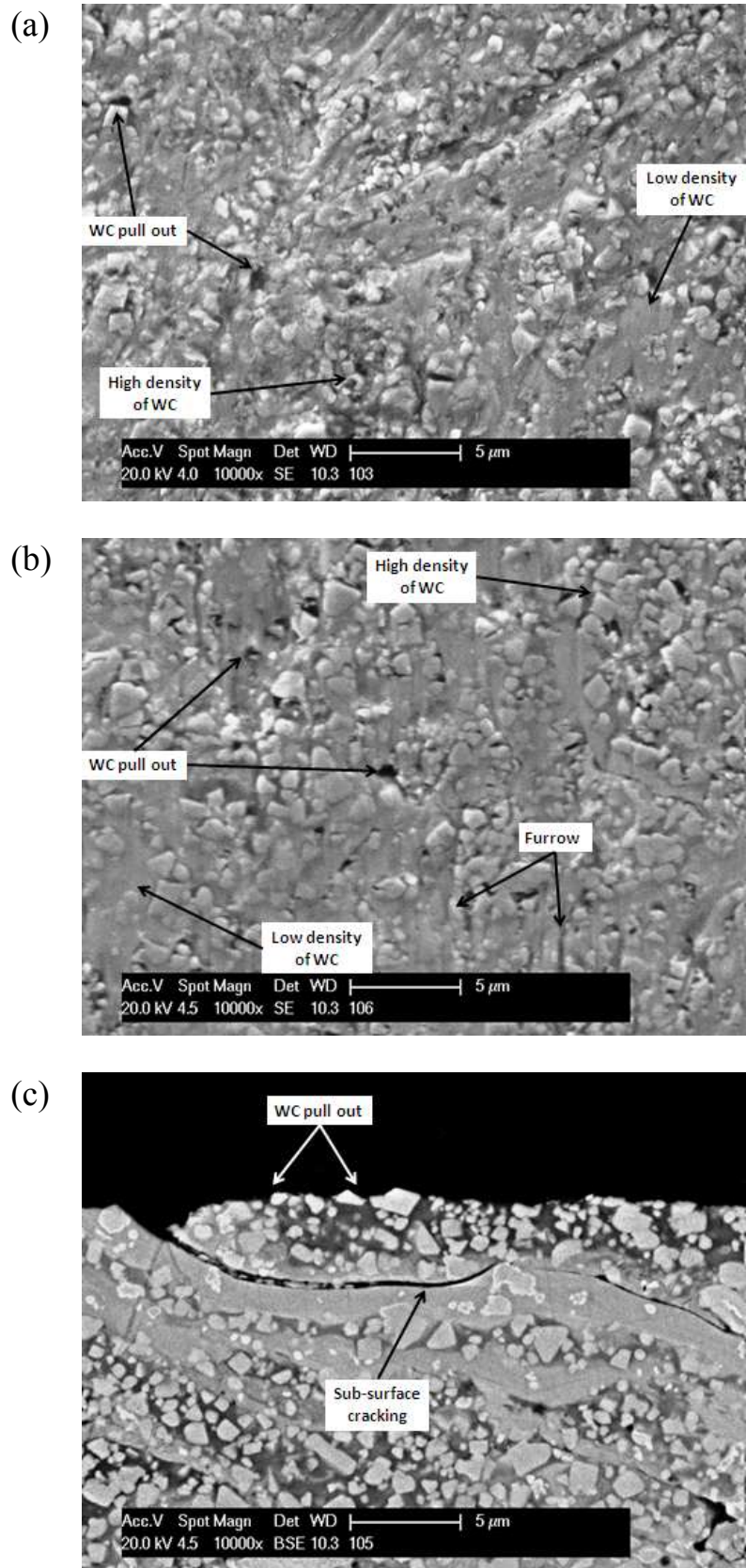


**Fig. 6.17** SEM images of the Co-III coating surface following abrasive wear test by silica 180-250μm showing (a) plan view image at the lowest load (19.6N), (b) plan view image at the highest load (127.5N) and (c) cross-sectional image at the highest load.

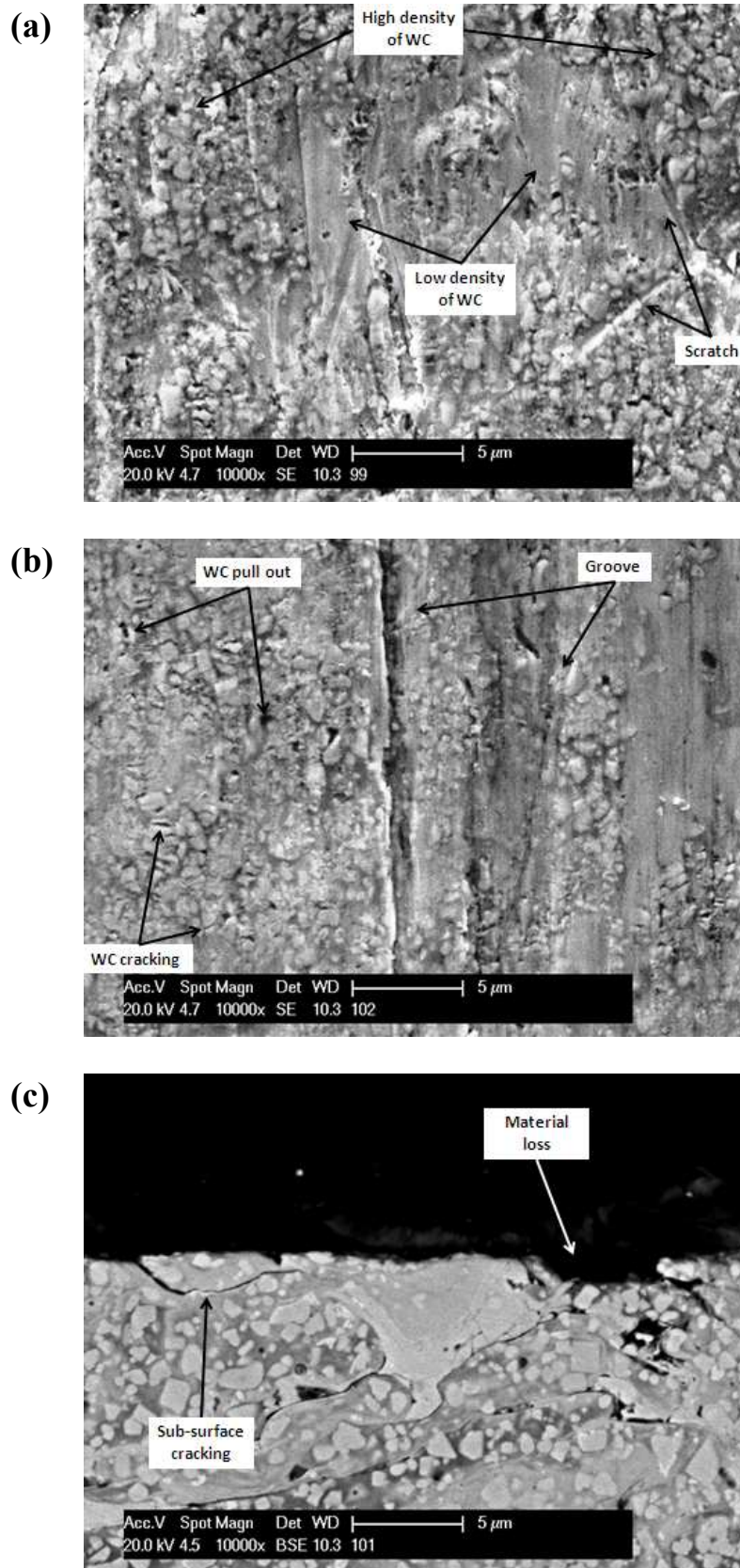


**Fig. 6.18** SEM images of the Co-III coating surface after abrasive wear test by alumina 60 showing (a) plan view image at the lowest load (19.6N), (b) plan view image at the highest load (127.5N) and (c) cross-sectional image at the highest load.

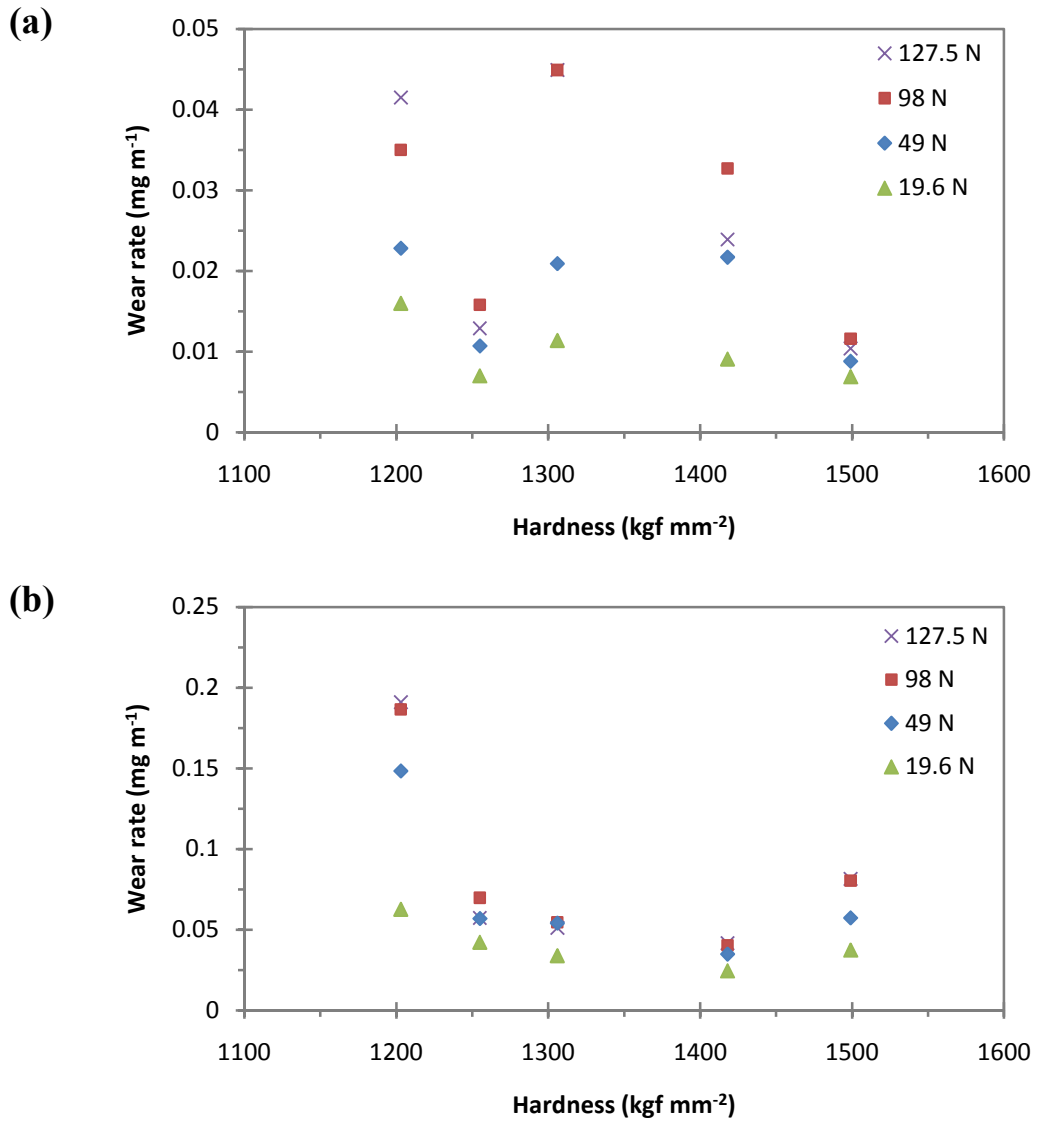


**Fig. 6.19** Wear rate of the coatings with (a) silica 70 and (b) alumina 60 under different applied loads as a function of the coating hardnesses.

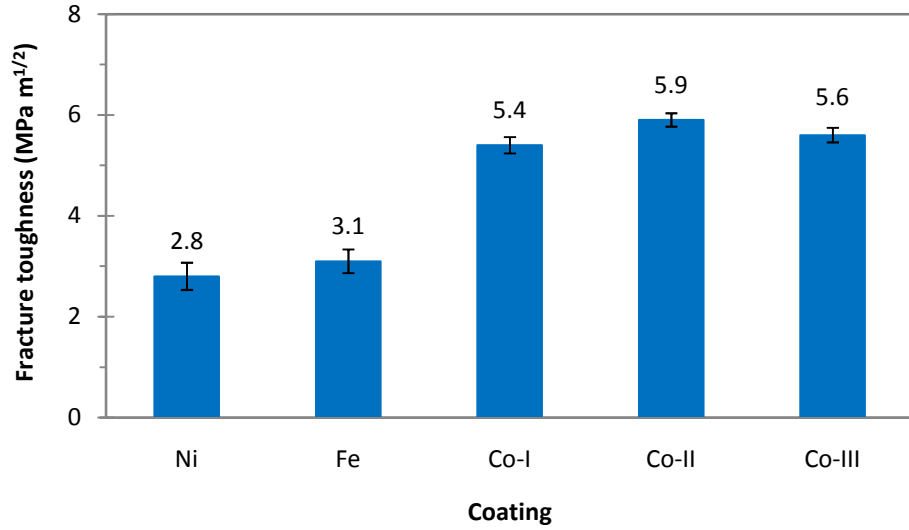


**Fig. 6.20** Fracture toughness of the coatings.

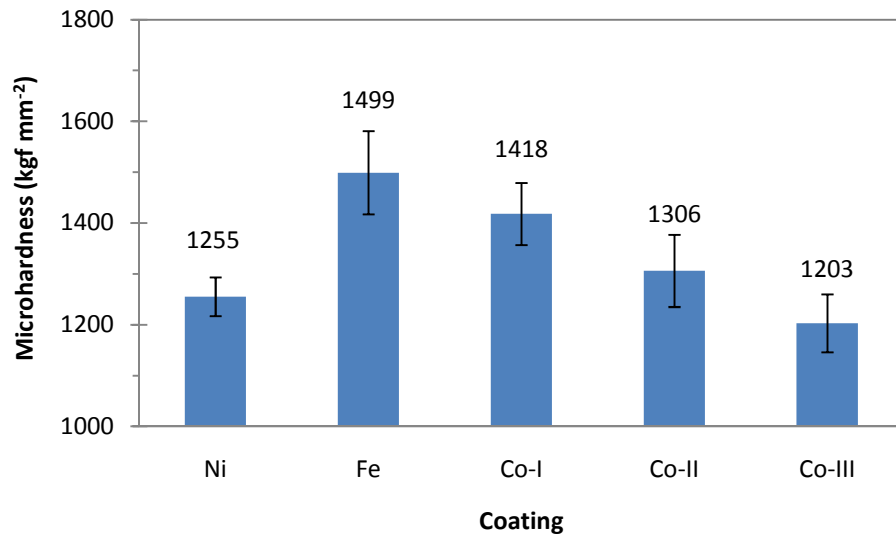


**Fig. 6.21** Microhardness of the sprayed coatings.

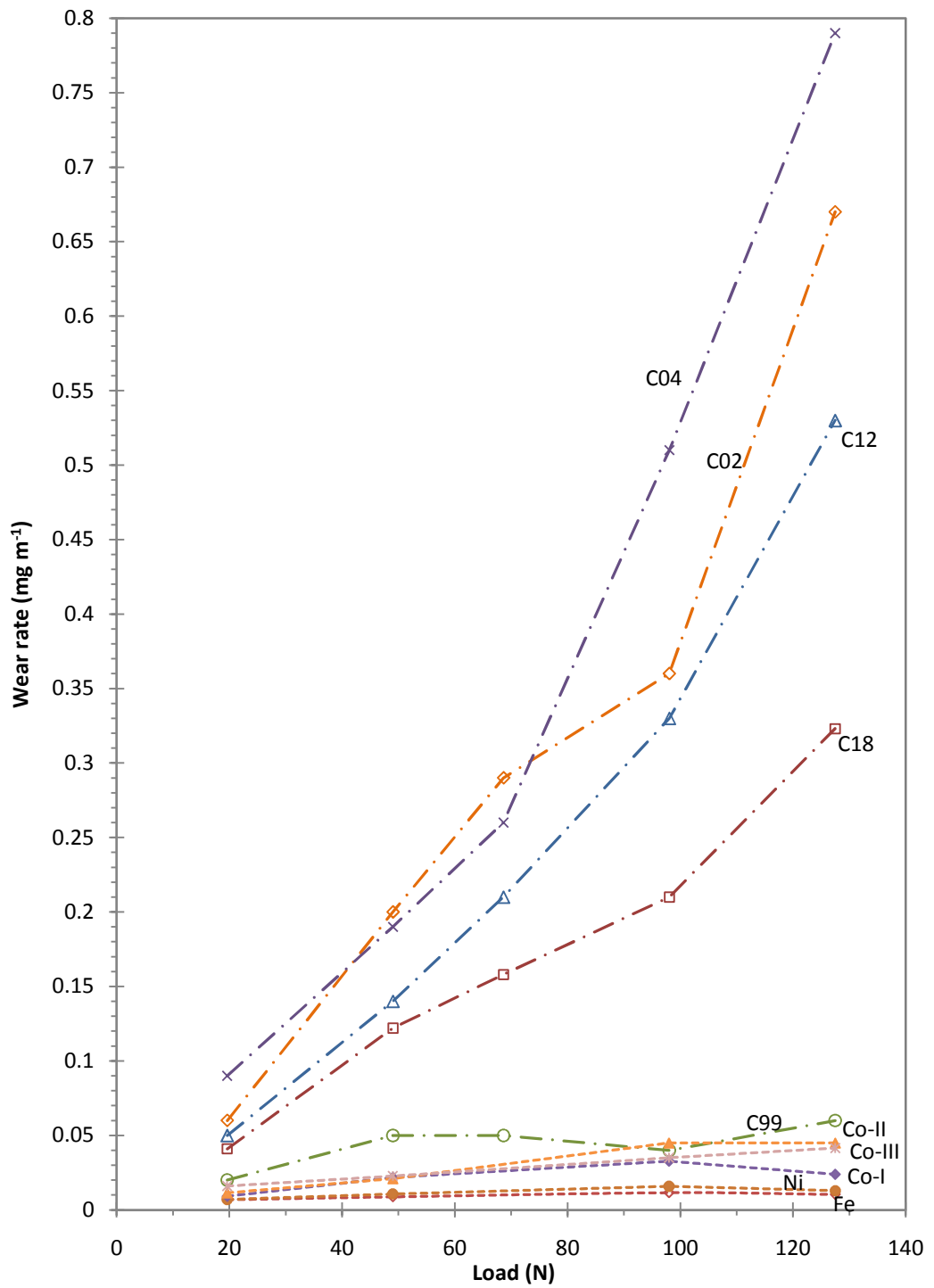


**Fig. 6.22** Comparison of the rate of wear for the five steels and the five coatings with silica 70.

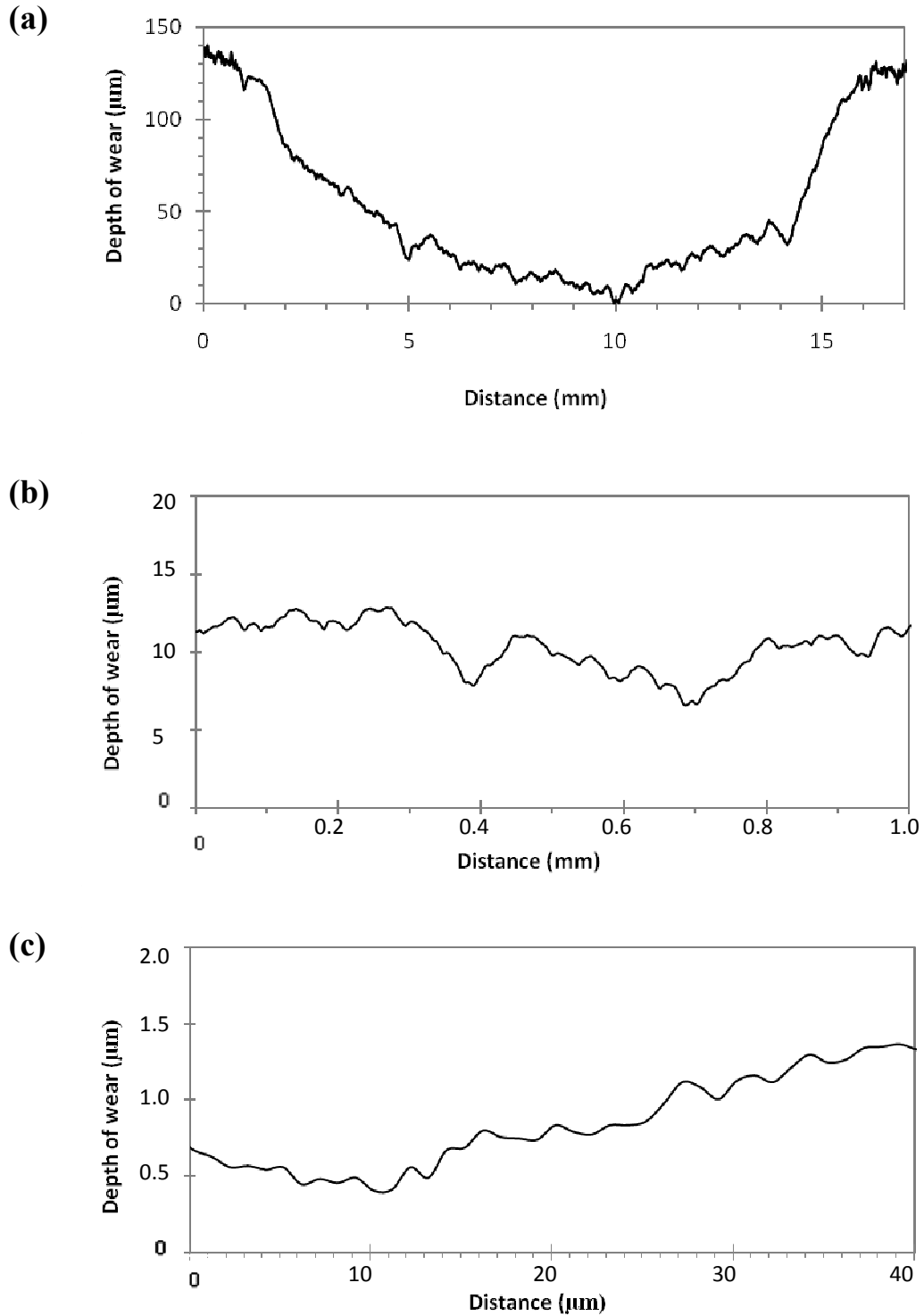


**Fig. 6.23** measured profiles of the Ni coating wear tracks with the alumina 60 across the wear scratch in different scales; (a) mm, (b)  $\text{mm} \times 10^{-1}$  and (c) micrometer.

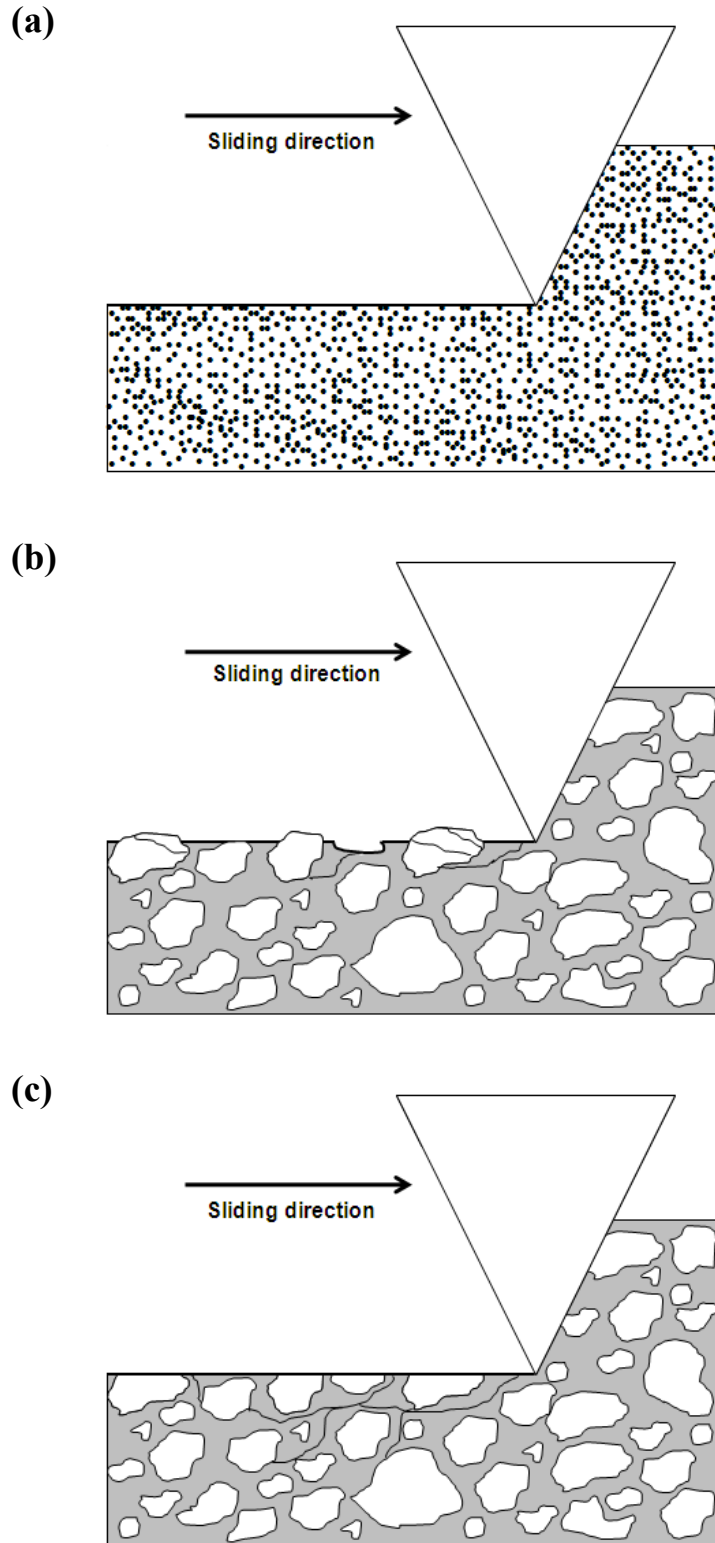


**Fig. 6.24** Sliding of an idealised conical abrasive particle which originates a groove on the surface of a composite material: (a) homogeneous behaviour; (b) heterogeneous behaviour with preferential wear of matrix followed by carbide cracking and pulling out and sub-surface cracking (for cobalt coatings), and (c) heterogeneous behaviour with cutting material followed by lateral and vertical cracking (for non-cobalt coatings).

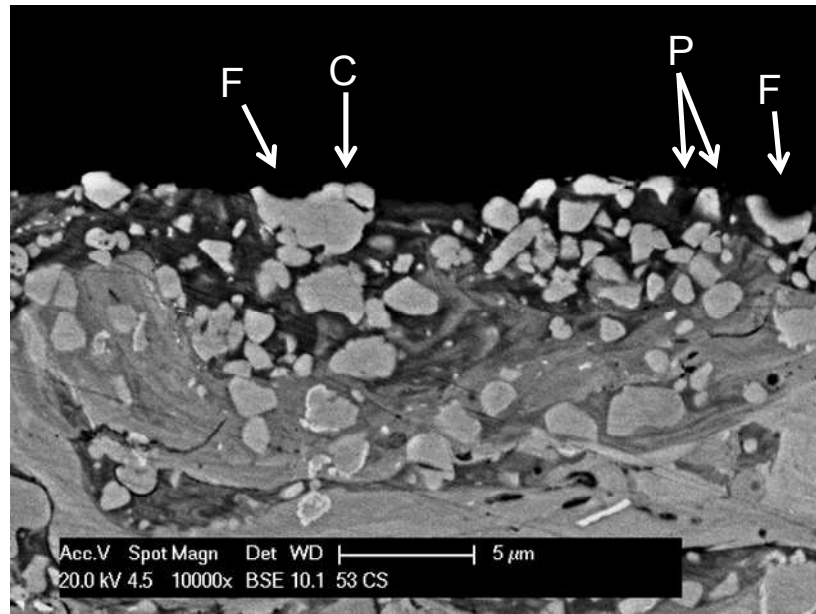


**Fig. 6.25** Cross-section BSE image of the Co-I following wear test with the silica abrasive showing preferential wear of the binder phase with fractured carbides, Carbide cracking and empty space of carbide grains after pulling out (F: fractured carbide, C: cracking of carbide, and P: pulled out carbide void).

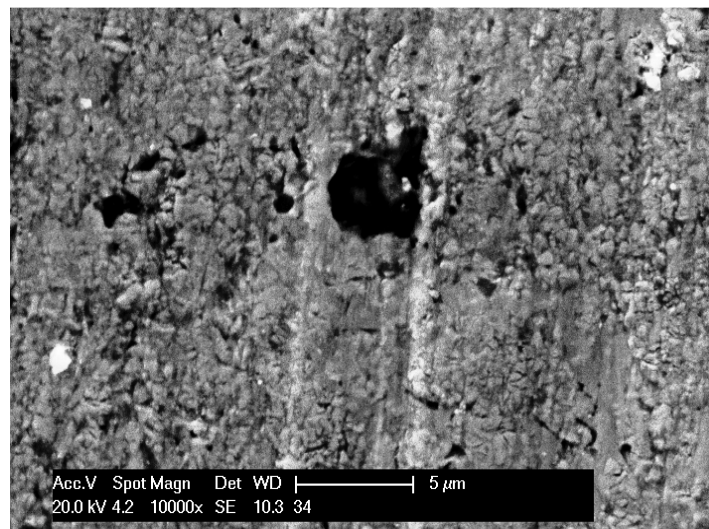


**Fig. 6.26** Starting point a single scratch from a surface open porosity in the wear area of the Fe coating following abrasion by alumina 60.

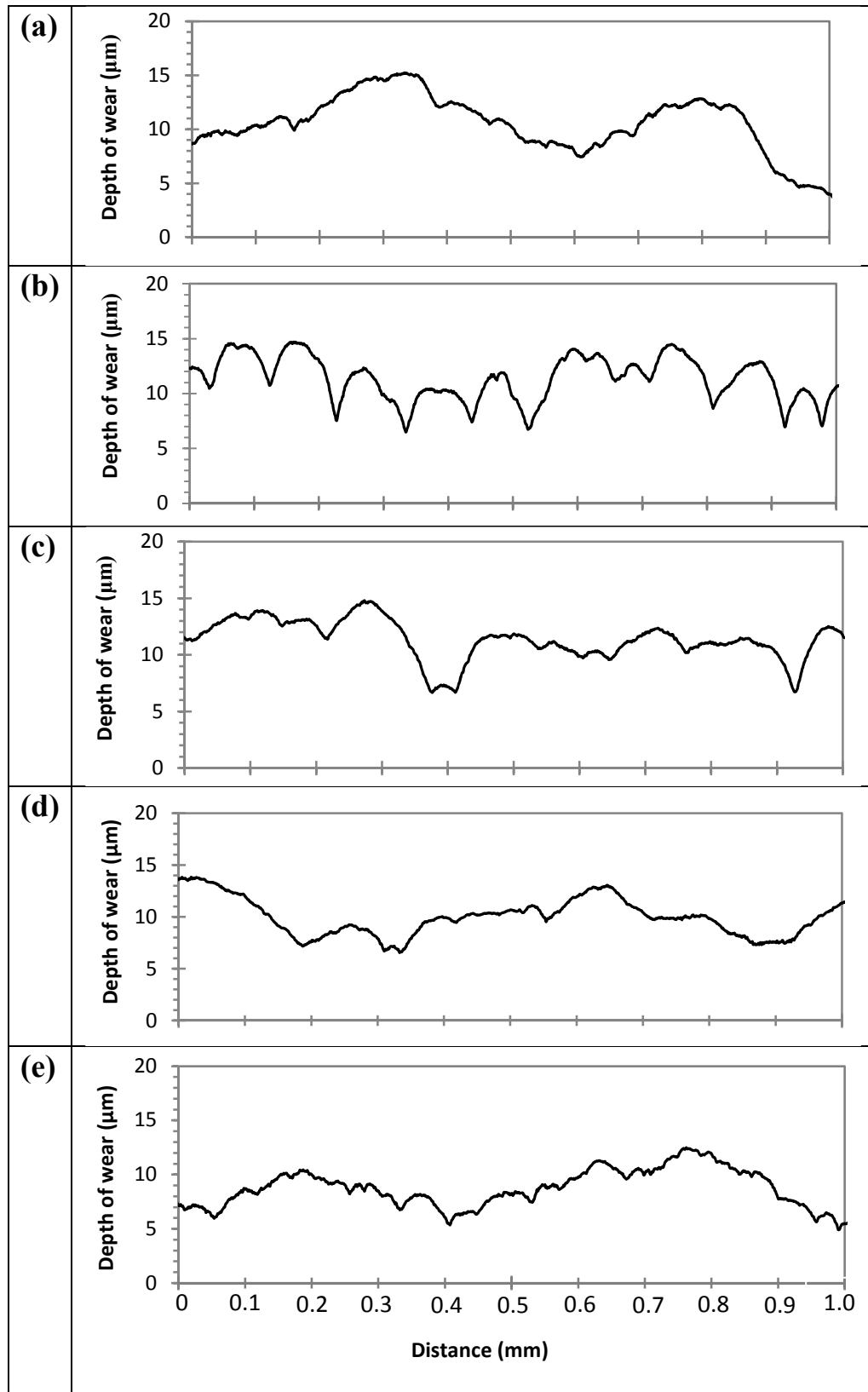


**Fig. 6.27** Measured profiles of the wear tracks following abrasion with alumina at the highest applied load across the wear scratch for: a) Ni, b) Fe, c) Co-I, d) Co-II, and e) Co-III coatings.

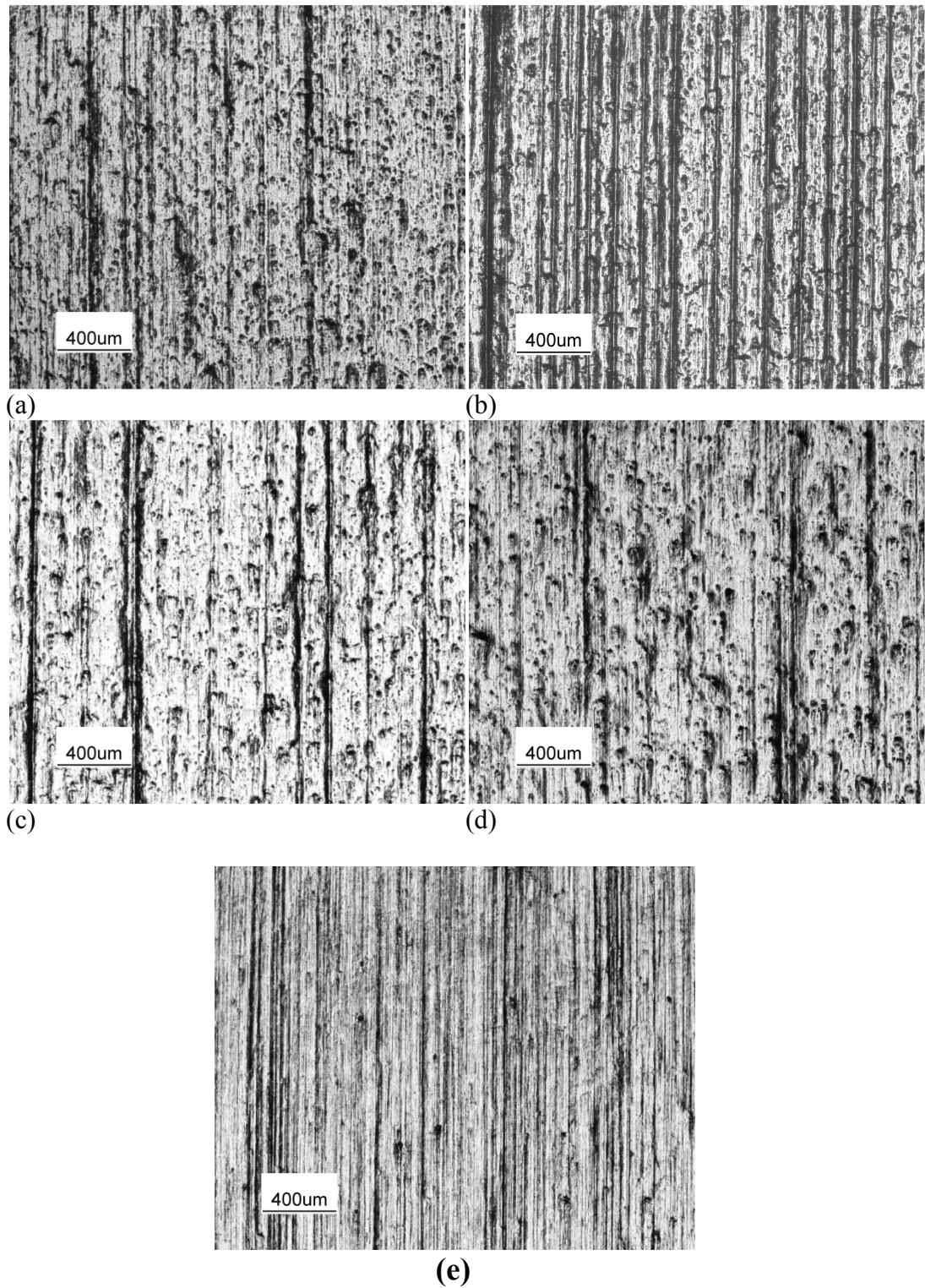


**Fig. 6.28** Optic microscopy plan view images of wear scars following abrasive wear with alumina 60 for: (a) Ni, (b) Fe, (c) Co-I, (d) Co-II, and (e) Co-III.

# Chapter 7

---

## Conclusions

---

### 7.1 Abrasion of Steel Substrates

In this part of the work, abrasive wear tests were carried out in two groups; firstly the abrasion of three steels with a bottom-ash from a biomass-fired power station and, secondly the abrasive wear of five steels with conventional silica sand.

Abrasion of three steels of significantly different hardness in the dry-sand rubber-wheel test has shown that as well as the ratio of abrasive to sample hardness being a significant factor in controlling the wear rates observed, the fracture of the abrasive particles can also influence wear rates. A silica sand was employed as an abrasive; the silica was a strong particle and fracture was not seen under the test conditions employed. The behaviour of the three steels under test was as expected, with the wear rate increasing with load for each material, and with the wear rates of the steels decreasing with increasing hardness. A substantial increase in wear resistance was observed as the sample hardness became greater than the 5/6 of the abrasive hardness, associated with the localisation of plastic flow in the abrasive particle itself under these conditions.

An ash from a biomass-fired power station with a wide particle size distribution was also employed as an abrasive with the same three steels. Due to the relatively low hardness of the abrasive compared to the two harder steels (the Hardox and GFS), the wear rates were much lower for these materials than those observed with the silica abrasive, despite the fact that the ash was an angular abrasive and the silica was a rounded abrasive. Significant fragmentation of the ash abrasive was observed during the wear test. The fragmentation was primarily of the large particles in the distribution, and fragmentation of the abrasives was shown to be almost independent of the applied load in the wear test. Through single particle crushing tests and estimates of the loads per particle during the abrasion tests, it was shown that the particles above 425 $\mu\text{m}$  are likely to be crushed during the abrasion tests, and evidence for this was presented from sieve analysis of used abrasives. It is concluded that the large particles dominate the wear of the steels for this soft abrasive, and that the loads applied to these particles are controlled by the crushing strength of the particles rather than the overall applied load, resulting in the anomalous result that the wear rates of the steels are not proportional to applied load.

In the second group, the abrasion of five different grades of steels with conventional silica sand was studied. The results from this work have shown that the movement patterns of abrasive particles through the gap in the DSRW test are a function of both applied load and hardness of the material under test. It has been shown that particle sliding (grooving) is favoured by high applied loads and by high substrate hardness. A model of the particle motion in the contact has been developed, based upon the work of Fang et al. [10]. The effect of hardness on

particle motion is well predicted by the model; however, the effect of the applied load on particle motion is counter to that which is produced by the model, where the experiments show that sliding (grooving) was favoured by high loads.

## 7.2 HVOF-Sprayed WC Cermet Coatings

Five different WC-metal cermet powders were deposited to form coatings under the same spray conditions using a Top Gun HVOF spraying system on the mild steel substrates. These powders had different average carbide grain sizes and binder compositions. Characterisation of the coatings by a range of techniques showed that the five coatings contained retained WC and reaction products such as  $W_2C$  and W and an amorphous binder phase containing tungsten and carbon, while the starting powders of the all coatings showed only presence of WC and crystalline phase of metallic binder with no evidence of any other carbides. Chemical analysis also revealed that all the coatings had a lower overall carbon content than the powder from which they were sprayed. Although the Ni and Co-I coatings both exhibited high carbon losses, the Ni coating has the highest  $W_2C$  phase fraction and the Co-I with the lowest volume fraction of carbide has high dissolution of tungsten in the binder. This shows that solubility of W and C in the cobalt binders is higher than that in the non-cobalt binders resulting in higher  $W_2C$  phase fraction in the non-cobalt coatings and higher W saturated amorphous binder fraction in the cobalt coatings.

Fracture toughness of the coatings indicates two distinct groups; the non-cobalt group with low fracture toughness and the cobalt coatings having high fracture

toughness. Higher cohesion of the WC grains and binder and strong intersplat interfaces in the cobalt coatings seem to be responsible for this significant difference. This can be due to more melting during spraying and also good wetting of the carbide grains with the cobalt binders compared with those for the Ni and Fe coatings.

The hardness of thermally sprayed WC cermet coatings depends on the volume fraction of remaining hard phase of WC, the hardness of the binder phase and the microstructural properties such as porosity of coating, mean free path of the binder and WC grain size. Although the result from the hardness test shows a relatively high level of hardness for the all coatings, some differences within the hardness of coatings are evident. The Fe coating with the lowest carbon loss and the high volume fraction of carbide also has the highest fraction of retained WC phase resulting in the highest level of hardness. The Co-I coating with the highest carbon loss exhibits high dissolution of W in the binder resulting in a binder with higher hardness. The hardening of the cobalt matrix due to the solution of tungsten and carbon into the binder phase compensated the detrimental effect of decreases in the volume fraction of the carbides due to decarburization on the hardness.

### **7.3 Abrasion of the WC Cermet Coatings**

Three body abrasive wear tests were performed using a modified dry sand rubber wheel apparatus with alumina and silica abrasives under a range of applied loads to assess the wear resistance of the five coatings. It was generally found that:

- i) The five coatings exhibited increases in wear rate with applied load when abraded with both silica and alumina abrasives.
- ii) The ratio of abrasive particle hardness to coating hardness indicated that for all coatings, the abrasive wear by alumina is “hard” compared to that by silica which is “soft”.
- iii) For all the coatings, the silica abrasive showed evidence for particle rolling with significant indentation of the surface (three-body abrasion) while with the alumina abrasive, grooves along the direction of abrasive flow are apparent (two-body abrasion).

### **Abrasive Wear with Silica**

The wear results of all the coatings with silica abrasive show that the preferential wear followed by WC fragmentation and pullout observed as wear mechanism for the all coatings, although sub-surface cracking has also been observed as a mechanism for removal of material in the Ni and Fe cases. In these cases the removal of material occurs by both preferential removal matrix phase and a sub-surface cracking process.

The abrasive wear results with silica particles showed two distinct wear behaviours of the cobalt group and non-cobalt group coatings; the wear resistance for the non-cobalt group is considerably higher than that for cobalt group. Lower mean free path for the non-cobalt coatings compared with that for cobalt coatings may be responsible for this difference in wear behaviour of these two groups of coatings.

In the cobalt group coatings, the wear rate of the Co-I coating is lower than that for the Co-II and Co-III probably because of the higher degree of its bulk hardness due to the high hardness of its binder (high enrichment of W in the binder). In the non-cobalt group, the Ni had a higher wear rate than the Fe coating. The lower mean free path and higher hardness of the Fe compared with those for the Ni coating are probably the main reasons for this difference.

### **Abrasive Wear with Alumina**

The wear testing results of all the coatings with alumina abrasive show that two main wear mechanisms are involved in material removal from the coatings, namely plastic deformation and fracture. In the first stage of the wear, the passage of the hard and sharp abrasive particles causes plastic deformation of the surface, resulting in the formation of grooves. The displacement and removal of material in this mode depends on the depth of grooves and consequently the bulk hardness of the coatings. At the second stage, sub-surface material deformation leads to cracking, which propagates into the coating. In this stage, fracture is the predominant source of material degradation. This mechanism results in a high material removal rate in the coatings with low fracture toughness.

Porosity has an important role in formation of grooves and consequently removal material by the micro-scale mode. Open surface pores will serve as origins for wear scratches made by individual abrasive particles. Thus, a higher fraction of pores leads to more grooves and results in a higher wear rate; the Fe coating with the highest magnitude of porosity has the highest number of deep grooves.

At the first stage of the wear, for the cobalt group of coatings, wear was observed to occur by plastic deformation of the surface along with fracture of large carbide grains and the carbide skeleton. For the non-cobalt group of coatings, wear was observed to occur by plastic deformation followed by sub-surface cracking. In this stage, the higher porosity of the coatings has an important role in creating more grooves and consequently more material removal. The second stage of wear is the formation of sub-surface cracks followed by delamination of the surface layers. In this stage, the fracture toughness of the coating is much more important. For the Ni and Fe coatings, the low fracture toughness results in a high rate of material removal. While the bulk hardness controls wear rate in the first stage, the fracture toughness has significant role in the final stage of the wear.

## 7.4 Industrial Aspects

Applications of thermally sprayed wear resistant WC cermet coatings for industrial parts and tools surface have been widely developed. Depending on the purpose of these coatings and their operation conditions, different requirements to mechanical properties and microstructural characteristics of a coating are established. Therefore, it is important to investigate effect of technological spraying parameters and material compositions on the coating properties.

In this work, it has been observed that the reaction during spraying, the solubility of the WC in binder phase and adhesion between binder and carbides influence the mechanical properties and wear performances of thermally sprayed WC cermet coatings. Porosity has also an important role in formation of grooves and

consequently removal material under the hard abrasion. Furthermore, the mean free path parameter which is associated with WC grain size and binder content, has important role in wear resistance of thermally sprayed WC composite coatings under the soft abrasion. In summary, the important parameters need to be considered in using thermally sprayed WC composite coatings are:

- Predominant wear regime such as soft abrasion and hard abrasion.
- Thermal history of particle during spraying process. It can be controlled by spray parameters such as fuel type, fuel/oxygen ratio and gun design.
- Starting powder feedstock characteristics such as WC grain size, binder composition and binder content.

# Chapter 8

---

## Future Work

---

### **Modelling of particle Motion**

The mechanics of the contact between the particle and the rubber wheel in the DSRW has been addressed by modifying the model to consider the effect of increased applied load (and thus friction) on the moment equations upon which the model is built. This modification to the model is qualitative in nature, and it is recommended to develop a robust model which describes the motion of particles in the contact which in particular addresses the detail of the particle–rubber wheel contact mechanics.

### **Thermal spray parameters**

The thermal spray system or spraying parameters for all the coatings were the same in this study. To validate the effect of solubility of W and C in different binders on the characteristics of the deposited coatings, it is suggested that coatings are deposited with variations in the spray parameters or even the spray process. This will produce coatings with different degrees of reaction resulting in different microstructural and mechanical properties. Also measuring the temperature and velocity of particle in-flight during spraying process for each

coating would help to understand the development of microstructure of coatings after spraying.

### **Characterisation of Coatings**

An important suggestion is measuring the microhardness of the binders for all the coatings, since it can help to provide an understanding of the effect of microstructural developments on the binder hardness and as such, on the bulk hardness of the coatings. Since the binder phase is physically small, nanoscale indentation will be required.

### **TEM analysis**

Different decomposition degree of particles during spraying along with different binder compositions cause to occur various type and amount of crystallised carbide phases. It is recommended that TEM work (with EDS analysis of as-sprayed coatings to get a diffraction pattern) is carried out. These patterns can be compared with the pattern obtained with XRD results to determine nature of the carbides present in the structure of the coatings.

### **Abrasive Wear Test**

DSRW tests were performed under different applied loads with two types of abrasive particles. It is suggested to study the wear behaviour with other types of abrasives and/or the same abrasives with different range of particle sizes. This can provide a more detailed understanding of the effect of abrasive particle characteristics on the wear mechanism and wear rate of these group of coatings.

# References

---

1. Eyre, T.S., **1978**, *The mechanisms of wear*. Tribology International, 11(2): p. 91-96.
2. Misra, A. and I. Finnie, **1982**, *A REVIEW OF THE ABRASIVE WEAR OF METALS*. Journal of Engineering Materials and Technology-Transactions of the Asme, 104(2): p. 94-101.
3. Hutchings, I.M., **1992**, *Tribology: friction and wear engineering materials*: Edward Arnold. 273.
4. ASTM, **2001**, *Standard Test Method for Measuring Abrasion Using the Dry Sand/Rubber Wheel Apparatus*, in *ASTM International*. p. 256-267.
5. Hawk, J.A., R.D. Wilson, J.H. Tylczak, and O.N. Dogan, **1999**, *Laboratory abrasive wear tests: investigation of test methods and alloy correlation*. Wear, 225: p. 1031-1042.
6. Tylczak, J.H., J.A. Hawk, and R.D. Wilson, **1999**, *A comparison of laboratory abrasion and field wear results*. Wear, 225: p. 1059-1069.
7. Trezona, R.I., D.N. Allsopp, and I.M. Hutchings, **1999**, *Transitions between two-body and three-body abrasive wear: influence of test conditions in the microscale abrasive wear test*. Wear, 225: p. 205-214.
8. Shipway, P.H., **2004**, *A mechanical model for particle motion in the micro-scale abrasion wear test*. Wear, 257(9-10): p. 984-991.
9. Fang, L., Q.D. Zhou, and Y.J. Li, **1991**, *AN EXPLANATION OF THE RELATION BETWEEN WEAR AND MATERIAL HARDNESS IN 3-BODY ABRASION*. Wear, 151(2): p. 313-321.
10. Fang, L., X.L. Kong, J.Y. Su, and Q.D. Zhou, **1993**, *MOVEMENT PATTERNS OF ABRASIVE PARTICLES IN 3-BODY ABRASION*. Wear, 162: p. 782-789.
11. Stringer, J., **1995**, *PRACTICAL EXPERIENCE WITH WASTAGE AT ELEVATED-TEMPERATURES IN COAL COMBUSTION SYSTEMS*. Wear, 186(1): p. 11-27.
12. Colaço, R. and R. Vilar, **2003**, *A model for the abrasive wear of metallic matrix particle-reinforced materials*. Wear, 254(7-8): p. 625-634.
13. Gurland, J. and P. Bardzil, **1955**, *Relation of Strength, Composition, and Grain Size of Sintered WC-Co Alloys*. Transactions of the American Institute of Mining and Metallurgical Engineers, 203(2): p. 311-315.
14. Ogilvy, I.M., C.M. Perrott, and J.W. Suiter, **1977**, *On the indentation fracture of cemented carbide part I -- Survey of operative fracture modes*. Wear, 43(2): p. 239-252.
15. Perrott, C.M., **1978**, *On the indentation fracture of cemented carbide II -- the nature of surface fracture toughness*. Wear, 47(1): p. 81-91.
16. Zum Gahr, K.H., **1997**, *Wear by hard particles*. in *1997 World Tribology Congress*. London, England: Elsevier Sci Ltd.
17. Larsen-Basse, J., **1987**, *EFFECTS OF HARDNESS AND LOCAL FRACTURE TOUGHNESS ON THE ABRASIVE WEAR OF WC-Co ALLOYS*. in *I Mech E Conference Publications (Institution of Mechanical Engineers)*. London, Engl: Mechanical Engineering Publ Ltd.
18. Barbezat, G., A.R. Nicol, and A. Sickinger, **1993**, *Abrasion, erosion and scuffing resistance of carbide and oxide ceramic thermal sprayed coatings for different applications*. Wear, 162-164(Part 1): p. 529-537.
19. Kraak, T., W. Herlaar, J. Wolke, K. Degroot, E.A. Hyduk, and I.N.T. Amer Soc Met, **1992**, *Influence of Different Gases on the Mechanical and Physical Properties on HVOF Sprayed Tungsten Carbide Cobalt in Thermal Spray : International Advances in Coatings Technology*. Materials Park: Asm International.

## References

20. Nerz, J.E., B.A. Kushner, and A.J. Rotolico, **1992**, *Microstructural evaluation of tungsten carbide-cobalt coatings*. in *4th National Thermal Spray Conf.* Pittsburgh, Pennsylvania, USA: ASM.
21. Sarkar, A.D., **1980**, *Friction and wear*. Academic Press.
22. Kennedy, D.M. and M.S.J. Hashmi, **1998**, *Methods of wear testing for advanced surface coatings and bulk materials*. *Journal of Materials Processing Technology*, 77(1-3): p. 246-253.
23. Davis, J.R., **2001**, *Surface Engineering for Corrosion and Wear Resistance*: ASM International. 319.
24. Ala-Kleme, S., P. Kivikyto-Reponen, J. Liimatainen, J. Hellman, and S.P. Hannula, **2007**, *Abrasive wear properties of tool steel matrix composites in rubber wheel abrasion test and laboratory cone crusher experiments*. *Wear*, 263: p. 180-187.
25. Stachowiak, G.W. and A.W. Batchelor, **2005**, *Engineering Tribology*: Elsevier-Butterworth-Heinemann.
26. Bliczensderfer, R., B.W. Madsen, and J.H. Tylczak, **1985**, *Comparison of several types of abrasive wear tests*. in *Int Conf. Wear of Materials*. Vancouver, Canada: ASME.
27. Gates, J.D., **1998**, *Two-body and three-body abrasion: A critical discussion*. *Wear*, 214(1): p. 139-146.
28. Fang, L., W.M. Liu, D.S. Du, X.F. Zhang, and Q.J. Xue, **2004**, *Predicting three-body abrasive wear using Monte Carlo methods*. *Wear*, 256(7-8): p. 685-694.
29. Fang, L., Q.D. Zhou, and Q.C. Li, **1998**, *An experimental simulation of cutting wear in three-body abrasion*. *Wear*, 219(2): p. 188-194.
30. Rabinowicz, E., L.A. Dunn, and P.G. Russell, **1961**, *A study of abrasive wear under three-body conditions*. *Wear*, 4(5): p. 345-355.
31. Zum Gahr, K.H., **1988**, *Modelling of two-body abrasive wear*. *Wear*, 124(1): p. 87-103.
32. Misra, A. and I. Finnie, **1980**, *A CLASSIFICATION OF 3-BODY ABRASIVE WEAR AND DESIGN OF A NEW TESTER*. *Wear*, 60(1): p. 111-121.
33. Borik, F., **1976**, *Testing for Abrasive Wear*, in *Selection and Use of Wear Tests for Metals*, R.G. Bayer, Editor., ASTM. p. 30-44.
34. Moore, M.a., **1979**, *Abrasive Wear*, in *Treatise on Materials Science and Technology*, D. Scott, Editor., Academic Press: New York. p. 217-257.
35. Rabinowicz, E., **1965**, *Friction and Wear of Materials*. John Wiley: New York.
36. Prasad, S.V. and T.H. Kosel, **1984**, *A STUDY OF CARBIDE REMOVAL MECHANISMS DURING QUARTZ ABRASION .2. EFFECT OF ABRASIVE PARTICLE-SHAPE*. *Wear*, 95(1): p. 87-102.
37. Evans, A.G. and T.R. Wilshaw, **1976**, *Quasi-Static Solid Particle Damage in Brittle Solids*. *American Ceramic Society Bulletin*, 55(4): p. 400-400.
38. Moore, M.A. and P.A. Swanson, **1983**, *The effect of particle shape on abrasive wear: A comparison of theory and experiment*. in *the international conference on wear of materials* reston, Virginia: ASME.
39. Moore, M.A., **1981**, *Abrasive Wear*, in *Fundamentals of friction and wear of materials* D.A. Rigney, Editor., American Society for Metals: Ohio p. 73-118.
40. Deuis, R.L., C. Subramanian, and J.M. Yellup, **1998**, *Three-body abrasive wear of composite coatings in dry and wet environments*. *Wear*, 214(1): p. 112-130.
41. Swanson, P.A. and R.W. Klann, **1981**, *Abrasive wear studies using the wet sand and dry sand rubber wheel tests*. in *Wear of materials*. ASME.
42. Avery, H.S., **1961**, *The measurement of wear resistance*. *Wear*, 4(6): p. 427-449.
43. Richards, R.C., **1968**, *WEAR OF METALS BY RELATIVELY SOFT ABRASIVES*. *Wear*, 11(4): p. 245-&.
44. Larsenbasse, J. and E.T. Koyanagi, **1979**, *ABRASION OF WC-CO ALLOYS BY QUARTZ*. *Journal of Lubrication Technology-Transactions of the Asme*, 101(2): p. 208-211.

## References

45. Tabor, D., **1956**, *The physical meaning of indentation and scratch hardness*. British Journal of Applied Physics, 7(5): p. 159.
46. Larsen-Basse, J. and B. Premaratne, **1983**, *Effect of Relative Hardness on Transitions in Abrasive Wear Mechanisms* Wear of Materials Va ; 11-14 p. 161-166.
47. Gahlin, R. and S. Jacobson, **1999**, *The particle size effect in abrasion studied by controlled abrasive surfaces*. Wear, 224(1): p. 118-125.
48. Eyre, T.S., **1979**, *Wear Resistance of Metals*, in *Treatise on Materials Science and Technology*, D. Scott, Editor., Academic Press: New York. p. 363-442.
49. Hutchings, I.M., **1994**, *Tribological properties of metal matrix composites*. Materials Science and Technology, 10: p. 513-517.
50. Khrushchov, M.M., **1974**, *Principles of abrasive wear*. Wear, 28(1): p. 69-88.
51. Haworth, R.D. and Jr., **1949**, *The abrasion resistance of metals*. Trans. Am. Soc. Met., 41: p. 819-869.
52. García, I., A. Ramil, and J.P. Celis, **2003**, *A mild oxidation model valid for discontinuous contacts in sliding wear tests: role of contact frequency*. Wear, 254(5-6): p. 429-440.
53. Harris, S.J., G.G. Krauss, S.J. Simko, R.J. Baird, S.A. Gebremariam, and G. Doll, **2002**, *Abrasion and chemical-mechanical polishing between steel and a sputtered boron carbide coating*. Wear, 252(1-2): p. 161-169.
54. Inman, I.A., S. Datta, H.L. Du, J.S. Burnell-Gray, and Q. Luo, **2003**, *Microscopy of glazed layers formed during high temperature sliding wear at 750 °C*. Wear, 254(5-6): p. 461-467.
55. Holmes, D.R. and R.T. Pascoe, **1972**, *Strain/Oxidation Interactions in Steels and Model Alloys*. Materials and Corrosion, 23(10): p. 859-870.
56. Jiang, J., F.H. Stott, and M.M. Stack, **2004**, *A generic model for dry sliding wear of metals at elevated temperatures*. Wear, 256(9-10): p. 973-985.
57. Moore, M.A., **1987**, *Laboratory Simulation Testing for Service Abrasive Wear Environments in Wear of Materials*. Houston, Texas.
58. Avery, H.S., **1977**, *Classification and Precision of Abrasion Tests* in *Int Conf. on Wear of Materials*. New York, N.Y: ASME
59. ASTM, **2002**, *Standard Test Method for Jaw Crusher Gouging Abrasion Test*. ASTM International: West Conshohocken, PA , United States.
60. Swanson, P.A., **1993**, *Comparison of Laboratory Abrasion tests and Field Tests of Materials used in Tillage Equipment*, in *Tribology; wear Test Selection for Design and Application*, A.W. Ruff and R.G. Bayer, Editors., ASTM: Philadelphia. p. 80-99.
61. Borik, F., **1972**, *USING TESTS TO DEFINE INFLUENCE OF METALLURGICAL VARIABLES ON ABRASION*. Metals Engineering Quarterly, 12(2): p. 33-&.
62. Avery, H.S., **1981** *AN ANALYSIS OF THE RUBBER WHEEL ABRASION TEST*. in *Wear of materials*. San Francisco, CA, USA ASME.
63. Stevenson, A.N.J. and I.M. Hutchings, **1996**, *Development of the dry sand rubber wheel abrasion test*. Wear, 195(1-2): p. 232-240.
64. Moore, M.A., **1974**, *A review of two-body abrasive wear*. Wear, 27(1): p. 1-17.
65. Modi, O.P., B.K. Prasad, A.K. Jha, R. Dasgupta, and A.H. Yegneswaran, **2003**, *Low-Stress Abrasive Wear Behaviour of a 0.2% C Steel: Influence of Microstructure and Test Parameters*. Tribology Letters, 15(3): p. 249-255.
66. Skrifvars, B.J., P. Yrjas, J. Kinni, P. Siefen, and M. Hupa, **2005**, *The fouling behavior of rice husk ash in fluidized-bed combustion. 1. Fuel characteristics*. Energy & Fuels, 19(4): p. 1503-1511.
67. Skodras, G., P. Grammelis, and P. Basinas, **2007**, *Pyrolysis and combustion behaviour of coal-MBM blends*. Bioresource Technology, 98(1): p. 1-8.
68. de Sena, R.F., A. Claudino, K. Moretti, Í.C.P. Bonfanti, R.F.P.M. Moreira, and H.J. José, **2008**, *Biofuel application of biomass obtained from a meat industry*

## References

- wastewater plant through the flotation process--A case study. Resources, Conservation and Recycling, 52(3): p. 557-569.
69. Cuddon, A. and C. Allen, **1992**, *THE WEAR OF TUNGSTEN CARBIDE COBALT CEMENTED CARBIDES IN A COAL ASH CONDITIONER*. Wear, 153(2): p. 375-385.
70. Hall, M.L. and W.R. Livingston, **2002**, *Fly ash quality, past, present and future, and the effect of ash on the development of novel products*. Journal of Chemical Technology and Biotechnology, 77(3): p. 234-239.
71. Babcock&Wilcox, C., **1978**, *Steam. Its Generation and Use*. 1978.
72. Kerner, J.W. and G.W. Stetler, **2006**, *Ash cooling screws - A retrospective and looking ahead*. Journal of Energy Resources Technology-Transactions of the Asme, 128(2): p. 154-158.
73. Loo, S.v. and J. Koppejan, **2007**, *The Handbook of Biomass Combustion and Co-firing*.
74. Zachary, J., **2008**, *Options for reducing a coal-fired plant's carbon footprint, Part II*. Power, 152(7): p. 50-+.
75. Stewart, D.A., P.H. Shipway, and D.G. McCartney, **1999**, *Abrasive wear behaviour of conventional and nanocomposite HVOF-sprayed WC-Co coatings*. Wear, 225: p. 789-798.
76. Chen, H., C. Xu, Q. Zhou, I.M. Hutchings, P.H. Shipway, and J. Liu, **2005**, *Micro-scale abrasive wear behaviour of HVOF sprayed and laser-remelted conventional and nanostructured WC-Co coatings*. Wear, 258(1-4): p. 333-338.
77. Liao, H., B. Normand, and C. Coddet, **2000**, *Influence of coating microstructure on the abrasive wear resistance of WC/Co cermet coatings*. Surface and Coatings Technology, 124(2-3): p. 235-242.
78. Verdon, C., A. Karimi, and J.L. Martin, **1998**, *A study of high velocity oxy-fuel thermally sprayed tungsten carbide based coatings. Part I: Microstructures*. Materials Science and Engineering A, 246(1-2): p. 11-24.
79. Bolelli, G., V. Cannillo, L. Lusvardi, and S. Riccò, **2006**, *Mechanical and tribological properties of electrolytic hard chrome and HVOF-sprayed coatings*. Surface and Coatings Technology, 200(9): p. 2995-3009.
80. Zhao, L., M. Maurer, F. Fischer, R. Dicks, and E. Lugscheider, **2004**, *Influence of spray parameters on the particle in-flight properties and the properties of HVOF coating of WC-CoCr*. Wear, 257(1-2): p. 41-46.
81. Wayne, S. and S. Sampath, **1992**, *Structure/property relationships in sintered and thermally sprayed WC-Co*. Journal of Thermal Spray Technology, 1(4): p. 307-315.
82. Wayne, S.F., J.G. Baldoni, and S.T. Buljan, **1990**, *ABRASION AND EROSION OF WC-CO WITH CONTROLLED MICROSTRUCTURES*. Tribology Transactions, 33(4): p. 611-617.
83. Shipway, P.H. and J.J. Hogg, **2005**, *Dependence of microscale abrasion mechanisms of WC-Co hardmetals on abrasive type*. Wear, 259(1-6): p. 44-51.
84. Gant, A.J., M.G. Gee, and B. Roebuck, **2005**, *Rotating wheel abrasion of WC/Co hardmetals*. Wear, 258(1-4): p. 178-188.
85. Guilemany, J.M., J. Nutting, J.R. Miguel, and Z. Dong, **1995**, *Microstructure characterization of WC-Ni coatings obtained by HVOF thermal spraying*. Scripta Metallurgica et Materialia, 33(1): p. 55-61.
86. Berger, L.M., S. Saaro, T. Naumann, M. Kasparova, and F. Zahalka, **2008**, *Microstructure and properties of HVOF-sprayed WC-(W,Cr)<sub>2</sub>C-Ni coatings*. Journal of Thermal Spray Technology, 17(3): p. 395-403.
87. Espallargas, N., J. Berget, J.M. Guilemany, A.V. Benedetti, and P.H. Suegama, **2008**, *Cr<sub>3</sub>C<sub>2</sub>-NiCr and WC-Ni thermal spray coatings as alternatives to hard chromium for erosion-corrosion resistance*. Surface and Coatings Technology, 202(8): p. 1405-1417.

## References

88. Kasparova, M., F. Zahalka, S. Houdkova, and P. Ctibor, **2010**, *Abrasive wear of WC-NiMoCrFeCo thermally sprayed coatings in dependence on different types of abrasive sands*. Kovove Materialy-Metallic Materials, 48(1): p. 73-85.
89. Sobolev, V.V., J.M. Guilemany, J.R. Miguel, and J.A. Calero, **1996**, *Investigation of the development of coating structure during high velocity oxy-fuel (HVOF) spraying of WC-Ni powder particles*. Surface and Coatings Technology, 82(1-2): p. 114-120.
90. Engqvist, H. and N. Axén, **1999**, *Abrasion of cemented carbides by small grits*. Tribology International, 32(9): p. 527-534.
91. Larsenbasse, J., **1983**, *EFFECT OF COMPOSITION, MICROSTRUCTURE, AND SERVICE CONDITIONS ON THE WEAR OF CEMENTED CARBIDES*. Journal of Metals, 35(11): p. 35-42.
92. Larsen-Basse, J. and N. Devnani, **1986**, *BINDER EXTRUSION AS A CONTROLLING MECHANISM IN ABRASION OF WC-Co CEMENTED CARBIDES*. in *Institute of Physics Conference Series*. Rhodes, Gr.
93. Blombery, R.I., C.M. Perrot, and P.M. Robinson, **1974**, *Abrasive wear of tungsten carbide-cobalt composites. I. Wear mechanisms*. Materials Science and Engineering, 13(2): p. 93-100.
94. Jia, K. and T.E. Fischer, **1996**, *Abrasion resistance of nanostructured and conventional cemented carbides*. Wear, 200(1-2): p. 206-214.
95. Larsen-Basse, J., **1990**, *Role of microstructure and mechanical properties in abrasion*. Scripta Metallurgica et Materialia, 24(5): p. 821-826.
96. Baldoni, J.G., S.F. Wayne, and S.T. Buljan, **1986**, *CUTTING-TOOL MATERIALS - MECHANICAL-PROPERTIES - WEAR-RESISTANCE RELATIONSHIPS*. Asle Transactions, 29(3): p. 347-352.
97. Chermant, J.L. and F. Osterstock, **1976**, *FRACTURE TOUGHNESS AND FRACTURE OF WC-CO COMPOSITES*. Journal of Materials Science, 11(10): p. 1939-1951.
98. Saito, H., A. Iwabuchi, and T. Shimizu, **2006**, *Effects of Co content and WC grain size on wear of WC cemented carbide*. Wear, 261(2): p. 126-132.
99. O'Quigley, D.G.F., S. Luyckx, and M.N. James, **1997**, *An empirical ranking of a wide range of WC-Co grades in terms of their abrasion resistance measured by the ASTM standard B 611-85 test*. International Journal of Refractory Metals and Hard Materials, 15(1-3): p. 73-79.
100. Gee, M.G., A. Gant, and B. Roebuck, **2007**, *Wear mechanisms in abrasion and erosion of WC/Co and related hardmetals*. Wear, 263(1-6): p. 137-148.
101. Pirso, J., M. Viljus, K. Juhani, and S. Letunovits, **2009**, *Two-body dry abrasive wear of cermets*. Wear, 266(1-2): p. 21-29.
102. Usmani, S., S. Sampath, D.L. Houck, and D. Lee, **1997**, *Effect of carbide grain size on the sliding and abrasive wear behavior of thermally sprayed WC-Co coatings*. Tribology Transactions, 40(3): p. 470-478.
103. Li, M., D. Shi, and P.D. Christofides, **2005**, *Modeling and control of HVOF thermal spray processing of WC-Co coatings*. Powder Technology, 156(2-3): p. 177-194.
104. Khan, M.S.A. and T.W. Clyne, **1997**, *Microstructure and Abrasion Resistance Of WC-Co coatings Produced by High Velocity Oxy-Fuel Spraying*. in *United Thermal Spray Conf*. Indianapolis, Indiana: ASM.
105. Stewart, D.A., P.H. Shipway, and D.G. McCartney, **2000**, *Microstructural evolution in thermally sprayed WC-Co coatings: comparison between nanocomposite and conventional starting powders*. Acta Materialia, 48(7): p. 1593-1604.
106. Yang, Q., T. Senda, and A. Ohmori, **2003**, *Effect of carbide grain size on microstructure and sliding wear behavior of HVOF-sprayed WC-12% Co coatings*. Wear, 254(1-2): p. 23-34.

## References

107. Watanabe, M., A. Owada, S. Kuroda, and Y. Gotoh, **2006**, *Effect of WC size on interface fracture toughness of WC-Co HVOF sprayed coatings*. Surface and Coatings Technology, 201(3-4): p. 619-627.
108. Berget, J. and T. Rogne, **2001**, *A summary of recent developments of HVOF sprayed ceramic-metallic coatings for corrosion and wear resistance*. Thermal Spray 2001: New Surfaces for a New Millennium, ed. C.C. Berndt, K.A. Khor, and E.F. Lugscheider. Materials Park: ASM International. 1157-1163.
109. Legoux, J.G., B. Arsenault, L. Leblanc, V. Bouyer, and C. Moreau, **2002**, *Evaluation of four high velocity thermal spray guns using WC-10% Co-4% Cr cermets*. Journal of Thermal Spray Technology, 11(1): p. 86-94.
110. Wood, R.J.K., **2010**, *Tribology of thermal sprayed WC-Co coatings*. International Journal of Refractory Metals and Hard Materials, 28(1): p. 82-94.
111. Khan, M.S.A. and T.W. Clyne, **1996**, *Microstructure and abrasion resistance of plasma sprayed cermet coatings*. in *9th national Thermal Spray Conf.* Cincinnati, Ohio: ASM.
112. Di Girolamo, G., L. Pilloni, G. Pulci, and F. Marra, **2009**, *Tribological Characterization of WC-Co Plasma Sprayed Coatings*. Journal of the American Ceramic Society, 92(5): p. 1118-1124.
113. Sánchez, E., E. Bannier, M. Salvador, V. Bonache, J. García, J. Morgiel, and J. Grzonka, **2009**, *Microstructure and Wear Behavior of Conventional and Nanostructured Plasma-Sprayed WC-Co Coatings*. Journal of Thermal Spray Technology, 19(5): p. 964-974.
114. Kreye, H., S. Zimmermann, and P. Heinrich, **1995**, *The role of the fuel gas in the HVOF process*. in *14th International Thermal Spray Conference*. Kobe, Japan: High Temperature Society of Japan.
115. Sudaprasert, T., P.H. Shipway, and D.G. McCartney, **2003**, *Sliding wear behaviour of HVOF sprayed WC-Co coatings deposited with both gas-fuelled and liquid-fuelled systems*. Wear, 255: p. 943-949.
116. Picas, J.A., M. Punset, M.T. Baile, E. Martin, and A. Forn, **2009**, *Properties of WC-CoCr Based Coatings Deposited by Different HVOF Thermal Spray Processes*. Plasma Processes and Polymers, 6: p. S948-S953.
117. Marple, B. and R. Lima, **2005**, *Process temperature/velocity-hardness-wear relationships for high-velocity oxyfuel sprayed nanostructured and conventional cermet coatings*. Journal of Thermal Spray Technology, 14(1): p. 67-76.
118. Schwetzke, R. and H. Kreye, **1999**, *Microstructure and properties of tungsten carbide coatings sprayed with various high-velocity oxygen fuel spray systems*. Journal of Thermal Spray Technology, 8(3): p. 433-439.
119. Verdon, C., A. Karimi, and J.L. Martin, **1997**, *Microstructural and analytical study of thermally sprayed WC-Co coatings in connection with their wear resistance*. Materials Science and Engineering A, 234-236: p. 731-734.
120. Li, C.J., Y.Y. Wang, G.J. Yang, A. Ohmori, and K.A. Khor, **2004**, *Effect of solid carbide particle size on deposition behaviour, microstructure and wear performance of HVOF cermet coatings*. Materials Science and Technology, 20: p. 1087-1096.
121. Li, C.J., A. Ohmori, and K. Tani, **1999**, *Effect of WC particle size on the abrasive wear of thermally sprayed WC-Co coatings*. Materials and Manufacturing Processes, 14(2): p. 175-184.
122. Kumari, K., K. Anand, M. Bellacci, and M. Giannozzi, **2010**, *Effect of microstructure on abrasive wear behavior of thermally sprayed WC-10Co-4Cr coatings*. Wear, 268(11-12): p. 1309-1319.
123. Ghabchi, A., T. Varis, E. Turunen, T. Suhonen, X. Liu, and S.P. Hannula, **2009**, *Behavior of HVOF WC-10Co4Cr Coatings with Different Carbide Size in Fine and Coarse Particle Abrasion*. Journal of Thermal Spray Technology, 19(1): p. 368-377.

## References

124. Tu, J.P., Z.Y. Mao, J. Li, and L.Z. Wang, **1991**, *Erosion behavior of a thermal sprayed Ni-WC coating at high temperature*. in *4th National Thermal Spray Conf.* Pittsburgh, Pennsylvania, USA: ASM.
125. Hartfieldwunsch, S.E., **1994**, *THE EFFECT OF MICROSTRUCTURE ON THE WEAR BEHAVIOR OF THERMAL SPRAY COATINGS*. 1994 Thermal Spray Industrial Applications: p. 19-24.
126. Chivavibul, P., M. Watanabe, S. Kuroda, and K. Shinoda, **2007**, *Effects of carbide size and Co content on the microstructure and mechanical properties of HVOF-sprayed WC-Co coatings*. *Surface and Coatings Technology*, 202(3): p. 509-521.
127. Qiao, Y., Y. Liu, and T. Fischer, **2001**, *Sliding and abrasive wear resistance of thermal-sprayed WC-CO coatings*. *Journal of Thermal Spray Technology*, 10(1): p. 118-125.
128. Kim, H., Y. Kweon, and R. Chang, **1994**, *Wear and erosion behavior of plasma-sprayed WC-Co coatings*. *Journal of Thermal Spray Technology*, 3(2): p. 169-178.
129. Almond, E.A., **1986**, *Indentation phenomena and wear of surfaces and edges*. *Materials Science and Technology*, 2: p. 641-646.
130. Lee, H.C. and J. Gurland, **1978**, *Hardness and deformation of cemented tungsten carbide*. *Materials Science and Engineering*, 33(1): p. 125-133.
131. DePalo, S., **2000**, *Fracture Toughness of HVOF Sprayed WC-Co Coatings*. *Proceedings of the 1st International Thermal Spray Conference*, 1(1): p. 245-250.
132. Smith, R.W., **1995**, *THERMAL SPRAYING I: POWDER CONSOLIDATION-FROM COATING TO FORMING*. *Journal of Metals*, 47(8): p. 32-39.
133. Pawlowski, L., **1995**, *The Science and Engineering of Thermal Spray Coatings*. New York, NY, USA: Wiley and Sons.
134. Kuroda, S., J. Kawakita, M. Watanabe, and H. Katanoda, **2008**, *Warm spraying-a novel coating process based on high-velocity impact of solid particles*. *Science and Technology of Advanced Materials*, 9(3): p. 17.
135. Brandt, O.C., **1995**, *MECHANICAL-PROPERTIES OF HVOF COATINGS*. *Journal of Thermal Spray Technology*, 4(2): p. 147-152.
136. Fauchais, P., G. Montavon, and G. Bertrand, **2010**, *From Powders to Thermally Sprayed Coatings*. *Journal of Thermal Spray Technology*, 19(1): p. 56-80.
137. Kubel, E.J., **1990**, *POWDERS DICTATE THERMAL-SPRAY-COATING PROPERTIES*. *Advanced Materials & Processes*, 138(6): p. 24-&.
138. de Villiers Lovelock, H.L., **1998**, *Powder/processing/structure relationships in WC-Co thermal spray coatings: A review of the published literature*. *Journal of Thermal Spray Technology*, 7(3): p. 357-373.
139. Coulson, W. and S.J. Harris, **1996**, *The microstructure of WC-Co coatings produced by HVOF spraying with liquid fuel*. in *INTERFINISH 96 World Congress*. Birmingham, England: Inst Metal Finishing.
140. Kamali, R. and A.R. Binesh, **2009**, *The importance of sensitive parameters effect on the combustion in a high velocity oxygen-fuel spray system*. *International Communications in Heat and Mass Transfer*, 36(9): p. 978-983.
141. Kim, B.H. and D.S. Suhr, **2001**, *Characteristics of HVOF-sprayed WC-Co cermet coatings affected by WC particle size and fuel/oxygen ratio*. *Materials Transactions*, 42(5): p. 833-837.
142. Irons, G., **1995**, *Thermal Spray Application Speeds*. in *14th International Thermal Spray Conference*. Kobe, Japan.
143. Jarosinski, W.J., M.F. Gruninger, and C.H. Londry, **1993**, *Characterization of Tungsten Carbide Cobalt Powders and HVOF Coatings*. in *National thermal spray conference*. Anaheim, California: ASM.

## References

144. Fincke, J.R., W.D. Swank, and D.C. Haggard, **1994**, *Comparison of the Characteristic of HVOF and plasma thermal spray*. in *7th National Thermal Spray conf.* Boston, Massachusetts: ASM
145. Karimi, A., C. Verdon, and G. Barbezat, **1993**, *MICROSTRUCTURE AND HYDROABRASIVE WEAR BEHAVIOR OF HIGH-VELOCITY OXY-FUEL THERMALLY SPRAYED WC-CO(CR) COATINGS*. *Surface & Coatings Technology*, 57(1): p. 81-89.
146. Li, C., A. Ohmori, and Y. Harada, **1996**, *Formation of an amorphous phase in thermally sprayed WC-Co*. *Journal of Thermal Spray Technology*, 5(1): p. 69-73.
147. Ramnath, V. and N. Jayaraman, **1989**, *CHARACTERIZATION AND WEAR PERFORMANCE OF PLASMA SPRAYED WC-CO COATINGS*. *Materials Science and Technology*, 5(4): p. 382-388.
148. Li, C.J., A. Ohmori, and Y. Harada, **1996**, *Effect of powder structure on the structure of thermally sprayed WC-Co coatings*. *Journal of Materials Science*, 31(3): p. 785-794.
149. Berger, L.-M., **2007**, *Hardmetals as thermal spray coatings*. *Powder Metallurgy*, 50: p. 205-214.
150. Shaw, K.G., M.F. Gruninger, and W.J. Jarosinski, **1994**, *HIGH TEMPERATURE INTERMETALLIC BINDERS FOR HVOF CARBIDES*. in *1994 Thermal Spray Industrial Applications*.
151. Sampath, S. and H. Herman, **1996**, *Rapid solidification and microstructure development during plasma spray deposition*. *Journal of Thermal Spray Technology*, 5(4): p. 445-456.
152. Guilemany, J.M., J. Nutting, J.R. Miguel, and Z. Dong, **1997**, *Microstructure formation of HVOF sprayed WC-Ni coatings deposited on low alloy steel*. *Materials and Manufacturing Processes*, 12(5): p. 901-909.
153. Shipway, P.H., D.A. Stewart, and D.G. McCartney, **2000**, *The role of substrate temperature during HVOF spraying in coating residual stress state and abrasive wear performance*. *9th Nordic Symposium on Tribology Nordtrib 2000, Vol 3*, 202: p. 990-999.
154. Guilemany, J., J. de Paco, J. Miguel, and J. Nutting, **1999**, *Characterization of the W<sub>2</sub>C phase formed during the high velocity oxygen fuel spraying of a WC + 12 pct Co powder*. *Metallurgical and Materials Transactions A*, 30(8): p. 1913-1921.
155. Grimberg, I., K. Soifer, B. Bouaifi, U. Draugelates, and B.Z. Weiss, **1997**, *Tungsten carbide coatings deposited by high-velocity oxy-fuel spraying on a metallized polymeric substrate*. *Surface and Coatings Technology*, 90(1-2): p. 82-90.
156. Deshpande, S., A. Kulkarni, S. Sampath, and H. Herman, **2004**, *Application of image analysis for characterization of porosity in thermal spray coatings and correlation with small angle neutron scattering*. *Surface and Coatings Technology*, 187(1): p. 6-16.
157. Nolan, D. and M. Samandi, **1997**, *Revealing true porosity in WC-Co thermal spray coatings*. *Journal of Thermal Spray Technology*, 6(4): p. 422-424.
158. Sobolev, V.V. and J.M. Guilemany, **1994**, *ANALYSIS OF THE POROSITY FORMATION DURING HVOF SPRAYING*. *1994 Thermal Spray Industrial Applications*: p. 733-741.
159. Tekmen, C., H. Cetinel, A. Turk, and E. Celik, **2004**, *Wear behaviour of plasma sprayed WC-Ni coatings*, in *Euro Ceramics Viii, Pts 1-3*, H. Mandal and L. Ovecoglu, Editors., Trans Tech Publications Ltd: Zurich-Uetikon. p. 589-592.
160. Qiao, Y., T.E. Fischer, and A. Dent, **2003**, *The effects of fuel chemistry and feedstock powder structure on the mechanical and tribological properties of HVOF thermal-sprayed WC-Co coatings with very fine structures*. *Surface and Coatings Technology*, 172(1): p. 24-41.

## References

161. Milman, Y.V., S. Luyckx, and I.T. Northrop, **1999**, *Influence of temperature, grain size and cobalt content on the hardness of WC-Co alloys*. International Journal of Refractory Metals & Hard Materials, 17(1-3): p. 39-44.
162. Zhao, L., M. Maurer, F. Fischer, and E. Lugscheider, **2004**, *Study of HVOF spraying of WC-CoCr using on-line particle monitoring*. Surface and Coatings Technology, 185(2-3): p. 160-165.
163. Jacobs, L., M. Hyland, and M. De Bonte, **1999**, *Study of the influence of microstructural properties on the sliding-wear behavior of HVOF and HVOF sprayed WC-cermet coatings*. Journal of Thermal Spray Technology, 8(1): p. 125-132.
164. Vinayo, M.E., F. Kassabji, J. Guyonnet, and P. Fauchais, **1985**, *Plasma sprayed WC-Co coatings: Influence of spray conditions (atmospheric and low pressure plasma spraying) on the crystal structure, porosity, and hardness*. Journal of Vacuum Science & Technology A: Vacuum, Surfaces, and Films, 3(6): p. 2483-2489.
165. Harvey, M.D.F., A.J. Sturgeon, F.J. Blunt, and S.B. Dunkerton, **1995**, *Investigation into the relationship between fuel gas selection, wear performance and microstructure of HVOF sprayed WC-Co coatings*. in *14th International Thermal Spray Conference*. Kobe, Japan: high Temperature Society of Japan.
166. Sahraoui, T., S. Guessasma, M. Ali Jeridane, and M. Hadji, **2010**, *HVOF sprayed WC-Co coatings: Microstructure, mechanical properties and friction moment prediction*. Materials & Design, 31(3): p. 1431-1437
167. Fang, Z.Z., **2005**, *Correlation of transverse rupture strength of WC-Co with hardness*. International Journal of Refractory Metals and Hard Materials, 23(2): p. 119-127.
168. O'Quigley, D.G.F., S. Luyckx, and M.N. James, **1996**, *New results on the relationship between hardness and fracture toughness of WC-Co hardmetal*. Materials Science and Engineering: A, 209(1-2): p. 228-230.
169. Krakhmalev, P.V., J. Sukumaran, and A. Gård, **2007**, *How hardmetals react to wear: Nano is not always the best*. Metal Powder Report, 62(2): p. 30-35.
170. SulzerMetco, **2008**, *Thermal Spraying*. 2008.
171. López Cantera, E. and B.G. Mellor, **1998**, *Fracture toughness and crack morphologies in eroded WC-Co-Cr thermally sprayed coatings*. Materials Letters, 37(4-5): p. 201-210.
172. Rubber, **2007**, *Vulcanised or thermoplastic-determination of hardness (hardness between 10 IRHD and 100 IRHD)*. p. 1-19.
173. Sikong, L., H. Hashimoto, and S. Yashima, **1990**, *Breakage behavior of fine particles of brittle minerals and coals*. Powder Technology, 61(1): p. 51-57.
174. Hiramatsu, Y. and Y. Oka, **1966**, *Determination of the tensile strength of rock by a compression test of an irregular test piece*. International Journal of Rock Mechanics and Mining Sciences & Geomechanics Abstracts, 3(2): p. 89-90.
175. Gates, J.D., M.S. Dargusch, J.J. Walsh, S.L. Field, M.J.P. Hermand, B.G. Delaup, and J.R. Saad, **2008**, *Effect of abrasive mineral on alloy performance in the ball mill abrasion test*. Wear, 265(5-6): p. 865-870.
176. Misra, A. and I. Finnie, **1981**, *ON THE SIZE EFFECT IN ABRASIVE AND EROSION WEAR*. Wear, 65(3): p. 359-373.
177. Shipway, P.H. and I.M. Hutchings, **1991**, *The influence of particle properties on the erosive wear of sintered boron carbide*. Wear, 149(1-2): p. 85-98.
178. Dube, N.B. and I.M. Hutchings, **1999**, *Influence of particle fracture in the high-stress and low-stress abrasive wear of steel*. Wear, 233-235: p. 246-256.
179. Torrance, A.A., **2005**, *Modelling abrasive wear*. Wear, 258(1-4): p. 281-293.
180. Jacobson, S., P. Wallén, and S. Hogmark, **1988**, *Fundamental aspects of abrasive wear studied by a new numerical simulation model*. Wear, 123(2): p. 207-223.
181. Hwang, T.W. and S. Malkin, **1999**, *Upper bound analysis for specific energy in grinding of ceramics*. Wear, 231(2): p. 161-171.

## References

182. Pintaude, G., D.K. Tanaka, and A. Sinatora, **2003**, *The effects of abrasive particle size on the sliding friction coefficient of steel using a spiral pin-on-disk apparatus*. *Wear*, 255: p. 55-59.
183. Goddard, J. and H. Wilman, **1962**, *A theory of friction and wear during the abrasion of metals*. *Wear*, 5(2): p. 114-135.
184. Bui, Q.V. and J.P. Ponthot, **2002**, *Estimation of rubber sliding friction from asperity interaction modeling*. *Wear*, 252(1-2): p. 150-160.
185. Barquins, M. and A.D. Roberts, **1986**, *RUBBER-FRICTION VARIATION WITH RATE AND TEMPERATURE - SOME NEW OBSERVATIONS*. *Journal of Physics D-Applied Physics*, 19(4): p. 547-563.
186. Schallamach, A., **1971**, *How does rubber slide?* *Wear*, 17(4): p. 301-312.
187. Barquins, M., **1985**, *Sliding friction of rubber and Schallamach waves -- A review*. *Materials Science and Engineering*, 73: p. 45-63.
188. Deladi, E.L., M.B. de Rooij, and D.J. Schipper, **2007**, *Modelling of static friction in rubber-metal contact*. *Tribology International*, 40(4): p. 588-594.
189. Barquins, M., **1993**, *Friction and wear of rubber-like materials*. *Wear*, 160(1): p. 1-11.
190. Barquins, M., **1992**, *Adherence, friction and wear of rubber-like materials*. *Wear*, 158(1-2): p. 87-117.
191. Hutchings, I.M., **1987**, *Wear by particulates*. *Chemical Engineering Science*, 42(4): p. 869-878.
192. Blau, P.J., **1992**, *ASM Handbook: Friction, Lubrication, and Wear Technology* Vol. 18: ASM International.
193. ASTM, **2005**, *Standard Specification for Low-carbon Nickel-Chromium-Molybdenum*, ASTM, Editor., ASTM International: USA. p. 4.
194. Sandvik, G., **2010**, *Material datasheets: Kanthal alloys*. 2010 23 Sep 2010]; <http://www.kanthal.com/products/material-datasheets/>.
195. Fullman, R.L., **1953**, *MEASUREMENT OF PARTICLE SIZES IN OPAQUE BODIES*. *Transactions of the American Institute of Mining and Metallurgical Engineers*, 197(3): p. 447-452.
196. Evans, A.G. and T.R. Wilshaw, **1976**, *Quasi-Static Solid Particle Damage in Brittle Solids .1. Observations, Analysis and Implications*. *Acta Metallurgica*, 24(10): p. 939-956.
197. Rodriguez, M., J. Klisans, L. Bavaresco, A. Scagni, and F. Arenas, **2001**, *Wear resistance of HVOF sprayed carbide coatings*. *Thermal Spray 2001: New Surfaces for a New Millennium*: p. 1061-1068.
198. Scussel, H.J., **1992**, *Friction and Wear of Cemented Carbides*, in *ASM Handbook*, S.D. Henry, Editor., ASM International. p. 795-800.
199. Christensen, M., S. Dudy, and G. Wahnstrom, **2002**, *First-principles simulations of metal-ceramic interface adhesion: Co/WC versus Co/TiC*. *Physical Review B*, 65(4): p. 9.
200. Guilemany, J.M., J.M. Miguel, S. Vizcaino, and F. Climent, **2001**, *Role of three-body abrasion wear in the sliding wear behaviour of WC-Co coatings obtained by thermal spraying*. *Surface and Coatings Technology*, 140(2): p. 141-146.
201. Nahvi, S.M., P.H. Shipway, and D.G. McCartney, **2009**, *Particle motion and modes of wear in the dry sand-rubber wheel abrasion test*. *Wear*, 267(11): p. 2083-2091.